Synthesis and Mechanical Characterization of Aligned Carbon Nanotube Metal- and Carbon-Matrix Nanocomposites

by

Amy Ruth Vanderhout

S.B., Massachusetts Institute of Technology (2018)

Submitted to the Department of Aeronautics and Astronautics
in partial fulfillment of the requirements for the degree of

Master of Science in Aerospace Engineering

at the

MASSACHUSETTS INSTITUTE OF TECHNOLOGY

May 2020

© Massachusetts Institute of Technology 2020. All rights reserved.

Author . . . .
Department of Aeronautics and Astronautics
May 19, 2020

Certified by. . . . .
Brian L. Wardle
Professor of Aeronautics and Astronautics
Thesis Supervisor

Accepted by . . . .
Sertac Karaman
Associate Professor of Aeronautics and Astronautics
Chair, Graduate Program Committee

Synthesis and Mechanical Characterization of Aligned Carbon Nanotube Metal- and Carbon-Matrix Nanocomposites

by

Amy Ruth Vanderhout

Submitted to the Department of Aeronautics and Astronautics
on May 19, 2020, in partial fulfillment of the
requirements for the degree of
Master of Science in Aerospace Engineering

Abstract

Carbon nanotube (CNT) assemblies are seeing increasing use in engineering applications due to their advantaged, mass-specific physical properties. The high strength-to-weight ratio, electrical and thermal conductivity, and elastic properties make CNTs ideal for many aerospace, automotive, and electrical applications. In structural materials, CNTs are an outstanding candidate to provide nano-reinforcement, both in hybrid composites and nanocomposites, and they have been found to improve the hardness, yield strength, and conductivity of their matrix material. Additional enhancement of these matrices can be realized by using aligned CNTs (A-CNTs) of increased volume fraction, as explored in this work.

In this thesis, ceramic matrix nanocomposites (CMNCs), specifically A-CNT/carbon matrix nanocomposites (A/C-NCs), are synthesized by first infusing a carbon precursor resin into A-CNT arrays with CNT volume fractions (v_f) ranging from 1-30 vol%, and then pyrolyzing the resin to create a carbon matrix around the A-CNTs. Previous work with A/C-NC hardness suggests that such a lightweight, superhard material may rival the density-normalized hardness of diamond at high v_f. Various processes were refined and tested in this work, yielding microscale void-free A/C-NCs up to 30% v_f, with an ~7% improvement in hardness over baseline pyrolytic carbon (PyC) for 1% v_f A/C-NCs and ~10% improvement in hardness for 5% v_f A-CNTs. A reinfusion (*i.e.* an initial infusion/pyrolysis cycle with three additional reinfusion/pyrolysis cycles) procedure was developed and implemented, and testing is recommended as immediate future work. Although hardness determination of these reinfused samples is left for future work, the X-ray μCT images of the final A/C-NCs after the fourth infusion show excellent infusion and few voids, suggesting that high hardness will be achieved.

This thesis also explores and develops synthesis techniques for metal matrix nanocomposites (MMNCs), focusing on an aluminum matrix. As the surface energy of A-CNTs is not conducive to wetting by Al (and many other metals), this surface energy must first be altered to allow Al matrix infusion for consistent composite fabrication. TiO_2 is conformally decorated onto ~100 μm-tall A-CNT arrays *via* atomic layer

deposition (ALD). A reduction process for the TiO_2 coating was developed, and a reduction to TiH_2 was determined to be promising, as the TiH_2 will not oxidize prior to Al infusion but can easily be reduced in a vacuum oven apparatus designed specifically to meet the needs of Al infusion. Towards MMNCs, both solder and aluminum matrices are infused into the TiO_2-decorated A-CNTs. The solder experiments yielded mixed success, as the results suggest that both the reduction and the vacuum infusion steps are important factors determining successful wetting. Although Al infusion into an A-CNT array was unsuccessful without a dedicated Al infusion apparatus, molten Al was found to wet Ti well, which suggests that the Ti coating may allow for successful A-CNT wetting. Additional recommendations are provided to further refine the A/Al-NC fabrication process to improve Al infusion.

Thesis Supervisor: Brian L. Wardle
Title: Professor of Aeronautics and Astronautics

Acknowledgments

Writing a thesis takes a village. First, I want to thank my research advisor Professor Brian Wardle for this experience. He was always prepared with out-of-the-box solutions to overcome roadblocks in the research process. He continually challenged me to keep improving, better preparing me for my future endeavors. This work would not have been possible if not for the support of everyone in Necstlab. Thank you to Luiz, for your guidance and creative problem-solving on the aluminum matrix work, for the sense of humor you brought to the lab, and for the conversations surrounding robotics and NASA. Next, I want to thank Ashley for first guiding me as a UROP and then as a graduate student. I appreciate your assistance at all hours, and our "tag-team" work with ceramic matrices. Thank you to Jeonyoon, Reed, and Xinchen for your assistance with various processes and lab equipment, as well as your encouragement and editing prowess as I wrote this thesis! I also want to thank all the professors and lab staff in AeroAstro, Materials Science and Engineering, and the Institute for Soldier Nanotechnologies for their advice on my projects and their technical support. A special thanks to Shaymus Hudson in the DMSE Metlab for his critiques and help with the unusual materials I brought to the polishing lab, and to Professor Chris Schuh for his expertise on aluminum matrices. Finally, this thesis is dedicated to my friends and family. Their support, advice, and ability to listen over the busy days and long nights kept me sane when the workload was not. I would not have been able to write this thesis without their backing.

ported by the U. S. Army Research Laboratory through the Oak Ridge Associated Universities (ORAU) Journeyman Fellowship.

Contents

List of Figures

17

18

19

22

List of Tables

Abbreviations and Symbols

Abbreviations

μCT	X-Ray Micro-Computed Tomography
A-CNT	Aligned Carbon Nanotube
A-PNC	Aligned CNT-Polymer Nanocomposite
A/Al-NC	Aligned-CNT/Aluminum-Matrix Nanocomposite
A/C-NC	Aligned-CNT/Carbon-Matrix Nanocomposite
ALD	Atomic Layer Deposition
BNNT	Boron Nitride Nanotube
C/C	Carbon Fiber/Carbon Matrix
CMC	Ceramic Matrix Composite
CMNC	Ceramic Matrix Nanocomposite
CNF	Carbon Nanofiber
CNT	Carbon Nanotube
CTE	Coefficient of Thermal Expansion
CVD	Chemical Vapor Deposition
CVI	Chemical Vapor Infiltration

DPA	Displacements per Atom
E-Beam	Electron-Beam Evaporator
EDS	Energy-Dispersive X-Ray Spectroscopy
FRP	Fiber-Reinforced Polymer
FSP	Friction Stir Processing
GND	Geometrically Necessary Dislocation
HACNT	Horizontally-Aligned Carbon Nanotube
HIP	Hot Isostatic Pressing
HPDC-CE	High Pressure Die Casting with Cyclic Extrusion
MMC	Metal Matrix Composite
MMNC	Metal Matrix Nanocomposite
MWCNTs	Multi-Walled CNTs
NC	Nanocomposite
OoO	Out of Oven
P-F	Phenol-Formaldehyde
PAN	Polyacrylonitrile
PIP	Polymer-Infiltration-Pyrolysis
PNC	Polymer Nanocomposite
py-PDA	Pyrolyzed Polydopamine
PyC	Pyrolytic Carbon
sccm	Standard Cubic Centimeters per Minute

SEM	Scanning Electron Microscope, Scanning Electron Microscopy
SPS	Spark Plasma Sintering
SWCNTs	Single-Walled CNTs
TDMAT	tetrakis(dimethylamino)titanium
TGA	Thermogravimetric Analysis
TMA	Trimethylaluminum
UTS	Ultimate Tensile Strength
VACNT	Vertically Aligned Carbon Nanotube
VARI	Vacuum-Assisted Resin Infusion
XPS	X-Ray Photoelectron Spectroscopy
XRD	X-Ray Powder Diffraction

Symbols

b	Burger's Vector
d_g	Diameter of the Grain, on Average
d_p	Diameter of the Particle
G	Shear Modulus
h	Tube Height
H_V	Vickers Hardness
k_y	Strengthening Coefficient
l	Length
r_c	Effective Radius

S	Spreading Parameter
T	Temperature
T_g	Glass Temperature
t	Infusion Time
t_p	Thickness of the Particle
u	Velocity of Liquid Flowing through a Tube
v_f	Volume Fraction of A-CNTs
v_p	Volume Fraction of Particles
$\alpha(T)$	Coefficient Representing the Material's CTE as a Function of Temperature
γ_L	Surface Tension of the Liquid with the Vapor
γ_S	Surface Tension of the Solid with the Vapor
γ_{SL}	Surface Tension between the Solid and the Liquid
ΔP	Capillarity Pressure
$\Delta \sigma_{CTE}$	CTE Mismatch Contribution
$\Delta \sigma_{HP}$	Hall-Petch Effect Contribution
$\Delta \sigma_{LT}$	Load Transfer Effect Contribution
$\Delta \sigma_{OR}$	Orowan Contribution
η	Viscosity of a Liquid
θ	Contact Angle
$\pi_{S/L}$	Tendency of the Liquid to Spread

$\pi_{S/V}$ Opposes the Spreading of the Liquid

σ_m Yield Strength of the Matrix

τ_m Shear Strength of the Matrix

Chapter 1

Introduction

Rapid developments in a variety of industries has led to demand for new materials that are able to perform in extreme environments: under higher loads, at higher temperatures, and in multiple functions, all at a weight savings. Carbon nanotube (CNT) architectures, due to their mass-advantaged[19] mechanical,[20–23] electrical,[24,25] and thermal properties,[26] have the opportunity when leveraged in bulk composites to fill this need, particularly in high-value industries, such as aerospace and defense, automotive, electronics, energy, and nuclear.

1.1 Carbon Nanotubes (CNTs) as Structural Reinforcement

High strength-to-weight ratio materials are important in a variety of industries, such as making lightweight armor for the defense industry or lighter, more fuel-efficient cars in the automotive industry. The aerospace industry, however, may have the highest demand for lightweight materials in a variety of applications. At the cost of ∼$1,000 per pound of payload,[27] the aerospace industry places a relatively high value on lightweight, stiff, and strong materials. To achieve NASA's goal of a constant human presence on the moon, lightweight materials are vital to maximize the payload capacity and send the required resources to the astronauts. Carbon fiber reinforced

plastic/polymer (CFRP) advanced composites, comprised of carbon microfibers in various polymer matrices, compete with aluminum for many lightweight aerospace applications due to their mass-advantaged mechanical (strength and stiffness) properties, seen in Figure 1-1. Additionally, these materials may need to withstand harsh environments, such as high temperatures, those containing hydrogen propellant[28] or the ionizing radiation (outside of the Van Allen radiation belt), protecting both the astronauts and the electronics.[29] For launch and landing of spacecraft, the materials will need to withstand high temperatures in addition to providing a lightweight, stiff, and strong structure.[30–32] It is rare to find a material that can serve multiple functions (*e.g.* self-healing structures or structural radiation shields), but CNTs may be the key to making materials that can be utilized in many of these applications, either as the sole reinforcing fiber, or as a complement to microfibers in traditional advanced composites.[33]

In addition to their excellent mechanical properties, the electrical properties of CNTs make them superior candidates for electronics applications, including field effect transistors,[28,34] sensors,[28,34] semiconductors,[28] as well as optoelectronics and electrochemical devices, such as solar cells, flat panel displays, and organic light emitting diodes (LEDs).[35] The energy industry also takes advantage of the outstanding electrical properties of CNTs, especially since next-generation energy storage devices must be able to provide a high density of energy storage[28] and CNT supercapacitors can deliver 1–2 orders of magnitude improvement in areal energy and power density over the current state-of-the-art supercapacitors.[36] While no one material can fulfill all these needs simultaneously, CNT architectures can be engineered to exhibit combinations of these properties in bulk materials. In the remainder of this chapter, the mechanical properties of CNTs and their use in hierarchical, multifunctional materials are discussed and an overview of the work in this thesis is given.

This thesis is motivated by the advantaged mass-specific mechanical[20–24], electrical,[20,37,38] and thermal,[24,37,39,40] properties of CNTs. CNTs are seamless cylinders of graphene sheets comprised of either a single sheet (single-walled CNTs, or SWCNTs) or multiple sheets (multi-walled CNTs, or MWCNTs).[20,37] CNTs have low density

(1.5-2 g cm^{-3})[19] and a tensile strength of 11–63 GPa for individual MWCNTs,[21] resulting in a tensile strength that is orders of magnitude higher than steel at a fraction of the weight of steel.[39] CNTs have also been experimentally determined to have a Young's modulus in the range of 270 to 950 GPa for MWCNTs[21] and ∼1000 GPa for SWCNTs. However, the modulus decreases in bulk assemblies: the Young's modulus of CNT bundles was found to be 80 GPa.[41] Given these properties, CNTs show an unrivaled performance when compared to other structural materials for modulus and strength per unit density, as illustrated in Figure 1-1[1].
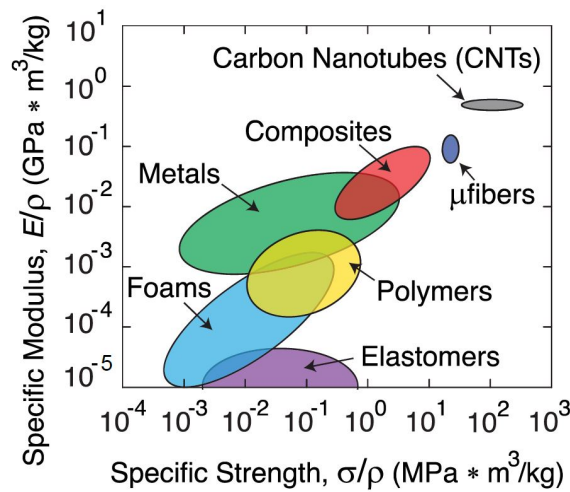
Figure 1-1: Ashby chart comparing the specific strength and specific modulus of structural materials. CNTs are clearly advantaged, with a significantly higher specific modulus and specific strength than any other known material.[1]

In addition to their outstanding mechanical properties, CNTs have excellent thermal and electrical properties as well. CNTs are ideal for high temperature applications, as they are chemically stable up to 2800°C in vacuum[39] and up to ∼500°C in air without surface modifications.[38] CNTs and Buckypaper, aligned CNT paper, have a reported and theoretical electrical and thermal conductivities that are high relative to other materials, particularly for their densities.[24,40]

Due to these excellent mechanical, electrical, and thermal properties, CNTs are ideal candidates for multifunctional, hierarchical structural composites. Hierarchical materials are designed to mimic the hard and tough materials in nature[42] by encompassing a variety of length scales, with intricate 1, 2, and 3D architectures

ranging from the nanoscale up to the macroscopic/bulk scale.[43] Typically, these bioinspired hierarchical materials at several scales are made from a hard phase, in this case the CNTs, and a soft phase, the matrix.[43] These composites can exhibit both extrinsic toughening, through using the hard phase to contact shield the crack tip, and intrinsic toughening, through enlarging the plastic zone of the soft phase (*e.g.* fibrilar sliding in collagen bone).[42,43] An additional benefit of the hierarchical materials is their ability to perform multiple functions; natural hierarchical materials are often porous, which provides means for mass transport and also decreases the composite's density.[43] CNT-reinforced materials can also enable multifunctionality, including heat dissipation, radiation shielding, and energy harvesting in addition to their more standard primary structural function.[8]

1.2   Aligned Carbon Nanotube (A-CNT) Arrays for Multifunctional Structural Composites

The aforementioned advantaged properties of CNTs can be challenging to achieve at an industrial scale, particularly due to the propensity of CNTs to agglomerate and cause stress concentrations.[44,45] However, arrays of aligned CNTs (A-CNTs) have desirable properties in bulk. A-CNT arrays have high compressive strengths near 15 MPa, which makes them ideal for compressive applications, such as vibration dampers and compressible electrodes.[35,46] A-CNT arrays are also useful for high-temperature electrical applications, as they have a negative temperature coefficient of resistance.[25] Additionally, CNTs have been reported to increase the thermal conductivity of the base polymer by double with 1 vol% A-CNT arrays and as much as 18.5 times the base polymer with 16.7 vol% A-CNTs.[26] To fully take advantage of the distinctive, mass-advantaged properties of CNTs, this thesis focuses on A-CNT arrays for their aligned morphology, leading to tunable anisotropic properties, and, as explained later, an advantaged processing mechanism due to capillarity.[20,37]

There exist a variety of methods to synthesize A-CNTs. Many methods produce

horizontally-aligned CNTs (HACNTs) and the alignment can be achieved both during and after CNT growth. Both substrate-bound chemical vapor deposition CVD growth and floating catalyst CVD are common CNT synthesis techniques that allow various degrees of alignment to be obtained during, or post, growth. For floating catalyst CVD, the catalyst gas (typically ferrocene) is introduced into the reactor either before or during growth.[47–49] During CNT growth through a CVD method, ultralong CNTs can be grown and aligned using the flow of gasses. For a horizontal growth using the substrate-bound technique, the CNTs are rooted on the substrate but grow from a catalyst particle at the tip in what is considered a kite mechanism tip growth.[50–52] Other methods for *in situ* horizontal alignment of CNTs include creating HACNT films from A-CNTs grown on Al foil and wound on a spindle,[53] and CNTs grown in the presence of magnetic[54] and electric[55,56] fields. Post-growth techniques also include the use of magnetic and electric fields,[57–59] where CNTs are ultrasonically dispersed in either polymer matrix[60] or solvents and then are aligned with a magnetic field, or a DC/AC electrical field.[61–63] Additional methods use fluid flow; CNTs in a solution are placed on a substrate and either hung to dry, such that the fluid flow aligns the CNTs as it dries,[64,65] or placed in the flow of N_2 to align the CNTs.[66] Other HACNT methods can be referenced in the review article by Ma *et al.*[67] Although most methods for aligning CNTs concern HACNT, vertically aligned CNTs (VACNTs) are also common and are typically vertically aligned as-grown from a CVD growth procedure.[68–71] In this thesis, the term A-CNT refers to vertically-aligned CNT arrays synthesized *via* substrate-bound CVD.

CNT nanocomposites (NCs) traditionally use a polymer matrix and are referred to as polymer nanocomposites (PNCs) and in the case of aligned CNTs, aligned CNT-polymer nanocomposites (A-PNCs).[36,72,73] For consistency with terminology in this thesis, A-PNCs from the literature would be designated as A/P-NCs, but we continue throughout with A-PNCs established by the extant literature. A-CNTs have been applied to polymer composites, such as CNT heaters for out of oven (OoO) curing[74] and as interlaminar reinforcements in order to increase the fracture toughness: an 115% increase was observed over a range of loadings from 60% to 90% and a 249%

increase was observed for high-cycle fatigue at 60% of the static strength load.[75] Additionally, HACNTs within a polymer matrix were measured to exhibit a high areal capacitance of 3.1 F cm^{-2} at 5 mA cm^{-2},[36] showing that A-CNTs can improve both the electrical and mechanical properties of their polymer matrices.

Polymer matrices are popular because polymers wet CNTs well and can fully infiltrate a CNT array. However, their relatively low operating temperatures, due to the relatively low glass transition temperature (T_g) of the polymer matrix, make them unsuitable for higher-temperature applications. Additionally, polymers have low strength compared to typical structural materials like aluminum and steel, and can degrade in the presence of radiation.[76]

Since A-CNT architectures are ideal reinforcements to create next-generation multifunctional materials, but the traditional polymer matrices are limited in their applications, this thesis focuses on a type of ceramic-matrix nanocomposite (CMNC), A-CNT/carbon-matrix nanocomposites (A/C-NCs, previously called A-CMNCs[71,77–80]) and a metal-matrix nanocomposite (MMNC), A-CNT/aluminum-matrix nanocomposites (A/Al-NCs). Some research has been completed to fabricate both A/C-NCs and A/Al-NCs, but their desired properties have not been obtained in previous work. Given the many applications in extreme environments for both A/C-NCs and A/Al-NCs, this thesis investigates techniques for synthesizing both of these materials, and their characterization and preliminary mechanical properties. These synthesis techniques are evaluated throughout the process and suggestions for future work are included.

1.3 Thesis Outline

In this thesis, the processing parameters of A/C-NCs are studied for composites ranging from 1 vol.% to 30 vol.% A-CNT loading and future paths for improving the process are suggested. The hardness of the A/C-NCs as a function of vol.% is investigated and compared to theoretical predictions. Processing of A/Al-NCs is also explored and future work to refine this process is suggested.

Chapter 2 provides an overview of the mechanical properties and typical synthesis methods of previously synthesized CMNCs. Chapter 2 also provides an overview of typical A/Al-NC processing procedures, their successes and limitations, and their properties. Chapter 3 discusses the objectives of the thesis: developing and mechanically testing higher hardness A/C-NCs by infusing higher volume fraction (v_f) A-CNT arrays as well as developing synthesis methods for A/Al-NCs with 100 μm-scale A-CNTs. Additionally, Chapter 3 explains the general approach used to synthesize these NCs.

Chapter 4 and Chapter 5 discuss the A/C-NCs in more depth. Chapter 4 discusses the synthesis parameters of A/C-NCs and how these parameters were determined. Procedures are discussed and evaluated for success. Chapter 5 reviews the Vickers hardness testing procedure and compares the experimental hardness values for composites up to 30 vol.% A-CNTs to the theoretically calculated values. Scanning electron microscope (SEM) imaging and micro-computed tomography (μCT) imaging are used to visualize the resin infusion and elucidate the hardness trends.

Chapter 6 focuses on different processing options for A/Al-NCs. This chapter examines the success of various synthesis methods, particularly through Raman spectroscopy, SEM, energy dispersive X-ray spectroscopy (EDS), and X-ray powder diffraction (XRD). Insight into the successes and challenges is provided as well as directions for future work. Finally, Chapter 7 discusses conclusions from this thesis and overall recommendations for future work.

Chapter 2

Background

The advantaged, mass-specific properties of CNTs make them ideal reinforcements for a variety of matrices. In addition to improving the mechanical properties of a matrix, CNTs can also improve the thermal and electrical properties, as well as provide reinforcement in harsh environments. For these reasons, CNT-reinforced composites, broadly termed nanocomposites (NCs), are excellent candidates for a host of multifunctional applications, especially when alignment is controlled, as discussed in Chapter 1. Aligned-CNT/carbon-matrix nanocomposites (A/C-NCs), a type of ceramic-matrix nanocomposite (CMNC), and aligned-CNT/aluminum-matrix nanocomposites (A/Al-NCs), a type of metal-matrix nanocomposite (MMNC), are particularly useful multifunctional materials, as these composites can withstand harsher, higher-temperature environments, due in part to their carbon and metal matrices, respectively. This thesis focuses specifically on aligned-CNT (A-CNT) composites synthesized with these two classes of matrices, reinforced with A-CNTs at increasing packing densities, where incorporating CNTs at high volume fractions (v_fs) can be challenging. This chapter first contains an overview of current-generation fabrication procedures for aligned-CNT Polymer Nanocomposites (A-PNCs) as a baseline for work with other matrices. The following sections review traditional and state-of-the-art fabrication procedures and the resulting material properties for both A/C-NCs and A/Al-NCs.

The purpose of this chapter is to provide the necessary background for understand-

ing both the motivation behind this thesis as well as the methodology used throughout the work in this thesis. Additional background information will be included in the subsequent thesis chapters as necessary.

2.1 Overview of A-CNT Polymer Nanocomposite (A-PNC) Fabrication

As discussed in Chapter 1, the advantaged properties of CNTs, especially when normalized to density, make them ideal reinforcements for a variety of matrices, and they have proved useful in synthesizing a variety of next-generation multifunctional architectures. CNT-polymer NCs can be fabricated in a variety of ways. Shear mixing, mechanically dispersing the CNTs in the polymer, [81–84] and ultrasonication, using ultrasonic waves and the cavitation of bubbles in the solution to disperse the CNTs in the polymer, [84–86] are particularly common methods. Both methods impart significant energy, although shear mixing imparts less energy than ultrasonication, and can cause the CNTs to break into smaller pieces through a process called scission. [84–88] Additionally, both methods use unaligned CNTs, which average the advantaged properties of the CNTs over all directions in the matrix instead of strategically reinforcing one direction. This section focuses specifically on the fabrication of A-PNCs, which better utilize advantageous properties of CNTs compared to other CNT-polymer matrix work. The synthesis of CNT NCs with advanced matrices, discussed in Section 2.2 and 2.3, draws on the work with A-PNCs as this work better preserves the properties of the CNTs.

Liquid polymer matrices, with viscosities over a large range (10-1,000,000 cP), [68] can relatively easily be infused into A-CNT arrays via capillary-driven wetting for the fabrication of A-PNCs. The work of Cebeci *et al.* shows experimentally that the epoxy resin is drawn up the sidewalls of the CNTs through capillary forces when only the tips of the A-CNTs are in contact with the resin. [45] By combining the Washburn-Darcy equation (Equation 2.1) [45] with a form of the Young-Dupré equation (Equation

2.2)[45], it is possible to calculate the time required for the forest to wet through capillary-driven wetting (Equation 2.3)[45]:

$$u = -\frac{r_c^2 \Delta P_c}{8\eta h} \tag{2.1}$$

$$\Delta P_c = \frac{2\gamma_L cos(\theta)}{r_c} \tag{2.2}$$

$$t = -\frac{4\eta h^2}{\gamma_L cos(\theta) r_c} \tag{2.3}$$

where u is the velocity of liquid flowing through a tube, r_c is the effective radius, since the wetting is occurring between CNTs, ΔP is the capillary pressure, η is the viscosity of the liquid, h is the height of the tube, γ_L is the surface tension of the liquid, θ is the contact angle of the liquid on the solid, and t is the infusion time. Contact angle measurements show that, when increasing the A-CNT v_f from 1% v_f to 20% v_f, the contact angle increased from 40° to 70°, which suggests that infusion becomes more difficult at higher v_f.[45] Initially wetting the mm-scale A-CNTs took only 27 seconds, but resin continued to fill the array for up to 50 seconds.[45] Although it is possible to infuse resin into A-CNT arrays of up to 20% v_f over a wide viscosity range[14,68] simply through capillary-driven wetting, this becomes more challenging at higher v_f. Additionally, some A-PNCs are fabricated with vacuum-assisted infusion, much like the vacuum-assisted resin infusion (VARI) methods commonly applied in making fiber-reinforced polymer (FRP) composites,[89,90] or with polymer Chemical Vapor Deposition (CVD) methods.[36,91,92] Neither of these methods have been utilized extensively for > 1% v_f as-grown A-CNT arrays. There is little data of their effectiveness at higher v_f, but VARI methods will be used to augment infusion processes in this work.

2.2 A-CNT/Carbon-Matrix Nanocomposites (A/C-NCs)

A/C-NCs have excellent mechanical[30,31,93–95] and thermal[19,30–32,95,96] properties, and maintain these properties at high temperatures.[19,31,97,98] CNT CMNCs are stable in air at temperatures from 550 to 1000°C[97] and in argon at temperatures in excess of 1650°C.[98] Additionally, some CNT CMNCs are reported to have a Young's Modulus of ∼1.6 GPa[99] and CNTs may improve the tensile and shear strengths of carbon fiber/carbon matrix (C/C) composites[95] as well as the fracture toughness and flexural strength of other ceramic matrices.[19] CNT/Carbon CMNCs have a thermal diffusivity four times greater than C/C composites,[2] and superconducting conductivities at elevated temperatures.[100] These properties make CNT CMNCs ideal candidates for a variety of multifunctional applications, particularly high-temperature compressive environments where excellent mechanical properties, such as high hardness and light weight, are required. Although there are multiple ceramic matrices that may be reinforced by CNTs, this thesis focuses specifically on carbon matrices.

A/C-NCs are advantaged candidates for replacing or enhancing C/C composites, as these materials are needed in high-temperature environments. C/C composites were initially developed to meet the needs of the aerospace and defense industry,[31] particularly the 1960's space program,[30,32] due to their low density, high thermal conductivity, and superior mechanical properties at elevated temperatures.[31] C/C composites have been used as thermal protection systems on launch and reentry vehicles for both commercial programs (*e.g.* the Space Shuttle) and defense programs (*e.g.* nuclear missiles) because of their ability to perform as a heat sink even at temperatures close to ∼2000°C.[30–32,96,101–103] A/C-NCs, with their improved mechanical properties, could replace traditional C/C composites in these areas while also serving a greater structural role. Additionally, solid rocket motors use C/C composites for the nozzle, especially the throat, due to their high temperature resistance and low ablation.[30,31] A/C-NCs would be an outstanding replacement for solid rocket nozzles, as even 0.15% v_f addition of CNTs can enhance ablation resistance by ∼30%.[94]

Since their advent in the space industry, C/C composites have been applied as brake pads because C/C composites withstand high temperatures, conduct heat away from the wheels quickly, and exhibit better wear characteristics than previous brake pad materials, such as asbestos. C/C composites were first applied as brake pads in the supersonic Concorde airliner in 1970, but were quickly adapted by military aircraft, Formula One race cars, heavy-duty transport vehicles, and eventually passenger vehicles.[30–32,102] In fact, brake pads comprise 75% of the C/C market.[30] Due to their improved wear resistance, A/C-NCs can be incorporated as brake pads in passenger and military aircraft, as well as Formula One race cars, despite the costs associated with an emerging material. Because of their high hardness and thus excellent wear resistance, A/C-NCs are also promising materials for high-wear applications, such as brake pads and automotive clutches.[104,105] By adding 10 vol% CNTs to a pyrolytic carbon (PyC) matrix, the resulting composites have a hardness 1.23x higher than PyC alone, and theory suggests that 30% v_f A/C-NCs will increase hardness by ∼250%.[78]

Although not typically made of carbon, composite-reinforced ceramics are commonly used in ballistic armor for both military personnel and vehicles,[106] since they are the lightest alternative to metal shielding.[107] Although ceramic composites are typically made from an alumina, silicon carbide, or boron carbide[106,107] layer over a fiber-reinforced polymer composite,[19,106,107] A/C-NCs may play a role by providing the same high strength, fracture toughness, and impact resistance at significant weight savings.[19]

In addition to replacing select C/C composites or improving upon current ceramics, A/C-NCs may be a breakthrough material in many multifunctional applications. A/C-NCs are excellent candidates for electrodes or structural components in fuel cells[30] due to their high thermal and electrical conductivities.[108] A/C-NCs may also perform well in structural electronics applications, such as electronic circuit board thermal plates and semiconductor manufacturing components.[31] A/C-NCs are outstanding candidates for similarly multifunctional applications such as plasma-facing surfaces, diverter plates, heat exchangers, and cladding elements for nuclear

reactors[30] because they are lightweight and can withstand the harsh environment in a reactor, including high temperatures, radiation, and corrosion.[30,44] Given the tremendous potential of A/C-NCs, particularly in multifunctional applications, further development of these materials is necessary.

2.2.1 Synthesis of A/C-NCs

Ceramic NCs can be synthesized with a variety of ceramic matrices, but carbon was chosen in this thesis due to its high temperature resistance, ease of manufacture, and aerospace heritage, as discussed above. Carbon can be split into two categories: graphitizing and non-graphitizing carbon. At low temperatures, graphitizing carbons form a compact structure and, when heated to elevated temperatures (1700 to 3000°C), graphitizing carbons form their typical graphitic carbon structure. Non-graphitizing carbons, unlike graphitizing carbons, strongly cross-link in a random orientation at low temperatures and thus form a turbostratic instead of a purely graphitic carbon structure upon heating to elevated temperatures. Due to their random orientation, non-graphitizing carbons have a porous structure, with porosity ranging from 20% to 50%.[109] Despite the porosity, non-graphitizing carbons are typically harder than graphitizing carbons, likely due to the strong crosslinking and greater bond strength between carbon crystallites.[109,110] Non-graphitizing, glass-like carbons, such as pyrolytic carbon (PyC)[79,110–112] are lightweight, highly resistant to deformations, and stable at elevated temperatures,[113] and they have a stable micro structure that makes them somewhat resistant to crack growth.[110] These qualities make A/C-NCs ideal for the high-temperature, high-hardness structural applications discussed previously. PyC was chosen because it can be prepared *via* pyrolysis at low temperatures and on a large scale from a variety of precursor polymers.[114]

The two most common polymer precursors to PyC are polyacrylonitrile (PAN) and phenol-formaldehyde (P-F) phenolic resins.[79] PAN is the most common high-strength carbon fiber precursor used in industry, particularly for aerospace and automotive applications,[79,115] but it can be used to synthesize A/C-NCs as well.[116] Although less common as a carbon fiber precursor, phenolic resins are most commonly used to make

C/C composites because they are significantly less expensive to obtain and are easier to synthesize.[110,114,117] Thus, it is possible to draw on industry best practices for the infusion and pyrolysis of P-F resins for C/C composites[8,97,98] as well as drawing on limited resin infusion research from previous work with A-PNCs.[108,110,114,118]

Another consideration when synthesizing A/C-NCs is the interface between the CNTs and the PyC matrix. As discussed in Section 2.2.2, it is important for the CNTs to be adhered to the matrix with neither too weak nor too strong of bonds for improved toughness[19] and hardness.[8] To address this, one process coated the CNTs with pyrolyzed polydopamine (py-PDA) to improve interfacial bonding without decreasing the electrical and thermal conductivities of the composite. However, an overabundance of relatively weak py-PDA decreased the composite's mechanical properties.[108] Due to trade-offs such as these, most A/C-NC processes have not found interface engineering a necessity. Although a concern at any v_f, interface engineering is a more important consideration at high v_f due to the challenge of infusing resin into such a small space.[9,114]

There are two common methods for infusing the P-F resin into the CNTs: chemical vapor infusion (CVI)[2,99,119] and polymer-infiltration-pyrolysis (PIP).[108,116] Both processes face some challenges with infusion. The composites made *via* CVI simply builds out carbon layers on top of the CNTs instead of synthesizing a fully infused composite, as seen in Figure 2-1.[2,99,119] It is speculated that CVI is better for higher v_f composites because a gas-phase infusion method is better able to infuse between the CNTs and because the carbon deposits, growing radially outward from the CNTs, have less space to fill, but experiments have shown that CVI still cannot fully infiltrate the CNTs even at ∼2 vol%.[120] Composites made *via* PIP are often infused with a 10 wt.% P-F resin solution in either acetone[108] or ethanol[118] to improve the resin's ability to infuse by decreasing the viscosity compared to non-dilute resins. Infusion challenges may be due to a layer of physisorbed water on the surface of A-CNTs ranging from 3–7 nm, which can alter the behavior of the CNT array, such as hydrophobic and hydrophillic tendencies, and impede deposition of a secondary material onto the CNT surface.[77] This water layer thickness increases in the CNT

loading range of most CNT CMNCs, from 1 to 5 vol.% CNTs, but decreases from 5 to 20 vol.%, likely due to the fluctuations in dipole moments, which lead to the Casimir forces.[77] Additionally, the accessible porosity, the inter-CNT area unoccupied by water, has a strong dependence on the inter-CNT spacing. For arrays with a $v_f \geq 5\%$, the accessible porosity may be <60%.
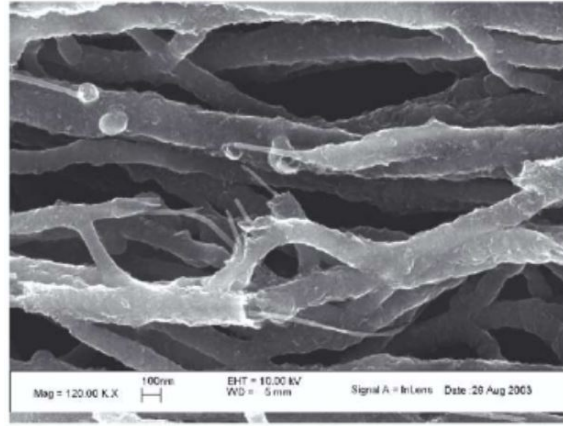
Figure 2-1: Scanning electron microscope (SEM) image of CNTs after CVI. As seen in this image, there are still large voids after the CVI process.[2]

Once the P-F resin has been infused into the CNTs and cured, the A-PNCs are pyrolyzed to create A/C-NCs. Pyrolysis, the thermochemical decomposition of polymers, occurs when specific polymers are heat treated in the absence of oxygen beyond their degradation temperatures to form a solid, non-graphitizing carbon material.[110] The A-PNCs are pyrolyzed at temperatures from slightly under 1000°C to over 2000°C in order to create the carbon matrix. The pyrolysis of the carbon can be confirmed using Raman spectroscopy, where carbon is defined by its D and G peaks; the D peak, found at $\sim$1355 cm^{-1}, is only visible in the presence of disorder. However, the G peak, found at $\sim$1590 cm^{-1}, is characteristic of carbon and is due to the relative motion of the sp^2 carbon atoms.[121] After P-F resin is heat treated at above 500°C, the D and G peaks become visible, and at about 600 °C, the P-F resin peaks disappeared. The intensity of the D peak, corresponding to an increase in disordered structure, was found to increase during pyrolysis, which suggests that non-graphitizing carbon is formed during the heat treatment.[117]

The specific pyrolysis temperature is important because elevated temperatures

affect the defect structure of graphite,[6] which strongly influences material strength and toughness.[122–124] Previous work shows that the hardness of A/C-NCs synthesized *via* PIP is maximized at 1000°C pyrolysis temperature.[6] Raman analysis also shows that the I_D/I_G ratio, the ratio of the intensity of the D peak to the intensity of the G peaks and an indicator of disorder, is maximized at 1000°C.[117]

During pyrolysis, the carbon precursor undergoes about 50% mass loss as non-carbon volatiles are released.[109] Additionally, because of the differences in coefficient of thermal expansion (CTE), a highly stressed region forms around the CNTs. This stress is relieved if the composite is heated to a sufficiently high temperature, as observed in Raman studies,[116] allowing the graphene sheets to rearrange into a more ordered structure. Thus, CTE mismatch can lead to a stress graphitization of the carbon matrix in an anisotropic structure extending radially from individual CNTs, up to about 500 nm.[113]

As noted earlier, non-graphitizing carbons are known for their porosity (up to 50%).[109] High porosity leads to a large variation in composite properties,[80] with more voids broadly corresponding to a decrease in the material's mechanical properties. To combat this, the already pyrolyzed A/C-NC may be reinfused by repeating the infusion, cure, and pyrolysis procedures.[80,125] Just one reinfusion was found to decrease the porosity by an average of ~10% across A-CNT v_f ranging from 1–20% v_f. It is important to note that there are diminishing returns after 4 reinfusions,[114] but it is through process modifications such as reinfusion that higher quality A/C-NCs with lower void fractions can be synthesized and their high-performance characteristics can be fully realized.

2.2.2 Mechanical Properties of A/C-NCs

For use in the variety of harsh environments discussed earlier in Section 2.2, A/C-NCs must be structural. Structural materials need to be strong, to meet loading requirements, and tough, so that they do not prematurely or catastrophically fail.[42] For almost all materials, improving strength and toughness are mutually exclusive.[42,126,127] Often, especially in safety-critical applications, lower-strength materials are favored

due to their higher toughness.[42] Strength is measured as a stress and represents a material's resistance to failure in the absence of cracks. Toughness, however, is measured as the energy necessary for fracture and represents a material's resistance to crack growth.[42,128] The stronger the material, the less plasticity is available for intrinsic toughening. This is one reason why pressure vessels and aluminum alloy airframes are manufactured from comparatively low strength alloy as the low strength, tougher alloy avoids problems from premature failure.[42]

Toughness is split into two mechanism classes: extrinsic and intrinsic toughening. Intrinsic toughening refers to enlarging the plastic zone, which is effective against both crack growth and crack initiation. Extrinsic toughening refers to mechanisms, such as crack bridging that reduce the local stresses and strains that would typically be used to extend the crack. With extrinsic toughening mechanisms, the inherent fracture resistance of the material is unchanged, allowing the strength of the material to remain unchanged as well.[42]

Adding CNTs to the carbon matrix may improve both the strength and the toughness of the matrix, as CNTs can provide an excellent extrinsic toughening mechanism. CNTs increase the toughness of the carbon matrix through four main toughening mechanisms drawn from previous work with fiber-reinforced ceramic matrix composites: fiber debonding, crack deflection, crack bridging, and fiber pull-out, as depicted in Figure 2-2.[3,44,102] Fiber debonding occurs when a crack encounters a relatively weak reinforcement/matrix interface and follows the interface, causing debonding. Crack deflection starts similarly – the crack encounters the reinforcement/matrix interface – but reaches a point where less energy is required to continue propagating through the matrix. Both of these mechanisms dissipate energy by rerouting the crack, but the second two methods – crack bridging and fiber pull-out – stem from the crack moving past the reinforcement phase.

Crack bridging, the third method, is when the reinforcement phase spans the crack, carrying some of the load and thus minimizing the load at the crack tip, which drives the crack forward to a lesser extent. In this respect, the strength of the CNTs determines the toughness of the composite.[129] Experimentally, Li *et al.* found that
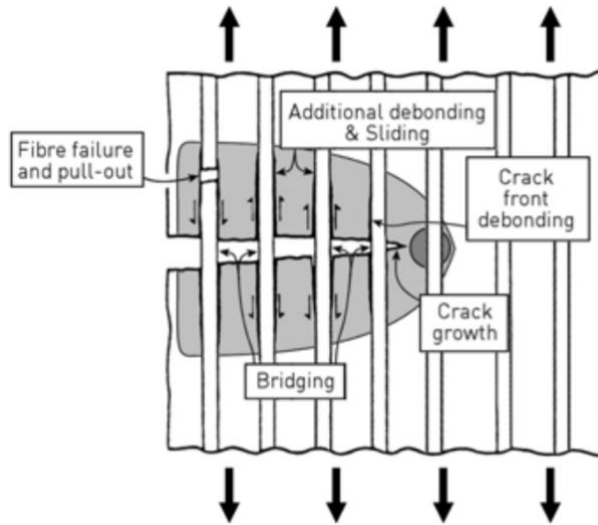
Figure 2-2: Illustration of the four main toughening mechanisms in microfiber composites: fiber debonding, crack deflection, fiber bridging, and fiber pullout. [3]

growing carbon nanofibers (CNFs) on carbon fiber for CNF/carbon fiber/carbon NCs improved the material's toughness, because the CNTs could transfer load across a crack from one CNF bundle to another. Load-displacement data shown in Figure 2-3 confirmed that the load decreased stepwise after the maximum load instead of dropping off in catastrophic failure as observed for the carbon fiber/carbon composites. [4] Friction from the matrix sliding on the fiber during crack bridging also dissipates a small amount of energy, but a more powerful toughening mechanism is fiber pull-out, where the fibers pull out of the matrix after bridging the gap. Because of their high surface area to volume ratio, a considerable amount of energy is consumed even for low vol% CNTs in the matrix. [3] Ideally, the interfacial adhesion between the reinforcement phase and the matrix is neither too high or low. Too high, and energy cannot be dissipated through fiber debonding or fiber pull-out. Too low, and not enough energy is dissipated. [19] A less common toughening mechanism is referred to as the "sword-in-sheath" mechanism where, instead of fiber pull-out, energy is dissipated when the concentric cylinders of a multi-walled CNT (MWCNT) pull apart. [21,129] For these reasons, interfacial engineering is a strong consideration beyond just processing, as discussed earlier in Section 2.2.1. These toughening mechanisms are summarized in Figure 2-2 and confirmed experimentally as shown in Figure 2-4.
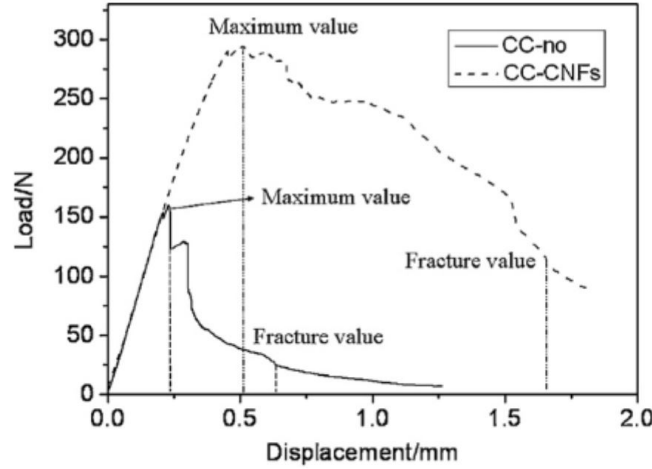
Figure 2-3: Flexural load/displacement curve for C/C composites with and without CNT reinforcement. The load for the CNT-reinforced composites decreased step-style instead of dropping quickly, signifying catastrophic failure, as the load for monolithic C/C composites did.[4]
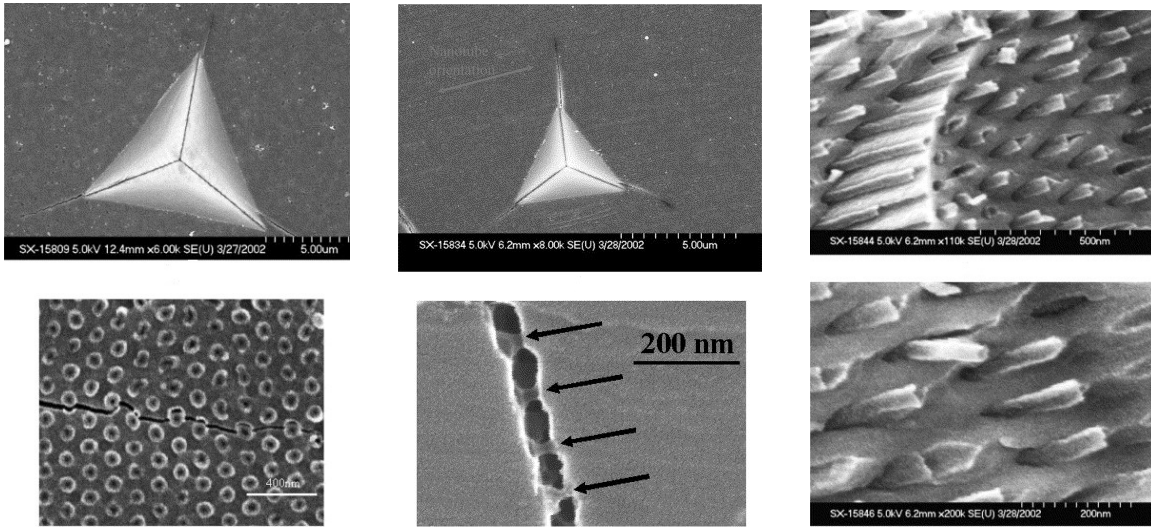
(a) Crack deflection.   (b) Crack bridging.   (c) Nanotube pull-out.

Figure 2-4: SEM images of CNT toughening mechanisms in a CNT-reinforced alumina-ceramic matrix NC. Modified after original.[5]

Hardness, related to the material's strength[130] and modulus[79] also increases with the addition of CNTs. Previous work shows that the addition of 10 vol% A-CNTs increases the hardness of the material over monolithic PyC by a factor of 1.23.[78] Additionally, theory shows that 30 vol% A-CNTs may increase the hardness of monolithic PyC by ~250%, rivaling diamond when normalized by density. The hardness/density

Ashby chart in Figure 2-5 displays the outstanding hardness properties of A/C-NCs in previous experimental work and the predictions of A/C-NC hardness compared to other hard materials.[6]
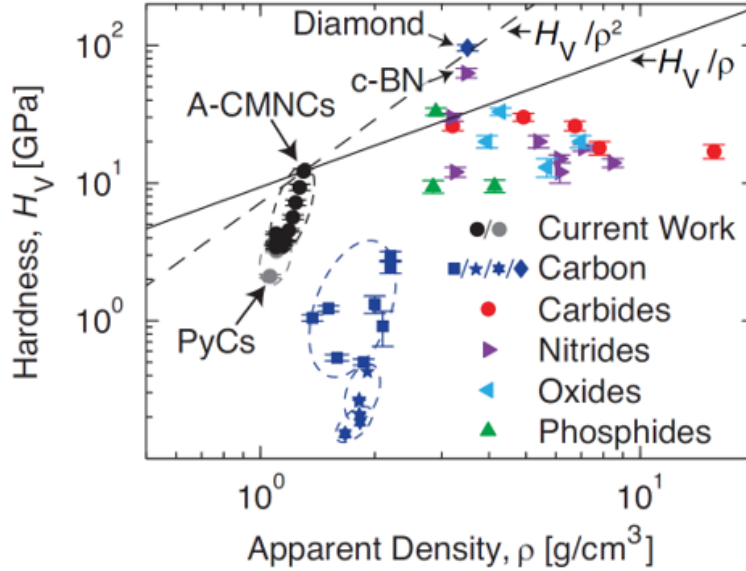
Figure 2-5: Ashby chart for hard materials showing hardness as normalized by density. A/C-NCs have outstanding properties and are expected to rival diamond at high CNT v_fs. Experimental results for low CNT v_f are plotted in the cluster with the theoretical higher hardnesses for higher v_f extending linearly upwards to be comparable to diamond at high v_f. Modified after original.[6]

Hardness is an excellent method for understanding a material's properties when more typical mechanical tests, like a uniaxial tensile test, are impossible due to the material's small size. Hardness can be measured in a variety of ways, and there exists both micro and nanoindentation methods to measure hardness. For a nanoindentation test, a loaded indenter tip is pressed into the material, and the load and indenter tip depth are recorded for the duration of the test. The hardness of the indented material, from the load per unit area, and the Young's modulus, from the stiffness of the unloading curve and area of the indentation, are calculated.[131] Nanoindentation hardness and modulus results are localized to the nanometer-scale area of nanoindentation, which makes these results less applicable to the bulk material, as nanoscale voids can affect the results.

Unlike nanoindentation, microindentation tests a larger area of the sample and

thus more accurately measures the bulk hardness. There are four common microindentation methods: Brinell, Rockwell, Vickers, and Knoop, which are characterized by variations in indenter tip geometry for greater accuracy or ease of testing. All four methods deduce the hardness by the size of the indent for a given indenter tip loading.[132,133] The Vickers indenter, illustrated in Figure 2-6, uses an inverted pyramid shape with a square cross-section and an angle of 136° between opposite sides of the pyramid.[128] Knoop, for example, uses a sharper diamond wedge, which actually results in a lower hardness value than Vickers hardness for the same load. Hardness values for the same sample measured by the different microindentation methods can vary by more than 10%, so it is important to note the hardness measurement technique when reporting hardness results.[132]
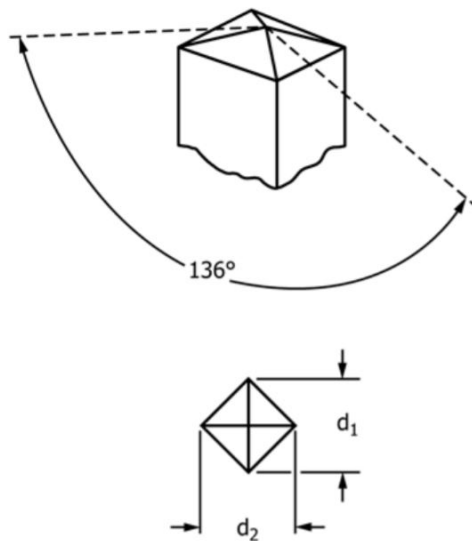
Figure 2-6: Vickers indenter diagram. The upper image illustrates the indenter tip geometry with specified indenter tip angle of 136°. The lower image illustrates the projected area of the tip, where d_1 and d_2 ($\sim$100 μm) are equal.[7]

More specifically, microhardness is measured by dividing the indentation load by the projected area of the indentation on the initial surface of the sample. The choice of load is important as it determines the size of the indent area ($\sim$5000 μm^2). This area must be large enough to measure but small enough that the entire indent is visible at once under the microscope. Since a larger load results in a larger indent volume, a larger indentation load will encounter more cracks and non-representative

imperfections in the material, leading to a decrease in microhardness with increasing load.[128] Additionally, indenting not only compresses but also shears the sample. Shear strength is highly sensitive to the presence of voids. Thus, microhardness values may vary by over 10% for the same sample and over 50% for samples in the same group,[128] particularly superhard materials (materials with a hardness greater than 40 GPa), due to the presence of voids in the composites.[132,133] The hardness testing procedure in this work was designed in accordance with ASTM Standard C1327-15: Standard Test Method for Vickers Indentation Hardness of Advanced Ceramics,[7] and the procedure will be discussed in more detail in Chapter 6. The next section further discusses the challenges of A/C-NC fabrication and their effect on measured properties.

2.2.3   Challenges Specific to A/C-NCs

A/C-NCs are a compelling material to study due to their outstanding physical properties, particularly at elevated temperatures. However, there are still challenges specific to A/C-NCs that must be addressed in this thesis.

A few challenges have already been discussed in the earlier sections. First, non-graphitizing carbons tend to have a high porosity[109] due to significant mass loss (about 50% of the resin)[114] from the pyrolysis process.[80,125] Previous work specifically with 1% v_f A/C-NCs found that the composites had ~60% porosity and 20% v_f A/C-NCs had up to ~94.5% porosity, likely due in part to poor infusion at the higher v_f.[8,114] The high porosity results in an increasingly inhomogeneous matrix structure, where areas with a greater void fraction correspond to areas with decreased mechanical properties.[80] To acquire more uniform, denser composites, it is necessary to reinfuse the composite with polymer precursor and then pyrolyze, repeating the infusion/pyrolyzation process ~4 times.[80,125] Reinfusions still have complications; modeling predicts diminishing returns after 4 infusion/pyrolysis steps (~51% porosity at 4 steps) because it is expected that, with each reinfusion, 10% to 70% of the remaining voids are sealed off from future reinfusions by the resin. Due to these diminishing returns, theory predicts that more than 10 processing steps are required

for $< 50\%$ porosity.[80] With current practices, modeling suggests that the $\lesssim 20\%$ porosity seen in carbon fiber-reinforced carbon matrix composites is not viable using the similar wet infusion method for A/C-NCs.[77]

A second challenge of working with PyC matrices is that ceramics are known for their brittle character,[102] which precludes them from safety-critical applications.[42] Since ceramics are so brittle, they can easily crack from impact or fail with no prior indication. The addition of CNTs to ceramics has improved both their strength[6] and toughness,[4] but the brittleness of ceramics still results in manufacturing and characterization challenges. Additionally, since the carbon matrix is more brittle than the phenolic resin precursor, the A/C-NCs are more sensitive to flaws than similar A-PNCs, and the flaws can lower the measured hardness values of the bulk composites.[102,116]

Finally, there are a few challenges of working with CNTs in the carbon matrices. The first challenge is keeping a uniform distribution of nanotubes. Particularly with bulk CNTs, the nanotubes can agglomerate[19,44] due to their high aspect ratios and surface areas, combined with the surface van der Waals forces,[19] as shown in Figure 2-7.[8] The work in this thesis focuses entirely on A-CNT arrays to avoid agglomeration issues with bulk CNTs, but volatiles evaporating from the P-F resin can cause the CNTs to densify in cell or pin formations, causing microscopic heterogeneity.[134] Agglomerates and heterogeneity from any source may act as defects and cause stress concentrations, thus lowering their material properties.[103,120] Additionally, it is harder for the matrix to penetrate the high-v_f region, causing premature failure due to the unevenly distributed resin and remaining voids.[19,44] Agglomeration in unaligned CNT NCs was more pronounced at what some researchers consider high v_f of 2–3%.[19] At 4 wt% (2 vol%) CNTs, wear loss in CNT-alumina composites was experimentally found to begin increasing, even though wear losses had decreased with a small addition of CNTs, as shown in Figure 2-8.[9] High v_f A-CNT NCs are envisioned to become a revolutionary advanced composite material, allowing for better performance in the aforementioned applications.[14] However, since CNT agglomeration impedes the continued improvement of the composite's properties at high v_f,

homogeneous CNT dispersion is the key to achieving the theoretical strength and hardnesses of CNT-reinforced ceramics and suggests the approach of PIP-processed A-CNTs taken in this thesis.[19,129]
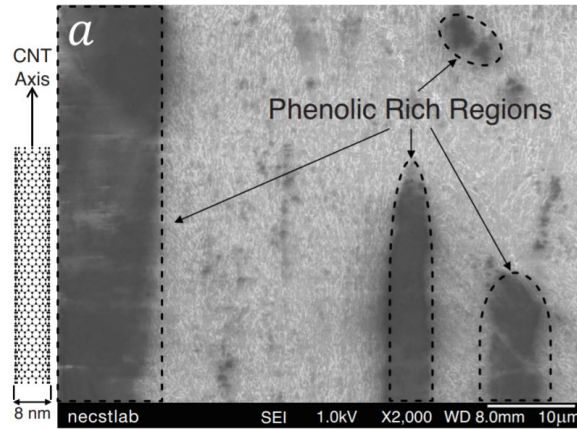
Figure 2-7: Resin-rich regions formed during infusion of an A/C-NC.[8]
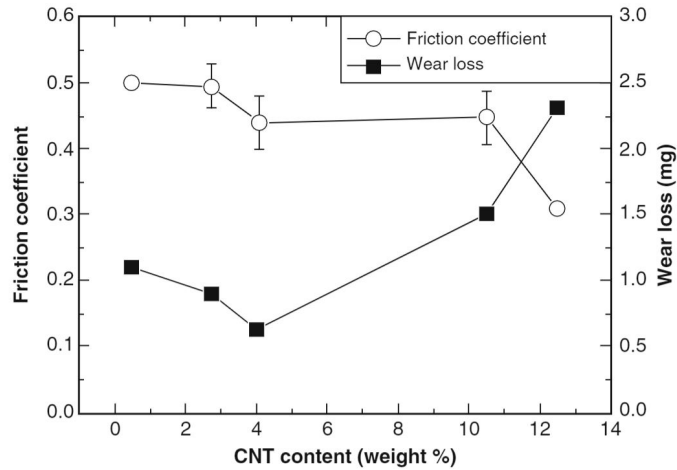
Figure 2-8: Wear losses decrease with the addition of CNTs, but only up to 4 wt% (~2 vol%), demonstrating that agglomeration effects at high v_f can begin to decrease the composite's properties.[9]

A second challenge with resin infusion arises from decreases in the inter-CNT spacing.[114] A-CNT arrays have a small inter-CNT spacing of ~80 nm in 1 vol% arrays,[14,71,79,80] which corresponds to ~6 nm spacing for 30 vol.% CNTs, calculated from Equations 2.4 and 2.5:[71]

$$\Gamma(D_{CNT}, v_f) = D_{CNT}(\xi(v_f)\sqrt{\frac{0.9069}{v_f}} - 1) \tag{2.4}$$

where:

$$\xi(v_f) = 11.77(2.511(v_f) + 3.932)^{-3.042} + 0.9496 \tag{2.5}$$

and D_{CNT} is the diameter of the MWCNT and v_f is the volume fraction of A-CNTs.

High and low molecular weight P-F resins are reported to have a radius of gyration between 0.65 nm and 2.48 nm, which suggests that the resin will be able to infuse between the CNTs but may not crosslink as fully at high v_f due to the confinement of the resin between small inter-CNT spacings.[114,135] Further research needs to be completed to determine the maximum CNT v_f at which A-PNCs, and subsequently A/C-NCs, can be fabricated for the P-F resin.

Although the P-F resin molecules are expected to fit between the high-v_f A-CNTs, the tight spacing makes fully wetting and infusing the P-F resin more challenging. In addition, CNTs may have a > 5 nm layer of adsorbed water on their surface.[77] This water layer can fill the entire inter-CNT spacing on high v_f composites and impede CNT wetting and resin infusion at any v_f, particularly for hydrophobic resins, such as P-F resins.[114] For best results, this water layer must be desorbed before infusion. Although there are a few challenges associated with A/C-NCs, this thesis aims to address these challenges to synthesize more uniform composites with improved material properties. The next section similarly discusses the applications of A-NCs, the other significant alternative to A-PNCs, as well as their historical and state of the art synthesis methods, mechanical properties, and manufacturing challenges.

2.3 A-CNT/Al-Matrix Nanocomposites (A/Al-NCs)

Like A/C-NCs, A/Al-NCs have advantaged properties for a host of applications. Several metal matrices have become popular in research, including aluminum,[136–142] titanium,[143–150] and copper.[136] Copper is particularly common for electrical applications because of its superior conductivity, and titanium is used for high-temperature

aerospace applications due to its high maximum working temperature. This thesis focuses on polycrystalline aluminum and aluminum alloy matrices, as aluminum is ubiquitous in many aerospace applications.

The addition of nanoparticles, particularly CNTs, has been used to improve the mechanical properties of metal matrices,[12,136,137,151–153] in addition to improving the thermal and electrical conductivities.[151,154] As discussed in Section 2.2.2, improvements in both strength and toughness are typically at odds, but experiments show that a small addition of CNTs to an Al matrix improves the material's strength and toughness as compared to a similarly-processed baseline Al sample. The Young's modulus shows an increase to 81.4 GPa for Al with CNTs compared to 76.2 GPa for pure Al.[153] Tensile strength shows a maximum increase of 300% over as-extruded pure Al[152] and yield strength shows a ~77% increase of 0.2 wt% (~0.15 vol%) CNTs,[136] although the gains in yield strength may not be significant for alloys that are typically tempered.[151] The hardness, like observed for A/C-NCs, also increases with the addition of CNTs; up to 67% with 2 wt% (~1.4 vol%) CNTs compared to unreinforced bars prepared with a similar process.[155] None of these improvements decrease toughness, and toughness increases of 20%–40% over pure Al and 7000 series Al alloy, respectively, were recorded with just 1 wt% (~0.8 vol%) CNTs.[137] In addition to these standard mechanical properties, the CNT-reinforced Al composites showed improved damping characteristics,[136] improved fatigue and creep resistance,[156] and improved radiation resistance.[29] The reinforcement mechanisms, which attempt to explain the improvements in mechanical properties due to the CNTs, are discussed further in Section 2.3.2 and the synthesis methods and their drawbacks in Section 2.3.3. Despite processing drawbacks, it is clear that the CNTs are contributing to the improvement of the mechanical properties. These properties make A/Al-NCs ideal candidates for a variety of multifunctional applications.

Although A/Al-NCs have a maximum service temperature greater than A-PNCs, their improved mechanical characteristics over pure Al and Al alloys are what makes A/Al-NCs attractive. The high strength to weight ratio of A/Al-NCs makes them good candidates for automotive,[156] armor, and aircraft parts, as weight savings are

vital in these industries, especially with the push for reduced fuel consumption.[157] Additionally, A/Al-NCs may find use as a replacement for driveshafts, as the maximum driveshaft speed is proportional to $\sqrt{\frac{E}{\rho}}$.[156] A/Al-NCs are specifically suggested for engine pistons and cylinder liners due to their improved wear resistance,[156] as well as CNT-Al matrix foams for vibration damping,[156] which would have applications in both automotive as well as aerospace industries. In aerospace, A/Al-NCs may improve aircraft performance by replacing exit guide vanes for jet engines, as these require a resistance to varied weather conditions and high stiffness and strength, all while maintaining the higher service temperature afforded by the aluminum matrix.[158]

Another useful property of A/Al-NCs is their improved radiation resistance. Work by So *et al.* found that the A/Al-NCs had a delayed onset of bubbles forming under He and Al ion irradiation, and that the CNTs stayed intact even after 72 displacements per atom (DPA) of irradiation.[29] They suggested that the CNTs provide pathways for He and other fission products to diffuse such that they do not stay trapped in the Al, which exacerbates embrittlement and swelling. Additionally, the CNT-matrix interface may be a venue for radiation defects to recombine, allowing the CNTs to preferentially strengthen the matrix when exposed to radiation.[29] Given this advantaged radiation resistance, A/Al-NCs are excellent candidates for use in nuclear power facilities as well as shielding for deep space missions, as light weight and radiation resistance are essential.

Given these exceptional mass-specific properties, A/Al-NCs are another promising alternative to A-PNCs, particularly since they take advantage of the Al matrix's notably higher strength and temperature resistance over polymer matrices, and improved fracture toughness over ceramic matrices. The next section, however, discusses the wetting of Al on CNTs, which differs considerably from, and is far more challenging than, A-PNCs.

2.3.1 CNT Wetting with Metals

Although A/Al-NCs are superior to A-PNCs for a variety of reasons, their synthesis is more challenging. At a high level, resins, like CNTs, have a low surface energy, which makes them compatible for good wetting.[159] However, the surface energy of metals is much higher, and the wetting process must be understood in greater depth to find compatible materials. The determination of wettability for nonporous and smooth solid surfaces comes from comparing the surface tensions of the solid (γ_S), liquid (γ_L), and their interaction, the surface tension between the solid and the liquid (γ_{SL}) using the Young-Dupré Equation (Equation 2.6)[10,159]:

$$\frac{\gamma_S - \gamma_{SL}}{\gamma_L} = \cos(\theta) \tag{2.6}$$

where θ is the contact angle. It is important to note that the validity of Equation 2.6 was called into question at the nanoscale,[160] but it has been proven applicable.[161] Possible materials for wetting CNTs will be discussed and their γ_S, γ_{SL}, and γ_L compared later in this section.

A contact angle of $\theta = 0$ corresponds to when a liquid wets a surface fully, whereas a high contact angle (>90°) corresponds to when a liquid does not wet the surface at all.[10,159] Figure 2-9 shows the contact angle measurement as well as the three surface tension interfaces used in the calculation of contact angle from the Young-Dupré Equation.[10] For good wettability and infusion, the contact angle should be within a few degrees of 0°. This corresponds to $\gamma_S - \gamma_{SL}$ slightly less than or equal to γ_L.
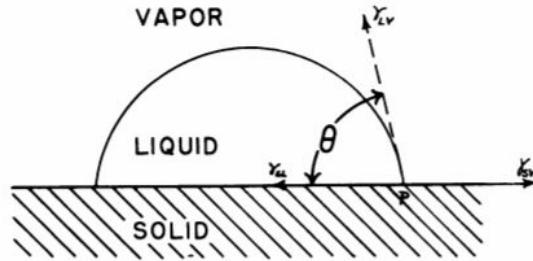
Figure 2-9: Diagram showing the contact angle and surface tension interfaces.[10]

The Young-Dupré equation can be arranged to provide more insight into the wetting process. Here, the spreading parameter S is defined in Equation 2.7[10]:

$$S = \gamma_S - (\gamma_{SL} + \gamma_L) \tag{2.7}$$

The spreading parameter indicates whether or not the liquid will spread, wetting the solid, where $S > 0$ indicates spreading and $S \leq 0$ indicates that the liquid will not wet.[10] This form of the equation provides better insight than the form in Equation 2.6; this form shows that the quantity $\gamma_{SL} + \gamma_L$ must be less than γ_S. This stipulation is particularly challenging for wetting CNTs, as their surface energies are low (~ 0.027 J m^{-2}). For resins, as they also have a low surface energy,[162] a favorable interfacial energy would allow successful wetting. For metals, however, the high γ_L typically precludes $S > 0$, but this is still dependent on γ_{SL}.

It is challenging to calculate the contact angle theoretically just from the surface energies, especially as surface energies and interfacial energies must be calculated from experiment under comparable conditions (*e.g.* temperature), and most of these values are not well-documented.[10,159] Thus, contact angle is most useful for comparing wettability of substances experimentally. The contact angle directly between polycrystalline graphite and molten aluminum, however, has been estimated at 130–140°, decreasing to 50–70° after a layer of Al$_4$C$_3$ has been formed.[163] This data suggests that Al will not wet CNTs without surface modifications.[164] In response to the challenge of calculating contact angles, Gibbs redefined the equation in terms of the work of adhesion of the liquid to the solid, taking a thermodynamic viewpoint:[10,159]

$$\cos \theta = \frac{\pi_{S/L} - \pi_{S/V}}{\gamma_L} \tag{2.8}$$

where $\pi_{S/L}$ is the tendency of the liquid to spread and $\pi_{S/V}$ opposes the spreading of the liquid.[159] Again, these values are not typically reported, but the important result of this equation is the condition that the solid surface should have a higher surface energy than the liquid for the liquid to wet the solid.[159] This stipulation accounts for the nonzero and typically positive γ_{SL}, resulting in a small contact angle

per Equation 2.6.

Table 2.1 shows a comparison of surface energies between CNTs, possible matrices, and common ceramics that could easily coat CNTs. Surface energies are not well-documented, so the data on the surface energy of materials with air is sparse, with even less data on interfacial energies in existence. There has been limited work on modeling the surface energies of metals and their interactions with CNTs, but this has not been broadly successful in matching experimental data. In particular, Al matched experimental data well (theory and experiment agreeing at $\sim$1.2 J m^{-2}), but Ti was farther off (theory suggesting a surface energy of 2.2 J m^{-2} for the $<$100$>$ plane compared to 2.632 J m^{-2} in experiments).[165] The interfacial energies included in the table below are all from models,[165] as no other data on interfacial energies was available. There is almost no information regarding the interfacial energies between metals, as metals tend to be combined in an alloy instead of applied in layers as in a wetting process. However, recent work puts the interfacial energy for liquid Al alloys on Ti, near the melting point of Al, at $\sim$0.9 J m^{-2}.[166]

Table 2.1: Comparison of relevant surface energies.

Material	Surface Energy (γ_S, γ_L) [J m^{-2}]	Interfacial Energy (γ_{SL}) [J m^{-2}]
CNT	0.027[167]	
Epoxy resin (Epon)	0.047[162]	
Al	1.152[165,168,169]	$\sim$1.3[165]
Ti	2.045[168]–2.63[165]	-0.23 ($<$100$>$ plane)[165]
Au	$\sim$1.7[165]	$\sim$1.44[165]
Fe	2.525[170]	
Ni	$\sim$2.4[165]	$\sim$2.2[165]
Sn 63% Pb 37% (solder)	$\sim$0.5[171]	
TiC	0.75[172]	
Al$_2$O$_3$	2.4[173]	

From the recorded surface energies, it is obvious that wetting of CNTs by matrices other than polymer resins is challenging due to the low surface energy of CNTs. CNTs have the lowest surface energies of all the materials listed in Table 2.1, meaning that only materials with a negative interfacial energy can wet CNTs per the Young-Dupré

Equation (Equation 2.6). Thus, a variety of surface modification methods have been tested to improve the wetting and interfacial adhesion of the Al matrix to the CNTs. The simplest method was oxidizing the CNTs in air for a maximum of 30 minutes at 550°C to functionalize the CNTs and improve solubility. While more environmentally friendly, this method was not as effective as the typical oxidation in H_2SO_4/HNO_3[174] Another method of improving CNT dispersion in solution was to decorate hydroxyl and carboxyl groups on CNTs, which is then leveraged for improved dispersion in the matrix.[175] Both TiC[38] and SiC[137] have been decorated onto CNTs through ball milling methods to improve dispersion in the Al matrix directly as well as improve the interfacial bonding. TiC specifically was found to improve the compressive yield strength over other CNT-Al NCs.[38] Oxides can also be decorated onto the CNTs through a plasma treatment and atomic layer deposition (ALD) for a uniform coating of monocrystalline grains over the CNTs, as demonstrated with a TiO_2 coating.[176] Ti, while having a high surface energy, does have a negative interfacial energy with CNTs, making the Ti interaction with CNTs energetically favorable over Ti-Ti interactions, and pure Ti was found to coat CNTs well in experiments.[165] Additionally, the spreading parameter for Al on Ti may be positive (liquid and solid surface energies are approximated to be similar; surface energy for <110> plane used for Ti):

$$S = 2.63 - (0.9 + 1.152) = 0.578 \tag{2.9}$$

which suggests that Al infusion into Ti-coated CNT arrays would be effective. However, a surface layer of an oxide of the metal, as well as uncertainties regarding the mechanics of wetting on a nanometer scale, leaves this as an open question. Despite the processing challenges, the next section describes how the addition of CNTs allows for significant improvements in Al mechanical properties.

2.3.2 Reinforcement Mechanisms in A/Al-NCs

Although the CNT toughening mechanisms discussed in Section 2.2 are also applicable to MMNCs,[140] this section discusses how nanoreinforcements can improve

the strength of any metal matrix and quantifies the contribution from each effect at the end of the section, in Figures 2-12 and 2-13. One such example, the addition of Al_2O_3 nanoreinforcements to a magnesium-metal matrix, shows that the strength improvement due to nanofillers is not restricted to carbon-based materials.[177] However, this section focuses on the four strengthening mechanisms applicable to A/Al-NCs: Orowan strengthening, load transfer effect, CTE mismatch, and the Hall-Petch effect. The first, and the dominant mechanism for low aspect ratio CNTs,[178] is Orowan strengthening. Since dislocations are unable to shear through CNTs, Orowan looping is the primary mechanism for dislocations to bypass CNTs and other nanofillers. This results in an increased yield strength in CNT-Al matrix composites.[138,179,180] The contribution from Orowan strengthening can be calculated with Equation 2.10:[175,178,181]

$$\Delta\sigma_{OR} = \frac{0.13bG}{d_p(\sqrt[3]{\frac{1}{2}v_p} - 1)} \ln(\frac{d_p}{2b}) \tag{2.10}$$

where $\Delta\sigma_{OR}$ is the contribution to strengthening from the Orowan mechanism, b is the Burger's vector, G is the matrix shear modulus, d_p is the particle diameter, and v_p is the v_f of the particles. A depiction of the Orowan looping process, where the dislocation moves past nanoreinforcement particles by forming loops around the particles, can be seen in Figure 2-10.[11]

The second reinforcement mechanism is the load transfer effect of composite materials, which is when load is transferred from the relatively compliant matrix to the stiff and hard particles.[12,13,175,180,182] This effect decreases with decreasing particle size,[180,182] but is dominant for long CNTs (aspect ratios above $\sim$40) and is the mechanism that best takes advantage of the excellent mechanical properties of CNTs.[178,183] The contribution from the load transfer effect can be calculated with a modified Shear Lag model, Equation 2.11:[13,175,178,180,181]

$$\Delta\sigma_{LT} = v_p\sigma_m \left[\frac{(l + t_p)}{4l}\right] \tag{2.11}$$

where $\Delta\sigma_{LT}$ is the strengthening contribution from the load transfer effect, σ_m is the
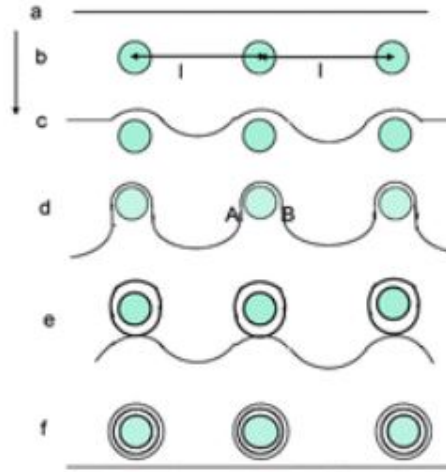
Figure 2-10: Illustration of the Orowan Looping mechanism, where dislocations move past nanoreinforcements by leaving behind loops.[11]

yield strength of the unreinforced matrix, l is the length of the particle, and t_p is the particle thickness. For load transfer to be effective, the CNT-matrix interface must be strong enough to transfer the load without failing in shear.

A third strengthening mechanism is the coefficient of thermal expansion mismatch. The CTE mismatch between the CNTs and the Al is accommodated by the formation of geometrically necessary dislocations (GNDs), which results in a strengthening effect. This contribution can be calculated with Equation 2.12.[13]

$$\Delta\sigma_{CTE} = \frac{0.5G_m b\sqrt{\rho} + \tau_m}{0.65} - \sigma_m \tag{2.12}$$

where $\Delta\sigma_{CTE}$ is the strengthening effect from the CTE mismatch, τ_m is the shear strength of the matrix, G_m is the shear modulus of the matrix, b is the Burgers vector, and ρ is the enhanced dislocation density.

$$\rho = 12\frac{\Delta\alpha\Delta T v_p}{bd_p(1 - v_p)}. \tag{2.13}$$

Here, $\Delta\alpha$ represents the difference in CTE between the matrix and reinforcements, and ΔT is the difference in temperature from cure to service temperature. As defined earlier in this section, v_p, b, and d_p are the particle volume fraction, Burgers vector,

and particle diameter. Since the differences in CTE cause residual stresses, any stresses not relieved by GNDs may decrease the stress the material can carry prior to fracture.[184]

The final reinforcing mechanism and one often with a small contribution[12] is Hall-Petch strengthening. Grain refinement increases the number of grain boundaries, which hinder dislocation motion because more energy is required to move between differently oriented planes.[12,13,38,178,180] This effect is especially prevalent in composites made through the powder metallurgy process, as milling the Al refines the grains. However, the Hall-Petch effect is augmented by the addition of CNTs or other nanofillers, as these nanofillers can pin the grain boundaries, which slows or stops the grain growth entirely.[180] The effect of CNTs on grain growth can be seen in Figure 2-11, which shows the grain size of Al and CNT/Al NCs during spark plasma sintering (SPS).[12]
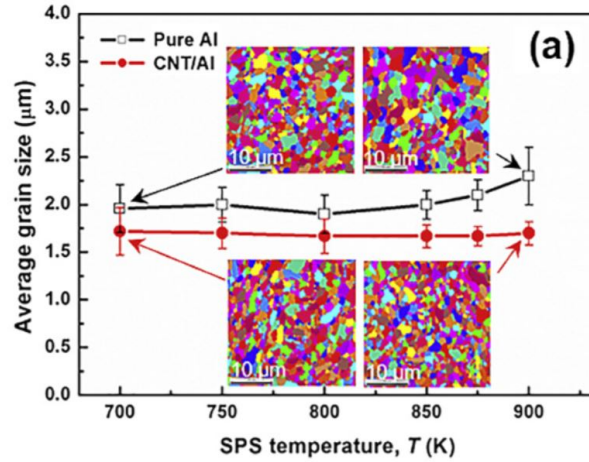
Figure 2-11: Grain size of Al and CNT/Al NCs during SPS. Adapted from original.[12]

The contribution from the Hall-Petch effect can be calculated with Equation 2.14:[12,13,178]

$$\Delta\sigma_{HP} = k_y / \sqrt{d_g} \tag{2.14}$$

where $\Delta\sigma_{HP}$ is the strengthening from the Hall-Petch effect, k_y is the strengthening coefficient, a characteristic constant of the material, and d_g is the average grain size.

As mentioned earlier, the Orowan Strengthening contribution is most significant for low aspect ratio CNTs and the load transfer effect most significant for high aspect ratio CNTs, but all four effects lead to strengthening the composite. The relative contributions of each method depend on the synthesis parameters, but examples of the relative contributions from each effect can be seen in Figures 2-12 and 2-13. There are few drawbacks to these reinforcement mechanisms, but it is important to note that the addition of any reinforcement phase can lead to void nucleation at the reinforcement/matrix boundary, especially if there is poor interfacial bonding, and thus resulting in early failure.[185] The next section will introduce various CNT-Al matrix NC synthesis methods that enable these reinforcement mechanisms to be used advantageously.
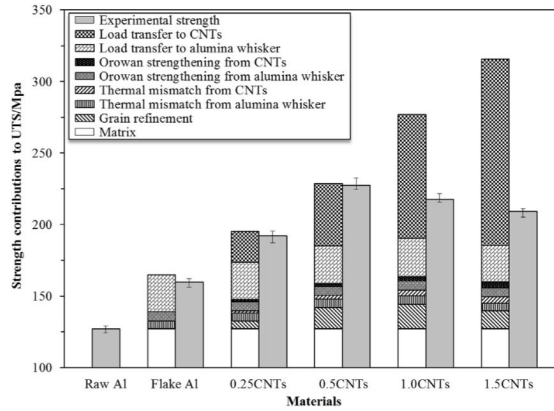
Figure 2-12: Strength contribution to the ultimate tensile strength (UTS) of the Al matrix from CNTs and Al_2O_3, showing expected contributions from each of the four strengthening mechanisms. While the theoretical calculation of the contribution from each mechanism is reasonably accurate at lower v_f, other effects appear to decrease the maximum UTS at higher CNT loadings. Figure adapted from original.[13]

2.3.3   Synthesis of A/Al-NCs

There are a variety of CNT-Al matrix NC synthesis methods, several of which will be reviewed here. More common processes will be discussed first, with a brief overview of some more innovative and state-of-the-art methods to follow.

Al matrix NCs are often synthesized through powder metallurgy methods, common to processing of many alloys.[139–142,186] This process may begin by dispersing
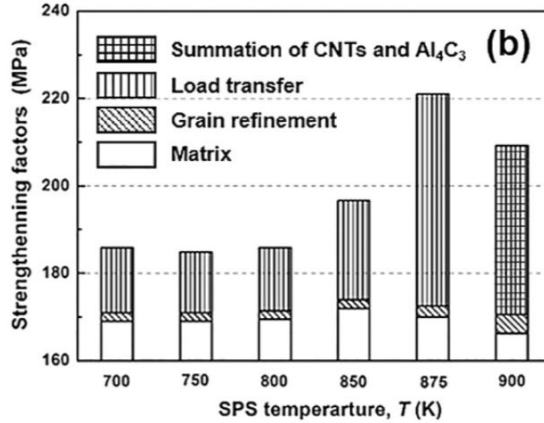
Figure 2-13: Strengthening contribution to the Al matrix from grain refinement (Hall-Petch Effect) and load transfer, showing that with high-aspect-ratio CNTs, the load transfer effect is most significant. Figure adapted from original. [12]

CNTs in a solution using a surfactant, such as ethanol[187] or isopropanol alcohol,[178] to improve dispersion later in the process. Alternatively, sometimes the CNTs are grown *in situ* on Al particles using a CVD method to adequately disperse the CNTs in the Al matrix and decrease the required ball milling time.[188,189] Shorter milling times cause less damage to the CNTs, better preserving their advantageous properties, as well as their original lengths,[178] which allows the CNTs to improve the composite's properties through the load transfer effect. Next, CNTs are milled with Al,[137,138,188] usually with a high-energy ball mill,[155,178,190] but sometimes a low-energy ball mill is used to reduce damage to the CNTs,[13] or a wet milling process.[38,178] All these processes contribute to the Hall-Petch effect because milling decreases the Al grain size. The CNTs further limit grain growth over just the effect from ball milling, as discussed in Section 2.3.2 and Figure 2-11, and thus increase strengthening *via* the Hall-Petch effect. As mentioned earlier, the ball milling process may cause damage to the CNTs, at a minimum causing them to break.[178] Many studies analyzed the damage caused by this process through Raman spectroscopy. The I_D/I_G ratio, a ratio of the disorder in the CNT structure to the characteristic G peak, indicates increasing defects with an increase in the I_D/I_G ratio. Slight process differences in the various methods resulted in different I_D/I_G ratios before and after ball milling. Some processes saw a significant jump in I_D/I_G ratio; for example, in the work by

71

Zhang *et al.*, the I_D/I_G ratio increased from 0.68 for as-received CNTs to ~1.0 as composites, with the bulk of the damage coming from the ball milling process.[13] Other processes caused only minor damage, such as the work by Yang *et al.*, which showed an increase in I_D/I_G ratio from 0.87 to 0.96 before and after ball milling, respectively.[188] Rocking milling, a type of ball milling, showed no damage with a constant I_D/I_G ratio of 1.2 for as-received CNTs, ball-milled CNTs, and CNTs in the completed composites.[186] While it is important to note that ball milling may cause significant damage, careful processing steps may be able to avoid significant damage. Although these studies did not typically compare to a carbon black nanofiller, the reported mechanical properties of carbon-reinforced aluminum covetics shows a smaller increase in mechanical properties than the CNT-reinforced Al NCs (23.4% increase in Vickers hardness with carbon black[154] compared to 67% with CNTs[155] and a 30% increase in yield strength with carbon black[154] compared to ~77% with CNTs[153] for ~1 vol% nanofillers).

Once the CNTs are adequately dispersed, the composites are formed by sintering the milled powder mixture.[188] This is typically an SPS process between 480–630°C, which shows no evidence of damage to the CNTs.[13,38,137,152,178] In particular, Kwon *et al.* and Trinh *et al.* measured the I_D/I_G ratios before and after SPS with no significant change; Trinh *et al.* reported that the CNTs had an I_D/I_G ratio of 0.88 prior to sintering and the CNTs after sintering had an I_D/I_G ratio of 0.89 in multiple trials.[142,152] Although sintering at typical temperatures did not cause any damage, sintering above 600°C does show an increase in defects and the formation of Al_4C_3, which the authors suggested did improve the material's mechanical properties. A greater discussion of compounds at the CNT-Al interface can be found in Section 2.3.4.

Other sintering processes include pressure-less sintering at 600°C and processed under vacuum,[138] hot isostatic pressing (HIP) at 350°C in an Ar atmosphere,[190] or simply hot pressing at 500°C.[187,191] Most processes also include a final extrusion step between 350°C and 500°C, typically in an inert atmosphere, for improved CNT alignment.[13,152,155,178,188,190] CNTs of their original diameters are observed in

the composite after synthesis in works by Chen *et al.* and Saba *et al.*,[38,178] and most processes show visuals of the CNTs intact, in the composite, with little degradation.[140,152,175,191–193]

Although somewhat debated, as discussed earlier, powder metallurgy methods have been shown to cause damage to the CNTs by increasing the number of defects and, at a minimum, decreasing the length of the CNTs in the composite.[181] Other methods that have been explored include a similar powder metallurgy process with a final friction stir processing (FSP) step, modeled after friction stir welding, which resulted in a continued increase in mechanical properties past 1.5 wt% ($\sim$1.15 vol%), whereas composites formed without the FSP step began to lose strength after the wt% of CNTs increased past 1.5 wt%. Additionally, only a minor increase in Raman I_D/I_G ratio, a measure of disorder and damage to the CNTs, where a higher I_D/I_G ratio corresponds to more damage, was observed after FSP.[181] However, this process resulted in considerably shorter CNTs than were originally added, decreasing the contribution from the load transfer effect. Larianovsky *et al.* also takes inspiration from industrial processes with a high pressure die casting with cyclic extrusion (HPDC-CE) process, using 4 extrusion steps to reduce agglomerates.[194] Harrigan also describes a casting process based on industrial procedures, using a vacuum-assisted Al casting method with nanoparticles mixed into molten Al, which does not damage the CNTs through ball milling.[195] Although CNTs begin to degrade around 500°C in air,[196] the vacuum process allows the CNTs to be stable throughout. This process does not address any agglomeration issues, as CNTs are not wet well by Al, but the vacuum-assistance and constant heating make it desirable for use with A-CNT arrays.

Two additional methods have been tested with A-CNTs and an Al matrix specifically. The first sputter coats the A-CNT array with Al, but finds that the Al begins to coalesce at the outer surfaces of the A-CNT array instead of conformally coating the individual CNTs.[164] The second is an electroplating method using anhydrous aluminum chloride in an electrolyte solution. This successfully coated the CNTs with Al prior to melting Al powder into the array, but coating was only successful at small scales (arrays of 3–5 μm in height),[157] suggesting limits to bulk processing, and no

mechanical data was provided.

The processes discussed above can cause damage to the CNTs both through milling and the high-temperature synthesis process. Additionally, processes with bulk CNTs do not fully take advantage of their properties because they form composites with a random CNT alignment, so the composite properties are unable to reach their full potential. For these reasons, the work in this thesis focuses on developing processes to synthesize an aluminum A/Al-NC using CNT arrays ∼100 μm tall, two orders of magnitude taller than other work on A/Al-NCs with CNT arrays, making this process more easily scalable for industry. Section 2.3.4 discusses the challenges of A/Al-NC synthesis in greater depth.

2.3.4   Challenges Specific to A/Al-NCs

The most notable challenge in A/Al-NC synthesis is the difference in surface energies between the CNTs and the Al matrix. This difference in surface energies aggravates two common issues with CNT composites discussed below: CNT agglomeration and poor interfacial adhesion. As stated above, the differences in surface energy cause CNTs to cluster away from the molten aluminum, causing the CNTs to agglomerate.[180] As with A-PNCs and A/C-NCs, the van der Waals forces between the CNTs contributes to the agglomeration,[13,181] and the differences in density between CNTs and the molten metal[136,194] may further aggravate the issue as well. CNT agglomeration is a significant challenge in CNT-metal matrix NC synthesis because it results in stress concentrations at the cluster sites,[194] which tend to be at the grain boundaries,[136,155,178,181,191] and result in lower CNT vol% composites with the highest mechanical properties.[137,190] More specifically, a decreased elongation at failure was found to correlate with a high CNT content, as voids tend to form along the CNT/Al interface.[181] Zhang *et al.* found that composite strengths peaked at 0.5 vol% CNTs, which does not agree with the strengthening mechanism calculations in Section 2.3.2, as composite strength should continue increasing with increasing CNT content.[13] Travessa *et al.* also found a statistical difference in hardness at different milling times, which suggests that the hardness increases with better CNT disper-

sion.[155] To combat the agglomeration challenge, CNT surfaces can be modified to improve dispersion. Additionally, the work in this thesis looks specifically at A-CNTs, since homogeneously distributed CNTs are better able to reach the theoretical maximum strengths.[187] To combat agglomeration due to differences in surface energies, a surface modification step as discussed in Section 2.3.1 to better wet the CNTs by the Al seems advantageous.[38,137,174]

The other common issue due to the difference in surface energies is poor interfacial adhesion. One possible solution to interfacial adhesion is through interfacial reactions, which are debated to both increase interfacial bonding and decrease the composite's characteristics. These interfacial reactions are the third substantial challenge of A/Al-NC synthesis. The formation of carbides at the CNT-Al interface is contested, as the carbides may improve the composite properties, but typically degrade the CNTs in the process. Al_4C_3, aluminum carbide, commonly forms in the processing of Al-CNT NCs due to the low free energy of formation ($\sim$12.7 kcal at 298°K); however, it is energetically favorable to form along the basal planes of carbon, which are not available in defect-free CNTs. For this reason, defect-free CNTs are thermodynamically stable in Al, even at high temperatures, and only form Al_4C_3 on the tips of the CNTs and with any amorphous or turbostratic carbon coating the CNT surface. CVD-grown CNTs have more defects and considerably more amorphous carbon on the CNTs, promoting Al_4C_3 formation. Al_4C_3 begins to form at 650°C, above the melting temperature of Al but below most of the processing temperatures.[197] Powder metallurgy methods, the most common CNT-Al matrix NC synthesis technique, cause damage to the CNTs,[136,175] which make these methods more likely to form Al_4C_3 at the interface.[13] Some ball milling methods found that the damaged CNTs interact with the Al matrix to form aluminum carbide, but this was not found to be true with all methods.[138,187] The formation of Al_4C_3 seems less than ideal, as CNTs degrade during processing to form Al_4C_3.[155,181] The degradation of the CNTs decreases their ability to reinforce the matrix. Although the layer of Al_4C_3 may lower the theoretical maximum reinforcement capability of CNTs, especially in MWCNTs where there exists extra CNT walls that are not consumed in Al_4C_3 creation, there

are many positives effects of an Al_4C_3 layer.

First, Al_4C_3 is harder than the Al phase, meaning that it can contribute to the load transfer effect[154,197]. The tightly-bound Al_4C_3 can stop the slipping of CNTs out of the Al coating, particularly by anchoring the ends in the matrix,[197] meaning that the Al_4C_3 improves the ability of CNTs to support the load. Chen *et al.* found this to be true experimentally, as the samples with a partial interfacial reaction of CNTs with Al had a higher ultimate tensile strength than similarly processed Al, Al with unreacted CNTs, or Al with fully reacted CNTs.[12] However, partially reacted CNTs were still found to decrease ductility of the composite over the material synthesized only with pure Al powder,[183] possibly suggesting that Al_4C_3 does not solve the agglomeration issues. In addition to its contributions to load transfer, Al_4C_3 contributes to the Hall-Petch effect and Orowan strengthening. Al_4C_3 does have a mismatched CTE from both the Al and the CNTs, which may alleviate stresses during thermal cycling. Al_4C_3 is theorized to play a considerable role in the increase in mechanical properties over the as-processed Al.[193]

An alternative to the layer of Al_4C_3 formed during CNT-Al matrix NC processing is a decorated layer of Al_2C_3 nanoparticles on the CNTs. These nanoparticles improved the interfacial adhesion between the CNTs and the matrix such that the CNTs fractured instead of being pulled out of the matrix.[192] While this does improve load transfer, it likely decreases the toughness contribution from CNT debonding and sliding, which is an important consideration.

While the formation of Al_4C_3 may not be ideal, it solves other challenges, specifically regarding the interfacial bonding between the CNTs and the Al matrix. A better mechanism of interfacial bonding should be studied, however, such that the CNTs are not being sacrificed significantly.

2.4 Conclusions

In this chapter, previous work in the study of both A/C-NCs and A/Al-NCs was reviewed. The limitations in both synthesis technique and final properties were dis-

cussed, as well as several lessons learned. In the next chapter, the objectives of this thesis and the approach to reach these objectives are outlined.

Chapter 3

Objectives and Approach

As reviewed in the prior chapters, aligned carbon nanotube (A-CNT) nanocomposites (NCs) may be ideal candidates for applications in harsh environments, such as high-temperature environments or environments with ionizing radiation. Although polymer matrices are not ideal for these types of applications, carbon and aluminum matrices are excellent candidates for high temperature applications. In order to fabricate A-CNT/carbon-matrix nanocomposites (A/C-NCs), a type of ceramic matrix nanocomposite (CMNC), and A-CNT/aluminum-matrix nanocomposites (A/Al-NCs), a type of metal matrix nanocomposite (MMNC), that take full advantage of the CNT reinforcements, the current synthesis processes must be improved. Drawing from previous work in the fields of A/C-NCs, A/Al-NCs, and A-CNT polymer nanocomposites (A-PNCs), fabrication processes are developed for high A-CNT volume fraction (up to 30 vol%) A/C-NCs as well as explored for A/Al-NCs.

3.1   Objectives

The objectives of this thesis are twofold. First, this thesis aims to develop higher hardness A/C-NCs through the complete infusion, curing, and pyrolysis of phenol-formaldehyde (P-F) resin into high A-CNT volume fraction (30 vol%) A-CNT arrays. Successful infusion requires the development of a process to desorb water from the CNT surface, combined with improvements to the previously developed resin infusion

processes. Second, this thesis aims to develop processes to synthesize $\sim$100 μm-tall A/Al-MMNCs. Since A/Al-NCs, much less A/Al-NCs with such tall CNTs have not been fabricated, as discussed in Section 2.3, this thesis provides a synthesis procedure and provides guidance on improving the synthesis and characterization methods.

3.2   General Approach

There are three elements to the experimental approach in this thesis: 1) A/C-NC synthesis methods and characterization and 2) mechanical properties, in addition to 3) A/Al-NC synthesis methods. The techniques applied in each area are outlined in the following sections, with additional details and results included in the following chapters.

Although previous work has investigated the infusion of polymer resin into high-volume fraction (20–30 vol%) A-CNTs, full infusion with corresponding improvement in mechanical properties has been a challenge. This thesis focuses on improving the synthesis methods such that an improvement in mechanical properties can be realized at high CNT volume fractions (v_f), up to 30 vol%. Taken together, the processing routes and characterizations contributed herein provide new high-temperature NC matrix materials compatible with A-CNT arrays, leading to new nanoengineered material capabilities that require further exploration.

3.2.1   A/C-NC Synthesis Methods and Characterization

In this thesis, A-CNT arrays grown *via* chemical vapor deposition (CVD) were densified to appropriate v_f using a mechanical biaxial densification process. A water desorption procedure of the A-CNT arrays prior to infusion of resin was developed. Then, the P-F resin was infused into the arrays and cured to form A-PNCs. Finally, the resin was pyrolyzed to create the final A/C-NCs. More detail on these methods as well as trial procedures can be found in Chapter 4. Preliminary characterization on cure shrinkage and porosity is also included in Chapter 4.

3.2.2 A/C-NC Mechanical Properties

To quantify the mechanical properties of these NCs, the NCs were polished and prepared for microhardness testing. Their Vickers hardness was measured in accordance with the ASTM Standard Test Method for Vickers Indentation Hardness of Advanced Ceramics (ASTM C1327).[7] These results are analyzed and discussed further in Chapter 5, particularly in the context of insights from scanning electron microscope (SEM) imaging and X-ray micro-computed tomography (μCT) volumetric imaging.

3.2.3 A/Al-NC Synthesis Methods

There is little literature on A-CNTs in metal matrices, as the typical methods build off of traditional powder metallurgy methods. Less literature exists for 100 μm-scale A-CNT arrays as reinforcements, as infusion becomes more difficult with taller matrices, and all extant methods have not been shown to be scalable to these heights. This thesis aims to develop synthesis techniques, described in Chapter 6, to enable Al infusion into tall A-CNT arrays. First, the A-CNTs were grown *via* CVD. Then, the surfaces were modified *via* decoration of TiO_2 *via* atomic layer deposition (ALD) with an optional plasma pretreatment. The TiO_2-coated A-CNTs were heat treated with the aim of producing Ti-coated CNTs. Solder (63% Pb, 37% Sn) was used to test a vacuum infusion process and rapidly iterate through infusion and surface modification methods, as the low melting point of solder allowed for tests to be completed with preexisting laboratory equipment. Al infusion was also explored with a casting method and an infusion method, using an electron beam lithography tool.

The results of each step of the A/Al-NC synthesis process are characterized. Raman analysis of CNTs before and after plasma treatments was performed to quantify any damage to the CNTs. SEM imaging and energy-dispersive X-ray spectroscopy (EDS) of the TiO_2-decorated A-CNTs were used to confirm and visualize the TiO_2 layer while also confirming continued alignment of CNTs from the processing steps. Finally, X-ray powder diffraction (XRD) of the TiO_2 powder exposed to the same treatment was performed to assess the results of reduction of the TiO_2. Results from

each processing step are presented and discussed in Chapter 6 with successful methods highlighted and future research avenues suggested.

Chapter 4

A/C-NC Synthesis Methods and Characterization

Aligned-carbon nanotube/carbon-matrix nanocomposites (A/C-NCs) are strong candidates for high temperature applications that require hard structural materials, as discussed in Chapter 2, due to their high temperature stability and the toughening effect from adding carbon nanotubes (CNTs). The A/C-NCs discussed here are fabricated by first growing aligned-CNT (A-CNT) arrays, mechanically densifying the arrays to the prescribed volume fraction (v_f), up to 30% v_f, and placing the A-CNTs into a mold for polymer infusion, as discussed in Section 4.1. Once the A-CNTs are ready to be placed in a mold, the procedures follow two different paths: a baseline process, where A/C-NCs are made in a silicone mold in a vacuum oven, and an improved process, where A/C-NCs are fabricated in a steel mold in an inert-atmosphere glovebox with an additional water desorption step. The A/C-NCs are fabricated from a phenol-formaldehyde (P-F) resin, drawing on a vast body of previous work with A-CNT polymer nanocomposites (A-PNCs) as well as industry techniques for creating carbon/carbon (C/C) composites with a polymer precursor. Resins with various wt% volatiles, fabricated by degassing the resin or diluting the resin with isopropanol, are tested, and the reasoning behind the design of each method is discussed in Section 4.2. The resin is then infused into the A-CNT arrays and cured to create A-PNCs. Pyrolysis is the final step to transform the A-PNCs to A/C-NCs and is discussed

in Section 4.3. In this chapter, both the initial synthesis methods and iterative improvements are discussed. Reasoning for procedure changes and the critical steps to improve in future work are also included.

4.1 A-CNT Array Preparation

A-CNT arrays for A/C-NCs are fabricated in three steps, as described in the subsections below. A-CNTs are grown on Si wafers to a density of 1 vol% using a chemical vapor deposition (CVD) process and then delaminated from the growth wafer for mechanical biaxial densification to 5, 10, 20, and 30% v_f. The 1–30% v_f arrays were placed in silicone, and later steel, molds for infusion.

4.1.1 A-CNT Growth

The A-CNT array growth procedure is performed *via* the following steps. 6" diameter silicon wafers were coated with a 1 nm layer of Fe and 10 nm Al_2O_3 catalyst *via* electron beam deposition. These wafers were then cut to 10 ± 1 mm squares to serve as substrates for A-CNT growth. Six wafers were placed into a 22-mm internal diameter quartz tube in a CVD furnace for growth, as shown in Figure 4-1.

Figure 4-1: Image of six Si wafer growth substrates in the growth furnace prior to A-CNT array synthesis.

The growth occurred in a mixture of hydrogen, helium, and water vapor, and used ethylene as the carbon source, similar to previously reported processes.[14,79,80,198,199] The growth process follows four basic steps: an ambient flush, a temperature ramp, the growth step, and finally a hydrogen anneal. For the flush, contaminants (*e.g.* humidity in the ambient environment) are purged from the growth system *via* helium gas flow at 1000 standard cubic centimeters per minute (sccm) and hydrogen gas flow at 200 sccm. Next, the system is preheated to the growth temperature, 700°C ±2°C, while continuing to more gently flush the system under 37 sccm of helium and 200 sccm of hydrogen flow. This step also serves to reduce the Fe catalyst to nanoparticles necessary for A-CNT growth. Once the furnace reached 600°C, water vapor is reintroduced at 7 sccm. After holding at the growth temperature for 5 minutes, ethylene is introduced at 150 sccm so that the A-CNT growth process can begin. A-CNTs were grown to mm-scale such that they could provide effective load transfer in the composite and such that they would maintain structural integrity during the subsequent processing steps. The A-CNT arrays grow at a roughly linear average growth rate of 1 μm per second. Thus, growth steps ranged from 15 minutes, corresponding to the 1 mm A-CNT arrays, to 35 minutes for the 2 mm A-CNT arrays. After the growth process, water and ethylene flow ceased and a 4-minute hydrogen anneal was implemented to weaken the adhesion between the CNTs and the catalyst on the growth wafer.[14] This step ensured that the CNTs would delaminate easily from the substrate for the densification step. The growth system was then cooled to 180°C and the six A-CNT arrays were carefully removed.

The CNTs have an average outer diameter of ~8 nm, inner diameter of ~5 nm, and consist of 3–7 walls.[14,79,80] The as-grown inter-CNT spacing in the arrays is ~80 nm, resulting in ~1% v_f.[14,79,80] Millimeter-scale arrays were chosen for this work for effective load transfer and so that bulk properties could be measured.[116]

4.1.2 A-CNT Densification

Since the as-grown A-CNT arrays had a 1% v_f and this parameter is not broadly tunable via CVD, the arrays required biaxial mechanical densification in order to

test a range of A-CNT volume fractions: 5, 10, 20, and 30% v_f. Biaxial mechanical densification allows for precise control of CNT volume fraction,[14] compared to other methods, such as capillary-induced densification.[134] The graphic in Figure 4-2 illustrates the biaxial densification concept.
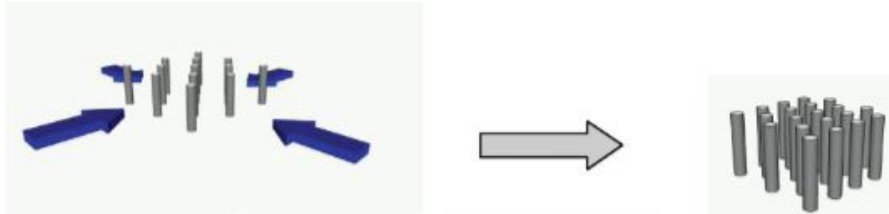
Figure 4-2: Illustration of the biaxial mechanical densification process, from low density (left) to high density (right).[14]

First, all A-CNT arrays were delaminated from the catalyzed Si growth wafers using a standard lab razor blade by gently separating the base of the array from the wafer. The arrays to be used for all higher v_f composites ($> 1\%$ v_f) were placed on a Teflon platform in preparation for the biaxial mechanical densification process with the CNT axis orthogonal to the plane of the platform and the tops of the A-CNT arrays facing downward. Biaxial densification followed a similar procedure to previous work.[18,200] The A-CNTs were placed in the tooling platform specific to the desired v_f and another acrylic tooling piece was placed on top to hold the A-CNTs in place. Then, a 1 cm x 1 mm (Teflon) or 2 mm (steel) compression rod, depending on the as-grown A-CNT array height, was used to compress the A-CNTs in one direction to their final dimension. This is somewhat approximate, as the compression rod is visually aligned with the gap in the platform for the second rod. The second steel rod, with dimensions specific to the v_f of A-CNTs being fabricated, was then slid into place and pushed until the A-CNTs visually formed a square. An illustration of this apparatus is shown in Figure 4-3 and detailed engineering drawings for a similar apparatus, designed for a process discussed in Section 4.4, can be found in Appendix A.1. The apparatus in Appendix A.1 differs in that all components are Teflon and includes holes extraneous to the process described above. Dimensions relevant to the biaxial mechanical densification are the same, but other dimensions have been

changed for ease of manufacture. Images from the densification of 10% v_f A-CNT arrays are shown in Figures 4-4a and 4-4b.
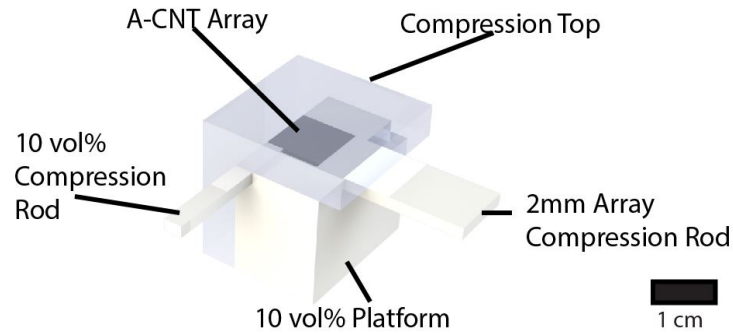
Figure 4-3: 3D illustration of the biaxial compression apparatus.
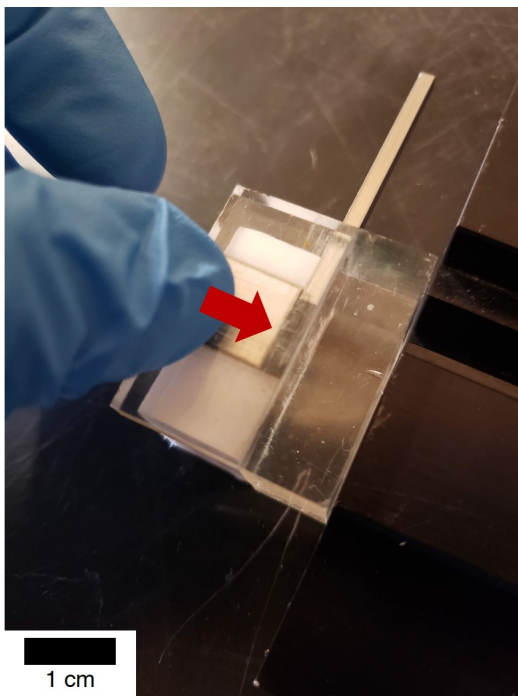
(a) First step: compression with a 2mm-wide compression rod.
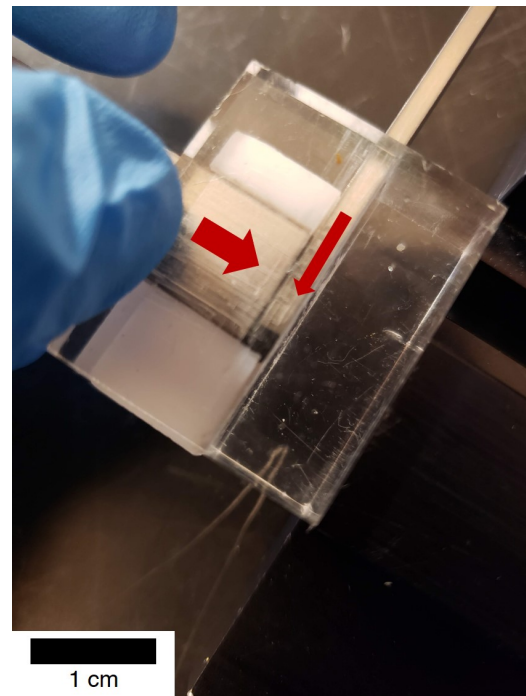
(b) Second step: compression with v_f-specific rod.

Figure 4-4: Images of the biaxial mechanical densification of a 10% v_f A-CNT array. The tooling is a Teflon platform with an acrylic cover and steel rods for densification.

The dimensions of the densified arrays were determined by Equation 4.1, explicitly modified from the original to include $v_{f,initial}$:[18]

$$v_f = v_{f,initial} * \frac{Area_{initial}}{Area_{densified}} \tag{4.1}$$

where v_f is the densified volume fraction, $v_{f,initial}$ is the as-grown (1%) v_f, $Area_{initial}$ is the initial array area (100 mm^2) and $Area_{densified}$ is the densified A-CNT array area. The areas of the arrays are referenced in Table 4.1[18]. All arrays were grown to 2 mm except for the 30% v_f arrays; inter-CNT forces made densifying the 30% v_f arrays challenging by hand, so the height of these arrays was kept to 1 mm to ensure full densification to 30% v_f. This work pushes the limits of densification, as previous A/C-NC work more commonly only reached 20% v_f.[14,78] Once densified, the A-CNTs arrays were prepared to be placed in molds for P-F resin infusion.

Table 4.1: Dimensions of densified A-CNT arrays. [18]

v_f	Densified Side Length	Densified Area	Height
1 vol%	10 mm	100 mm^2	2mm
5 vol%	4.47 mm	19.98^2	2mm
10 vol%	3.16 mm	9.99 mm^2	2mm
20 vol%	2.23 mm	4.97 mm^2	2mm
30 vol%	1.83 mm	3.35 mm^2	1mm

4.1.3   Preparation of Molds for A-CNT Infusion

A-CNT array fabrication for both the baseline and improved methods follow the same procedure until the arrays are placed in molds for infusion. Baseline P-F resin infusion trials were completed using a silicone mold in a vacuum oven. ECOFLEX® 0030 Platinum Cure Silicone Rubber parts A and B were combined in a 1:1 ratio according to the manufacturer instructions, poured into a negative, and cured for 4 hours at room temperature. Additional information on the manufacturing of the mold negative can be found in Appendix A.2. The molds were then post-cured for 2 hours at 80°C and 1 hour at 100°C on a hot plate, following the manufacturer recommendations. Then, densified A-CNT arrays were placed in the appropriately-sized molds with the carbon crust, found at the top of the array, placed at the base of

the mold so as not to interfere with infusion. Prepared arrays at 5%, 10%, 20%, and 30% v_f are shown in the silicone mold in Figure 4-5. Remaining spots in the molds are for the 1% v_f arrays and elongated neat resin samples.

Figure 4-5: Image of A-CNT arrays ranging from 5% to 30% v_f placed in a silicone mold.

It was found that residue on the fully cured silicone molds caused greater CNT densification into a cellular structure, as was found with other work using solvents.[134] Due to the silicone residue as well as the inferior thermal properties of the silicone mold, a two-piece steel mold was used for the improved resin infusion procedure. The steel mold consisted of two parts: a mold with holes through the thickness and a separate plate to serve as the baseplate for the mold. Dimensions and manufacturing information for the steel mold can be found in Appendix A.3.

The steel mold was coated with Frekote 700-NC or 770-NC Mold Release following the manufacturer directions. Two coats were applied and allowed to dry completely. Optionally, the steel mold was effectively sealed to the baseplate with high temperature vacuum tape (Airtech International Inc., A-800-3G). The vacuum tape sealed in lower-viscosity resins and kept the assembly from shifting during processing. The CNTs were then placed in the prepared mold. As with the silicone mold procedure, the CNTs were placed with the crust at the base of the mold, and the primary CNT axis was always kept orthogonal to the plane of the mold to facilitate polymer infusion

into the vertically aligned CNTs along their length. An image of a fully assembled steel mold with A-CNT arrays ranging from 1% to 30% v_f, prior to infusion, is displayed in Figure 4-6. The remaining two openings are for neat resin.

Figure 4-6: A-CNT arrays: 1% v_f (left), then 5%, 10%, 20%, and 30% v_f (right, prior to second set). A-CNT arrays were placed in the steel mold and sealed with vacuum tape prior to P-F resin infusion.

4.1.4   Water Desorption from A-CNT Arrays

As discussed in Subsections 2.2.1 and 2.2.3, infusing P-F resin into the A-CNT arrays can be a challenge, especially at high v_f. This is partly due to a 3–7 nm layer of physisorbed water on the surface of the A-CNTs, which impedes deposition of a secondary material onto the A-CNTs and can alter the behavior of the array, as discussed in Section 2.2.3.[77] Baseline infusion trials were completed in a vacuum oven, but the physisorbed water motivated the addition of a water desorption step prior to P-F resin infusion. For this improved procedure, the CNTs were placed in the steel mold, as steel has a maximum working temperature higher than the desorption temperatures. The water desorption step and all subsequent processing steps took place in a nitrogen-filled glovebox to ensure that the A-CNT arrays were not re-exposed to humidity from ambient conditions.

The water desorption process was as follows. The steel mold containing the A-CNTs was placed into a quartz boat in a 2" quartz tube and inserted in the KSL-1100X-S-H Compact Hybrid (Muffle/Tube) Furnace from MTI, inside the glovebox. The quartz tube containing the A-CNTs was connected to a vacuum pump, which

pulled a vacuum to 5 mbar during the process. Initially, an aggressive desorption process was attempted, where the A-CNTs were heated to 600°C under vacuum. The furnace was heated at a ramp rate of 5°C and held at 600°C for 6 hours. However, as discussed further in Chapter 5, this process was found to result in poor infusion, likely due to the removal of amorphous carbon on the outer CNT walls that hindered phenolic resin infiltration. For future water desorption processes, the furnace was heated to 280°C at a ramp rate of 5°C and held at 280°C for 6 hours. Literature shows that all the water will be desorbed from the A-CNTs at temperatures above 260°C, [201] but any amorphous carbon on the A-CNT outer walls will begin to transform into graphitic carbon at ~300°C [202] and degrade above ~500°C, even in an inert atmosphere. [202,203] For this reason, the desorption process was designed for 280°C. After the 6 hour hold, the furnace was cooled to room temperature (~23°C) and the A-CNTs were returned to atmospheric pressure.

4.2 Phenolic Resin Degassing and Infusion into Arrays

Once prepared per Section 4.1, the A-CNTs were ready for P-F resin infusion. As discussed in the previous section, the baseline procedure, based on previous work, [8,80] was performed in an ambient environment (without a glovebox), as the vacuum oven was thought to be sufficient to assist in the wetting process at high v_f. However, the adsorbed water seemed to inhibit wetting significantly. Thus, in the improved procedure, a desorption step was added and all subsequent processing steps occurred in a N_2 environment in a glovebox.

4.2.1 Baseline Infusion Procedure without Desorption

The first step in the baseline infusion procedure was to prepare the resin. The resin, Durite SC-1008 from Momentive Specialty Chemicals, was formulated at ~20 wt% IPA [94] with a total of ~40 wt% volatiles [204] by the manufacturer to reduce its viscos-

ity, which improves wetting. This solid (phenolic) loading is common for P-F resins, as others are also only ∼60 wt% solids as well.[117] Given the low solids loading, the resin was degassed to remove volatiles prior to infusion. Degassing resin is a standard procedure[117] because it eliminates volatiles, which could cause the A-CNTs to densify during infusion or agglomerate as the volatiles degas. For all the baseline trials, the resin was first removed from storage in the freezer and allowed to equilibrate to room temperature for an hour prior to pouring the resin into smaller vessels for degassing. Then, the resin was degassed at 60°C under a 5 mbar vacuum for 15 hours in a Memmert vacuum oven. Other trials found that higher temperatures and longer degassing periods made the resin too thick for successful infusion. Conversely, lower temperatures or shorter degassing periods did not eliminate enough volatiles from the resin, resulting in the resin degassing during the cure stage. This degassing procedure reduced the volatile content to 20–25 wt% volatiles and 75–80 wt% resin, as measured *via* thermogravimetric analysis (TGA).

As the baseline procedure did not include a water desorption step, the remainder of the process occurred in the Memmert vacuum oven and silicone molds. After the resin was sufficiently degassed, the vacuum was removed and the A-CNTs in molds were placed in the vacuum oven, as shown in Figure 4-7. The degassed resin was carefully poured on top of the arrays in an ambient environment, and the vacuum was reset to 5 mbar and held for 9 hours. The vacuum assisted the capillary-driven wetting of the A-CNTs, which is especially important at high v_f due to the reduced inter-CNT spacing. The temperature was then increased to 70°C and the pressure was increased to 500 mbar for 15 hours. The intermediate temperature steps (60° and 70°C) allowed the volatiles to continue offgassing prior to the cure. The increase in pressure also kept excess volatiles below their boiling point as the cure began. Trials that skipped the 70°C step or neglected to increase the pressure with increasing temperature often resulted in the resin curing into a foam-like consistency, as the resin was offgassing and curing concurrently. After the 70°C step, the temperature was increased to 110°C at atmospheric pressure for 9 hours, 160°C for 15 hours, and ∼200°C for 9 hours based on manufacturer recommendations for this application. Additional intermediate hold

temperatures were tested, but no improvement in degree of cure was found. As more volatiles offgassed and the P-F resin infused, the system was brought to ambient conditions and excess resin at the same cure stage was added to the A-CNT arrays before being returned to a 5 mbar vacuum. Once the cure process completed, the oven was left closed to cool to room temperature. This process was found to have a >90% degree of cure as measured by differential scanning calorimetry (DSC), indicating that the cure schedule was successful. Figure 4-8 shows the DSC curves for the as-received (uncured) and cured phenolic resin, the latter of which was subjected to the cure cycle described herein. The absence of an exothermic peak for the cured resin compared to the uncured resin signifies a near 100% degree of cure. After the cure cycle, no exothermic residual curing is observed during the DSC measurement.

CNT alignment was expected to be maintained throughout infusion[14] unlike other processes, which may cause the CNTs to randomly disperse, crush, or buckle.[97] Inspection of a 10% v_f A-PNC *via* scanning electron microscopy (SEM), shown in Figure 4-9, confirms that A-CNT alignment was maintained, as expected from prior work. The SEM image was taken of a surface fractured at room temperature rather than a polished surface, because the fracture surface is more effective to visualize the

15 cm

Figure 4-7: Three silicone molds with CNTs in the vacuum oven prior to infusion as part of the baseline process. Degassed resin is in the aluminum boats, ready to be poured into the molds.
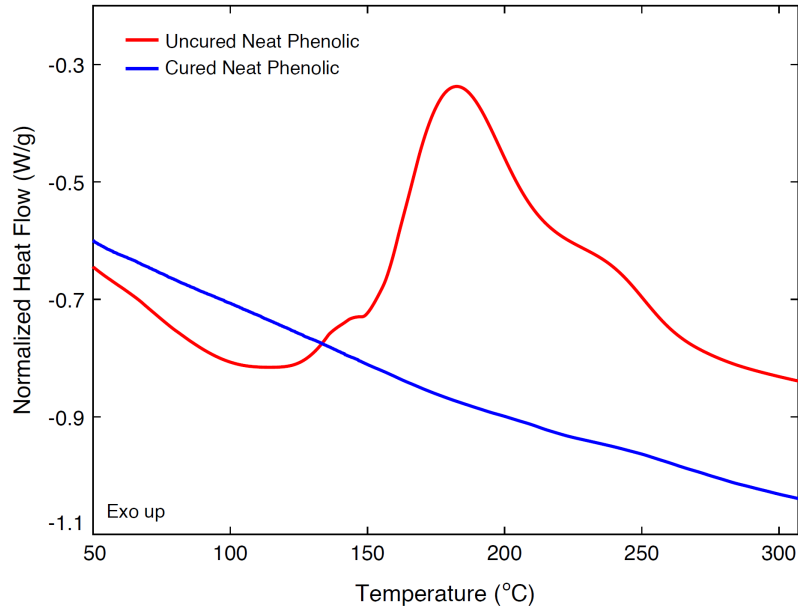
Figure 4-8: DSC curves for as-received (uncured) and cured phenolic resin, the latter of which was subjected to the cure cycle described herein. The absence of an exothermic peak for the cured resin, compared to the uncured resin, signifies a near 100% degree of cure.

internal morphology of the nanocomposites (NCs).[14]
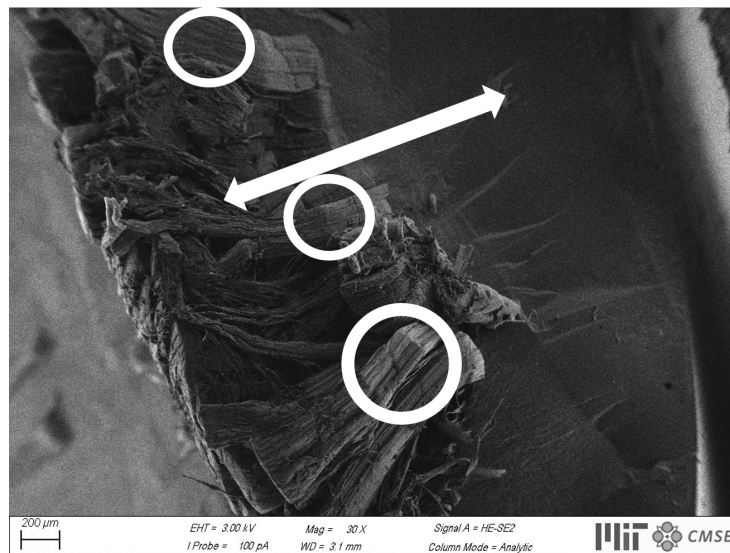
Figure 4-9: SEM image of a 10% v_f A-PNC prepared *via* the baseline procedure, confirming that the A-CNTs stay aligned after infusion. The arrow indicates the direction of A-CNT alignment, and the circled areas indicate where alignment - the parallel lines - is most visible.

4.2.2 Improved Infusion Procedures with Desorption in Glovebox

Trials were completed with adjustments to the desorption temperature (high-temperature desorption at 600°C and low-temperature desorption at 280°C, discussed in Section 4.1.4 and solids (phenolic) loading of the resin (~80 wt%, 60 wt%, 50 wt%, and 10 wt% solids). These adjustments resulted in a total of 5 procedures: high-temperature desorption with ~80 wt% (degassed) resin (improved 80 wt% HT), low-temperature desorption with ~80 wt% (degassed) resin (improved 80 wt% LT), low-temperature desorption with 60 wt% (as-received) resin (improved 60 wt% LT), low-temperature desorption with 50 wt% resin (improved 50 wt% LT), and low-temperature desorption with 10 wt% resin (improved 10 wt% LT). The process overview can be seen in Figure 4-10, with details following in this section.
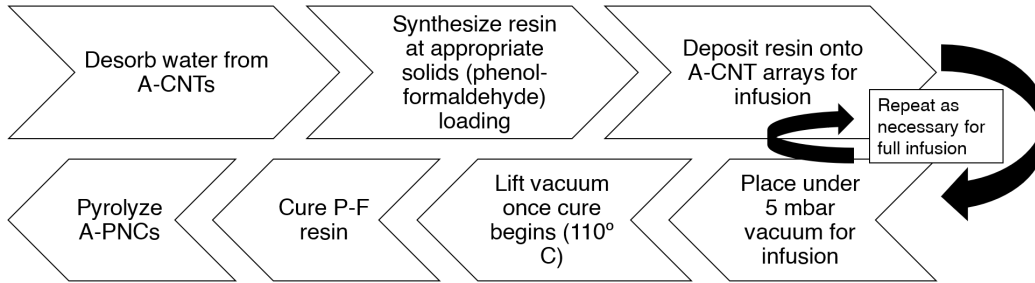
Figure 4-10: Overview of A/C-NC synthesis process *via* the improved procedure with seven major steps. Details of each step for the different procedures are provided in the remainder of this section.

As mentioned in Section 4.1, the silicone mold caused low-v_f A-CNT arrays to densify *via* capillary forces. Additionally, the silicone mold has a maximum service temperature of ~230°C, which is below the temperature necessary for the desired desorption step. Together, these factors motivated the shift to a steel mold.

For all the improved infusion processes, the A-CNTs were placed in the prepared steel mold, transferred to a glovebox with an N_2 atmosphere, and the water was des-

orbed from the A-CNTs prior to infusion. This water desorption step was applied for all improved infusion procedures, and the shift to the glovebox made these improved procedures different from the previously discussed baseline procedure. The glovebox setup can be seen in Figure 4-11, which includes the KSL-1100X-S-H Compact Hybrid (Muffle/Tube) Furnace from MTI, the 2" quartz tube inserted into the furnace and connected to the red vacuum pump on the left. The pressure gauge monitors the pressure and ensures the 5 mbar vacuum necessary for synthesis steps.

Figure 4-11: Image of the glovebox setup used for all desorption and improved infusion procedures. Image credit: A. L. Kaiser (MIT). Modified after original.

Initially, resin degassed at 60°C for 24 hours was used for the infusion, similar to the baseline procedure. In this improved procedure, the resin was degassed and then cooled prior to infusion, whereas the resin was kept at 60°C in the baseline procedure. The improved 80 wt% LT process is referred to as degassed, as this process underwent a full 24-hr degassing step to remove volatiles from the resin. However, as the resins with lower solids loadings needed these volatiles, all other (60 wt%, 50 wt%, and 10 wt%) resin formulations were only degassed for 30 minutes to remove bubbles from the resin. Thus, it needed to be heated to 60°C–70°C to lower the viscosity prior to infusion. After a few trials, it was determined that the degassed resin was too viscous to sufficiently infuse. Separate infusions were tested using the following resin

96

formulations to determine the appropriate starting viscosity for improved infusion: as-received resin (60 wt% resin), 50 wt% resin diluted with isopropanol, and 10 wt% resin diluted with isopropanol, as suggested in literature.[108,118] For the 10 wt% resin, A-800-3G vacuum sealant tape from Airtech International Inc. was placed around the mold to seal the mold to the base plate and keep the resin from flowing out of the mold at the mold-base plate interface. The vacuum tape may be applied at any point prior to infusion except in the case of a high-temperature (600°C) desorption. The vacuum tape is unnecessary for thicker resins ($\geq$ 50 wt%) as this resin did not flow out of the mold and typically was not applied in these experiments. Once the mold was prepared, it was placed in a quartz boat for infusion.

The three highest viscosity resin formulations ($\sim$80 wt% degassed resin, 60 wt% as-received resin, and 50 wt% resin) underwent the same cure procedure, all in the glovebox: first, P-F resin, either at room temperature or heated to 60°C to decrease viscosity, was added to each sample using a pipette. The quartz boat was placed in the 2" quartz furnace tube and inserted into the furnace. The quartz tube was sealed and a 5 mbar vacuum was pulled. Mimicking the baseline infusion and cure procedures, the furnace followed a 10-minute ramp to 60°C, a 9-hour hold, a 5-minute ramp to 70°C, and a 15-hour hold before turning off the vacuum pump and returning the system to atmospheric pressure. These steps allowed for the degassing of resin and infusion of the resin into the A-CNT arrays prior to cure. Then, the furnace followed a 20-minute ramp to 110°C, a 9-hour hold, a 20-minute ramp to 160°C, a 15-hour hold, a 20-minute ramp to 200°C, and a 6-hour hold. Finally, the furnace cooled to room temperature and the cure process was complete. The two resins that were not degassed prior to infusion (as-received resin and 50 wt% resin) were expected to lose 40% of their mass from volatiles as they degassed. Thus, additional resin was added to the A-PNCs throughout the infusion process. The system was returned to atmospheric pressure and resin was added as necessary and when possible before returning the system to a 5 mbar vacuum. This process was repeated until the vacuum pump was turned off. Resin was never added after the vacuum pump was turned off, as the higher cure temperature could cause the volatiles to boil off during the cure.

For the as-received resin, this resin was added to top off each sample every 6 hours, on average. The 50% resin followed a similar procedure but additional 50% resin – typically a mix of excess 50% resin in the infusion boat and fresh resin – was added to top off the samples every 5 hours on average.

Since the 10 wt% resin was primarily volatiles, a few modifications were applied to the infusion procedure. Like the other resin formulations, the resin was added to the samples using a pipette. Then, the quartz boat was placed in the quartz furnace tube, inserted into the furnace, sealed, and placed under a 5 mbar vacuum. The furnace followed a 10-minute ramp to 60°C, a 15-hour hold, a 5-minute ramp to 70°C, and another 15-hour hold before turning off the vacuum pump and returning the system to atmospheric pressure. The infusion times at 60°C and 70°C were increased from the baseline procedure, as the resin needed time to degas during infusion, and 15 hours at each step was determined to be sufficient as experiments were run. Additional resin was then added to the A-CNTs by pipetting enough resin solution to cover the samples every ∼2 hours, breaking the vacuum but leaving the oven at temperature. As this was necessary but not feasible overnight, the resin solution was poured into the quartz boat to fill it to ∼90%; this was enough resin to cover the arrays with excess, but not enough such that the resin spilled out of the quartz boat during handling. This was repeated the next day as more resin was necessary, at ∼2-hour intervals, until the vacuum pump was turned off prior to cure. The A-CNT arrays underwent the same cure procedure as before: a 20 minute-ramp to 110°C, a 9-hour hold, a 20 minute ramp to 160°C, a 15-hour hold, a 20 minute ramp to 200°C, and a 6-hour hold. Finally, the furnace cooled to room temperature.

All three of the new resin formulations appeared to have more complete infusion after the improved procedure, as these samples were stiffer to the touch compared to the A-C/NCs synthesized *via* the improved procedure with 80 wt% (degassed) resin. The samples produced with 10 wt% resin showed some capillary-induced densification effects from the solvent in the resin, particularly at low v_f, so it was determined that the lowest-viscosity resin should only be used when higher-viscosity resins were ineffective (*e.g.* during reinfusion procedures after initial NC cure, a process discussed

in Section 4.4). This densification effect is visible in Figure 4-12. As the 50 wt% resin had a slightly lower viscosity than the 60 wt% as-received resin, this was expected to infuse best and thus have the highest Vickers hardness. A full analysis of infusion, based on imaging data, and the hardness of these samples will be discussed in Chapter 5. All the PNCs discussed in this section preserve the original volume fraction of CNTs (*e.g.* ∼1 vol.% CNTs in air becomes ∼1 vol.% CNTs and ∼ 99 vol.% phenolic resin). Since the density of the phenolic resin is ∼1.1±0.1 g/cm^3,[6,79] this corresponds to a CNT mass fraction of ∼1.5±0.1 wt% and resin mass fraction of 98.5 ± 0.1 wt%.
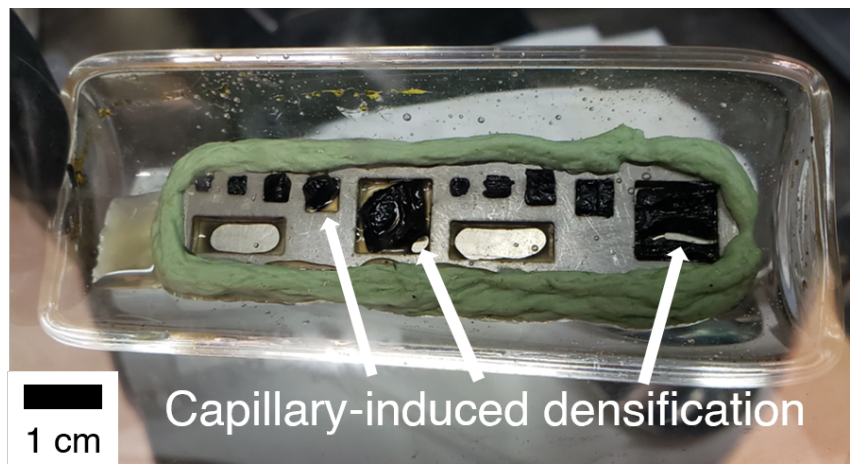
Figure 4-12: Minor capillary-induced densification effects are visible in the CNTs after a 10 wt% resin infusion.

4.3   Pyrolysis of Phenolic Resin to form A/C-NCs

To synthesize A/C-NCs from A-PNCs, the A-PNCs must be heated to transform the phenolic resin into pyrolytic carbon (PyC). Previous work with 1% v_f A-CNT arrays and this P-F resin shows that graphitic crystallites exhibit the highest aspect ratio when heat treated at 1000°C, which is linked to higher hardness.[79]. Thus, a 30-minute, 1000°C hold for pyrolysis was followed for all A/C-NCs.

4.3.1 Baseline Pyrolysis Procedure

For the baseline procedure, all samples were placed on an alumina plate in a commercial, hot wall tube furnace (STT-1600 Tube Furnace from SentroTech Corp, shown in Figure 4-13) with a 90 mm (3.5 in) inner diameter SiC tube. Ambient air was flushed from the tube and replaced with Ar in three cycles to ensure an Ar environment. The furnace temperature was increased to 1000°C at a 5°C/minute ramp rate and held at 1000°C for 30 minutes. The pyrolysis temperature profile can be seen in Figure 4-14. Due to inaccuracies in the furnace thermocouple, the process was designed to reach 1000°C and stay below 1015°C for approximately 30 minutes, which resulted in a maximum temperature of 1013.1°C and 33 minutes above the desired 1000°C threshold. The ramp rate was confirmed to be approximately 5°C/minute as set. Figure 4-15 compares A-PNCs prior to pyrolysis with A/C-NCs after the pyrolysis process.

Figure 4-13: STT-1600 Tube Furnace during baseline pyrolysis procedure.
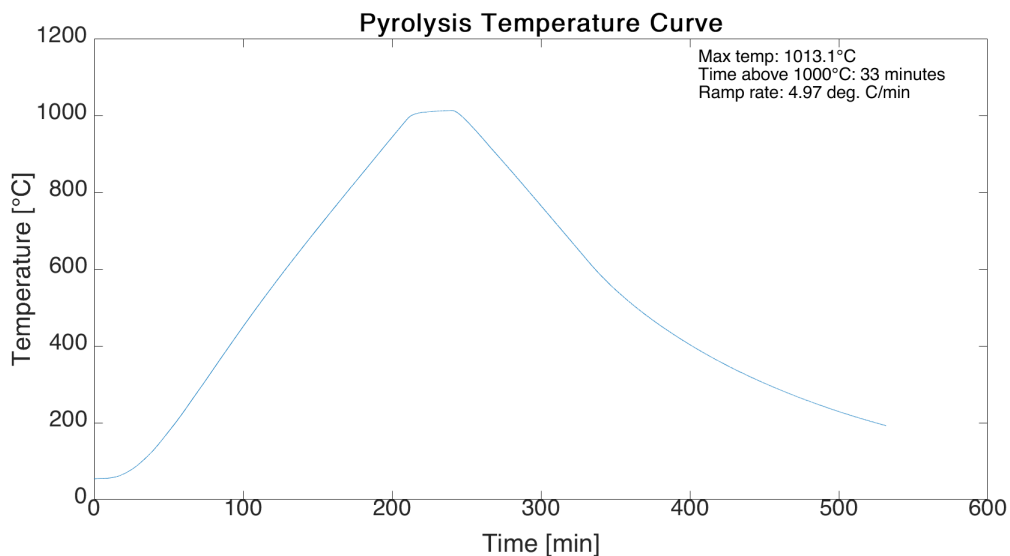
Figure 4-14: Baseline pyrolysis temperature profile. The furnace ramp rate was approximately 5°C as set, and held above 1000°C for 33 minutes, reaching a peak temperature of 1013.1°C.
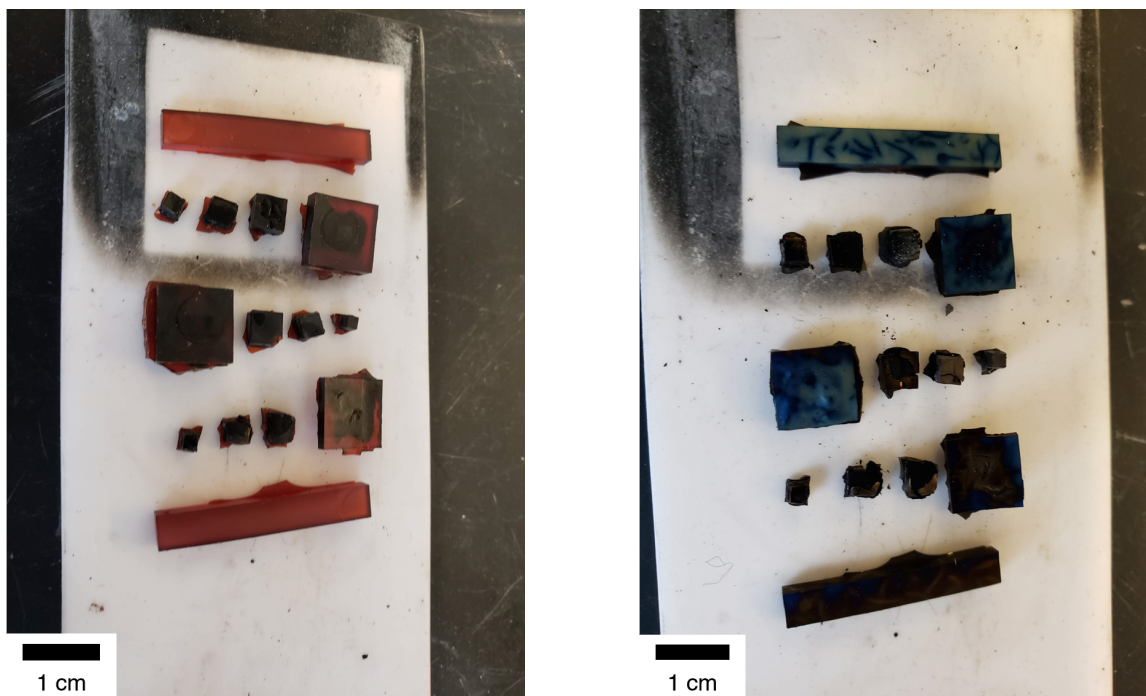
(a) A-PNCs (before).

(b) A/C-NCs (after).

Figure 4-15: Comparison of samples before and after baseline pyrolysis.

4.3.2 Improved Pyrolysis Procedure in Glovebox

For the improved procedure, the A-PNCs were removed from the steel mold and placed on an alumina plate in the KSL-100X-S-H Compact Hybrid (Muffle/Tube)

Furnace, described in Section 4.1.4, all while in the N$_2$ atmosphere. A-PNCs prior to pyrolysis are shown in Figure 4-17a. To match the baseline procedure, the A-PNCs were pyrolyzed at 1000°C for 30 minutes under atmospheric pressure. The furnace heated to approximately 1000°C over 4 hours and 10 minutes at a ramp rate of ~4°C/minute. The furnace held at 1000°C for 30 minutes and was allowed to cool to room temperature to complete the process. Although this process was not characterized from room temperature as with the baseline procedure, a temperature curve was measured up to 1000°C for furnace calibration. The relevant portion of the calibration is included in Figure 4-16, showing that this furnace was better able to hold a temperature and held at ~1015°C for 30 minutes when set to 1000°C. A/C-NCs were prepared for X-ray micro-computed tomography (μCT) after pyrolysis, and this image is included in Figure 4-17b for comparison to A-PNCs prior to infusion.
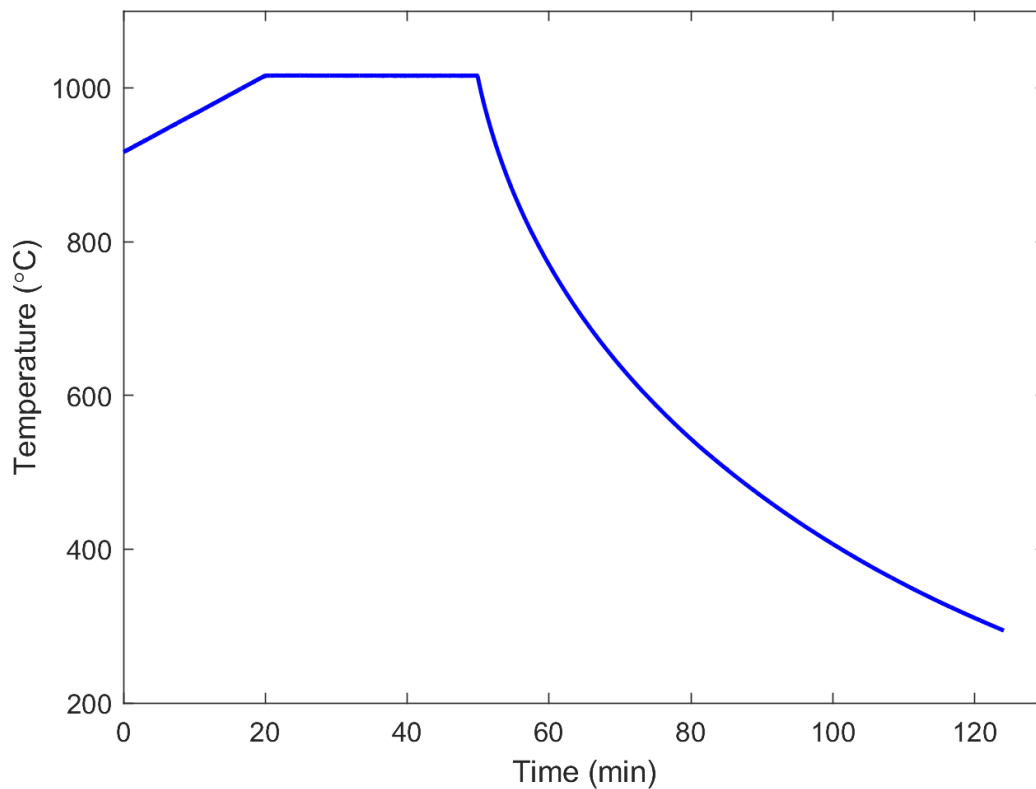
Figure 4-16: Portion of furnace calibration curve relevant to pyrolysis, showing a 4°C/minute ramp rate and 30-minute hold at 1015°C.

102

(a) A-PNCs prior to pyrolysis using improved procedures.

(b) A/C-NCs after pyrolysis as prepared for μCT.

Figure 4-17: Comparison of images of A-PNCs prior to pyrolysis and A/C-NCs after pyrolysis.

4.4   Conclusions and Recommendations for Future Work

In summary, various methods for the creation of A/C-NCs were tested. In preparation for P-F resin infusion, vertically aligned CNTs were grown to 1–2 mm heights using a CVD method. Initial trials were completed in a vacuum oven in an atmospheric environment and utilized a tube furnace for the pyrolysis step. Poor infusions during these trials were attributed primarily to adsorbed water on the surface of the CNTs, which impeded resin infiltration and decreased the inter-CNT spacing through which resin could flow. A secondary cause of poor infusion was attributed to the silicone molds used to create the A-PNCs, as silicone by-products seemed to absorb into the CNTs and cause minor capillary-induced densification in lower v_f (1 and 5% v_f) A-CNTs. Both of these concerns were addressed when the improved infusion procedure was developed. To address the densification due to the silicone molds, the silicone molds were replaced with two-piece steel molds. For the adsorbed water, an initial desorption step, which dried the CNTs at 280°C in an N_2 environment, was added

103

to the process. Higher temperature desorption steps were not found to improve the wetting either, as these likely graphitized the amorphous carbon on the outer walls of the A-CNTs, decreasing the ability for the resin to wet effectively. A similar infusion process to the baseline procedure was attempted used in the N_2 atmosphere. A third infusion challenge, the high viscosity of the resin, which motivated the development of 3 new resin formulations: as-received resin, a 50% isopropanol/50% resin solution, and a 90% isopropanol/10% resin solution, which were tested in addition to the baseline degassed resin. A full discussion of the relative successes of each method, particularly in terms of infusion and hardness characteristics, will be discussed in Chapter 5. However, visual and physical evidence suggest that the ~50% resin solutions resulted in the best wetting and would provide the highest mechanical performance. Finally, all samples were pyrolyzed at 1000°C, as this was found to be the optimal temperature from previous work.

When designing the improved procedure, a few areas for future work became apparent. First, the biaxial densification method leaves minor room for error, as the second compression rod is slid into the apparatus until the array appears square. While the A-CNTs all fit in the molds, ensuring that all arrays are properly densified, an automated biaxial mechanical densification tool would increase throughput and ensure that exactly the same force is applied to densify the samples to a more precise tolerance where a human operator cannot. Additionally, as higher v_f can be synthesized, a motorized process could provide adequate force to densify A-CNT arrays of increased height to greater v_f.

Second, a resin infusion using a resin diluted to ~50% is suggested. However, there is room to adjust this process to find the appropriate dilution to both maximize infusion and minimize capillary-induced densification. As the resin must degas during infusion as well, the length and temperature of the infusion process may be adjusted to ensure complete infusion prior to the beginning of the cure cycle. Additionally, the timing of the addition of extra resin during infusion and the dilution of the extra resin added during infusion may be adjusted to ensure that there is sufficient resin to wet the array and that the resin is an appropriate dilution to infiltrate the array.

Finally, a reinfusion process after pyrolysis should be more thoroughly investigated. Previous work suggests that ∼4 infusions (an initial infusion and 3 additional reinfusions) should be completed to decrease porosity.[80] Modeling in the previous work suggests diminishing returns for porosity reduction after 4 processing steps, although more than 10 processing steps are required for a matrix porosity less than 50 vol% in a 1% v_f A-CNT array.[80] A reinfusion process was developed to use the 50 wt% resin and 4 cycles of infusion and pyrolysis, but more data must be collected to determine the success of the procedure. Initial results on this process are included in Section 5.4, but this process was not fully investigated due to unforeseen lab closures in the final semester of this thesis, and characterization of the reinfused samples remains future work.

If the infusion of resin into high-v_f (> 20 vol%) composites continues to be insufficient with the traditional resin infusion procedures, the infusion of degassed resin into 1% v_f A-CNT arrays and a subsequent biaxial densification of the infused, but not cured, array may improve the wetting at high v_f, as the resin has already been infused into the arrays. Appendix A.1 includes drawings for Teflon biaxial densification apparatuses designed specifically to allow excess resin to flow out of the arrays during densification. A final infusion procedure that may be investigated is the use of chemical vapor infusion (CVI) to fill in voids. As discussed in Chapter 2, this method was not entirely effective at a 2% v_f, and thus was not investigated for these higher-v_f A-CNTs. However, the traditional infusion processes are promising methods to provide complete infusion, and their hardnesses, as informed by SEM imaging and micro-computed tomography, will be discussed further in Chapter 5.

Chapter 5

A/C-NC Mechanical Properties

As discussed in Chapter 2, aligned-carbon nanotube (A-CNT)/carbon-matrix nanocomposites (A/C-NCs) are excellent candidates for high-temperature, high hardness applications, such as thermal protection systems and brake pads. A/C-NCs were fabricated in five steps, as discussed in Chapter 4: A-CNT array growth *via* CVD, array densification to the prescribed volume fraction (v_f), water desorption, phenol-formaldehyde (P-F) resin infusion to create A-CNT polymer nanocomposites (A-PNCs), and pyrolysis to transform the A-PNCs to A/C-NCs. Preliminary studies helped to determine which of the methods resulted in the most complete infusion and hardness. The baseline method did not include an A-CNT water desorption step, as detailed in Section 4.1, and used degassed resin for the infusion. Since this method was unsuccessful for high v_f ($\geq$ 10 vol%) composites, an improved method was developed. This method used a water desorption step tested at two temperatures (600°C and 280°C) and kept the samples in an N_2 environment throughout the desorption, infusion, and pyrolysis processes. Four resin processes, using Durite SC-1008 resin, were tested: degassed ($\sim$80 wt%) resin, as-received (60 wt%) resin, 50 wt% resin diluted with isopropanol, and 10 wt% resin diluted with isopropanol. Although the 60 wt%–10 wt% resins were also degassed, these resins underwent a 30-minute degassing process to remove air from the resin, whereas the 80 wt% resin, denoted as degassed, underwent a 24-hour degassing process to remove both air and volatiles from the resin.

A/C-NCs created with the baseline procedure and five improved procedures were tested. A/C-NCs were imaged using X-ray micro-computed tomography (μCT) to image the sample, visually evaluate the extent of infusion and any micron-scale voids, and determine if the infusion was sufficient to merit hardness testing. X-ray μCT is discussed further in Section 5.1. Since a key use of these A/C-NCs is in high hardness applications, the success of a method was determined by the sample's hardness, as measured *via* Vickers hardness. This is an end-point evaluation, as the hardness is to first order a function of the CNT vol% and the relative amount of carbon matrix compared to voids. High vol% A/C-NCs benefit from increased CNT reinforcement, but due to processing, may be disadvantaged due to increased void fraction. Thus, hardness trends are to first order interpreted as increasing with CNT vol% and decreasing with void vol%. However, confirming studies, such as thermogravimetric analysis (TGA) and/or He picnometry, to determine the nano-scale void vol%, were not undertaken. Section 5.2 discusses the details of the Vickers hardness testing procedure. Using X-Ray μCT and scanning electron microscope (SEM) images in concert with the Vickers hardness data, the effectiveness of the infusion procedures is evaluated in Section 5.3. Based on the data collected, future avenues for A/C-NCs with greater v_f, and thus greater hardness improvements, are outlined in Section 5.4.

The list of resin infusion procedures and the tests conducted on each procedure are included in Table 5.1. For a full planned set of tests, X-ray μCT images were collected of the A-PNCs and A/C-NCs. However, due to sudden lab closures not all experiments were completed. Hardness data for samples was also often collected in lieu of X-ray μCT data as equipment was available, and because X-ray μCT images without voids was not an indicator of hardness improvements. However, due to rapid lab shutdown in the final semester of this thesis, not all tests were conducted. X-ray μCT of A/C-NCs was only taken for the baseline 80 wt% noT procedure, as the takeaway from this data was that there was mass loss inherent to the pyrolysis process, as expected from previous work. Until the initial infusions were successful at high v_f (20%–30% v_f), images of A/C-NCs did not add to the work. Some X-ray μCT images are not included for the A-PNCs as well due to equipment failures. In this

case, only samples with $v_f \geq 10\%$ were imaged to decrease the necessary imaging time and share the equipment with the backlog of users. Not all hardness data is included as well: some A/C-NCs with 20% v_f were too compliant to the touch and were damaged during normal handling. Thus, these were not tested for Vickers hardness values. The improved 80 wt% LT (low-temperature) procedure (as defined in Table 5.1) was also not tested for Vickers hardness as all the samples were compliant to the touch. Pyrolytic carbon (PyC) (0% v_f) values were not collected for all the improved procedures, as well, since these values were expected to be the same (or similar within experimental error) across all processes. This assumption held true for the improved 60 wt% LT and improved 50 wt% LT procedures, as the hardness values for 0% v_f samples are within the standard error.

Table 5.1: List of resin infusion procedures and tests conducted on each procedure. Some processes were partially completed or not yet begun due to unexpected lab closures. Data collection focused on X-ray μCT of A-PNCs and Vickers hardness values, as these informed future infusion trials. However, data for samples that were compliant to the touch were not indented, as well as some X-ray μCT images due to equipment failures.

Procedure	Desorb	Degas	Resin wt%	μCT (A-PNCs)	μCT (A/C-NCs)	Vickers Hardness
Baseline 80 wt% noT	None	24 hrs	80 wt%	Completed	Completed	Completed
Improved 80 wt% HT	600°C	24 hrs	80 wt%	Not Begun	Not Begun	Partial
Improved 80 wt% LT	280°C	24 hrs	80 wt%	Completed	Not Begun	Not Begun
Improved 60 wt% LT	280°C	30 min	60 wt%	Partial	Not Begun	Partial
Improved 50 wt% LT	280°C	30 min	50 wt%	Partial	Not Begun	Completed
Improved 10 wt% LT	280°C	30 min	10 wt%	Completed	Not Begun	Partial

5.1   A-PNC and A/C-NC Evaluation *via* X-Ray Micro-Computed Tomography

Computed tomography (CT) is a nondestructive evaluation technique[205] used in this thesis as quality control, as this method may reveal voids and cracks in the nanocomposite (NC). Originally used in medicine,[206–208] CT scans have been adapted to provide up to sub-micron resolution (μCT scans) for research in materials science.[209,210] In addition to the lab-scale X-Ray μCT, X-ray CT can use monochromatic syn-

chrotron radiation, which permits faster scans due to high photon levels and is better for *in situ* work.[211] However, lab-scale X-Ray μCT equipment provides adequate scans and allows for greater tool access, so all discussions of X-Ray μCT work in this thesis refer to a lab X-Ray μCT, here the Zeiss Xradia 520 Versa.

The X-Ray μCT functions by colliding electrons with a target, which produces a polychromatic X-ray source of Bremsstrahlung X-rays.[212] The radiation passes through the sample to varying degrees, as different phases block the radiation to different extents. The degree of attenuation of the X-ray beam is measured as the image is projected onto a scintillator, magnified, and collected by a CCD detector, as depicted in Figure 5-1.[15,212] By rotating the sample, projections from every angle are collected in order to reconstruct the internal geometry of the sample. For the imaging completed in this thesis, a 2 μm voxel size (4–5 μm-scale feature resolution) was used to balance resolution with scan time. This used the 4X objective and 1601 projections per sample.
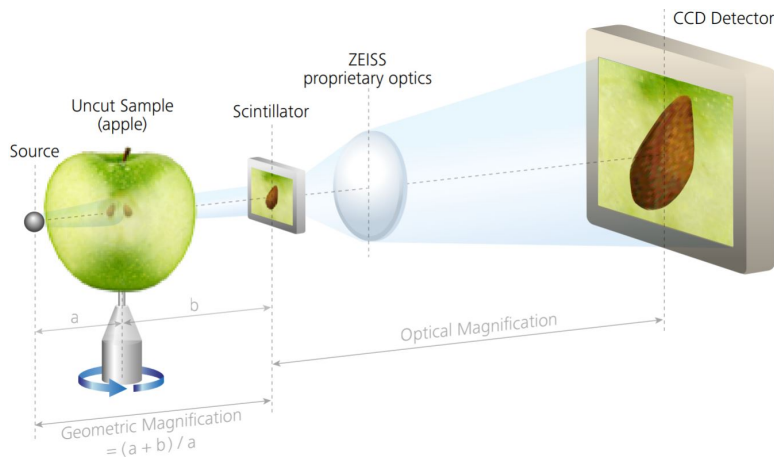
Figure 5-1: Depiction of X-Ray μCT equipment.[15]

Reconstruction of the internal geometry of the sample is typically done *via* the filtered back-projection method. The collected projections are first filtered to reduce noise and then summed along the projection direction. The constructive interference of these projections is used to deduce the internal geometry.[205,213] Despite being the most commonly used technique, this technique requires sufficient projections and a high signal-to-noise ratio. To obtain a more robust reconstruction, the images used

in this thesis are reconstructed *via* the iterative reconstruction method, where a 3D model is built over many iterations.[213]

To analyze this 3D image, it is important to segment the image by labeling voids, matrix, and reinforcements, which is typically done by assigning gray values to each of these categories. The darker sections of the image represent less dense regions in the composite, such as voids, and lighter sections represent the denser regions, the nanocomposite in this case. However, this approach may be too simplistic and requires a significant time investment. These limitations prompted the use of machine learning.[211] In this thesis, X-Ray µCT is used to qualitatively analyze the extent to which the polymer infusion process wets the A-CNTs by evaluating the void content of A-PNCs. X-ray µCT was also used to evaluate the void content of the baseline A/C-NCs, but studies of the void content of A/C-NCs fabricated *via* the improved processes were not in the scope of this thesis, as these studies were more relevant to the reinfusion process, discussed further in Section 5.4. This qualitative data was used in concert with the quantitative hardness data, which will be discussed in the following section, to determine the relative success of polymer infusion and understand the Vickers hardness values.

5.2 Vickers Hardness Testing

As discussed in Section 2.2.2, the Vickers hardness of A/C-NCs was tested to quantify the effectiveness of experimental polymer infusion processes on A/C-NC matrix performance. The Vickers hardness method, a type of microhardness test, measures hardness by indenting the sample with a Vickers indenter and measuring the projection of the indent. For accurate Vickers hardness testing, all samples must be polished. First, A/C-NCs were mounted such that the excess PyC, located on the top of the sample after infusion, was mounted inside of the resin puck and the bottom of the A/C-NC, with the entangled A-CNT layer formed in the initial growth stage, was mounted at the edge of the puck. Thus, the A-CNT axes were mounted perpendicular to the exposed plane used for Vickers hardness measurements. To mount the

A/C-NCs in this orientation, a piece of double-sided tape was placed on the base of the Struers 25 mm (1 in) FixiForm mounting cups, and then either Buehler Release Agent or Vaseline®, both of which are equally as effective, were applied to the remaining area of the base and the sides of the mold with a cotton swab. All A/C-NCs were adhered to the base of the mounting mold with double-sided tape to keep the entangled A-CNT layer at the bottom of the mold and to ensure that the low-density A/C-NCs would not float in the resin. Pace Technologies ULTRATHIN 2 Low Viscosity Resin was mixed according to the package directions. A wooden stick was placed in the mold and angled over the sample, and then resin was poured onto the stick to fill the mold without disturbing the sample. Mounted A/C-NCs were allowed to cure for 24 hours before removal from the mold. Figure 5-2a shows an image of a piece of pure PyC mounted in a resin puck as an example. The puck face visible in this image would have the entangled A-CNT layer exposed for any samples with A-CNTs. Figure 5-2b shows a side view of the resin puck with A/C-NC orientation labeled and typical thicknesses. The amount of A/C-NC removed by the grinding and polishing processes is expected to be on the order of 200 µm or less, and the indentation depth is less than 18 µm. However, the amount removed during the polishing process was directly affected by A/C-NC hardness, and the vertical distances in Figure 5-2b are not to scale. For a valid test per the standard test method, the indented sample must be 10 times thicker than the indentation depth, which is typically ≥0.5 mm. As all tested samples were visually ≥0.5 mm thick, their thicknesses were not specifically measured.

To polish these mounted A/C-NCs, the exposed face was first ground using 320 grit sandpaper for 2 minutes with water under a 15 N force with pucks rotating in the same direction as the sandpaper wheel. This was repeated at two-minute intervals until the excess resin and double-stick tape layer had been ground down. The short, 2-minute interval and 15 N force were found to balance effective grinding of the surface layer while not removing an excessive amount of the sample. The pucks were then rinsed and checked for any large scratches from handling, as all scratches should match the sandpaper grit. Next, mounted A/C-NCs were ground using 400, 600, 800, and
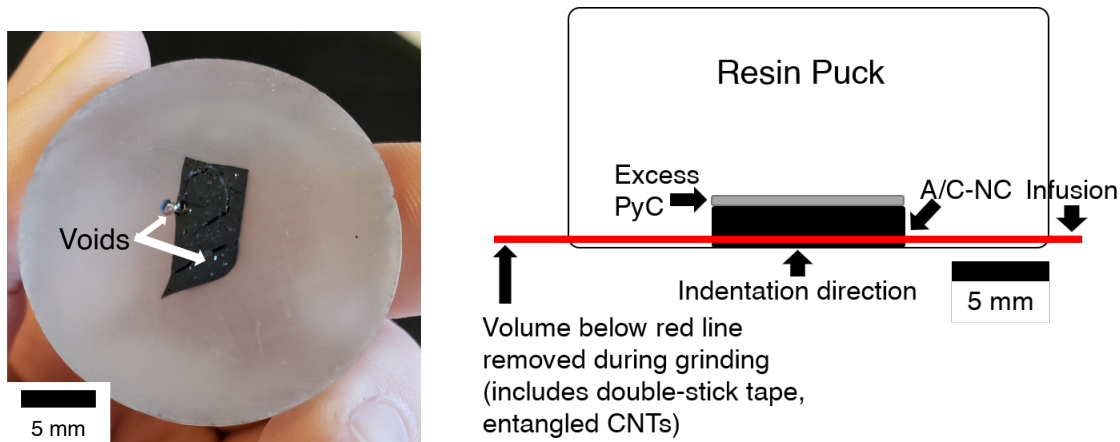
(a) Pure PyC sample made *via* the baseline 80 wt% noT procedure, mounted in a resin puck after initial grinding. Reflective areas are indicative of voids, since the PyC and the mounting resin appear reflective.

(b) Diagram showing the side view of a resin puck. As discussed in Chapter 4, resin infusion always proceeded into the aligned-CNTs from the base of the A-CNT growth, (*i.e.*, the side opposite the crust.)

Figure 5-2: Bottom (a) and side (b) views of the A/C-NC mounted for Vickers hardness testing. For A/C-NC samples, the entangled A-CNT layer would be exposed on the visible bottom face in Figure (a), as this sample was only ground to remove the double-stick tape. Vertical distances in (b) are typical but not exact, as the amount of A/C-NC polished differs as a function of hardness. The puck is ~20 mm, the A/C-NC is ~1.8 mm, and the A/C-NC removed by the grinding and polishing processes is ~200 μm.

1200 grit sandpaper at 4-minute intervals. After each interval, the mounted A/C-NCs were washed and inspected under an optical microscope. Prior to increasing grit, all scratches needed to appear to be the same size (from the most recent grit used) to ensure successful polishing. If all scratches did not appear to be from the same grit, the grinding process at that grit sandpaper was repeated until the scratches were of uniform size. The Struers TegraForce-5 was used for automatic grinding. Grinding could also be done by hand, using just a grinding wheel with sandpaper, but this method was significantly more time intensive and therefore is not suggested. The grinding process removed any excess PyC and the entangled A-CNT layer from the bottom of the A/C-NC, leaving the bulk of the sample exposed for hardness testing instead of any anomalies at the entangled A-CNT layer.

    Once the mounted A/C-NCs were ground to a 1200 grit surface finish, they were

polished on the Buehler AutoMet 250, using 3 μm and 1 μm diamond suspensions. The 3 μm suspension was used with the Buehler VerduTex polishing pad, and polishing occurred for 4 minutes under a 15 N force, 60 rpm head speed, and a 150 rpm polishing pad rotation in the same direction as the head based on manufacturer recommendations. Again, mounted A/C-NCs were cleaned and inspected between polishing steps. This process was repeated as necessary until all the scratch marks were of uniform size (∼3 μm in width). Finally, the 1 μm diamond suspension was used with the Buehler Tex Met C polishing pad and the same settings as the 3 μm suspension. Once cleaned and inspected, the mounted A/C-NCs were fully prepared for hardness testing.

All A/C-NCs were tested using the LECO LM 248AT Microhardness Tester with PAXcam camera and Cornerstone test software from LECO Corporation, following the ASTM Standard C1327-15, Standard Test Method for Vickers Indentation Hardness of Advanced Ceramics.[7] All pucks were placed on modeling clay on a glass slide and pressed until level so that the indentations would be on a flat surface. After polishing, the interior of the A/C-NC is exposed and the indentation surface is perpendicular to the A-CNT axis to measure hardness in the reinforced direction. For all indentations, the dwell time was chosen to be 10 seconds, as suggested in the test method,[7] and the load was chosen to be 500 grams-force, as this made a large indent (a diagonal of ∼100 μm) but was still measurable under the 50X objective magnification lens. For A/C-NCs with a lower hardness due to poor infusion, the load was adjusted such that the entire indent was visible under the 50x objective lens. The indenter and projected indentation geometry, with diagonals labeled, can be found in Section 2.2.2 and Figure 2-6. At least ten indentations per synthesis method were completed for each v_f available, and each indentation on the same sample was spaced away from previous indentations by at least four times the length of the diagonal to avoid any effects from the previous indentations.[7] As discussed in Section 5.3, most indentations were free of cracks, but cracking was representative of some samples and thus the hardness values from these indents were included in the average hardness values. Indentations with excessive cracking, more cracking than shown in the images

114

in Section 5.3, are not included in the data as these indents were not representative of the bulk of the sample. The initial indentation location was chosen randomly, and future locations were typically chosen along a horizontal path from the initial testing location. The brittle character of the carbon matrix makes the A/C-NC more sensitive to flaws (*e.g.* voids due to the pyrolysis process), and makes accurate hardness values more challenging to measure. Although initial indentation locations were chosen randomly, areas that obviously showed excessive flaws or voids were not used, as these were not representative of the bulk material. All samples satisfied the minimum thickness requirements, as discussed at the beginning of this section.

Hardness values were expected to be on the order of 4 GPa based on previous work by Stein *et al.* using a similar P-F resin precursor reinforced with A-CNTs.[78] The work by Stein *et al.* found that pure PyC had a Vickers hardness (H_V) of 3.5 ± 0.06 GPa (mean $\pm$ standard error), which increased up to a H_V of 4.3 ± 0.10 GPa for 10 vol% A-CNTs. Other work with PyC coatings, reported by Zhang *et al.* suggests hardness values from 1.68 ± 0.17 GPa for the lowest density PyC coating to 4.90 ± 0.19 GPa for the highest density PyC coating.[130] Thus, values around 4 GPa are reasonable for these mm-scale A/C-NCs. However, these values were determined by nanoindentation, which is affected by the local structural/morphological characteristics as opposed to reporting a bulk value. Additionally, the PyC showed viscoelastic characteristics, so the final indentation depth was calibrated from 10% of the original load instead of to 0% unloading to account for the viscoelasticity.[214] Vickers hardness values from the A/C-NC synthesis procedures presented in Chapter 4 will be presented in the next section so that all A/C-NC synthesis procedures presented in this work are compared to each other and to values from the literature, presented above.

5.3   Results and Discussion

Here, data from the 6 synthesis processes are discussed. This section focuses on the hardness values for these methods, using X-Ray μCT and SEM images of the

A/C-NCs as well as optical microscope images of the indentation area to analyze the findings. A-PNC μCT imaging and analysis supplements the A/C-NC evaluations where appropriate, as discussed (see Table 5.1). Data may be omitted for A/C-NCs that were compliant when handled with tweezers, suggesting that infusion was incomplete and additional tests would not add value to the work. Comparisons are drawn between different procedures and previous work.

5.3.1 Results for Baseline 80 wt% noT Procedure

The baseline infusion process, discussed in detail in Chapter 4, used degassed resin for infusion in a vacuum oven and did not include a water desorption step. The Vickers hardness values, measured in GPa, for each v_f are listed in Table 5.2 and displayed in Figure 5-3. The standard error for each hardness value is specified as well as the number of indents. Samples with poor infusion, evaluated with X-ray μCT images, have their hardness values shaded in gray and are denoted with square markers on the graph. This labeling will be followed in the rest of the chapter. There were 10 indents per A/C-NC, so some hardness values were averaged across different A/C-NCs that used the same infusion procedure (e.g. 4 A/C-NCs were tested for a total of 40 indents). The hardness value from the highest hardness sample is also included, as some samples resulted in better infusion than others. Future work should investigate the cause of variability in sample manufacture.

Table 5.2: Average Vickers hardness and standard error in GPa for 0–30% v_f A/C-NCs fabricated *via* the baseline 80 wt% noT procedure. The hardness value from the highest hardness sample is also included, showing improvements up to 5% v_f. Samples with poor infusion, based on X-ray μCT images, have hardness values shaded in gray.

A-CNT v_f	# Indents	Avg. Hardness (GPa)	Highest Hardness (GPa)
0%	50	3.289 ± 0.063	3.834 ± 0.094
1%	50	3.506 ± 0.053	3.822 ± 0.115
5%	40	2.693 ± 0.201	4.057 ± 0.238
10%	40	1.734 ± 0.269	3.782 ± 0.196
20%	40	1.008 ± 0.231	3.495 ± 0.080
30%	40	1.457 ± 0.244	3.234 ± 0.274

Figure 5-3: Average Vickers hardness and standard error in GPa for 0–30% v_f A/C-NCs fabricated *via* the baseline 80 wt% noT procedure. Samples with good infusion are denoted with diamond markers whereas samples with visibly poor infusion are denoted with square markers.

The hardness value decreased significantly after 1% v_f to a value below that of pure PyC, which is indicative of poor infusion. Infusion was investigated through multiple means, including SEM and X-Ray μCT imaging. SEM images of an A-PNC prior to pyrolysis indicate poor infusion. Figure 5-4 shows the fracture surface of a 10% v_f A-PNC that broke during normal handling and a close-up of the top view of the array. The A-CNTs have bundled together due to the P-F resin infusion; however, the resin has not fully infused to fill all the gaps between the A-CNTs. This is undesirable because the poor infusion, particularly into the A-CNT bundles, decreases the hardness due to the increased void fraction. Since the half of the A-CNT array to the right of the midline, at the bottom of the infusion, is fully infused, this poor infusion is likely because the resin needed more time to infuse into the gaps between A-CNTs prior to curing. As there was typically pure resin on top of the A/C-NCs after the cure, it is unlikely that there was insufficient resin for continued infusion.
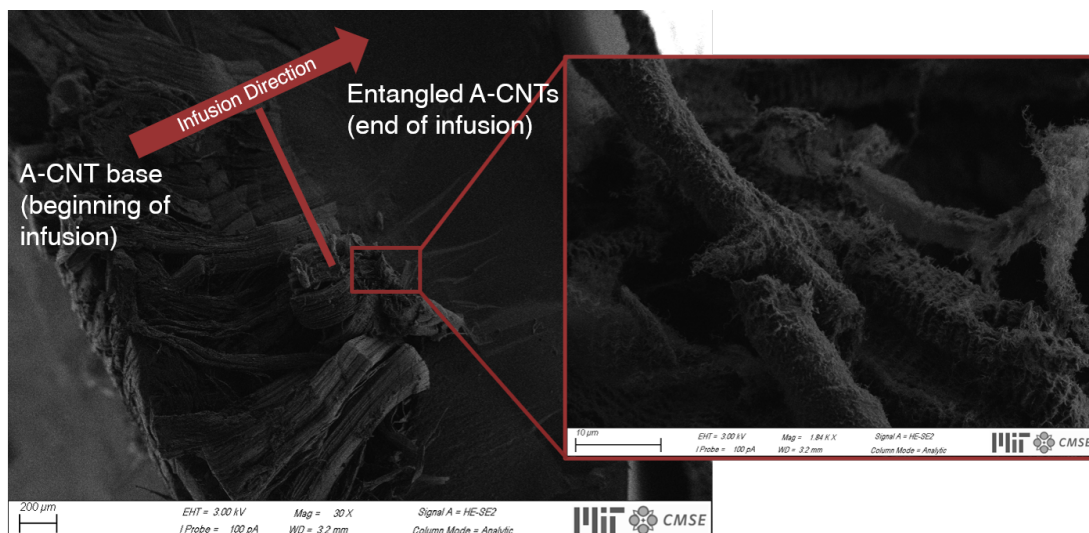
Figure 5-4: SEM image of a 10% v_f A-PNC made *via* the baseline 80 wt% noT procedure with a higher-magnification inset of the interior of the A-PNC. The arrow shows the direction of resin infusion and the midline separates the well-infused portion, to the right, from the poorly-infused portion, to the left. These images show wetted, bundled A-CNTs but poor overall infusion.

In addition to the poor infusion visible from SEM images, poor infusion is also visible during hardness testing. The 10% (Figure 5-5a) and 20% (Figure 5-5b) v_f A/C-NCs, imaged with an optical microscope during hardness testing, show A-CNT bundles in the interior of the sample, confirming that the poor infusion and A-CNT bundling visible in SEM was common across multiple A/C-NCs.

X-ray µ-CT images for all v_f A-PNCs can be seen in the left column of Figure 5-6, where the lighter grayscale values represent dense (*e.g.* fully infused composite) regions and the dark grayscale values represent low-density regions (*e.g.* voids), with grayscale values relative to other values within an image. Figure 5-6 includes a mounting tape callout, void callouts, resin-rich (polymer) regions, location of uninfused A-CNTs if visible, and scale bar on all images. The mounting tape callout shows the location of the mounting tape or, in the case of the 5% v_f A-CNTs, the direction of the mounting tape, located outside the field of view. Note that the entangled A-CNT layer is on the mounting tape, and excess PyC is at the bottom for all images. Hardness indentations are in the interior of the sample, on a plane perpendicular to the A-CNT direction that is near the bottom of the infusion (on the mounting tape).

(a) 10% v_f A/C-NCs   (b) 20% v_f A/C-NCs
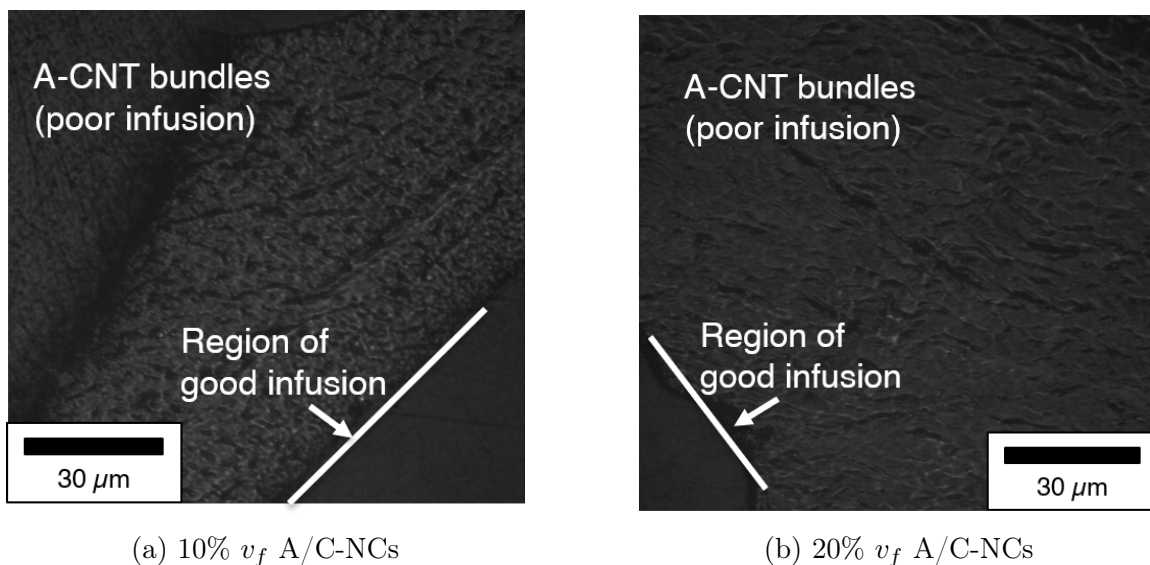
Figure 5-5: Images are of polished A/C-NCs visible under optical microscope during hardness testing, showing wetted A-CNT bundles fabricated *via* the baseline 80 wt% noT procedure. This area of poor infusion suggested that process adjustments were required.

There are clearly visible resin-rich regions and A-PNC regions in the 10%–30% v_f A-PNCs, and large voids visible in both the 5% and 10% v_f A-PNCs, both of which indicate an unsuccessful infusion. Poor infusion was attributed to the adsorbed water layer, first described in Section 2.2.3, and thus a water desorption step was implemented. X-ray µCT images of a different set of A/C-NCs also fabricated *via* the baseline 80 wt% noT procedure are included in the right column of Figure 5-6. The 0% v_f A/C-NCs provides a baseline for the expected void content after pyrolysis and the 1% v_f A/C-NC shows a similar void content, as expected from pyrolysis. The 5% v_f A/C-NC, however, shows a large layer of PyC sitting atop the sample (at the bottom of the image) and then a low-density area before the mounting tape (not pictured). This low-density area is indicative of pure A-CNTs or wetted bundles of A-CNTs but not full infusion, like the 1% v_f A/C-NCs. The following A/C-NCs – 10, 20, and 30% v_f – also show low-density A-CNT regions. This is especially noticeable in the 30% v_f image, where it is obvious that resin infused along the side of the mold to create a layer at the bottom of the mold and a much thicker layer at the top, but did not infuse into the array at all. These images additionally provide

information about the A/C-NCs after pyrolysis, and the the significant mass loss due to the pyrolysis process ($\sim$50%)[114] is visible in the voids that formed in the 0%, 1%, and 5% v_f A/C-NCs. These voids may contribute to the low hardness and high standard error discussed earlier in this section, and a process to address this mass loss will be discussed further in Section 5.4.

Once the average hardness drops below that of the pure PyC, the standard error on the hardness value increases significantly, from $\sim$0.06 to $\sim$0.25. Some areas of an A/C-NC have better infusion than others, which results in a large variation in hardness across the A/C-NC. Figure 5-7, shows indents in areas of the A/C-NCs that show cracking, suggesting poor infusion, and areas that do not show cracking, suggesting good infusion. Areas with significant voids had increased cracking. This data primarily supports the need for a process with improved infusion, but it also indicates that uniformity in the infusion will be key. This suggests that reinfusions, aimed at decreasing the void content arising during pyrolysis, may be a key process once the primary infusion is uniform. It is important to note that the customary diamond-shape, used for measuring the projected area of the indentation, is only indicated by the cross-shape. This less-apparent indent causes greater error in measuring the hardness values, as these diagonals must be manually measured instead of automatically measured by the Cornerstone software with the LECO Microhardness Tester. Samples with cracking were included as they were representative of one of the samples tested for both the 5% and 10% v_f A/C-NCs discussed here. The only sample with obvious cracking for the 30% v_f A/C-NC is pictured, but this datapoint was included as it was in line with the hardness values in that region from non-cracked indents.

5.3.2 Results for Improved 80 wt% HT Procedure

The first of the improved infusion processes introduced in Chapter 4, the improved 80 wt% HT procedure, added a high-temperature (600°C) water desorption step to the baseline 80 wt% noT procedure and moved all A-CNT processes to an N_2-filled glovebox to ensure no water was adsorbed in processing steps after the desorption. The Vickers hardness values from this synthesis method are given in Table 5.3 and
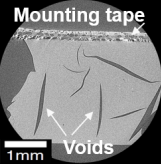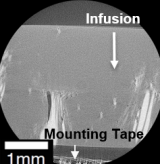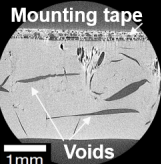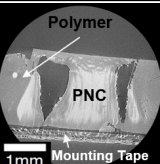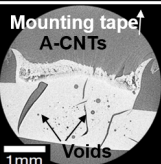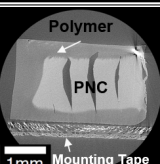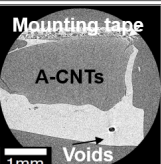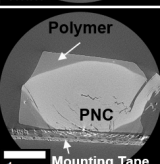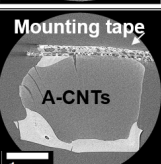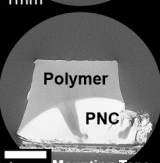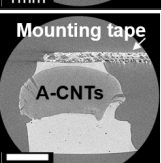
A-CNT Volume %	μCT of A-PNCs	μCT of A/C-NCs
0%	N/A	
1%		
5%		
10%		
20%		
30%		

Figure 5-6: Representative X-Ray μCT images of 0–30% v_f A-PNCs (left) and A/C-NCs (right) synthesized *via* the baseline 80 wt% noT procedure. Only one A-PNC was imaged per v_f. All images include a mounting tape callout, void callouts, location of uninfused A-CNTs if visible, resin-rich (polymer) regions, and scale bar. The entangled A-CNT layer was placed on the mounting tape, the excess P-F resin is at the top and the excess PyC is at the bottom, and the infusion direction is perpendicular to the mounting tape for all images, with the infusion beginning where there is excess P-F resin or PyC visible. Hardness indentations are in the interior of the sample, on a plane perpendicular to the A-CNT direction and the indentation direction is towards the excess P-F resin or PyC. ower density areas appear darker within an image, showing poor infusion starting at 5% v_f A/C-NCs, but grayscale values are not comparable between images. A-PNC images show clear voids and resin-rich regions. The A/C-NC images confirm the extent of infusion in the hardness data and also show the creation of voids due to the pyrolysis process.
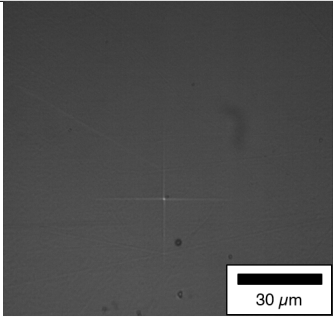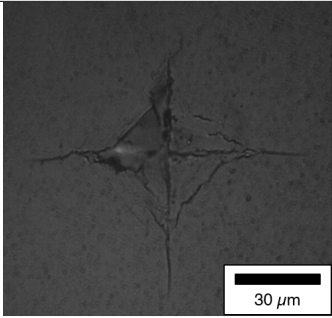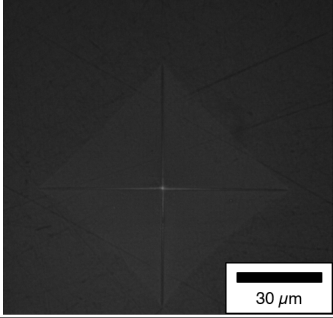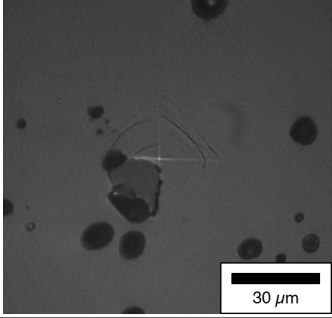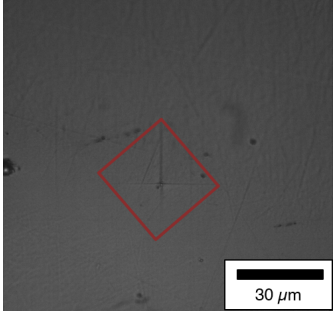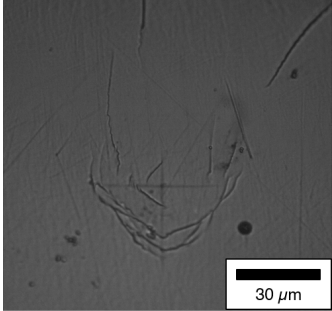
A-CNT Volume %	Indentation without Cracking	Indentation with Cracking	Approximate % of Indents without Cracking
5%			$\sim 80\%$
10%			$\sim 90\%$
30%			98%

Figure 5-7: Images of indentations with and without cracking and void formation for 5, 10, and 30% v_f A/C-NCs synthesized *via* the baseline 80 wt% noT procedure, exemplifying the variation in hardness leading to the large standard error. Samples where indents typically caused cracking were included in the hardness data collected as the indents with cracks were representative of one of the samples tested for both the 5% and 10% v_f A/C-NCs discussed here. The only sample with obvious cracking for the 30% v_f A/C-NC is pictured, but this datapoint was included as it was characteristic of the hardness in that region. Any indentations with more excessive cracking than shown here were not used.

shown in Figure 5-8. Samples with poor infusion are grayed out in the table and denoted with square markers on the graph. Highest hardness values are included in the table in addition to the average values, but are in line with the average values. Although the difference between average and highest hardness for the 5% v_f samples

is large, these values are within the margin of error and indicative of poor infusion. No values are recorded for 0% or 20% v_f A/C-NCs due to lab closures, as the initial 20% v_f samples were too compliant for polishing. Overflow resin was typically used for the 0 vol% A-CNT samples, and while this data will be collected in future work, there was not sufficient excess resin collected for the initial hardness tests in order to test the 0% sample in the scope of this work. An average hardness for the 0% v_f samples produced *via* all infusion procedures is included on the graph and denoted with an asterisk marker. All the A/C-NCs were compliant to the touch when picked up with tweezers, suggesting poor infusion, and both of the 20% v_f A/C-NCs synthesized with this process collapsed under normal handling and thus hardness tests were unable to be performed.

Table 5.3: Average Vickers hardness and standard error in GPa for 1, 5, 10, and 30% v_f A/C-NCs fabricated *via* the improved 80 wt% HT procedure. Highest hardness values are also included, but are typically in line with the average values. Although the difference between average and highest hardness for the 5% v_f samples is large, these values are within the margin of error and indicative of poor infusion. Samples with poor infusion, based on X-ray μCT images, have hardness values shaded in gray. As data was not collected on the 0% v_f sample with this procedure, an average value across all the improved procedures is included for comparison.

A-CNT v_f	# Indents	Avg. Hardness (GPa)	Highest Hardness (GPa/0
0% (Improved average)	30	3.137 ± 0.153	3.154 ± 0.217
1%	20	3.068 ± 0.122	3.088 ± 0.232
5%	20	0.595 ± 0.238	1.022 ± 0.444
10%	10	1.953 ± 0.136	1.953 ± 0.136
30%	10	0.038 ± 0.007	0.038 ± 0.007

The Vickers hardness values decreased from the 1% v_f A/C-NCs to 5% v_f A/C-NCs. This suggests that the baseline 80 wt% noT procedure does not directly transfer with the addition of a high-temperature desorption step, and therefore, this process was not further investigated. A low-temperature desorption process, discussed in Section 4.1.4, was implemented to replace the high-temperature desorption process, and results are discussed in the following section.

**Hardness Values for
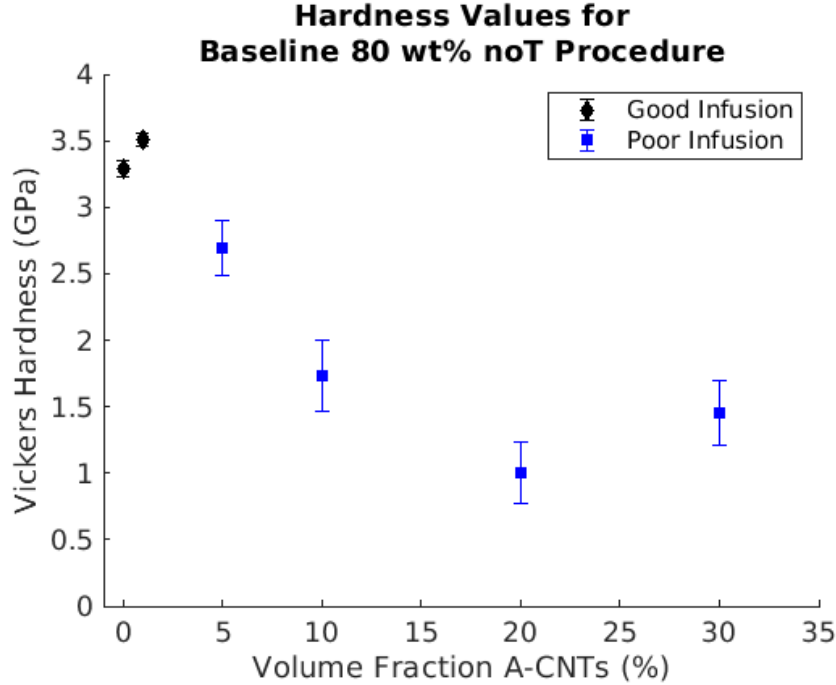Improved 80 wt% HT Procedure**

Figure 5-8: Average Vickers hardness and standard error in GPa for 1, 5, 10, and 30% v_f A/C-NCs fabricated *via* the improved 80 wt% HT procedure. Samples with good infusion are denoted with diamond markers whereas samples with visibly poor infusion are denoted with square markers. As 0% v_f data was not collected for this procedure, an average hardness calculated from the other improved procedures is used and denoted with an asterisk marker.

5.3.3 Results for Improved 80 wt% LT Procedure

The second improved infusion process was the improved 80 wt% LT procedure. The low-temperature desorption was chosen so as to leave the amorphous carbon on the A-CNT exterior, which the improved 80 wt% HT procedure was hypothesized to have removed, as described in more detail in Chapter 4. X-ray μCT imagery of the A-PNCs, along with physical indications while handling the A/C-NCs, demonstrated that this process was not a sufficient improvement, and no hardness data were taken. X-Ray μCT images from the 1–30% v_f A-PNCs, included in Figure 5-9, show that there was better infusion than the baseline 80 wt% noT procedure, as all but the 10% v_f A-PNCs show 2D slices of the 3D image without any micrometer-scale voids, and these images were representative of most of the slices of the 5%, 20%, and 30% v_f A-CNT arrays imaged. However, the whole sample is not without pores, as seen in the

"worst-region" images, indicating the need for a more consistent infusion procedure. At v_f above the baseline (*i.e.* 1 vol% A-CNTs), the X-Ray μCT imagery shows evidence that the A-CNT arrays floated in the resin (10% v_f) and densified to varying degrees (most noticeable in the 30% v_f image). The 1%–20% v_f images have the mounting tape, the porous layer, labeled on the bottom of the image, and the 30% v_f images show where the mounting tape is located, outside of the field of view. The entangled A-CNT layer was placed on the mounting tape, and the excess P-F resin on top of the A-PNCs is at the top of the image. Hardness indentations are in the interior of the sample, on a plane perpendicular to the A-CNT direction that is near the bottom of the infusion (on the mounting tape). Unlike the X-ray μCT images of the A/C-NC included for the baseline 80 wt% noT procedure, all X-ray μCT images of the improved 80 wt% LT procedure are of the A-PNCs, prior to infusion, as this provides information about voids due solely to infusion, not voids arising from the pyrolysis process.

As this procedure did infuse resin into the arrays, the low-temperature desorption step was included in subsequent trials, but the degassed resin was determined to be too thick for successful infusion. For the next iteration of the improved procedure, as-received resin was substituted for the resin degassed for 24 hours at 60°C.

5.3.4   Results for Improved 60 wt% LT Procedure

The third improved procedure, improved 60 wt% LT, was the first of three different wt% resins tested with the low-temperature desorption process. The Vickers hardness values and standard error, measured in GPa, are listed in Table 5.4 and displayed in Figure 5-10. The Vickers hardness values for the samples with highest-hardness are included as well, but are in line with the average values. Samples with poor infusion, based on X-ray μCT images, are denoted with gray shading in the table and with square markers on the graph. Samples with no X-ray μCT images are denoted with a red circle on the graph. A 0 vol% A-CNT (pure PyC) sample was tested as a baseline, since the resin wt% changed, which may have an affect the properties of the PyC sample. There is no data on the 20% v_f A/C-NCs, as these were not sturdy
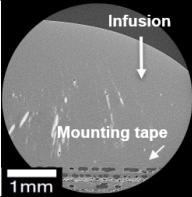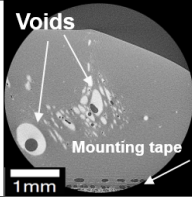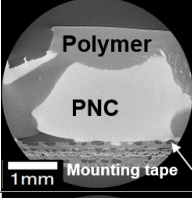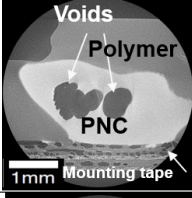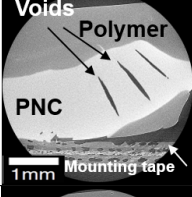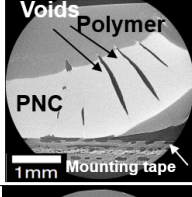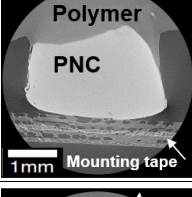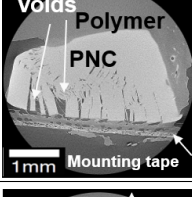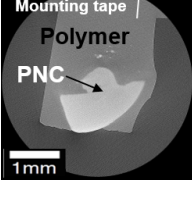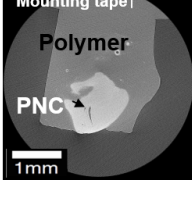
A-CNT Volume %	X-Ray µCT Images	
	Best Region	Worst Region
1%		
5%		
10%		
20%		
30%		

Figure 5-9: Representative X-Ray µCT images of 1–30% v_f A-PNCs synthesized *via* the improved 80 wt% LT procedure. Only one A-PNC was imaged per v_f. All images include a mounting tape callout, void callouts, location of uninfused A-CNTs if visible, resin-rich (polymer) regions, and scale bar. The entangled A-CNT layer was placed on the mounting tape (labeled in 1–20% v_f and outside of the image area in the 30 % v_f samples), the excess P-F resin on top of the A-PNCs is at the top of the image, and the infusion direction is perpendicular to the excess resin, with the infusion beginning on the side with excess resin. Hardness indentations are in the interior of the sample, on a plane perpendicular to the A-CNT direction that is near the mounting tape. Lower-density areas appear darker within an image, showing voids, starting with the 5% v_f samples. Grayscale values are not comparable between images. Although this process resulted in an improvement over the baseline infusion, the resin infusion needs to be improved further such that there are consistently no visible voids.

enough to withstand normal handling and polishing procedures, suggesting that there was insufficient infusion.

Table 5.4: Average Vickers hardness and standard error in GPa for 0–30% v_f A/C-NCs fabricated *via* the improved 60 wt% LT procedure. Hardness values for the samples with the highest hardness are also included, but are in line with the average values. Samples with poor infusion, based on X-ray μCT images, have hardness values shaded in gray.

A-CNT v_f	# Indents	Avg. Hardness (GPa)	Highest Hardness (GPa)
0%	20	3.120 ± 0.089	3.142 ± 0.162
1%	20	3.326 ± 0.186	3.440 ± 0.198
5%	20	2.895 ± 0.174	3.070 ± 0.287
10%	20	2.360 ± 0.115	2.414 ± 0.150
30%	10	1.794 ± 0.214	1.794 ± 0.214
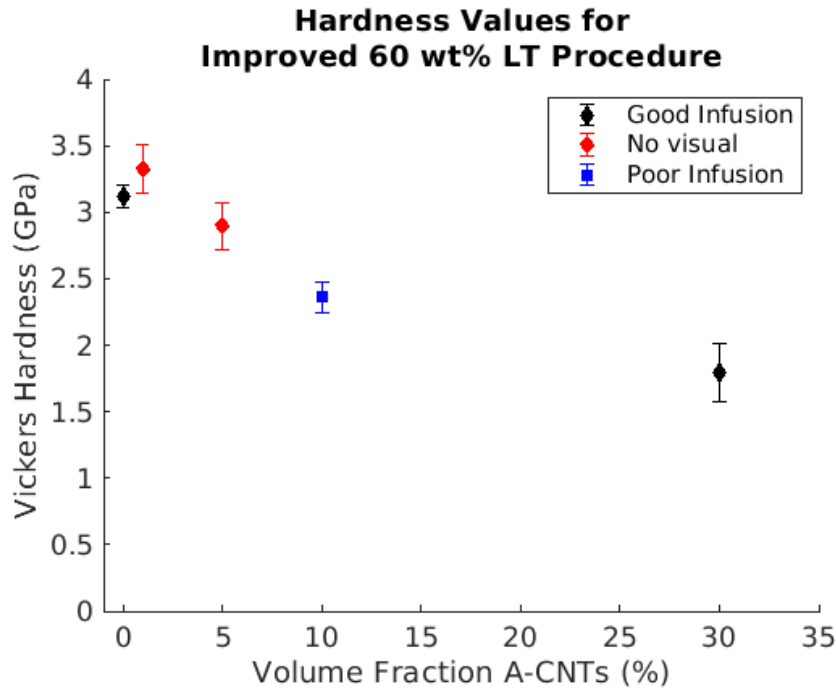
Figure 5-10: Average Vickers hardness and standard error in GPa for 0–30% v_f A/C-NCs fabricated *via* the improved 60 wt% LT procedure. Samples with good infusion are denoted with diamond markers whereas samples with poor infusion are denoted with square markers. Samples without X-ray μCT images are denoted with a red circle.

Unlike the procedures with degassed resin, there is no sharp decrease in hardness values with increasing v_f, indicating that the resin infusion is only slightly less suc-

cessful with increasing v_f. The hardness begins to slowly decrease, starting with the 5% v_f A/C-NCs, which necessitates a less viscous resin for proper infusion. As with the baseline 80 wt% noT procedure, there is significant variation in the hardness of these A/C-NCs, suggesting that the A/C-NCs are not homogeneous, and certain areas of the sample had more complete infusion. An example of this variation is shown by the indentations in the 30% v_f A/C-NC sample presented in Figures 5-11a and 5-11b. In Figure 5-11a, the 30% v_f A/C-NC easily reacted the indenter tip load because that area had sufficient infusion. Conversely, in Figure 5-11b, the same 30% v_f sample cracked significantly under the tip load due to poor infusion in the underlying A/C-NC. As the areas with poor underlying infusion were not visible from the sample face, these areas were sometimes indented, and cracked indentations were encountered for 30% of the indents, which suggests that this poor infusion was representative of a portion of the sample and not just this specific location.
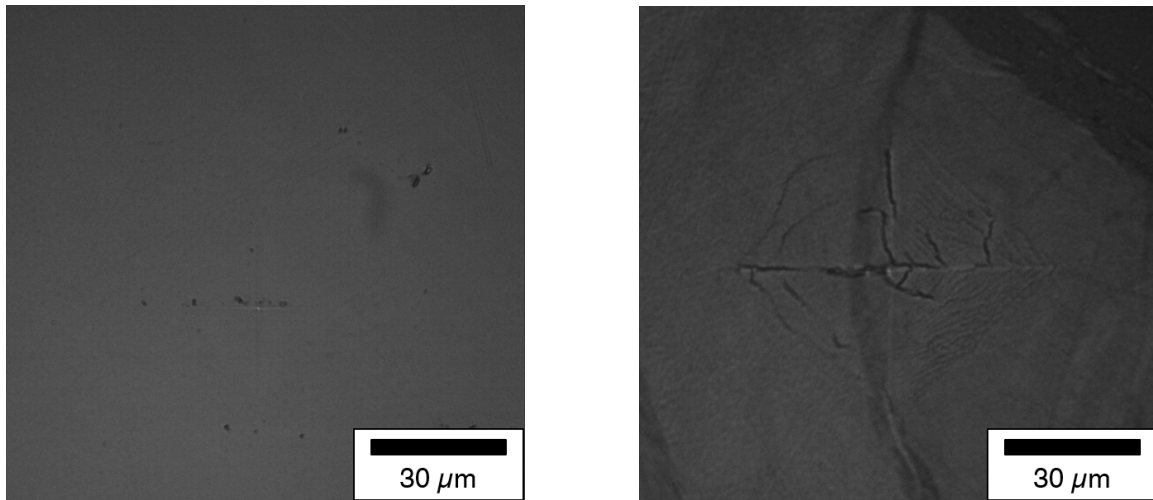
(a) Indent without cracks.

(b) Indent with cracks. As lower values were representative of some areas of the sample, the value from this test was included in the hardness data presented.

Figure 5-11: An indented region with no cracks, suggesting good infusion (left), and an indented region with cracks, suggesting poor infusion (right) in 30% v_f A/C-NCs synthesized *via* the improved 60 wt% LT procedure.

X-ray µCT images of the A-PNCs, included in Figure 5-12, support the conclusion that infusion was improved as compared to the degassed (80 wt%) resin but was not

yet sufficient. Since the infusion clearly was not complete, only the 10% and 30% v_f A/C-NCs were studied using the X-Ray µCT to better understand in what way the resin failed to completely infuse into the A-CNT array. From the X-Ray µCT images, it appears that the resin was capable of thoroughly infusing the 30 vol% A-CNT array, although there are a few defects (one circled in red). However, the resin did not fully infuse the 10 vol% A-CNT array. This partial infusion appears similar to the partial infusion in the SEM image of a 10% v_f A/C-NC synthesized *via* the baseline 80 wt% noT procedure. As with that baseline A/C-NC, this 10% v_f A/C-NC fabricated *via* the improved 60 wt% procedure may not have fully infused as the viscosity of the resin may have been too high, blocking resin from infusing into that region of the A/C-NC. The images in Figure 5-12 are oriented such that the mounting tape is at the bottom of the image (visible and labeled on the 30% v_f images; out of the field of view but below the 10% v_f images). Voids are called out for the "worst region" images, although only small defects were seen in the 30% v_f A-PNC. The A-PNCs were placed such that the excess P-F resin was adhered to the mounting tape, and the bottom of the sample during infusion, where the entangled A-CNT layer lies, is at the top of the image. Hardness indentations are in the interior of the sample that is on a plane perpendicular to the A-CNT direction, near the bottom of the infusion (on the mounting tape). Given the relative success of this procedure, only a small change was made: isopropanol was added to the resin to lower the viscosity and thus improve infusion prior to the resin curing, as discussed in Section 5.3.5

5.3.5   Results for Improved 50 wt% LT Procedure

Since the as-received (60 wt%) resin was concluded to be slightly too viscous for consistent, complete infusion, the improved 50 wt% LT procedure was developed. The hardness values and standard error, measured in GPa, are listed in Table 5.5 for all v_f, and displayed in Figure 5-13. Samples with poor infusion are denoted with gray cells in the table and square markers on the graph. Hardness values for the samples with the highest hardness are included but are in line with average values for v_f below 20% v_f. 20% and 30% v_f samples show an increase over the average values,

A-CNT Volume %	A-PNC X-Ray µCT Images	
	Best Region	**Worst Region**
10%		
30%		
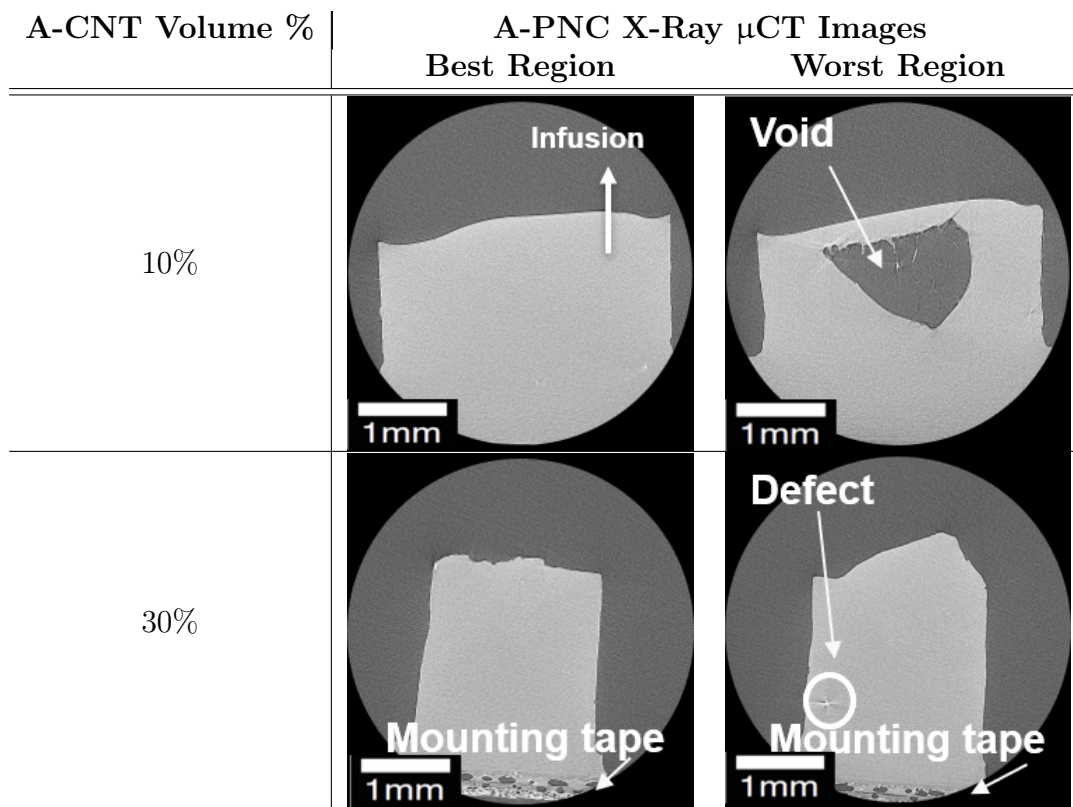
Figure 5-12: Representative X-Ray µCT images of a 10% and a 30% v_f A-PNC synthesized *via* the improved 60 wt% LT procedure. Only one A-PNC was imaged per v_f. 30% v_f images include a mounting tape callout as the 10% images have the mounting tape at the bottom but outside of the field of view. Voids and defects are also called out, and a scale bar is included on all images. The excess P-F resin on top of the A-PNCs was adhered to the mounting tape, the entangled A-CNT layer is at the top of the image, and the infusion direction is perpendicular to the excess resin with the infusion beginning on the side with excess resin. Hardness indentations are in the interior of the sample, on a plane perpendicular to the A-CNT direction that is near the top of the image and the indentation direction is towards the excess P-F resin on the mounting tape. Lower-density areas appear darker within an image, and voids have been labeled as such. Grayscale values are not comparable between images. The defect in the 30% v_f sample may be dust or an artifact of the reconstruction, as voids typically have a dark (low-density) spot in the center. Although this procedure is an improvement over the previous infusions, the resin infusion needs to be further studied and likely improved such that the resin fully infuses prior to cure.

but the hardnesses are below that of the baseline PyC, suggesting that nano-scale voids resulted in reduced hardness and increased standard error. Only the 10% v_f samples showed visibly poor infusion, but not all A-CNT v_f were imaged using X-ray µCT. Samples with no X-ray µCT images are denoted with red circles on the graph.

The 30% v_f samples, which showed no visible voids, may have had submicron-scale voids or more significant voids during pyrolysis, which resulted in reduced hardness. Although unlikely at this v_f, the resin may not have had the same degree of cure as the 0% v_f resin due to confinement effects, and this hypothesis should be tested in future work.

Table 5.5: Average Vickers hardness and standard error in GPa for 0–30% v_f A/C-NCs synthesized *via* the improved 50 wt% LT procedure. Hardness values for the samples with the highest hardness are included but are in line with average values for v_f below 20% v_f. 20% and 30% v_f samples show an increase over the average values, but the hardnesses are below that of the baseline PyC, suggesting that nano-scale voids resulted in reduced hardness and increased standard error. Samples with poor infusion, based on X-ray μCT images, have hardness values shaded in gray.

A-CNT v_f	# Indents	Avg. Hardness (GPa)	Highest Hardness (GPa)
0%	10	3.154 ± 0.217	3.154 ± 0.217
1%	20	3.207 ± 0.094	3.396 ± 0.138
5%	20	3.465 ± 0.208	3.617 ± 0.389
10%	20	2.333 ± 0.284	2.716 ± 0.543
20%	20	1.475 ± 0.131	2.643 ± 0.602
30%	20	1.480 ± 0.222	2.187 ± 0.122

This method was the most successful of the 5 methods discussed (baseline 80 wt% noT, improved 80 wt% HT, improved 80 wt% LT, improved 60 wt% LT, improved 50 wt% LT). As shown in Table 5.5, the hardness increases with increasing v_f of A-CNTs through the addition of 5 vol% A-CNTs to the carbon-ceramic matrix. Additionally, the relatively poor hardness values at 20 vol% and 30 vol% A-CNTs (despite good infusion for the 20% v_f A/C-NCs) plateaued at ~1.5 GPa, which is a higher minimum hardness than measured for other processes. This data suggests that the 50 wt% resin infused better than the previous resin processing and this resin processing is promising for future trials, particularly with reinfusions, as discussed in Section 5.4.

The hardness values alone were not enough to understand why the hardness began to decrease with the addition of 10 vol% A-CNTs. Images of hardness indents for the A/C-NCs with the largest standard error, displayed in Figure 5-14, also indicate that the infusion was not uniform, as some indents are resisted by the A/C-NC and others show cracks from the indent. The scale bar on the 5% v_f A/C-NC images applies to all
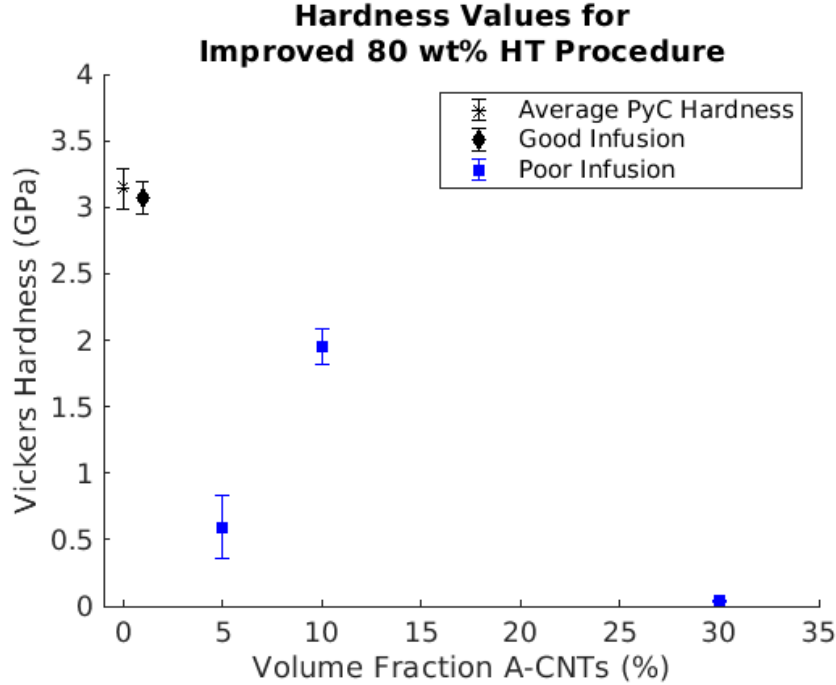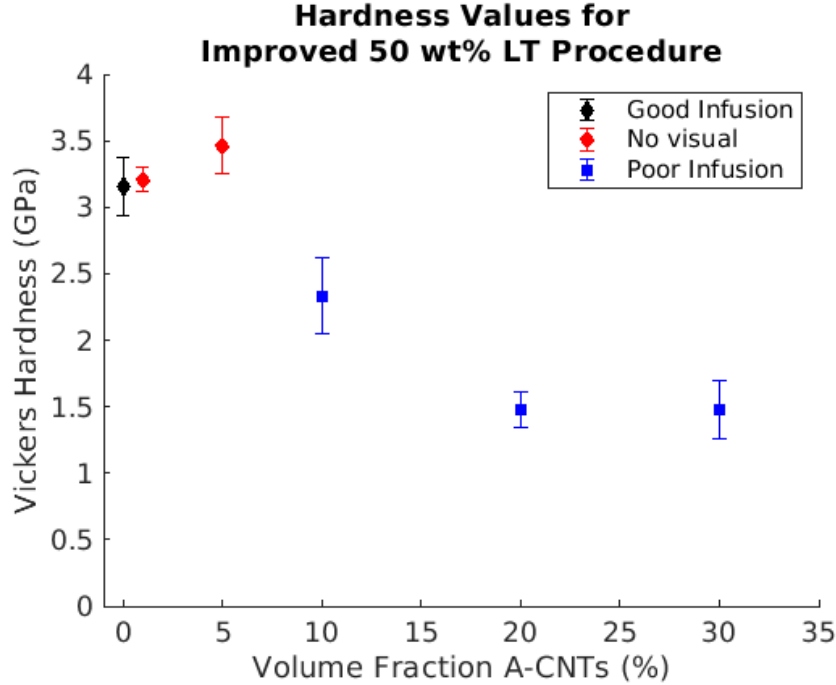
Figure 5-13: Average Vickers hardness and standard error in GPa for 0–30% v_f A/C-NCs synthesized *via* the improved 50 wt% LT procedure. Samples with good infusion are denoted with diamond markers whereas samples with visibly poor infusion are denoted with square markers. Samples with no X-ray μCT data are denoted with red circles.

images in Figure 5-14. Significant cracking during indentation suggests a multitude of voids, which are often crack nucleation sites and may facilitate crack growth. Another cause of cracking is that the A-CNTs may have densified due to the volatile content in the resin, such that there are fewer A-CNTs to resist crack formation in certain areas. However, this is not visible in the X-ray μCT, as the relative difference in densities between regions with slightly densified A-CNTs and P-F resin is too small for a significant difference in grayscale values. The cause of the large standard error in these A/C-NCs should be investigated further but is broadly consistent with physical nano-scale heterogeneity in the sample morphology as described above.. Indentations with cracking were included as they were representative of some of the samples tested for all v_f discussed here. Any indentations with more excessive cracking than shown in this table were not used.

X-Ray μCT images of the 10, 20, and 30% v_f A-PNCs were analyzed to better
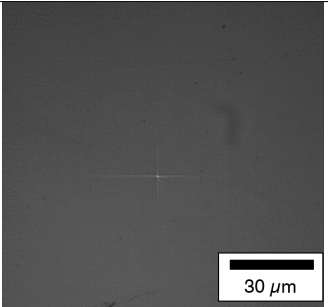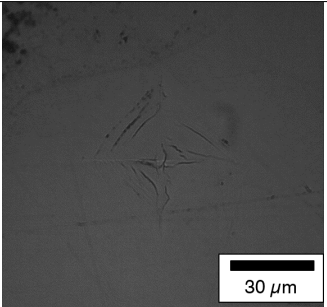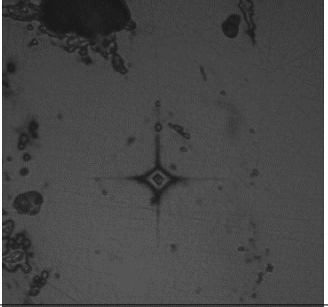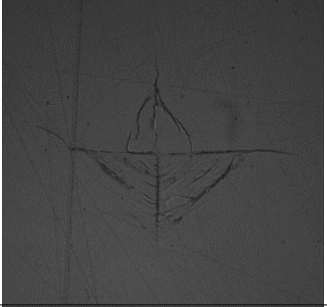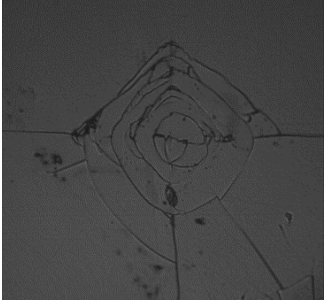
A-CNT Volume %	Indentation without Cracking	Indentation with Cracking	Approximate % of Indents without Cracking
5%			70%
10%			55%
30%			60%

Figure 5-14: Images of indentations for hardness testing with and without for 5, 10, and 30% v_f A/C-NCs, exemplifying the variation in hardness in A/C-NCs synthesized *via* the improved 50 wt% LT procedure, leading to the large standard error. Samples with cracking were included in the data presented here as they were representative of some of the samples tested for all v_f discussed here. Any indentations with more excessive cracking than shown in this table were not used.

understand the lower hardness values for these three v_f. Images of the best and worst 2D slices of these A-PNCs are included in Figure 5-15. The excess P-F resin is at the top of the image, the entangled A-CNT layer, at the bottom of the infusion, is at the bottom of the image (on the mounting tape; not pictured), and the P-F resin infusion was perpendicular to the excess resin in the direction of top to bottom. Hardness indentations are in the interior of the sample, on a plane perpendicular to the A-CNT

direction that is near the bottom of the infusion (on the mounting tape). Both 10% and 20% v_f images show that, while there was generally good infusion, there were still a few areas of poor infusion, and voids are called out. However, future work should improve this process for the 30% v_f A-PNCs, as these do not appear infused. Thus, the application of a slightly less viscous resin during the infusion, a longer infusion time, or reinfusions of P-F resin as part of a second polymer infiltration/pyrolysis cycle would likely allow for full infusion.

5.3.6   Results for Improved 10 wt% LT Procedure

The final infusion trial, improved infusion with low-temperature desorption and 10 wt% resin, used isopropanol to reach a significantly higher resin dilution that was also used in previous work.[108,118] This resin processing was expected to infuse uniformly due to its low viscosity, but also result in a randomly densified A-CNT structure for all v_f, as found in previous work with solvents.[134] Due to the densification of A-CNTs, this resin dilution is not suggested as a candidate for future work. However, this method was implemented to understand how this dilution, common in literature,[108,118] would affect the A-CNT arrays and to bound the range of acceptable dilutions. As expected, the hardness values for all v_f, included in Table 5.6 and Figure 5-16, were below the ∼3 GPa expected hardness of pure PyC, suggesting that the resin wetted the A-CNTs but left voids between A-CNT bundles due to the low solid polymer loading, as shown in the SEM image of a 10% v_f A-PNC synthesized *via* the baseline 80 wt% noT procedure, Figure 5-4. The lower-viscosity resin resulted in a decrease in hardness at a higher v_f due to incomplete infusion; the hardness significantly decreases between the 10 and 20% v_f A/C-NCs, instead of after the 1 or 5% v_f A/C-NCs as with other synthesis processes. The resin is assumed to have infused into the 1, 5, and 10% v_f A/C-NCs with the same effectiveness, since they all have Vickers hardness values above 2 GPa, and suggesting that the structure of the PyC matrix is not affected by A-CNTs up to 10 vol%. However, the infusion is also assumed to result in significant submicron-scale voids or micron-scale voids after pyrolysis, as the hardness values begin to decrease without voids visible in the X-ray

134
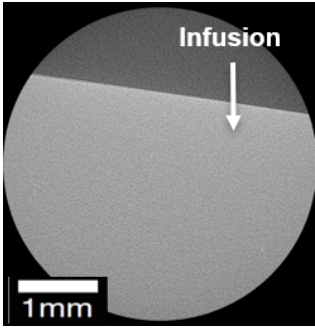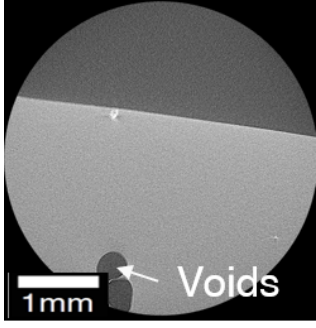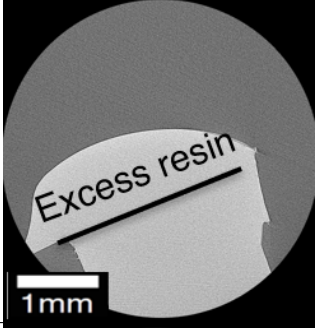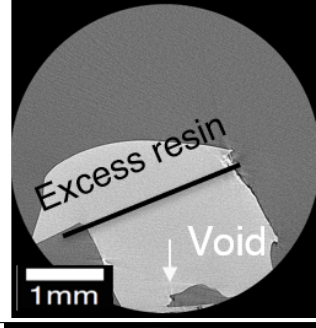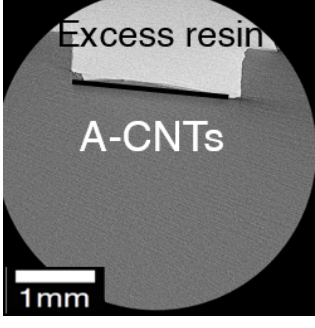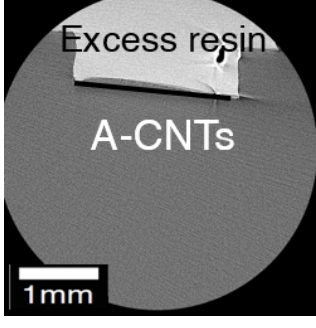
A-CNT Volume %	A-PNC X-Ray μCT Images	
	Best Region	Worst Region
10%		
20%		
30%		

Figure 5-15: Representative X-Ray μCT images of a 10, a 20, and a 30% v_f A-PNC synthesized *via* the improved 50 wt% LT procedure. Only one A-PNC was imaged per v_f. All images include void callouts, the location of uninfused A-CNTs, and excess resin regions where applicable, as well as a scale bar. Excess resin is delineated from A-PNC or A-CNTs (called out) with a black line. The entangled A-CNT layer is at the bottom of the image, the excess P-F resin on top of the A-PNCs is at the top of the image, and the infusion direction is perpendicular to the excess resin, with the infusion beginning on the side with excess resin. Hardness indentations are in the interior of the sample, on a plane perpendicular to the A-CNT direction that is near the bottom of the image. Lower-density areas appear darker within an image, showing voids starting with the 10% v_f images, but grayscale values are not comparable between images. Although significantly improved over previous processes both in hardness and visible infusion, the resin viscosity should be increased slightly to provide full infusion throughout the A-PNCs.

µCT images. The low solids loading of the resin may have contributed to a low wt% carbon matrix, which would cause these voids. The poor hardness values at high v_f may be due to confinement effects on the hardness of the resin, and this should be investigated more in future work. Due to rapid lab shutdown, Vickers hardness values from only one A/C-NC were collected for this process. Although the 10 wt% resin is not recommended for future infusions due to the lower hardness values and increased A-CNT densification, this study shows that decreasing the resin viscosity allows for improved infusion. Thus, a longer infusion time under vacuum and a slight decrease in resin viscosity from the 50 wt% resin would likely produce A/C-NCs with a specific hardness rivaling that of diamond, as suggested in previous work. [79]

Table 5.6: Average Vickers hardness and standard error in GPa for 1–30% v_f A/C-NCs fabricated *via* the improved 10 wt% LT procedure. As only one A/C-NC was tested, only the average value is included in this table. As no data was collected on the 0% v_f sample for this procedure, an average of the values across the improved procedures was included. The low hardness values for 20% and 30% v_f are hypothesized to be due to the low wt% carbon matrix, since the resin had a low solids loading.

A-CNT v_f	# Indents	Avg. Hardness (GPa)
0% (Improved average)	30	3.137 ± 0.153
1%	10	2.906 ± 0.144
5%	10	2.463 ± 0.124
10%	10	2.876 ± 0.222
20%	10	0.844 ± 0.081
30%	10	1.651 ± 0.112

The X-Ray µCT images for all v_f A-PNCs, compiled in Figure 5-17, confirm the earlier conjectures that infusion was uniform but imperfect. All the images in Figure 5-17 have the mounting tape and entangled A-CNT layer, at the bottom of the infusion, at the bottom of the image, and the excess PyC is at the top. All A-PNCs have similar gray values within each sample, confirming uniformity within samples. Additionally, few large voids but many small voids, labeled and circled in white, were seen in the A-PNCs. These small voids suggest that the A-PNCs are very porous, possibly from the degassed volatiles in the resin, but also that more of the pores may be too small to be resolved using the X-Ray µCT. The only large void observed in these A-PNCs was in the 20% v_f A-PNCs, where there is a clear break
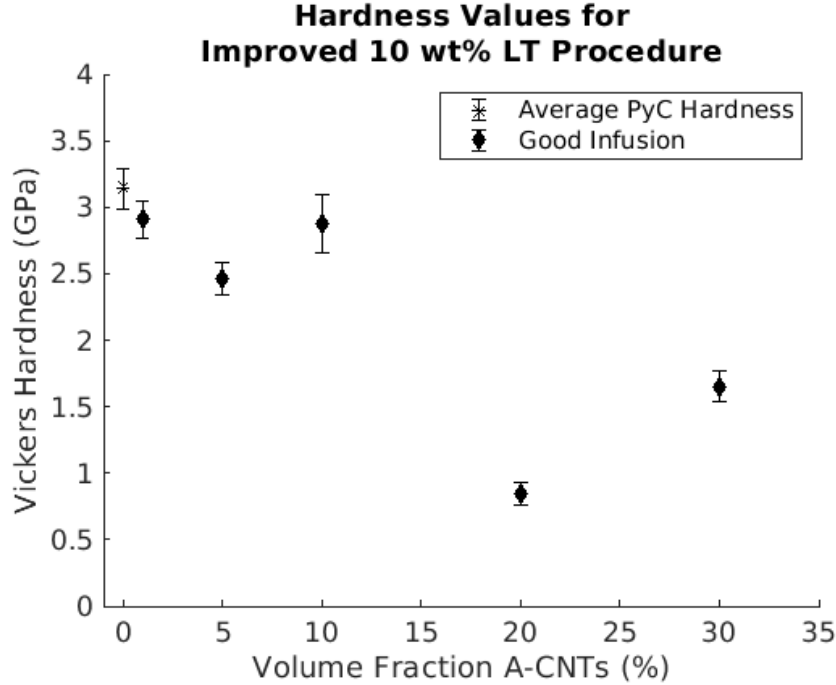
Figure 5-16: Average Vickers hardness and standard error in GPa for 1–30% v_f A/C-NCs fabricated *via* the improved 10 wt% LT procedure. Samples with good infusion are denoted with diamond markers. As no data was taken for the 0% v_f resin samples made *via* this procedure, an average hardness based on data from the other improved procedures is included and denoted with an asterisk marker.

in the interior of the sample. This may be due to the densification of the A-CNTs away from the center line as the resin with high volatile content was infused into the A-CNT array. Mounting tape is also labeled and is out of the field of view for the 5% v_f samples, but noted that it would be at the bottom of the image. Hardness indentations are in the interior of the sample, on a plane perpendicular to the A-CNT direction that is near the bottom of the infusion (on the mounting tape).

5.3.7 Comparison of Infusion Procedures

The Vickers hardness values across all v_f, measured in GPa, are summarized in Table 5.7 for the five synthesis procedures with measured Vickers hardness values. The highest Vickers hardness, ignoring standard error considerations, for a given v_f is highlighted in light green, and the lowest hardness is in light red. A/C-NCs with visibly poor infusion, evaluated with X-ray μCT images, are shaded in gray.
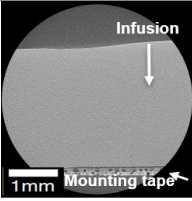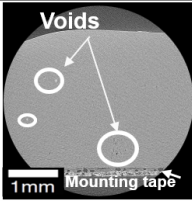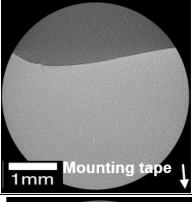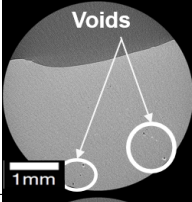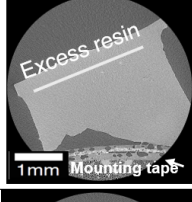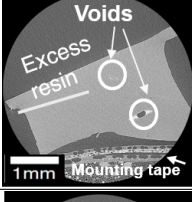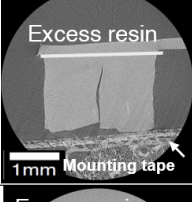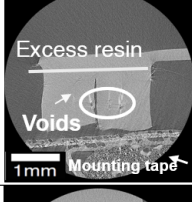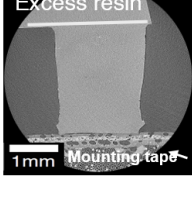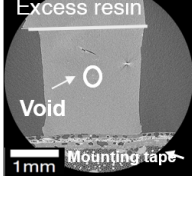
A-CNT Volume %	A-PNC X-Ray µCT Images	
	Best Region	Worst Region
1%		
5%		
10%		
20%		
30%		

Figure 5-17: Representative X-Ray µCT images of 1–30% v_f A-PNCs synthesized *via* the improved 10 wt% LT procedure. Only one A-PNC was imaged per v_f. All images include a mounting tape callout, void callouts where appropriate, and a scale bar. The entangled A-CNT layer was placed on the mounting tape (shown out of the field of view for the 5% v_f samples), the excess P-F resin on top of the A-PNCs is at the top of the image, and the infusion direction is perpendicular to the excess resin, with the infusion beginning on the side with excess resin. Hardness indentations are in the interior of the sample, on a plane perpendicular to the A-CNT direction that is near the mounting tape and the indentation direction is towards the excess P-F resin.Lower-density areas appear darker within an image, showing no large voids before the 10% v_f A/C-NCs, but grayscale values are not comparable between images. Although infusion visibly improved over previous processes, this method has some small voids, circled in red, and likely has nanoscale voids that are not visible with the X-Ray µCT.

Table 5.7: Comparison of Vickers hardness values and their standard error values, in GPa, for five of the synthesis processes with Vickers hardness values discussed above. The highest average hardness for each v_f is highlighted in green and the lowest average hardness for each v_f is highlighted in red. A/C-NCs with visibly poor infusion based on X-ray µCT, are shaded in gray, as this hardness data only denotes poor infusion.

	0% v_f	1% v_f	5% v_f	10% v_f	20% v_f	30% v_f
Baseline 80 wt% noT	3.289 ±0.063	3.506 ±0.053	2.693 ±0.201	1.734 ±0.269	1.008 ±0.231	1.457 ±0.244
Improved 80 wt% HT		3.068 ±0.122	0.595 ±0.238	1.953 ±0.136		0.038 ±0.007
Improved 60 wt% LT	3.120 ±0.089	3.326 ±0.186	2.895 ±0.174	2.360 ±0.115		1.794 ±0.214
Improved 50 wt% LT	3.154 ±0.217	3.207 ±0.094	3.465 ±0.208	2.333 ±0.284	1.475 ±0.131	1.480 ±0.222
Improved 10 wt% LT		2.906 ±0.144	2.463 ±0.124	2.876 ±0.222	0.844 ±0.081	1.651 ±0.112

As shown in Table 5.7, the baseline 80 wt% noT (degassed) procedure has the highest hardness for low v_f, as the pure PyC and the 1% v_f A/C-NCs have the highest hardness with this process. This may be due in part to the differences in initial resin processing (*e.g.* dilution with isopropanol to 50 wt% or 10 wt% resin) or degassing procedures (*e.g.* degassing the 80 wt% resin for 15 hrs to increase the solids loading). Since this method is promising at low v_f, a procedure that utilizes this method at low v_f and later densifies the A-CNTs to a higher v_f may be a viable alternative. The effect of dilution on final resin hardness should also be evaluated in future studies, as the average hardness of the as-received (60 wt%) 0% v_f resin is lower than the baseline 80 wt% noT procedure by the standard of error.

For the improved 80 wt% HT procedure, the hardness values are either the lowest or the second-lowest for any process, and within the margin of error when they are the second-lowest. This poor performance motivated the change to the low-temperature desorption and a less viscous resin, as the low-temperature vacuum desorption would remove the adsorbed water layer without affecting the amorphous carbon coating on the A-CNTs. TGA shows that more amorphous carbon remained on the A-CNTs after the low-temperature desorption.

Conversely, the improved 50 wt% LT procedure had the highest hardness for the

5% v_f by at least the margin of error. The 0% and 1% v_f A/C-NCs were within the margin of error of the highest-hardness samples, so no conclusions can be drawn on the relative effectiveness of this procedure. More work should be completed to decrease the standard error by synthesizing samples with greater uniformity and performing more tests. The 10% v_f A/C-NCs did perform worse than the 10% A/C-NCs, as the less viscous resin showed good infusion whereas the 50 wt% resin did not show good infusion. As these results were promising, this process is expected to yield the highest-hardness A/C-NCs with a longer infusion time, ensuring complete degassing and infusion, and a slightly less viscous resin, similar to the 10 wt% LT procedure.

Finally, the improved 10 wt% LT procedure also typically underperformed. This procedure had the lowest hardness values for both 1% and 20% v_f A/C-NCs, possibly because the added volatiles could require a significantly longer degassing/infusion step than other resin dilutions tested, or because the infusion caused the densification of A-CNTs into cell or pin-like structures. However, this process performed reasonably for the 5% v_f A/C-NCs, and the 10% v_f A/C-NCs showed the highest hardness of all samples. These results may be because the less viscous resin was better able to infuse higher v_f arrays than more viscous resins. These results indicate that the lower viscosity resin, or possibly a longer infusion time to accommodate a higher viscosity resin, would be successful avenues to investigate further. Although at least 10 hardness measurements were taken per A/C-NC, only one A/C-NC per v_f synthesized *via* the 10 wt% LT procedure was tested, and typically only two A/C-NCs per v_f synthesized *via* the other improved procedures were tested. Thus, more samples should be tested to confirm these trends and that no anomalies affected the procedure.

In addition to comparing processes studied in this work, these values were compared to other work that used the Durite SC-1008 P-F resin, as discussed in Section 5.2. As some of the work was done with thin films, size effects cause the ~4 GPa hardness for a PyC thin film to overshoot what is viable in bulk. [214] However, previous work using the Durite SC-1008 P-F resin for infusion into A-CNTs found that the average hardness was maximized for 10 vol% A-CNTs with a Vickers hardness of 4.3 GPa and the average hardness was least for pure PyC, with a Vickers hardness

of 3.5 GPa.[79] These results were unable to be replicated, even for the pure PyC. The Durite resin appeared to have different physical properties, such as color and viscosity, in this work than in previous studies. Additionally, the P-F resin required modifications to the cure procedure to reach the desired 90% degree of cure. This change in properties indicated a slight change in as-received resin formulation, which may change the ease of infusion due to a change in viscosity, and/or result in different measured hardness values, especially for the pure PyC. As the degree of cure was not recorded in previous work, this measurement cannot be used to compare the resin in the previous work to the resin used in this work as well. Thus, this work cannot be directly compared to previous work due to these discrepancies.

5.4   Conclusions and Recommendations for Future Work

In summary, six different synthesis procedures (see Table 5.1) were tested to create A/C-NCs with v_f ranging from 1% to 30%. These procedures were evaluated primarily *via* their Vickers hardness values, with X-Ray µCT images contributing to understanding the extent of infusion. X-Ray µCT images were taken of the baseline A/C-NCs following pyrolysis to study both the infusion and voids produced by the pyrolysis process. For the A/C-NCs synthesized *via* the improved procedures, X-ray µCT images were taken of A-PNCs after the cure cycle but prior to pyrolysis to study the voids solely due to infusion. Then A/C-NCs were cold mounted and polished for hardness testing. A/C-NCs that were clearly poorly infused were not always imaged and tested. Due to rapid lab closures this term, not all planned tests and experiments were able to be completed.

Results show that the baseline 80 wt% noT procedure is most successful for 0 and 1% v_f A/C-NCs, with a ~7% increase in hardness with 1 vol% A-CNTs over the baseline PyC. However, the improved 50 wt% LT procedure is most promising overall, showing an ~10% increase in hardness with 5% A-CNTs over the baseline PyC. The

higher solids loading may have made the baseline procedure more successful at low v_f, as the degassed resin from the baseline procedure appeared to have a higher hardness than the resins cured following the improved procedures in the glovebox. However, the least viscous resin (improved 10 wt% LT procedure) was most successful at 10% v_f, which suggests that the lower viscosity allowed for infusion into higher-v_f A-CNT arrays.

Since the improved 50 wt% LT procedure was most promising overall, making a few small adjustments to this procedure is recommended. Future work should investigate at what volatile percentage the resin begins to have negative effects on the A-CNTs, likely due to solvent-mediated capillary densification, in order to choose the resin that infuses most completely into the A-CNT array without significant detrimental effects. Experiments should be run with longer infusion times as well since the longer infusion time might help improve the extent of infusion without requiring volatiles in the resin, which may cause A-CNT densification. Another method of decreasing the resin viscosity slightly to improve infusion would be to use resins with different solids loadings between the resin initially placed on the arrays for infusion and the resin added to the arrays during infusion. SEM and X-Ray μCT images suggested that, for a viscous resin, the resin viscosity inhibited complete wetting, but for a less viscous resin, the A-CNTs bundled and were coated in P-F resin without the space between bundles being infused with resin. If the ∼50 wt% resin was not sufficient to address these challenges, future work may need to investigate the appropriate resin viscosity as resin is added to a single infusion to top off the resin in an A-CNT array.

A different solution to the infusion challenges would be to proceed with the baseline 80 wt% noT procedure at 1 vol% A-CNTs and, after infusion but prior to cure, use a set of Teflon biaxial densification tooling to increase the A-CNT volume fraction, as was typically performed prior to infusion. This set of tooling was designed, and drawings are included in Appendix A.1.

Since some A/C-NCs had a large standard error, up to 0.287 GPa, it is clear that samples had some porosity both due to poor infusion (either resulting in micron-scale

voids visible with the X-ray μCT or submicron-scale voids not visible with the X-ray μCT) and due to the inherent mass loss caused by pyrolysis. Once the infusion challenges discussed above have been resolved, filling voids (reducing micro- and nano-scale porosity) will be the next step towards improving the hardness. In processing of traditional C/C CMCs, CVI is used to "bulk up" or reduce porosity. A reinfusion procedure, introduced in Section 4.4, was developed to address the micron-scale voids caused by the pyrolysis process. For the reinfusion procedure, 50 wt% resin was infused into 1%–30% v_f A-CNT arrays and the A-PNC was pyrolyzed. Then, the sample was reinfused and pyrolyzed 3 more times for a total of 4 infusions. Due to rapid lab shutdown, these samples were fabricated and imaged, but no Vickers hardness data could be taken at the time. Although hardness determination of these samples is left for future work, the X-ray μCT images of the final A/C-NCs after the fourth infusion, included in Figure 5-18, show excellent infusion and few voids, suggesting that high hardness will be achieved.

In addition to the suggested future processes, there exists a few other areas for further investigation. First, the indentations used for measuring hardness are not clear enough to use the automated Cornerstone software to calculate the projected indentation area. Instead, the user must manually mark the corners of the diamond indentation shape, which allows for human error. Although both a gold and a TiO_2 coating were applied to A/C-NCs, neither provided enough reflectivity to adequately identify the full diamond shape with only the software.

Second, A/C-NCs made from the five processes with measured Vickers hardness values were found to have a significant decrease in hardness, typically starting with 10 to 20 vol% A-CNTs. This was attributed to poor infusion, but an investigation of the inter-CNT spacing necessary for adequate crosslinking may be beneficial and the degree of cure should be confirmed for 30% A-CNTs in addition to the degree of cure measured for the pure PyC (> 90%). The confinement effects are not expected to, but may lead to, poor crosslinking, which could also be the cause of a decrease in Vickers hardness as compared to the expected Vickers hardness.

Although A/C-NCs are excellent candidates for high-temperature, high-hardness

A-CNT Volume %	A-PNC X-Ray µCT Images
0%	
1%	
5%	
10%	
20%	
30%	

Figure 5-18: Representative X-Ray µCT images of 0–30% v_f A/C-NCs synthesized *via* the reinfusion procedure (improved 50 wt% LT procedure with 3 reinfusions, as detailed in Section 4.4). Only one A/C-NC was imaged per v_f. All the images include a mounting tape callout, scale bar, and arrow for infusion direction. The location of the entangled CNT layer was not tracked during reinfusions. Lower-density areas appear darker within an image, showing few voids in these samples and suggesting excellent infusion. However, grayscale values are not comparable between images. These samples show excellent infusion with minor voids (small lines throughout some samples but no large voids) at all v_f, suggesting that this process will also have excellent hardness. Image credit: A L Kaiser (MIT); modified after original.

applications, their brittle character can make them unsuitable for some applications. Thus, A/Al-NCs were also investigated, as this new material is expected to increase the strength-to-weight ratio of Al parts without decreasing the metal's superior impact resistance. Synthesis methods and their results are discussed in Chapter 6.

Chapter 6

A/Al-NC Synthesis Method Development

Metal matrix nanocomposites (MMNCs) are a growing field of study, as nanorein-forcements can improve the structural and electrical properties of the metal matrix while also decreasing the density of the material. For aligned carbon nanotube (A-CNT)/Al nanocomposites (A/Al-NCs), improvements in Young's modulus,[153] tensile strength,[152] yield strength,[136] hardness,[155] radiation resistance,[29] and damping characteristics[136] were noted, as discussed in Chapter 2. These characteristics make A/Al-NCs particularly suited to applications in aerospace, defense, automotive, and nuclear industries, serving as high strength-to-weight ratio structural materials in harsh environments, such as high-temperature environments, while also reducing weight and fuel consumption.

While applicable to many fields, A/Al-NCs are not simple to fabricate. Wetting CNTs with Al is challenging due to their difference in surface energies, discussed in greater depth in Section 2.3.1. Most CNT/Al-NCs are fabricated through powder metallurgy methods,[139–142,186] discussed in Section 2.3.3. However, the ball milling, sintering, and hot extrusion used to combine CNT bundles with the Al matrix often causes significant damage to the CNTs.[13,186,188] Additionally, these metallurgy methods are unable to align the CNTs to preferentially reinforce one direction, which is often the most effective use of fibers in a composite. Thus, this chapter focuses on

synthesizing A/Al-NCs, as opposed to unaligned CNT/Al-NCs, to utilize the advantages from A-CNT alignment. This chapter covers processes explored and developed herein for manufacturing A/Al-NCs: A-CNT growth, A-CNT surface modification, and both solder and Al matrix infusion. The parameters for each step will be discussed, as well as the effectiveness of the different procedures and future avenues of research.

6.1   A-CNT Growth

A-CNTs for A/Al-NCs are grown in a similar process to those for A/C-NCs, as mentioned in Chapter 4. Here, 100 um height was chosen for this work to balance the need for effective load transfer, typically requiring longer CNTs for load transfer to be the dominant reinforcement mechanism, and the need for surface modifications and wetting, typically requiring A-CNT heights less than 100 μm. The A-CNTs growth rate is faster at the beginning of the growth process, at a rate of ∼100 μm per minute, so growth times were approximately 1 minute. Unlike the A-CNTs for A/C-NCs, there was no hydrogen anneal step, as initial trials required the A-CNTs to stay on the Si substrate for ease of handling.

6.2   CNT Surface Modification for Al Wetting of A-CNTs

Once grown, the surfaces of the A-CNTs needed to be modified to alter their surface energy before they can be wet with Al. To review, the interaction of the surface energies of two materials (the surface energy of the solid γ_S, the surface energy of the liquid γ_L, and their interfacial energy γ_{SL}) determines the contact angle of a liquid on a solid, following the Young-Dupré equation. Contact angles near zero indicate that the liquid spreads on the solid, which results in good wetting. By reframing the equation, Gibbs determined that the solid surface should have a higher surface energy than the liquid for the liquid to wet the solid.[159] The surface energy of CNTs is taken

as 0.027 J m^{-2},[167] which is two orders of magnitude lower than the surface energy of molten Al ($\gamma_l = 1.152$ J m^{-2})[165,168,169], making the CNTs challenging to wet with Al. To address this issue, the A-CNTs must be coated with a material having a surface energy at least as high as that of Al. A more thorough discussion of CNT wetting with metals can be found in Section 2.3.1.

Of the common surface modification methods discussed in Section 2.3.1, only the atomic layer deposition (ALD) of a metal oxide is viable for an A-CNT array of $\sim$100 μm in height.[176] Other methods include surface modifications or surfactants for loose CNTs to help disperse them in a solution with Al particles,[175] sputtering of a metal, which is not conformal,[164] and electroplating Al, which has only been shown to be effective for arrays $\leq$5 μm.[157] Additionally, electroplating may cause A-CNTs to densify *via* capillary action due to the solvent used in the electroplating process.

ALD is an advanced process for conformal deposition of thin films on non-flat surfaces, particularly when control at the Ångstrom level is necessary.[215] The model process with ALD deposits Al_2O_3 using alternating pulses of trimethylaluminum (TMA) as the precursor and H_2O.[215] The $Al(CH_3)_3$ deposits on the material, but then the CH_3 in the TMA reacts with H_2O to form CH_4, leaving behind a layer of Al_2O_3. Although most commonly used with H_2O, ALD processes with TMA have been performed with O_3 instead of H_2O as the oxidizing agent. O_3 is more reactive with the A-CNT surface, successfully creating defects necessary for nucleation sites. Since O_3 produces fewer defects than other processes for equivalent coating, an O_3 process is desirable.[215,216] ALD processes can deposit other metal oxides, such as TiO_2[217–219] and α-Fe_2O_3.[220,221] As with Al_2O_3, the deposition of TiO_2 can be performed with tetrakis(dimethylamino)titanium (TDMAT) and either H_2O[217] or O_3,[218,219] although H_2O is the more common oxidizing agent in this process as well. As TMA and TDMAT were more readily available, these two precursors were considered. However, the reduction of Al_2O_3 would have been challenging, if possible,[222] with the available laboratory equipment, and an oxide layer between the Al matrix and A-CNTs was not desirable since oxides are brittle and the Al_2O_3 was expected to

decrease the properties of the A/Al-NC. Thus, a TDMAT process was chosen. Both deposition with O_3 and H_2O were investigated, along with various reduction methods, all described in detail in the following Sections.

6.2.1 Plasma Treatment for Improved TiO$_2$ Deposition

Two ALD methods were tested for decorating TiO_2 onto the A-CNT arrays, one with O_3 as the oxidizer and the other with H_2O. Previous work shows that, when depositing TiO_2 on A-CNTs with H_2O, only 8% of the final mass of the coated A-CNTs was TiO_2. However, when a plasma pretreatment step was implemented to functionalize the A-CNTs, creating necessary nucleation sites, 80% of the final mass of the coated A-CNTs was TiO_2.[176] Thus, plasma treatments were adapted for implementation on available equipment based on the work by Acauan *et al.*[176] Raman spectra of A-CNT arrays were measured before and after plasma treatment to quantify the defect creation, as successful plasma treatments should functionalize the arrays for sufficient wetting without causing excess damage. The defect ratio, measured *via* Raman spectroscopy, is a normalized value used to quantify damage. The defect ratio is calculated by taking the ratio of the maximum intensity of the D peak, characteristic of defects, to the maximum intensity of the G peak, characteristic of all CNTs, and is referred to as I_D/I_G.

The two most successful plasma treatments will be discussed in detail here. The MSynth Plasma Etcher was used to remove the tangled A-CNT crust layer, formed as the A-CNTs self-order at the beginning of the growth process.[223] This procedure, an 80-W plasma treatment for 30 seconds with a 10 standard cubic centimeters per minute (sccm) O_2 flow,[223] was primarily used for the Al wetting experiments *via* electron beam (e-beam) infusion, discussed in Section 6.4.2, as this process was designed to remove any physical barrier to infusion. As the MSynth Plasma Etcher was not designed for long, power-intensive processes, the functionalization process designed by Acauan *et al.* was adapted for a reactive ion etching (RIE) tool.

The plasma treatment for A-CNT functionalization was executed using an RIE tool, the Shuttlelock System VII SLR-770/734. This tool was not initially utilized

due to the significant process time for short plasma treatments, but its ability to precisely control the chamber atmosphere for long processes made it a suitable tool for A-CNT functionalization. A variety of plasma treatments were tested in this tool as well, with 20 sccm Ar and O_2, maintaining the 50% Ar, 50% O_2 environment used by Acauan *et al.* Additionally, the chamber was kept at 30 mTorr, the lowest pressure for this machine, and the process power was 30 W. The power and pressure settings for the functionalization process directly contrast with those used to remove the A-CNT crust, as the shorter, more power-intensive process targets the tips of the A-CNTs as opposed to a longer, low-power process, which has a more uniform effect. Despite the more precise control on this tool, A-CNT arrays from the same growth, placed in the tool at the same time, were still etched unevenly, with one being unharmed and the other visibly damaged by the process, as shown in Figure 6-1. The repeatability issues were attributed to inherent variability in the A-CNT growth process, but were not expected to have such a significant effect on the plasma treatment process. The variability in plasma treatments should be investigated further, and once the process becomes more consistent, the optimal plasma treatment for improved surface functionality with minimal A-CNT damage should be determined. Thus, no functionalization of the CNTs was used prior to TiO_2 deposition via ALD. Only the plasma etch of the top crust of the array was utilized in work using the e-beam to create a melt of Al (see section 6.4.2).

6.2.2   TiO$_2$ Deposition on A-CNT Arrays

Conformal deposition of an oxide coating on structures with high-aspect ratio morphologies is a nontrivial task, as precursor collisions with the top of the structure are more likely than full penetration of the structure through its pores. [224] Thus, the efficacy of three processes were evaluated to deposit TiO_2 on high-aspect ratio A-CNTs *via* ALD: TDMAT with O_3, TDMAT with H_2O, and a combination of the two processes.

The first process used the GEMStar XT ALD system with TDMAT as the precursor and O_3 as the oxidizing agent. O_3 is preferable to H_2O as it creates nucleation
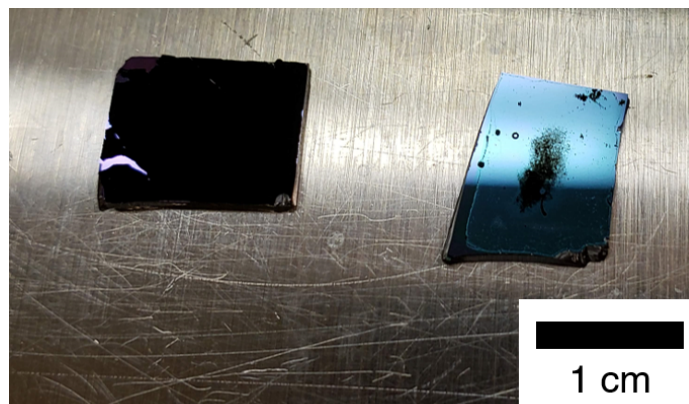
Figure 6-1: Image of two A-CNT arrays after plasma etching using a reactive ion etching tool (Shuttlelock System VII SLR-770/734). Despite being grown and etched in the same batch, the arrays reacted differently to this treatment.

sites on the A-CNTs without necessitating a plasma pretreatment.[224] However, there was no previously developed O_3 and TDMAT recipe for the equipment, so a TMA and O_3 recipe to deposit Al_2O_3 was adapted for the deposition of TiO_2. For this process, the deposition chamber was held at 150°C for 200 cycles, alternating between TDMAT and O_3 pulses with a chamber evacuation between each pulse. An iteration of 200 cycles was chosen for initial trials to ensure a conformal coating over the A-CNTs, based on previous work that suggested a minimum of 50-100 cycles for a conformal coating.[224] This was doubled to ensure that the TiO_2 was thick enough to be observed as described later in this section. The TDMAT pulse time was 22 milliseconds and the O_3 pulse time was 100 milliseconds, both at 40 sccm. However, this treatment was found to completely destroy all the A-CNTs on the Si substrates. The cause of the A-CNT degredation is unknown, but it is expected that the interaction between the O_3 and TDMAT at this temperature (150°C) had a deleterious effect on the A-CNTs, as the limited other work depositing TiO_2 *via* TDMAT and O_3 occurred at a lower temperature (100°C).[225]

Instead of continuing to develop a TDMAT and O_3 process for this particular tool, a hybrid method was developed to use the O_3 to more effectively functionalize the A-CNTs for the first few pulses, but then deposit TDMAT with H_2O. This method was designed to cause less damage to the A-CNTs over the 200-cycle process. For

152

this method, the first five cycles used TDMAT with O_3 to functionalize the A-CNTs and start building the TiO_2 layer. Previous work with this tool suggested that 3–5 cycles would be sufficient for TiO_2 to coat the A-CNTs, and then the remaining cycles would deposit on the already established TiO_2 layer. This hybrid process was successful in that the O_3 treatment did not visibly harm the A-CNTs; however, this procedure was also not effective. The efficacy of this process was tested by heating the TiO_2-coated A-CNTs in air to 800°C for 6 hours to burn the A-CNTs and leave the TiO_2 layer. Although CNTs burn in air above 500°C, the 800°C temperature was chosen to be sufficiently high to burn the A-CNTs within the insulating TiO_2 layer.[38] After this heat treatment, the A-CNT array had successfully been burned; however, the TiO_2 layer did not remain. Thus, this process was also unsuccessful at depositing the TiO_2 layer. Suspecting a malfunction with the tool, future processes used an ALD by Cambridge Nanotech.

The ALD from Cambridge Nanotech was limited to TDMAT and H_2O as the precursors. A standard TDMAT and H_2O recipe, developed specifically for this tool, was used successfully to deposit TiO_2 on the A-CNTs at a chamber temperature of 225°C. This process, with 200 cycles, was confirmed to be successful *via* Raman spectroscopy. The strongest peak at 144 cm^{-1}, shown in Figure 6-2, is indicative of the as-deposited anatase phase of TiO_2.[226,227]

The TiO_2 coating was confirmed to be conformal and penetrated the entire A-CNT array. A-CNTs were burned at 800°C for 6 hours, leaving the TiO_2 coating. Images of two ∼35 μm A-CNT arrays after a 1 nm-thick TiO_2 coating *via* ALD, one before and one after this heat treatment, were taken *via* scanning electron microscopy (SEM). It was found that, while still aligned, the TiO_2 nanotubes were not as straight as the original A-CNTs, as shown in Figure 6-3. Additionally, the height was found to decrease from ∼35 μm to ∼18 μm, likely due to the added waviness of the TiO_2 nanotubes. The cause of the waviness is not well understood, but may be due in part to the change in TiO_2 phase from amorphous (anatase) to crystalline (rutile).

153
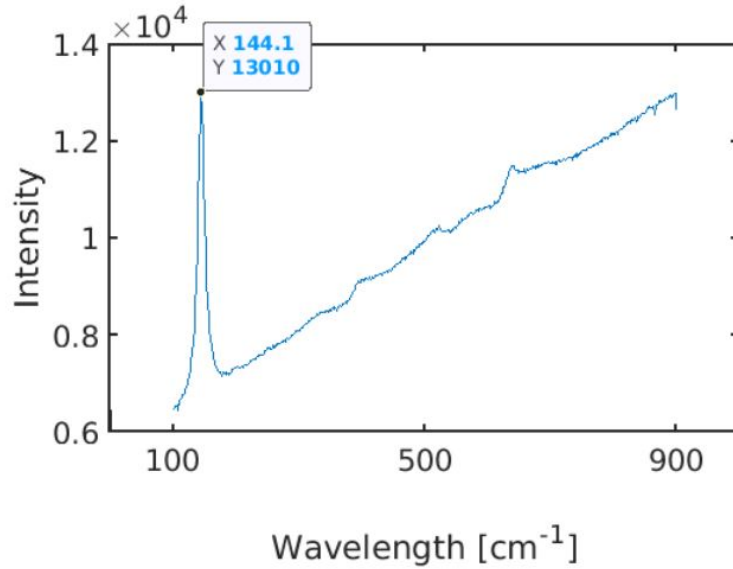
Figure 6-2: Raman spectra of a TiO_2-coated A-CNT array. Successful TiO_2 deposition was confirmed by the peak at $\sim$144 cm^{-1}, indicative of anatase TiO_2.
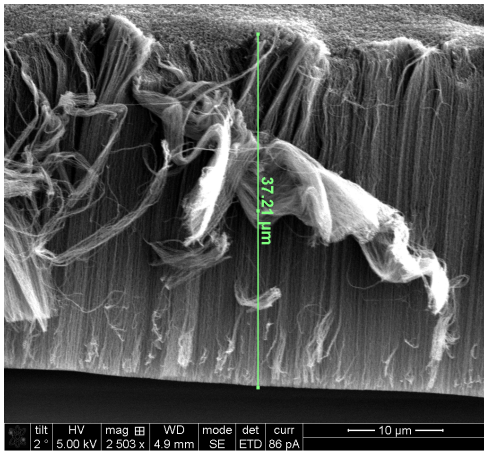
(a) SEM image of A-CNTs coated with TiO_2.
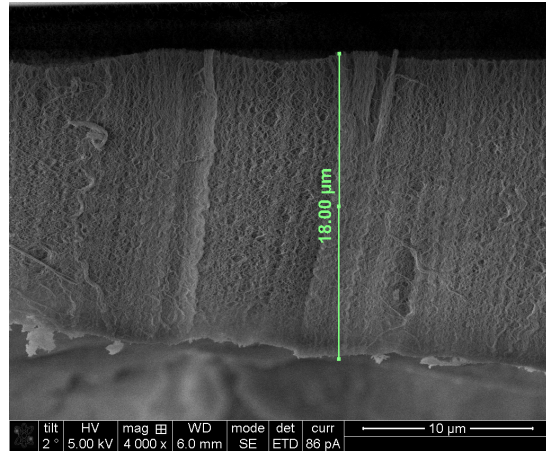
(b) SEM image of TiO_2 nanotubes fabricated by first depositing TiO_2 on an A-CNT array and then heat treating the array to burn the A-CNTs, leaving TiO_2 nanotubes.

Figure 6-3: SEM images of a TiO_2-coated A-CNT array compared to TiO_2 nanotubes. A small height decrease and added waviness of the nanotubes were observed after the heat treatment.

This process was decreased to 25 cycles to provide a 1 nm coating instead of the thicker 8 nm coating from a 200-cycle deposition process. The TDMAT and H_2O process using the Cambridge Nanotech ALD was confirmed to be successful on

154

A-CNT arrays up to $\sim$100 μm without any plasma pretreatment, as these arrays were still intact after burning the A-CNTs. Since the plasma pretreatment was not necessary, further development of this process was placed on hold until the remainder of the A/Al-NC processing steps were developed. However, it should be noted that the plasma pretreatment is necessary for A-CNT arrays greater than $\sim$150 μm in height. The plasma treatment increases the number of nucleation sites for TiO_2 deposition, thus increasing the chances for TiO_2 deposition in areas where gas access is limited (*e.g.* the middle of an A-CNT array). To improve TiO_2 penetration, the A-CNT arrays may be placed into stapled mesh holders, shown in Figure 6-4, as this allows penetration from both the top and bottom of the A-CNT array by removing the substrate on the bottom. The mesh holders were necessary to keep the A-CNTs from fracturing or shifting during the vacuum steps in the process, as the holders kept the A-CNTs together and were heavy enough not to be pulled into the vacuum. A Teflon mesh was chosen as it could withstand the high temperatures.

Figure 6-4: Image of A-CNT arrays prior to ALD of TiO_2, contained in mesh for improved deposition penetration.

6.2.3 TiO_2 Reductions

A reduction was designed to reduce TiO_2 to Ti. Although a well-documented process, TiO_2 reduction process temperatures and hold times vary across the literature based

on the scale of the process and the tools used. This process was initially designed based on the work by Hong *et al.* for TiO_2 pellets, [228] and thus the temperature for reduction was set to 700°C. Since this process was adapted for use on a nanoscale layer of TiO_2, the process hold time was initially set for 30 minutes.

Both A-CNT arrays and micron-scale TiO_2 powder were used to test these reduction treatments. A-CNT arrays were prepared for metal infusion steps later in the process, and TiO_2 powder was placed on quartz boats to provide a visual of reduction (see Figure 6-5), downstream of the A-CNTs, such that the additional H_2O reduction products would not affect the arrays. Additionally, the powder could easily be inspected *via* X-ray powder diffraction (XRD) to determine the extent of the reduction, and, as the powder particles were larger than the 1-nm of TiO_2 decorated on the A-CNTs, the TiO_2 coating on the A-CNTs was expected to reduce more easily than the TiO_2 powder. Thus, a procedure for the TiO_2 powder with partial reduction was likely to cause complete reduction of the TiO_2 coating on the A-CNT arrays.

Figure 6-5: Two quartz boats containing TiO_2 powder prior to reduction.

A furnace system, similar to the one used for A-CNT growth, was adapted for this reduction process. First, the system was placed under vacuum to ensure that there were no leaks and to remove any oxygen or water in the system. As the A-CNTs were unaffected by the vacuum, they could be placed in the 22 mm-diameter quartz tube prior to the vacuum step, as this step would remove oxygen and water in the array as well. Once a full vacuum was confirmed, the system was returned to atmospheric pressure by a flow of Ar at 1000 sccm. However, as TiO_2 powder was disturbed by the vacuum, the downstream end of the quartz tube needed to be opened and TiO_2 powder was added downstream of the A-CNTs, after the vacuum step. The constant Ar flow during this step limited ambient air from entering the quartz tube. Once

the system was prepared, the quartz tube was flushed with 750 sccm of Ar gas for a 2-minute purge. Then the Ar gas flow was reduced to 400 sccm with 100 sccm of H_2 and the furnace began heating to 700°C. Once the 700°C was reached, the Ar/H_2 ratio was inverted such that Ar flowed at 100 sccm and H_2 at 400 sccm for reduction. The system was held at this reduction environment for 30 minutes. Once complete, H_2 gas flow ceased and Ar flushed the system at 500 sccm as it cooled in order to decompose the TiH_2 that formed during reduction, a process discussed later in this section in light of the data presented.[229,230] The powder visually appeared to have reduced from TiO_2 to Ti, shown in Figure 6-6, as there was visible mass loss and a darkening of the color from white to blue/black. However, later XRD analysis suggests that this powder had only begun to reduce. Due to unexpected time constraints, data was unable to be collected on the coated A-CNT arrays. However, XRD analysis of the powder was much faster and could ensure full reduction (as the particle powder size was 3 orders of magnitude larger than the TiO_2 coating), so processes were designed to fully reduce the TiO_2 powder. Thus, the reduction step was increased to a 1 hour hold and the process was repeated, but XRD analysis of the TiO_2 powder after this procedure with prolonged reduction time still suggested that the powder was primarily comprised of TiO_2. The observed XRD spectra is shown in Figure 6-7 with the XRD spectra of the compounds comprising this spectra overlayed. Table 6.1 lists the most likely compounds and the percentage of the powder comprised by that compound. Two different forms of TiO_2 are listed, as well as C, which is likely a small contaminant of the powder. Since the powder was still primarily TiO_2, other processes were explored to reduce TiO_2.
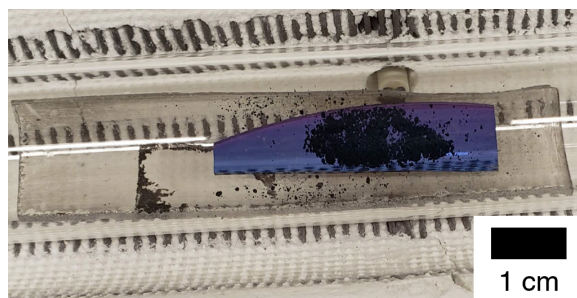
Figure 6-6: Image of TiO_2 powder after reduction at 700°C for 30 minutes. The mass of the powder is reduced and the color has changed from white to blue/black.
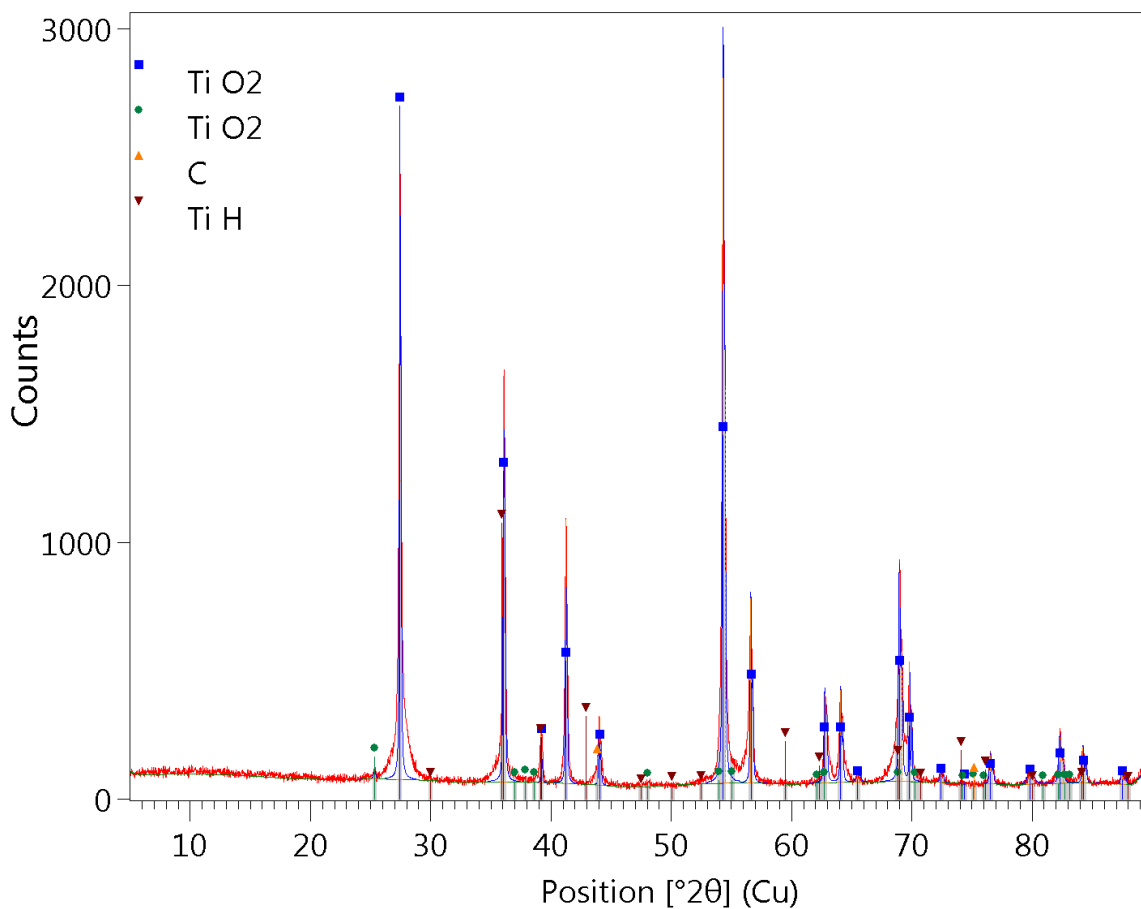
Figure 6-7: XRD spectrum, in red, of TiO_2 powder after a 60-minute, 700°C heat treatment in 80% H_2. The XRD spectrum matches the peaks of TiO_2 but also shows a small amount of TiH, suggesting that reduction had started but did not progress far.

Table 6.1: Percentage of each of the five compounds found in the TiO_2 power reduced at 700°C for 60 minutes. TiO_2 is most prevalent, although the formation of TiH was successful.

Compound Name	Chemical Formula	% Composition
Titanium Oxide	TiO_2	77%
Titanium Oxide	TiO_2	2%
Carbon	C	9%
Titanium Hydride	TiH	13%
	Total	100%

Both higher temperatures and longer reduction times were tested. The final four trials reduced the TiO_2 using a process that occurred at 1000°C. Two trials used the 80% H_2/20% Ar ratio during reduction and two trials used forming gas with 5% H_2 and 95% N_2. The forming gas was used as there was concern that the TiH_x formed during reduction was not fully decomposed during the cool down step and thus less H_2 should be used. For each H_2 ratio, a trial was performed for 60 minutes and another for 90 minutes. The first trial, reduction at 1000°C for 60 minutes in an 80% H mixture, was visually promising as the TiO_2 powder was very dark with visible mass loss, as seen in Figure 6-8. The XRD spectrum for this powder is shown in Figure 6-9 with the peaks of the compounds that constitute the powder labeled in other colors. The spectrum was not clear enough to determine the percentage of each compound in the powder, so this information is not included. The XRD spectrum shows Ti_xO_y, Ti, and TiH_x, which suggests that the reduction process was occurring.
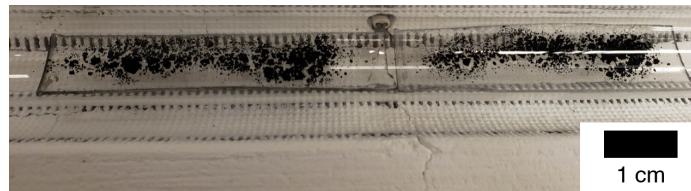
Figure 6-8: Image of TiO_2 powder after reduction for 60 minutes at 1000°C in 80% H_2, showing substantial visible mass loss and a color change to blue/black.

The second trial, reduction at 1000°C for 60 minutes in 5% H_2, also seemed visibly reduced, as shown in Figure 6-10. The XRD spectrum is included in Figure 6-11 with the compounds that constitute the reduced powder labeled. Table 6.2 lists the
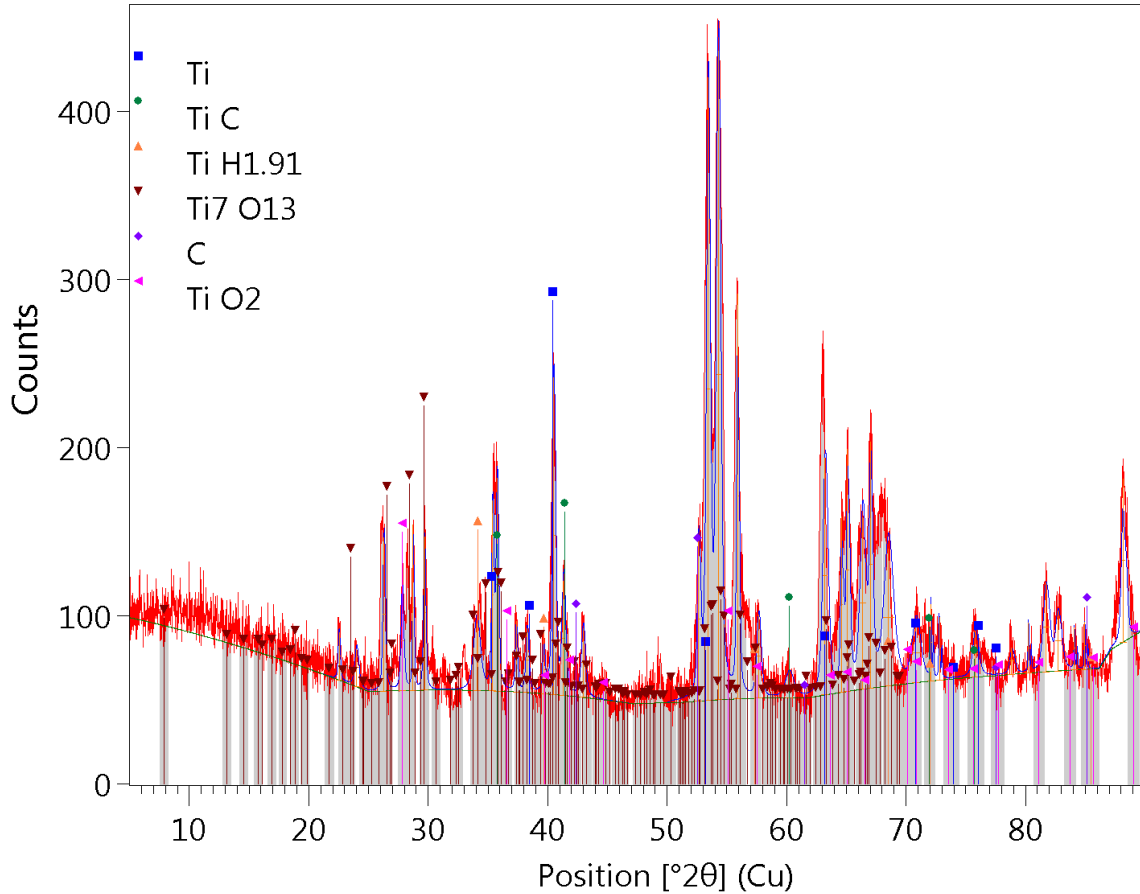
Figure 6-9: XRD spectrum, in red, of the powder after a 1000°C, 60-minute reduction in 80% H_2. Peaks representative of the six different components in the powder are labeled.

percentage of each compound in the reduced powder. Given the lower H_2 % in the reduction atmosphere, less TiH_2 was formed in this process, as expected. Moreover, less TiO_2 was reduced, suggesting that the reduction requires more time to reduce all the TiO_2 prior to decreasing the H_2 flow.
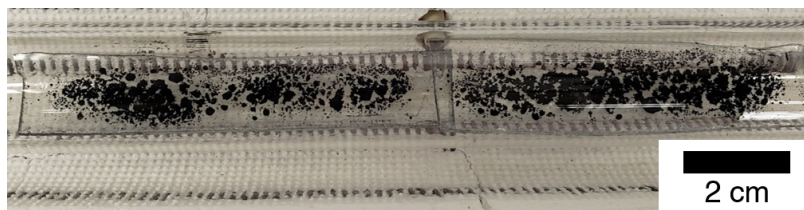
Figure 6-10: Image of TiO_2 powder after reduction for 60 minutes at 1000°C in 5% H_2, showing mass loss and color change to blue/black.
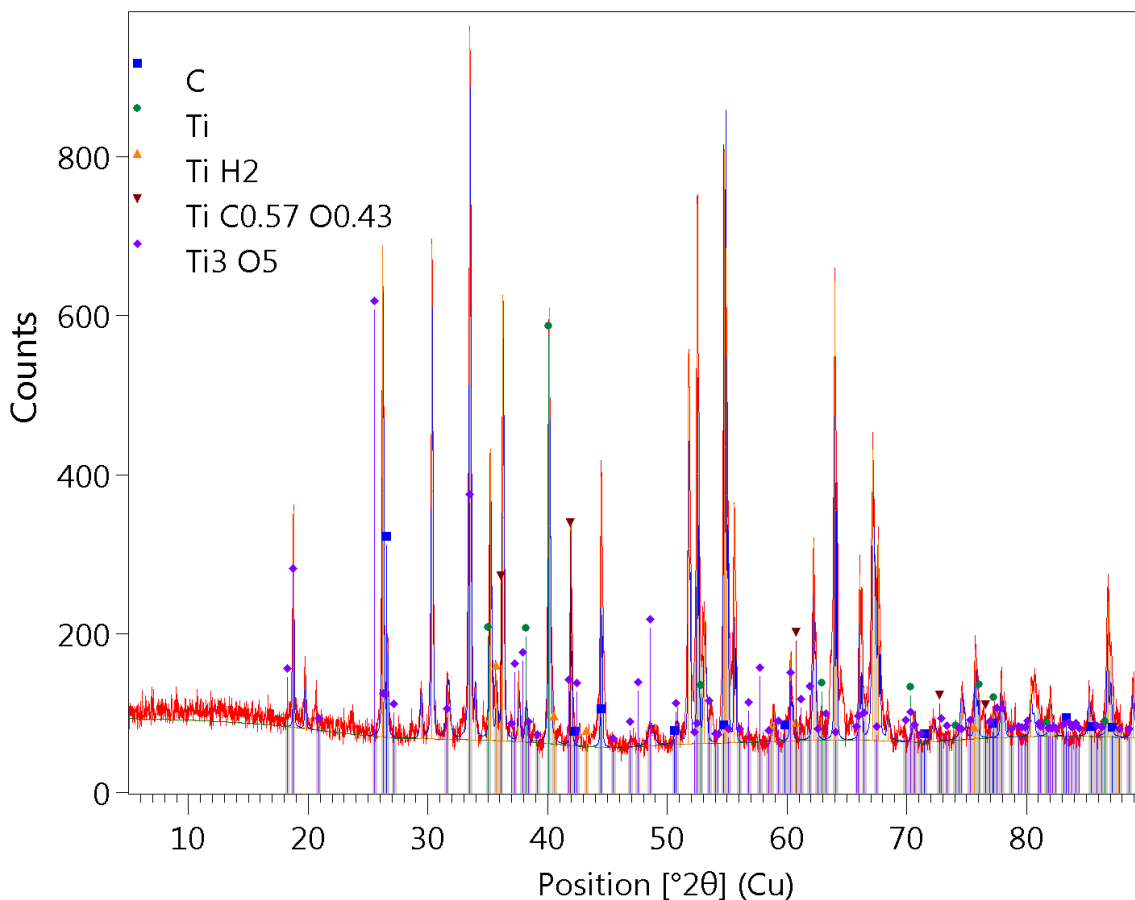
Figure 6-11: XRD spectrum, in red, of the powder after a 1000°C, 60-minute reduction in 5% H$_2$. Peaks representative of the five different compounds in the powder are labeled.

Table 6.2: Percentage of each of the five compounds found in the TiO$_2$ power reduced at 1000°C for 60 minutes in 5% H$_2$. Ti$_3$O$_5$, Ti, and TiH$_2$ are all present, showing that reduction did occur, but the large percentage of Ti$_3$O$_5$ suggests that a longer reduction or increased H$_2$ flow are required for reduction.

Compound Name	Chemical Formula	% Composition
Carbon	C	14%
Titanium	Ti	11%
Titanium Hydride	TiH$_2$	2%
Titanium Carbide Oxide	TiC$_{0.57}$O$_{0.43}$	9%
Titanium Oxide	Ti$_3$O$_5$	65%
Total		100%

The final two trials, reductions for 90 minutes at 1000°C in 80% and 5% H$_2$ respectively, had similar results to the two 60-minute reductions, with XRD results

161

suggesting that the process with an 80% H_2 atmosphere was more effective. The XRD spectrum from the 80% H_2 atmosphere is shown in Figure 6-12. The spectrum was not clear enough for the percent composition of each compound to be determined. However, the matched XRD spectra include Ti_xO_y and Ti, which suggests partial reduction. However, there is no pure TiH_x, which may suggest increased C contamination with longer reduction times at 1000°C.
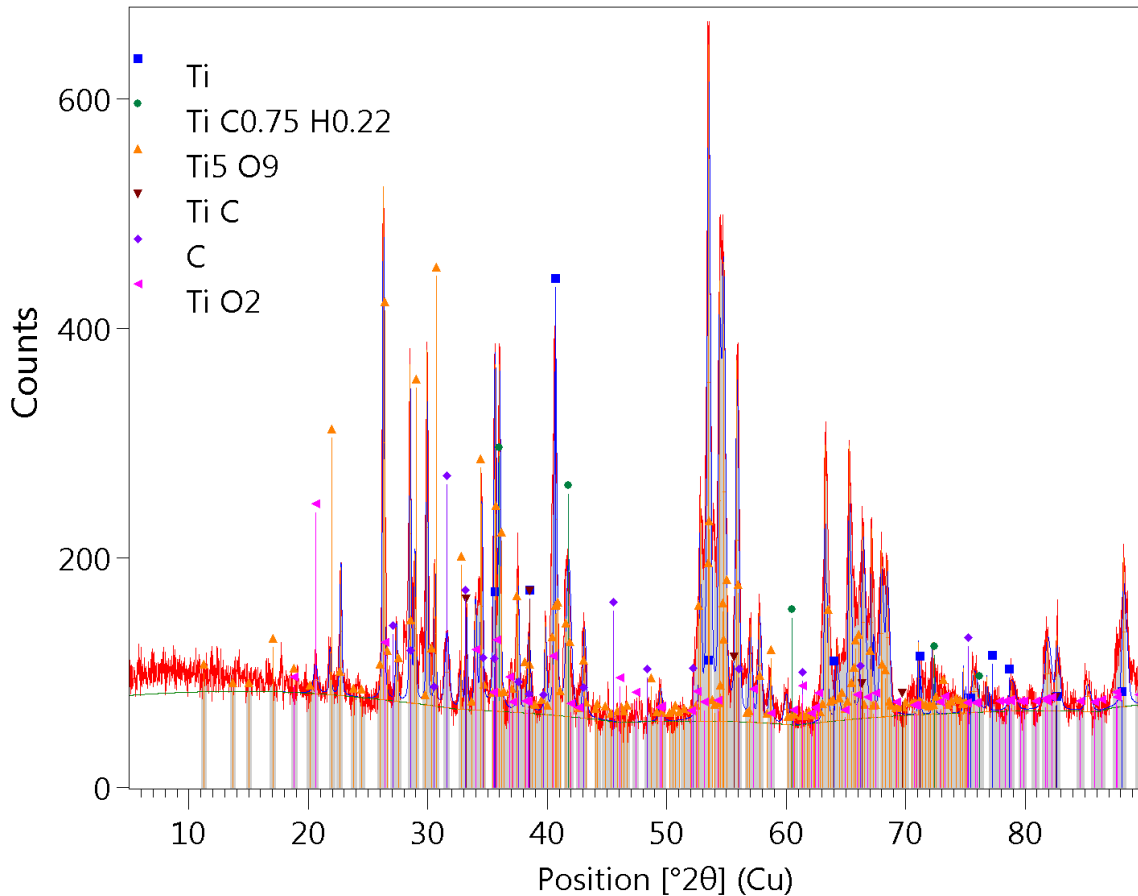
Figure 6-12: XRD spectrum, in red, of the powder after a 1000°C, 90-minute reduction in 80% H_2. Peaks representative of the six compounds comprising the powder are labeled.

An image of the TiO_2 powder after reduction with 5% H_2 is shown in Figure 6-13. The XRD spectrum is included in Figure 6-14 with the compounds that constitute the reduced powder labeled. Table 6.3 lists the percentage of each compound in the reduced powder. Less Ti_3O_5 is observed than the 60-minute process, but other forms of Ti_xO_y make up a larger percentage of the partially-reduced powder. There

is also an increase in composition % of hydrogen products, but these bonded with the carbon at the higher temperature. Thus, a lower temperature, longer process should be investigated in future work.
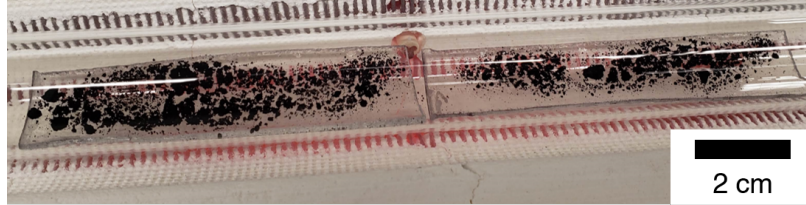
Figure 6-13: Image of TiO_2 powder after reduction for 90 minutes at 1000°C in 5% H_2, showing mass loss and color change to blue/black.
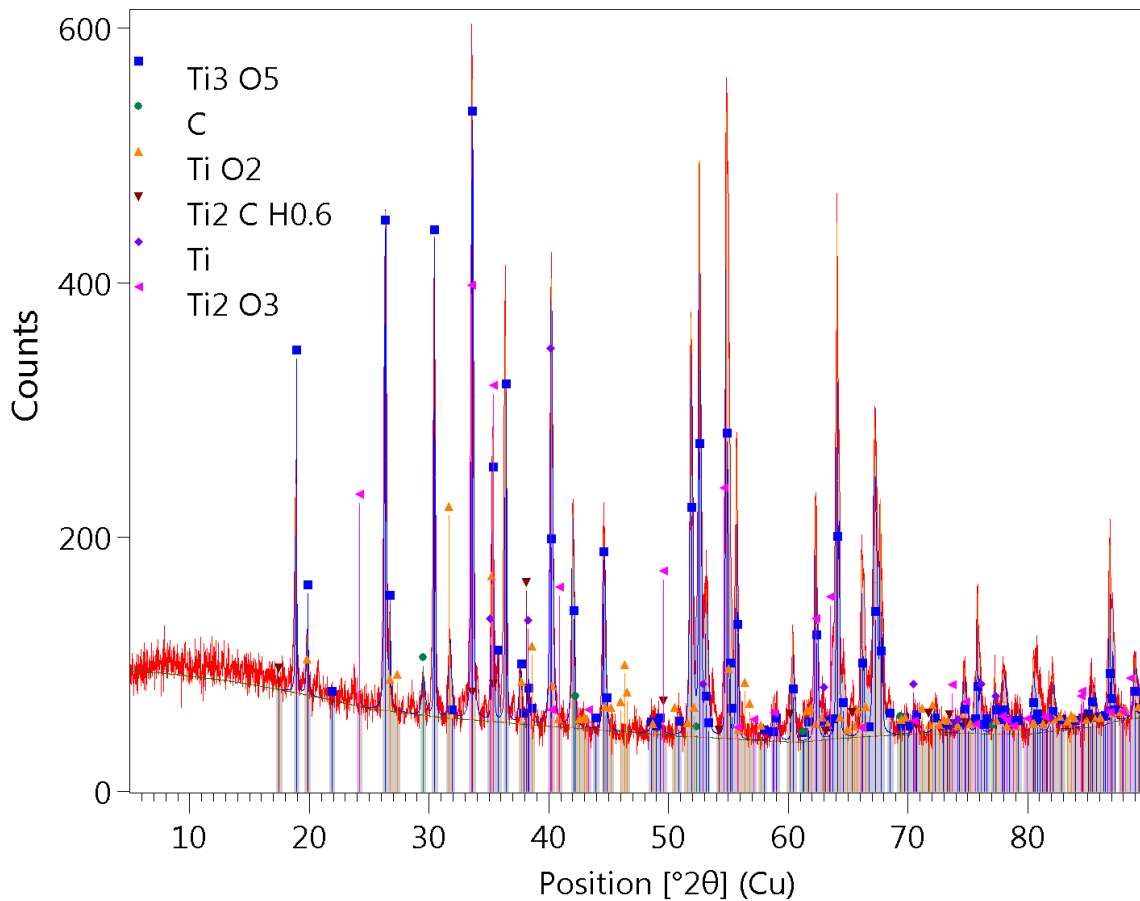
Figure 6-14: XRD spectrum, in red, of the powder after a 1000°C, 90-minute reduction in 5% H_2.

Table 6.3: Percentage of each of the six compounds found in the TiO_2 power reduced at 1000°C for 90 minutes in 5% H_2. Given the high composition % of Ti_xO_y, a longer decomposition process must be implemented.

Compound Name	Chemical Formula	% Composition
Titanium Oxide	Ti_3O_5	53%
Carbon	C	5%
Titanium Oxide	TiO_2	13%
Titanium Carbon Hydride	$Ti_2CH_{0.6}$	4%
Titanium	Ti	6%
Titanium Oxide	Ti_2O_3	20%
Total		100%

Literature review explains how the results visually seemed to be successful without fully reducing. Once the TiO_2 began to reduce, it formed a compound called "blue TiO_2", or blue hydrogenated rutile titanium oxide.[231] Blue Ti_xO_y is an electron-rich[232,233] compound formed *via* partial hydrogen reduction, such that there are partial oxygen vacancies.[231,232] Black Ti_xO_y, another titanium oxide compound formed due to oxygen vacancies,[234] is likely the cause of the dark color in the reduced TiO_2. Since the compound matches blue and black TiO_2 in both color and synthesis procedure, it is likely that all trials formed blue/black TiO_2 due to incomplete reduction.

Although there was significant blue TiO_2 in partially-reduced powders, the formation of blue TiO_2 is a step in the process of becoming TiH_x. A study by Tsarev *et al.* studied the oxidation of TiH_x powder in a furnace between 440°C and 540°C. The oxidation occurred in 3 phases:

$$TiH_x \rightarrow TiH_yO_z \rightarrow Ti_2O \rightarrow TiO_2$$
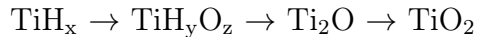
and the color changed from gray (TiH_x) to lilac to blue to gray/blue with increasing temperature.[229] These results suggest that the process discussed in this thesis was likely the reverse. Since this work started with TiO_2, the reduction likely was successful in removing some of the O_2, creating blue TiO_2, and would have become TiH_x given more time and a greater H_2 flow. Tsarev *et al.* used a 1 hr hold, which was clearly not enough to reverse the process.[229] Work by Rekoske *et al.* confirms this hypothesis, as this study of reaction kinetics suggests that the reduction of TiO_2 in

H_2 forms TiH_2.[230] As the TiO_2 powder particles were larger than the 1 nm coating of TiO_2 on the A-CNT arrays, any procedure that was successful on the powder was expected to be successful on the TiO_2-decorated A-CNT arrays. Future work should focus on the A-CNT arrays, as the initial evaluation of the processes using the TiO_2 powder as an indication is complete. The effect of these processes on the A-CNTs can be evaluated using X-ray photoelectron spectroscopy (XPS), with the goal of ensuring a TiH_x coating on the A-CNT array.

6.3   Solder Infusion

As an initial proof-of-concept, solder infusion into the modified A-CNT arrays was tested. Solder was chosen as a substitute metal matrix since it can be melted in a vacuum oven due to its low melting temperature ($\sim$200°C). The vacuum oven was chosen to displace the air originally in the A-CNT array, thus improving wetting, much like the phenol-formaldehyde resin infusion processes used in A-CNT/carbon-matrix nanocomposite (A/C-NC) synthesis. The vacuum oven also holds both the temperature and vacuum long enough for complete wetting ($\sim$20 minutes for A-PNC fabrication).[45] In addition to the low melting temperature, solder contains flux, which lowers its surface energy and thus allows it to wet surfaces more easily than Al. Thus, any wetting process must work with a solder matrix for the procedure to work with an Al matrix. Solder wetting was expected to be successful as solder was found to wet untreated A-CNTs at $\sim$258°C with enough flux.[235]

For the solder wetting trials (specifics given below), surface-modified A-CNT arrays were typically placed in Al foil boats with the wafer on the bottom. Solder, measuring $\sim$300 mm^3 to ensure sufficient matrix material for 1 cm x 1 cm x 100 μm A-CNT arrays used for this work, was carefully coiled into a disk and placed on top of the arrays, directly on the entangled A-CNT layer, as shown in Figure 6-15. These A-CNT arrays were then placed in a vacuum oven and held at 200°C under a 5 mbar vacuum for $\sim$2 hours, much longer than the required wetting time for polymer resin nanocomposites (NCs) such that there was sufficient time for successful wetting.[45]

After ∼2 hours, the vacuum was lifted and the temperature decreased for immediate inspection; however, in more recent trials, the A-CNT/solder NCs were allowed to cool before the vacuum was lifted such that the solder could solidify.
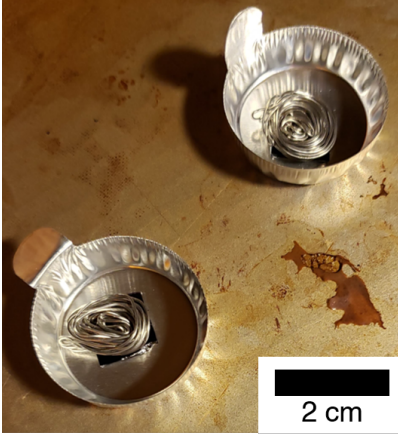
Figure 6-15: Surface-modified A-CNT arrays prepared for infusion with a ∼300 mm^3 coil of solder on top of the array.

Solder infusion trials had mixed results. Initial trials using TiO_2-coated A-CNTs reduced at 700°C for 30 minutes in an 80% H_2 environment were met with limited success, seen in Figure 6-16. Although the flux from the solder appeared to densify the arrays significantly, visible in the NC to the right, the A-CNTs were wetted by the solder to the point where they delaminated from the wafer prior to pulling out of the matrix. However, the A-CNTs could easily be removed from the matrix with a pair of tweezers, suggesting that the A-CNTs were not fully wetted. Additionally, not all trials were successful. Solder wetting was attempted on TiO_2-coated A-CNTs treated at 1000°C for 90 minutes in an 80% H_2 atmosphere with no success. For these surface-modified A-CNT arrays, the solder was repelled by the A-CNT arrays and instead wetted the Al boat, seen in Figure 6-17, as the interfacial energies between the solder and the Al boat were more favorable. Future work should investigate if the solder wetting process inherently produces variable results or if the 1000°C reduction produces a Ti/O compound with a higher surface energy that is harder to wet.

Figure 6-16: Image of successfully wetted TiO$_2$-decorated A-CNTs heat treated at 700°C for 30 minutes in an 80% H$_2$ atmosphere. Although the solder-wetted A-CNTs could be detached from the wafer, the A-CNTs were easily pulled out of the solder matrix, suggesting there was still insufficient wetting to form a true A-CNT/solder matrix nanocomposite.

Figure 6-17: Image of unsuccessfully wetted A-CNTs with surface modification (reduced at 1000°C for 90 minutes in an 80% H$_2$ atmosphere), demonstrating variability in the process.

Two additional baseline trials were conducted as well to determine the efficacy of the vacuum oven. For the first trial, treated A-CNTs were placed with solder in the oven at 200°C but without vacuum. This trial was completely unsuccessful and suggested that the vacuum was a necessary step in the process to aid wetting. For the second trial, untreated A-CNTs were placed with solder in the vacuum oven at 200°C under a 5 mbar vacuum. Again, this trial was completely unsuccessful, as the solder (surface energy taken as 0.5 J m^{-2}) was unable to wet the untreated A-CNTs (surface

energy taken as 0.027 J m^{-2}), as expected from the wetting calculations explained in Section 2.3.1. Additional trials were not conducted due to time constraints and parallel co-development of the Ti surface coating. Future work in this area is explained in Section 6.5.

6.4 Aluminum Infusion Methods and Results

Although the initial solder infusions were met with mixed success, two Al infusion trials were also completed. Al infusion was envisioned to follow melt casting methods, where either Al powder or pellets would be melted on top of the surface-treated A-CNT arrays under a vacuum. The vacuum would serve two purposes: improving A-CNT wetting by removing air from the array, and by removing oxygen such that the A-CNTs would not degrade at the melting temperature of Al.

Both infusion trials were meant to simulate the melt casting environment, aiming to predict the success of a special melt casting apparatus prior to manufacturing this specialized tool. The first trial used equipment for full-scale Al forging and casting to pour the Al onto a Si wafer coated with 500 nm of Ti *via* e-beam deposition as well as onto surface-treated A-CNT arrays (details to follow). The second method aimed to simulate the powder infusion in a vacuum environment by repurposing an AJA ATC Electron Beam Evaporator to melt powder and pellets into an A-CNT array in a vacuum environment. Both of these methods and the corresponding results are discussed in detail in the subsections below.

6.4.1 Infusion *via* Casting Methods

The first infusion process was completed *via* traditional aluminum casting methods. Pure (99.99%) Al was melted in a crucible. Once fully melted, Al_2O_3 was skimmed off the top of the melt and the pure Al was poured first onto a Si wafer that was coated with 500 nm-thick Ti and the remainder of the molten Al was poured onto the surface-modified A-CNT arrays. The e-beam was used to coat the wafer with 500 nm of Ti instead of using the ALD tool to deposit 1 nm of TiO_2 and then reducing this

168

layer, as described in Section 6.2.3 for the A-CNTs for two reasons. First, the thicker layer was less affected by oxidation, and second, the Ti deposition ensured that the material being wet was Ti, as the reduction process requires further development.

As the crucible and tongs, which were used to handle the crucible, were designed for large-scale manufacturing, precise movements of the large equipment to carefully pour the molten Al onto the Ti-coated Si wafer and surface-modified A-CNT array was a challenge. Controlling the Al flow to place a single Al drop onto the Ti-coated Si wafer, similar to a Sessile Drop method to measure contact angle, was impossible. However, the Al poured onto the Ti-coated wafer appeared to spread quickly, which provided promising results for the ability of the Al to wet the Ti-coated A-CNTs, as seen in Figure 6-18.

Figure 6-18: Ti-coated Si wafer wetted with molten Al. The Al spread well across the wafer, suggesting that Al will wet the Ti-coated A-CNTs.

The A-CNTs, coated with 1 nm of TiO_2, were reduced *via* a reduction process, described in Section 6.2.2, with a 30-minute hold at 700°C in an 80% H_2 atmosphere, as this was successful for the solder wetting trials. Infusion of Al into the A-CNT arrays was unsuccessful *via* traditional casting methods, as seen in Figure 6-19. Once removed from the furnace, the Al cooled quickly and likely solidified before any infusion was possible, which necessitated the use of equipment that could keep the Al above its melting point (660°C) for at least 15–20 minutes, as previous work determined that was the time required for polymer resin to wet A-CNTs ∼1 mm in height.[45] However, future work should determine the required wetting time for Al. This temperature is above the decomposition temperature in air of A-CNTs (500°C);[196] thus, the next iteration of the process would also need to occur in a vacuum.
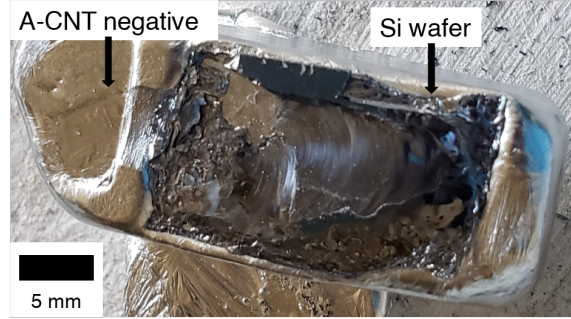
Figure 6-19: Al that was poured into a crucible over A-CNT arrays. The A-CNT array that was originally in the negative to the left was easily pulled out and thus is not seen in this image. Another Si wafer, pictured to the right, melted when it came in contact with the molten Al, fusing the Si to the Al.

6.4.2   Infusion *via* Electron-Beam Heating

The second Al infusion trial repurposed an AJA ATC Electron-Beam Evaporator for Al infusion into the surface-modified A-CNT array. Under typical use, the e-beam is used to deposit thin films, up to 1 μm in thickness, on surfaces by heating a powder or pellets *via* an electron beam, causing the solid to sublimate and adsorb on the desired surface from the gas phase.[236]

For the application in this work, two separate trials of surface-modified A-CNT arrays were placed in a crucible with Al powder (≤ 30 μm powder size, Sigma Aldrich) and pellets. The e-beam was used to melt the Al in a vacuum environment. For the first trial, the A-CNTs were coated in TiO_2 *via* ALD with TDMAT and H_2O. The TiO_2 coating was reduced in an 80% H_2 environment for 60 minutes at 1000°C and covered in Al powder for the e-beam infusion test. Al was initially evaporated at 85–90 mA and was adjusted to keep the appropriate melting rate for this equipment. The most important result from this trial was that the e-beam quickly sublimated the Al powder and then hit the A-CNT array and edge of the crucible, burning the A-CNTs and causing sparks, even after decreasing the current to 40 mA. Thus, a mixture of Al pellets and Al powder were used in the second trial.

For the second trial, ∼1 mm A-CNT arrays were substituted for the ∼100 μm A-CNTs used for most of the procedures in this thesis. The taller arrays ensured that the A-CNTs would be visible in the matrix once infusion was complete. Due

to their height, the A-CNTs were plasma treated to remove the A-CNT crust but not to functionalize the A-CNT arrays, and then the arrays were delaminated from the Si wafer, using a standard lab razor blade. The A-CNT arrays were placed in Teflon mesh holders, shown in Figure 6-4, and coated with a 1 nm layer of TiO_2 *via* ALD. The TiO_2 was reduced in an 80% H_2 atmosphere for 90 minutes at 1000°C and allowed to cool in a H_2 atmosphere. The H_2 atmosphere was expected to form TiH_2, which would then decompose once in contact with molten Al. These A-CNTs were placed in the e-beam with Al pellets (99.99% purity, Kurt Lesker) to better shield the surface-modified A-CNT arrays and then were filled with Al powder. The Al was melted more successfully, following a procedure similar to the first trial, with slight changes to the current and beam dispersion to better match the Al pellets.

All A/Al-NCs were cut into quarters to see how the Al wetted the surface-modified A-CNTs, but the A-CNTs were not visible. To ensure that the A-CNT arrays had not densified inside one of the Al quarters, these pieces were imaged *via* micro-computed X-ray tomography (μCT); however, no trace of the A-CNTs was visible. Two explanations were developed to understand this result: first, the A-CNTs may have dispersed in the matrix such that they are not visible. However, this was determined to be unlikely. ALD should not have conformally coated the 1 mm-tall A-CNTs without a plasma functionalization, and thus the Al should not have wet along the full length of these A-CNTs. A second possible explanation may be that the A-CNTs, despite the TiO_2/TiH_2 coating, reacted with the Al to form Al_4C_3 once heated above the melting point of Al, as suggested by the work of Deng *et al.*[237] Since the e-beam delivers much more heat than necessary to melt the Al, Ti or TiO_2 coatings may keep the A-CNTs from reacting with the Al, but the reaction of Al with Ti for melt casting methods is still an open issue. In addition to providing a summary of the A/Al-NC work performed in this thesis, the next section will discuss open issues and suggest future avenues of research.

6.5 Conclusions and Recommendations for Future Work

Multiple steps to fabricate A/Al-NCs were investigated in this chapter. First, $\sim$100 μm A-CNT arrays were synthesized *via* a CVD growth method. These A-CNTs required a surface modification prior to metal matrix (Al or solder) infusion, so two ALD methods with TDMAT and either O_3 or H_2O as oxidizers were investigated, and a plasma pretreatment was developed to functionalize the A-CNTs for ALD with H_2O. Reduction of the TiO_2 coating was attempted *via* a hydrogen reduction, but all reductions were incomplete. Both the TiO_2 deposition and reduction should be investigated further to develop a repeatable process with a conformal A-CNT coating.

Solder was tested for infusion in addition to Al as an initial method of gauging infusion success. Solder infusion trials had limited success; TiO_2-decorated A-CNTs reduced at 700°C for 30 minutes in an 80% H_2 atmosphere were successfully infused with solder, but the A-CNTs tended to densify from the solder flux or easily pull out of the matrix. Taller A-CNTs should be tested in future trials as the A-CNT pull-out may be due to the height of the A-CNT array. Other solder infusion trials, including TiO_2-decorated A-CNTs reduced at 1000°C for 90 minutes in an 80% H_2 atmosphere, were unsuccessful. As different compounds were formed from the TiO_2 powder at these temperatures, these compounds may have affected wetting, but later work should confirm and explore this phenomenon. Future work should investigate the effect of different TiO_2 reduction processes on the final degree of wetting to increase the repeatability of the infusions as well. Both untreated A-CNT arrays in a vacuum and treated A-CNT arrays without vacuum infusion were tested and exhibited unsuccessful wetting, suggesting that both the surface treatment and the vacuum infusion are necessary for A/Al-NC fabrication.

Al infusion was tested as well *via* traditional casting methods and a nontraditional use of the e-beam. Traditional casting methods were unsuccessful, at least because the molten Al cooled much faster than necessary to infiltrate the A-CNT array. Molten Al did spread well over a Ti-coated wafer, however, which suggested that Al would

wet the Ti-decorated A-CNT arrays well. Although the nontraditional use of the e-beam for liquid Al infusion allowed the liquid Al more time to infuse, analysis of the A/Al-NCs suggested that the A-CNTs reacted completely with the Al, forming Al_3C_4, likely due to excessive heating of the Al inside the e-beam beyond the melting temperature. More trials should be completed to determine if the A-CNTs would react with Al at lower infusion temperatures as well.

In the remainder of this section, suggestions are provided for refining the A/Al-NC synthesis to synthesize ∼100 μm scale A/Al-NCs. Additionally, other possible paths from the literature reviewed, as well as areas of improvement for the synthesis of mm-scale A/Al-NCs. Although shown to be unnecessary for ∼100 μm scale A/Al-NCs, the plasma pretreatment should be investigated to better understand why A-CNTs with the same synthesis procedure reacted to the plasma pretreatment differently. Once the mechanisms behind the plasma pretreatment are better understood, the plasma process should be tuned such that ALD can conformally decorate TiO_2 on taller A-CNT arrays and mm-scale A/Al-NCs can be realized.

The ALD process must also be adjusted to scale up this work. Analysis of the ALD deposition suggests that penetration depth can be improved by increasing the time of the TDMAT pulse, as the penetration depth was determined to be proportional to the square root of pulse time, $\sqrt{t_{pulse}}$.[224] As layers of TiO_2 are decorated onto the A-CNTs, the surface area to coat increases and the inter-CNT spacing for diffusion decreases; thus, it may be necessary to adjust the pulse times and other process parameters during the coating process.[224] Additionally, if the A/Al-NCs were to be densified to higher volume fractions (v_f), similar to the A/C-NCs, the A-CNTs should be densified after the surface modification step to provide adequate space for precursor diffusion. Although a TDMAT and H_2O ALD process was developed for this work, the TDMAT and O_3 process could be developed based on the literature[225] towards eliminating the need for a plasma pretreatment.

Even though a TiO_2 coating was determined to be optimal for this work, other A-CNT coatings that could be deposited via ALD should be considered. Fe_2O_3 has also been deposited via bis[bis(trimethylsilyl)amide]iron [Fe(btmsa)$_2$] with hydrogen

peroxide as the oxidizer and may be adaptable to A-CNT arrays. [220] Iron also has a higher surface energy than Al[170] and can be reduced in H_2 between 550°C and 570°C, [238,239] resulting in Fe-coated A-CNTs. However, this reduction would also need to occur immediately prior to infusion to avoid reoxidation.

For the TiO_2 coating applied in this thesis, a suitable reduction process must continue to be developed as well. To fully reduce the TiO_2, longer reduction times should be tested in order to allow the H_2 to bond with all the O molecules. Since this process forms TiH_2, [229] this work cooled the furnace without H_2 flow such that the TiH_2 would decompose. [240,241] However, since Ti would likely oxidize immediately, [242] another 1000°C reduction process was attempted where the A-CNTs were kept in the 80% H_2 atmosphere as the system cooled to room temperature. Although the efficacy of this process was never confirmed, the purpose of this process was to form TiH_2 such that the TiH_2 could be decomposed in the vacuum apparatus immediately prior to the Al melt. Alternatively, the Al infusion could cause the decomposition of TiH_2, as TiH_2 decomposes 7°C above the melting temperature of Al, resulting in A/Al-NCs with a pure Ti interface layer. [243]

Other surface coating options that could be investigated include TiO_2 and TiN. [244] However, there was no available data on TiN surface energies or TiN interaction with Al, so the wetting of Al on TiN would first need to be investigated. Future work may also investigate how well Al wets TiO_2, as the O_2 may diffuse through the molten Al, leaving a pure Ti coating on the A-CNT after A/Al-NC synthesis. [245] For any future procedures, once the interface layer has been determined and the appropriate reduction process implemented, the coating should be confirmed *via* XPS.

For the work presented in this chapter, an open area of research is how the Ti nanolayer would interact with the Al. The Ti nanolayer was expected to remain in its solid form and thus the Al would wet the Ti coating. However, it is possible that the Al would alloy with the Ti, even at the low temperature, because of the thin coating. Referencing the binary phase diagram for Ti and Al at low wt% Ti (Figure 6-20 [246]), the temperature required for both the Ti and Al to be a liquid approaches 660°C as the Ti concentration goes to zero, which suggests that the Ti may melt when in

contact with the Al. As the Al would be held near 800°C to ensure that the Al is fully liquid, a thicker Ti coating may be necessary to keep a solid coating around the nanotubes.

Temperature, °C

L

TiAl₃ rt + L

Al   at. %   Ti
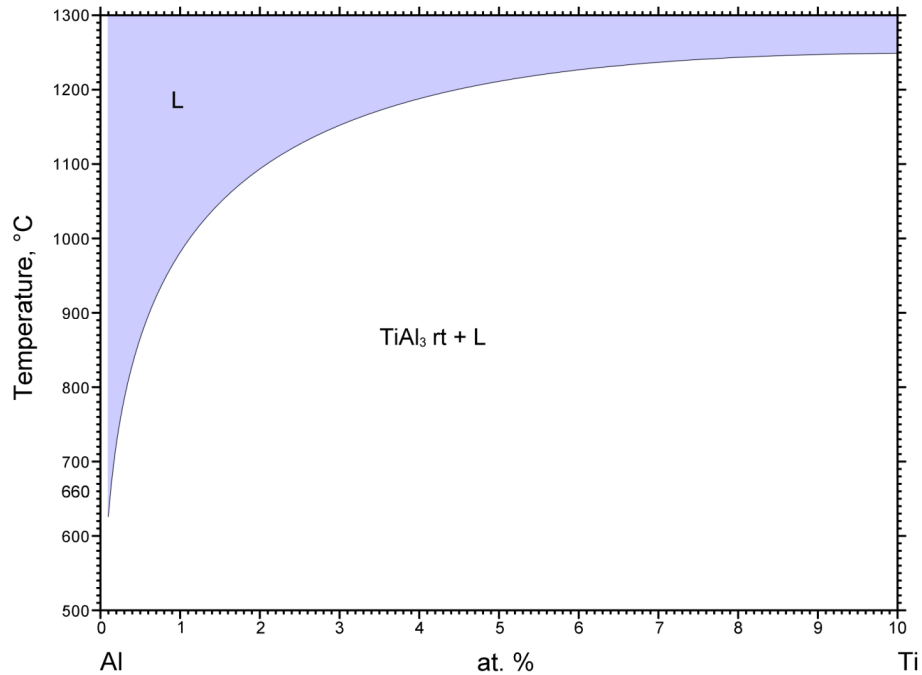
Figure 6-20: Binary phase diagram for Ti and Al, which suggests that the 1 nm-thick layer of Ti could melt in contact with the molten Al.[16]

Given that the Ti may melt, the Al may react with both the Ti and C to form $Ti_{1.1}Al_{2.9}$ and Al_4C_3, as shown in the ternary phase diagram (Figure 6-21[17]). This ternary phase diagram is for Al, C, and Ti slightly above the melting point of Al (727°C), so the three elements may interact differently closer to the melting point of Al. Although work by Deng *et al.* found that CNTs react with the Al matrix, they also found that the CNTs do not begin to react with the Al until at least ~10°C above the melting point of Al.[237] Since the work by Deng *et al.* continued to increase temperature throughout the experiment, the reaction of CNTs with Al may occur at a lower temperature than measured.[237] However, powdered Al has been infused into A-CNT arrays successfully in other work,[157] which suggests that powdered Al could be infused into Ti-coated A-CNT arrays as well.
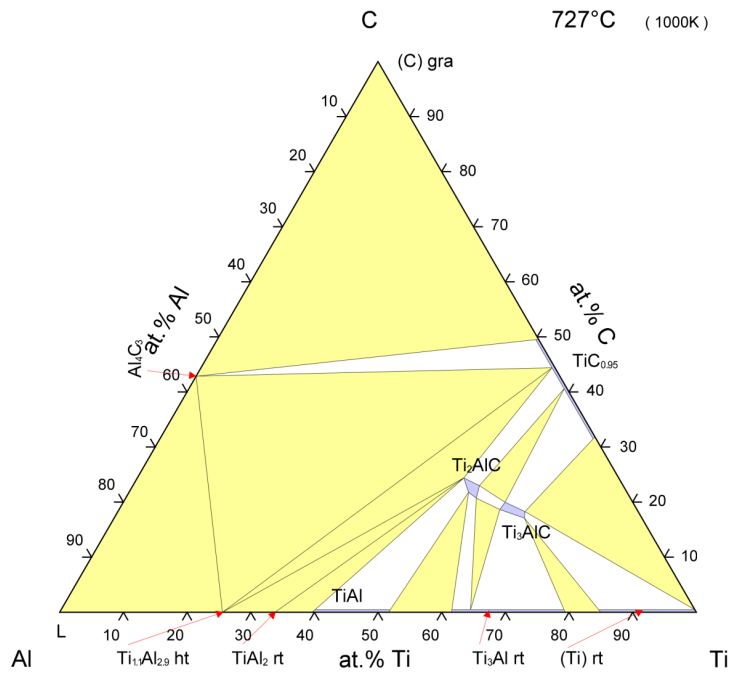
Figure 6-21: Ternary phase diagram for Al, C, and Ti; the Al will bond with all the available Ti and C at 727°C, slightly above the melting temperature of the Al.[17]

Finally, a dedicated Al infusion apparatus should be developed. No designs for this apparatus were completed, but a specialized vacuum oven with a crucible for holding the surface-modified A-CNT array was envisioned. The vacuum would be necessary both for the infusion and possibly a TiH_2 decomposition step prior to infusion. The oven would need to reach 660°C–700°C for the duration of the infusion as well to keep the Al molten. Excess Al could be added to the infusion apparatus such that the Al_2O_3 from the Al could float to the surface, and this surface layer could be removed prior to testing the A/Al-NCs.

Chapter 7

Conclusions and Recommendations

This thesis aims to improve the synthesis processes of aligned-carbon nanotube (A-CNT) nanocomposites (NCs). The contributions are twofold: first, improvements to A-CNT/carbon matrix NCs (A/C-NCs) fabrication allowed for the manufacture of high volume fraction (v_f), and thus relatively high-hardness, A/C-NCs. Second, work with A-CNT/Al matrix NCs (A/Al-NCs) reveals a path for synthesizing A/Al-NCs using $\sim$100 μm-tall A-CNT arrays, which are an order of magnitude taller than other A/Al-NC work.

A/C-NCs were fabricated by first growing 1–2 mm tall A-CNTs *via* a chemical vapor deposition (CVD) method. The as-grown A-CNTs had a v_f of 1 vol%, and were then biaxially mechanically densified up to 30% v_f. The A-CNT arrays, in 1, 5, 10, 20, and 30% v_f, were placed in a mold for phenol-formaldehyde (P-F) resin infusion. The mold for the baseline procedure was made of silicone, but was upgraded to steel for the improved procedure. Steel was chosen because it could both withstand higher processing temperatures and because it did not cause the A-CNT arrays to densify, as opposed to the silicone molds. The improved procedure also implemented a water desorption step at 280°C to remove the layer of adsorbed water from the A-CNTs, which improved infusion. Next, the P-F resin was prepared for infusion. For the baseline procedure and initial trial of the improved procedure, resin was degassed per industry practice to decrease the wt% volatiles from 40 wt% to 20–25 wt%. However, this was unsuccessful in the improved procedure and trials were performed with as-

received (60 wt%) resin, 50 wt% resin, and 10 wt% resin. All samples were cured to synthesize polymer matrix NCs (PNCs) through a 5-step process with holds at 60°C, 70°C, 110°C, 160°C, and ~200°C. PNCs were then pyrolyzed at 1000°C to create A/C-NCs from the PNCs. These A/C-NCs were mounted and polished in preparation for Vickers hardness testing. Hardness values for A/C-NCs were measured and compared to select a process that produces high volume fraction A/C-NCs towards the highest hardness NC.

A/Al-NCs were also fabricated by first growing A-CNTs *via* a CVD method, but the A/Al-NCs were grown to ~100 µm in height for this initial proof-of-concept work. Unlike the A/C-NCs, which were fabricated by infusing a polymer precursor resin, the A/Al-NCs were fabricated by directly infusing the Al metal matrix. Since CNTs have a very low surface energy, their surfaces must first be modified for sufficient wetting of the matrix. Various A/Al-NC fabrication methods were investigated for this work, but a Ti coating was chosen due to the excellent wetting between Al and Ti as well as the ease of access to the required equipment. The Ti precursor, TiO_2, was decorated using a process designed to yield a 1 nm-thick layer onto the A-CNT arrays *via* atomic layer deposition (ALD). Development of a plasma pretreatment to improve TiO_2 deposition was begun, but was placed on hold for future work, as this pretreatment was shown to be unnecessary for ~100 µm A-CNT arrays. Once decorated with TiO_2, the A-CNT arrays were placed in a tube furnace at 700°C–1000°C in an 80% H_2 and 20% Ar atmosphere, where the TiO_2 coating was expected to reduce to a TiH_2 coating, which would subsequently be decomposed to a Ti coating either immediately before or during the Al infusion step. Future work will complete the development of this process. The remainder of this chapter presents a summary of contributions made by this thesis (Section 7.1) followed by future work (Section 7.2).

7.1 Summary of Thesis Contributions

Two key contributions were made through the work in this thesis and are summarized below.

Water Desorption and Resin Dilution Procedures for High-Hardness A/C-NCs

This thesis aims to increase the hardness of A/C-NCs by increasing the v_f of A-CNT nanoreinforcements in the carbon matrix. However, P-F resin infusion becomes more challenging with increasing A-CNT v_f because the inter-CNT spacing decreases, which may result in poor resin infusion and lead to a compliant and porous NC. Thus, this work developed two methods that, when used together, result in higher v_f A/C-NCs with improved hardness. First, the desorption of the a ~ 5 nm of water layer on the surface of as-grown A-CNTs was implemented, which was found to improve resin infusion. Literature shows that water desorbs at temperatures above 260°C, but significantly higher temperatures were found to remove amorphous carbon from the A-CNT outer walls, which also inhibited wetting. For this reason, A-CNTs were held at 280°C for 6 hours under vacuum to ensure the desorption of all water. This water desorption step necessitated a few other changes to the baseline procedure, including the shift to a steel mold for A-PNC synthesis to accommodate the higher temperatures required by the desorption process. Additionally, beginning with the water desorption step, all A/C-NC process steps occurred in an N_2-filled glovebox to ensure that water would not readsorb onto the A-CNTs. The final process change was to adjust the resin formulation. The original degassed resin (75–80 wt% resin) was found to infuse poorly into the desorbed A-CNTs. Thus, new resin formulations with different solvent to resin ratios (60 wt% as-received resin, 50 wt% resin, and 10 wt% resin) and different processing recipes were infused into the A-CNT arrays. Once complete, the A/C-NCs were evaluated both qualitatively *via* X-ray micro-computed tomography (µCT) imaging, and quantitatively based on the Vickers hardness test. The 50 wt% resin formulation was determined to be most promising, as this resin suc-

cessfully infused into the 5% v_f A-CNT array for a hardness improvement of ~10%. Although the complete test matrix was not completed, the evaluated processes provided direction towards the development of a second-generation reinfusion process which yielded specimens that were untested, but appeared to have a higher degree of infusion when imaged with the X-ray μCT.

A-CNT Surface Modification for Molten Al Infusion

In addition to the work with A/C-NCs, this thesis also aims to improve synthesis techniques to fabricate A/Al-NCs with ~100 μm-tall A-CNTs. A TiO_2 coating was investigated and successfully deposited on 100 μm-tall A-CNTs using TDMAT and H_2O. Progress was made on a reduction process to produce a TiH_2 coating from the decorated TiO_2. This process was determined to be promising because the TiH_2 will keep the coating from oxidizing and will easily decompose to Ti prior to or during Al matrix infusion. Molten Al wetting of a titanium flat film deposited via electron beam (e-beam) suggests that the Ti-x decorations are a promising route towards A/Al-NCs. Development also began on a plasma pretreatment process to improve penetration depth of the TiO_2 coating decorated *via* ALD for use on mm-scale A-CNT arrays such that the process can be scaled up in the future.

7.2 Recommendations for Future Work

Although this thesis progresses towards achieving high-hardness A/C-NCs and taller A/Al-NCs, there is still research required to refine these processes.

7.2.1 A/C-NC Recommendations

For A/C-NCs to reach specific hardnesses comparable to diamond, A-CNT infusion must be further improved to reduce nanoscale porosity. The following areas of research have been identified to reach these predicted hardnesses:

- Confirm that the 50 wt% resin is ideal for resin infusion by repeating these findings and testing similar (*e.g.* 40 wt% resin) formulations.

- Test various resin formulations for reinfusions during the degassing/infusion phase of A-PNC synthesis to determine if the initial formulation has the best infusion throughout the degassing phase (*e.g.*, begin infusion with 50 wt% resin but add 10 wt% resin during infusion to aid in filling voids).

- Increase the length of the degassing/infusion phase of A-PNC synthesis to determine if a longer degassing/infusion time results in improved infusion.

- Compare the current process to a process in which the A-CNTs are first infused with resin and then densified prior to cure to determine the most effective process.

- Test samples fabricated *via* the reinfusion process with four reinfusions (*i.e.*, four polymer infiltration and pyrolysis cycles). Due to rapid lab shutdown, these samples were fabricated and imaged with the X-ray µCT, but not tested. Future work should confirm the hardness of these samples and the repeatability of this process.

- Perform confirming studies, such as thermogravimetric analysis (TGA) and/or He picnometry, to determine the nano-scale void vol%.

- Investigate the effects of decreasing inter-CNT spacing on resin infusion and resin cross-linking to determine the maximum viable v_f of A-CNTs in the carbon matrix.

Through these trials, A-PNC infusion can be improved, thus decreasing the nanoscale void content towards increasing the hardness of the A/C-NCs. Once improved infusion has been achieved on this scale, future work should explore ways to scale this process for industrial-scale applications.

7.2.2   A/Al-NC Recommendations

Significant progress was made in developing 100 µm-scale A/Al-NCs, but the development of this process highlighted future research areas necessary to successfully

synthesize A/Al-NCs both at this scale and towards mm- and bulk-scale A/Al-NCs.

100 μm-Scale A/Al-NCs

First, the following areas of research have been identified to successfully fabricate ~100 μm-tall A/Al-NCs.

- The reduction process must be refined such that the TiO_2 coating is reduced to TiH_2. This will likely include a longer reduction time and the continuation of H_2 flow as the furnace cools down. Once refined, the results should be confirmed on TiO_2 powder *via* X-ray powder diffraction (XRD) and on the A-CNTs *via* X-ray photoelectron spectroscopy (XPS).

- Investigate the effect of molten Al on the TiH_2 coating to confirm the TiH_2 successfully decomposes during infusion.

- Investigate the effect of molten Al on the Ti coating to determine if the Al wets the Ti as expected, or if the Al alloys with the Ti given the small wt% of Ti in the composite. If the Al alloys with the Ti, effects of this alloy on the A-CNTs should be explored to determine if the Al will bond with the C to form Al_4C_3.

- Develop an infusion apparatus that allows for TiH_2 decomposition prior to or during the Al infusion, as well as constant heat and vacuum for the duration of the Al infusion (at least 30 minutes). Additionally, the apparatus may hold excess Al such that all Al_2O_3 that formed on the Al prior to the melt will rise to the surface of the NC and thus can be removed, leaving only the unavoidable oxide layer to form on the outside surface of the NC.

Millimeter-Scale A/Al-NCs

In addition to these areas of research, more work must be completed to fabricate mm-scale A/Al-NCs, including:

- Investigating the cause of variability in the plasma pretreatment process.

- Exploring other techniques for conformal decoration of the A-CNTs with Al-compatible materials such as Ti-x.

- Finishing development of a plasma pretretament process that allows for TiO_2 decoration *via* ALD of TDMAT and H_2O on the mm scale; alternatively, developing a successful ALD process for TDMAT and O_3 that allows for TiO_2 decoration on the mm scale.

- Improving the ALD conformability (penetration depth into the A-CNT array) by increasing pulse time as necessary throughout the process.

Other Work for Al-Matrix NCs

Other work to improve the specific strength and hardness of Al may include:

- Decorating the A-CNTs with Al_2O_3 or Fe_2O_3 if these compounds are easier to deposit, reduce, or wet with Al. Future work must be completed to investigate the specific processing parameters if either of these oxides are chosen.

- Not reducing the TiO_2, if Al can easily wet TiO_2 and the O_2 can diffuse through the Al as suggested in the literature.[245]

- Reducing the TiO_2 to form TiN in an N_2 environment. However, more research must be completed to determine how easily Al wets TiN before this avenue is developed.

- Using nanofibers other than A-CNTs, such as boron nitride nanotubes (BNNTs), as these nanofillers have improved wetting properties over CNTs.[247]

Appendix A

Supplementary Drawings for Process Tooling

This appendix contains descriptions and drawings for three sets of tooling: biaxial densification tooling, a mold negative for silicone molds used for baseline aligned carbon nanotube (CNT)/carbon-nanocomposite (A/C-NC) synthesis, and a two-piece steel mold used for improved A/C-NC synthesis. The first set of tooling, the biaxial densification tooling, was designed based on current tooling for biaxial densification, but was adapted to allow the aligned-CNT (A-CNT) arrays to be densified after resin infusion. The second two sets of tooling were used as molds for infusion of resin into the A-CNT arrays. The first, an acrylic a mold negative, is used to fabricate silicone molds for the baseline phenol-formaldehyde (P-F) resin infusion process. The second, a steel mold, was used directly to contain the A-CNTs during the improved P-F resin infusion process.

A.1   Biaxial Densification Tooling

In order to densify the A-CNTs to higher v_f than the as-grown 1 vol%, a biaxial densification process was used, as described in Section 4.1, using tooling described in previous work.[72] Tooling drawings included here (Figures A-1–A-11) are very similar to the tooling used in the processes described in this thesis, however, these tools have

been modified for future work as described in Section 4.4, where the 1 vol% A-CNTs would have resin infused prior to densification. Thus, these biaxial densification tools are modified to be made entirely of Teflon and include channels to allow for the release of excess resin. Tools for 5 vol% to 30 vol% A-CNT arrays are included such that this process can be compared to other processes at all v_f. Table A.1 lists the tools used for each v_f. The 2-mm Compression Rod is used for all 2-mm tall arrays, the 5 vol% to 20 vol% arrays, and the 1-mm Compression Rod is used for all 1-mm tall arrays, the 30 vol% arrays. All v_f arrays use the Compression Platform Top to hold the array in place during densification. All dimensions in the drawings are in inches for easier machining and all tools are made of Teflon. Additional tooling for higher vf (*e.g.*, 40 vol%) would follow the designs given here.

Table A.1: Table specifying which components correspond to the densification of which v_f arrays.

v_f	Compression Rods	Compression Platform
5 vol%	2 mm Compression Rod 5 v_f Compression Rod	5 v_f Compression Platform
10 vol%	2 mm Compression Rod 10 v_f Compression Rod	10 v_f Compression Platform
20 vol%	2 mm Compression Rod 20 v_f Compression Rod	20 v_f Compression Platform
30 vol%	1 mm Compression Rod 30 v_f Compression Rod	30 v_f Compression Platform

Figure A-1: Drawing of Teflon compression rod for 2 mm-tall A-CNT arrays (5 vol%–20 vol%). Dimensions in inches and scale accurate for figure on a full standard letter page.
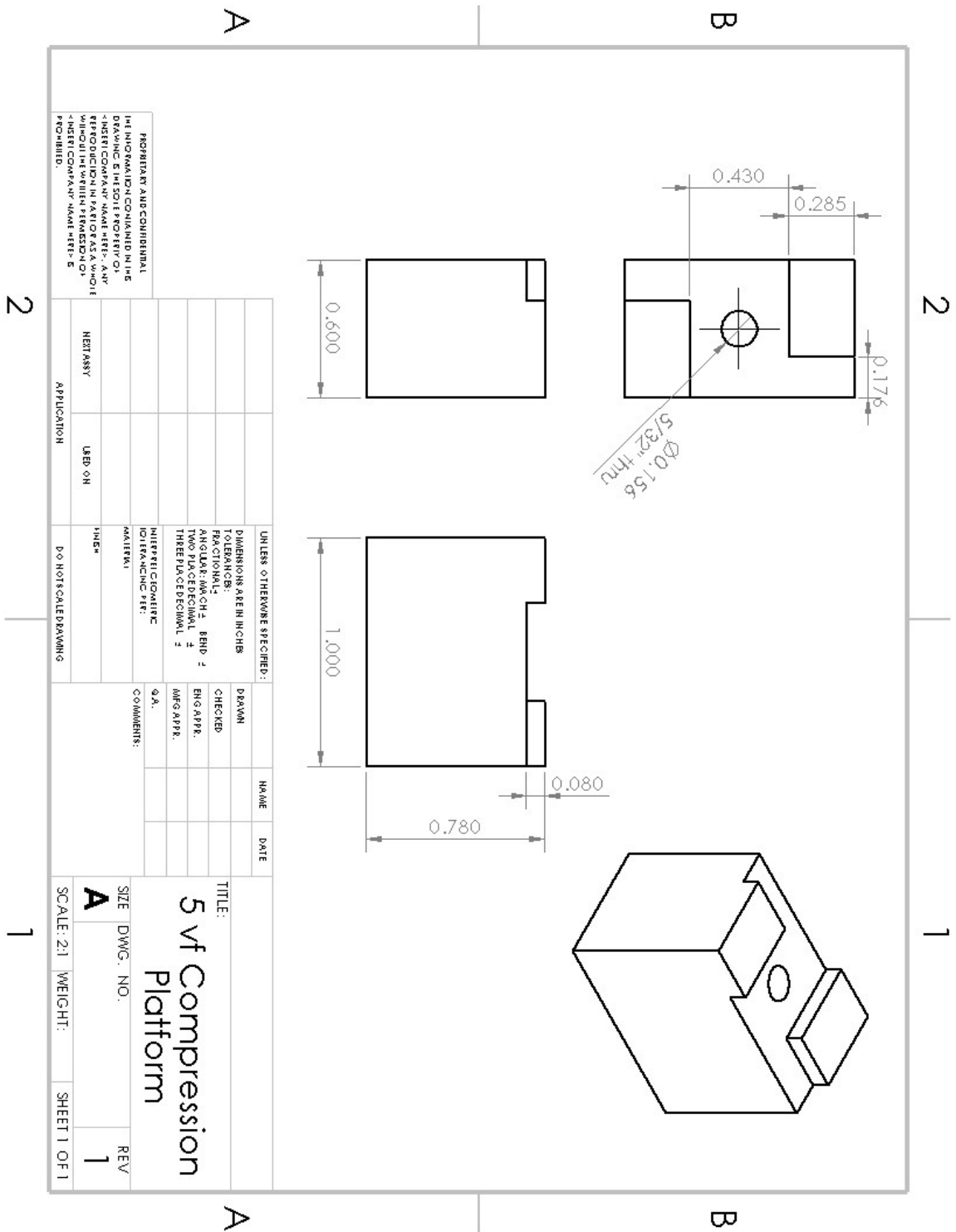
Figure A-2: Drawing of Teflon platform for compression to 5 vol% A-CNT arrays. Dimensions in inches and scale accurate for figure on a full standard letter page.
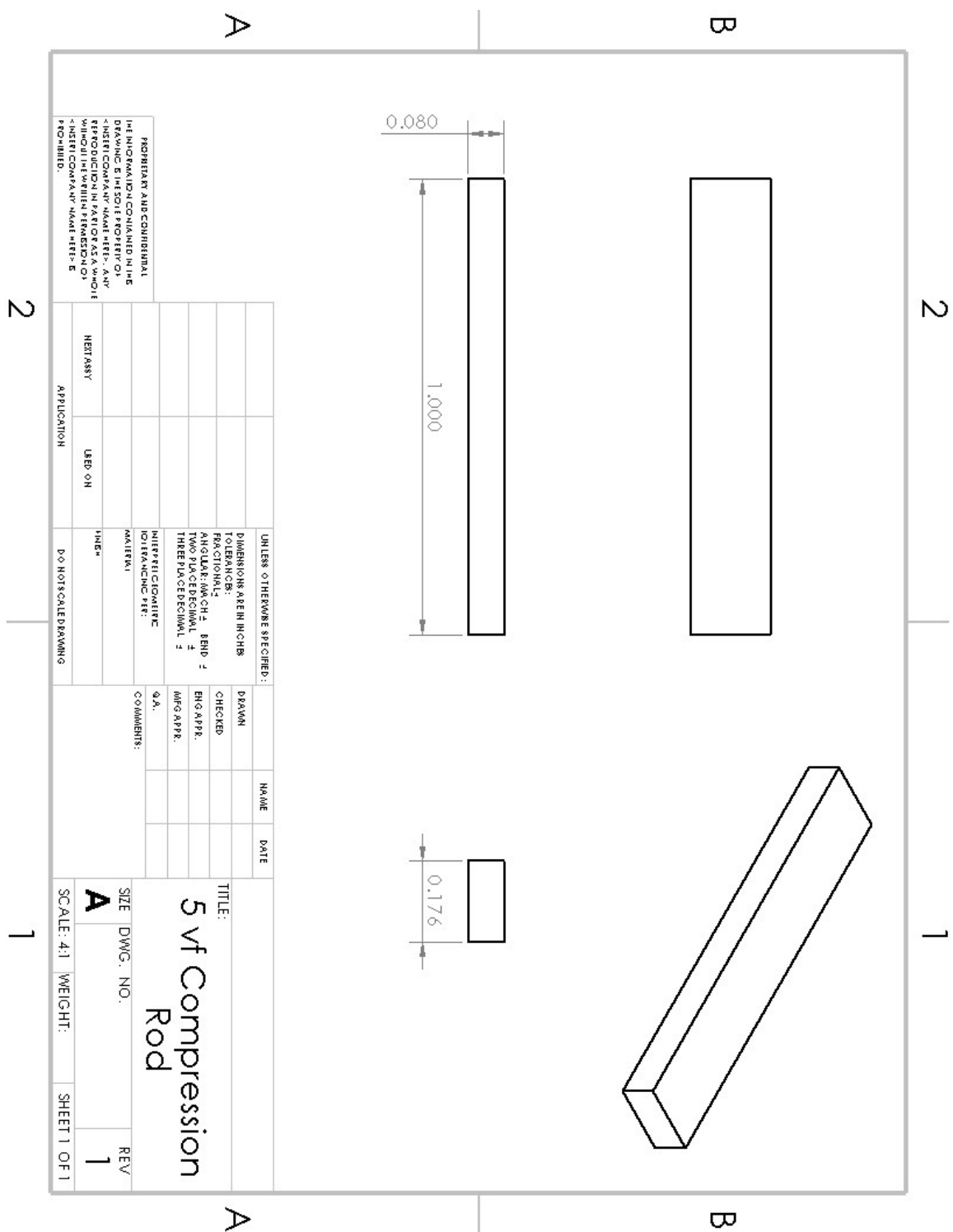
Figure A-3: Drawing of Teflon rod for compression to 5 vol% A-CNT arrays. Dimensions in inches and scale accurate for figure on a full standard letter page.

189
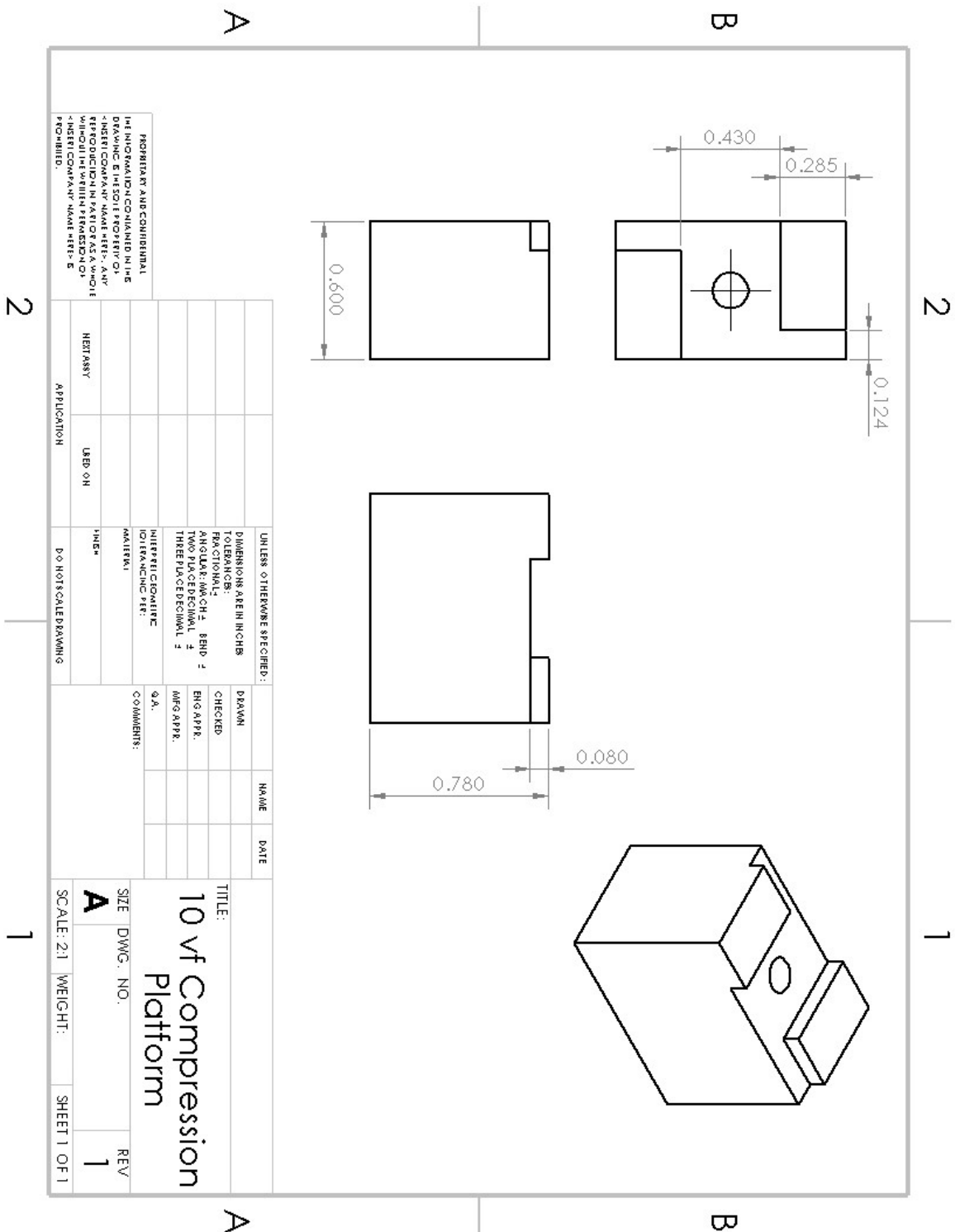
Figure A-4: Drawing of Teflon platform for compression to 10 vol% A-CNT arrays. Dimensions in inches and scale accurate for figure on a full standard letter page.

UNLESS OTHERWISE SPECIFIED:

DIMENSIONS ARE IN INCHES
TOLERANCES:
FRACTIONAL±
ANGULAR: MACH± BEND ±
TWO PLACE DECIMAL ±
THREE PLACE DECIMAL ±

INTERPRET GEOMETRIC
TOLERANCING PER:

MATERIAL

FINISH

DO NOT SCALE DRAWING

NEXT ASSY   USED ON

APPLICATION

	NAME	DATE
DRAWN		
CHECKED		
ENG APPR.		
MFG APPR.		
Q.A.		
COMMENTS:		

TITLE:

10 vf Compression Rod

SIZE A DWG. NO.   REV
1

SCALE: 4:1   WEIGHT: SHEET 1 OF 1

0.080

1.000

0.124
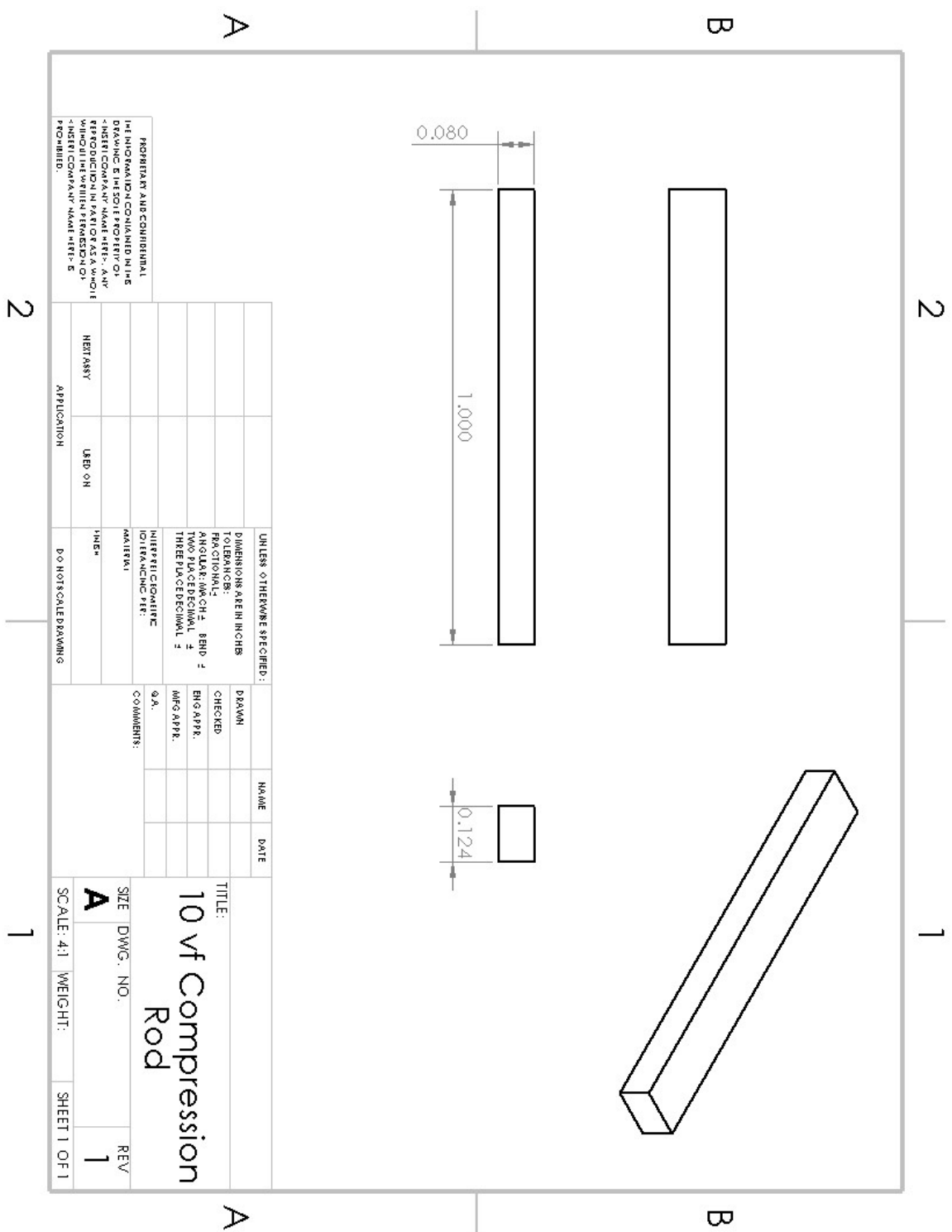
Figure A-5: Drawing of Teflon rod for compression to 10 vol% A-CNT arrays. Dimensions in inches and scale accurate for figure on a full standard letter page.

191
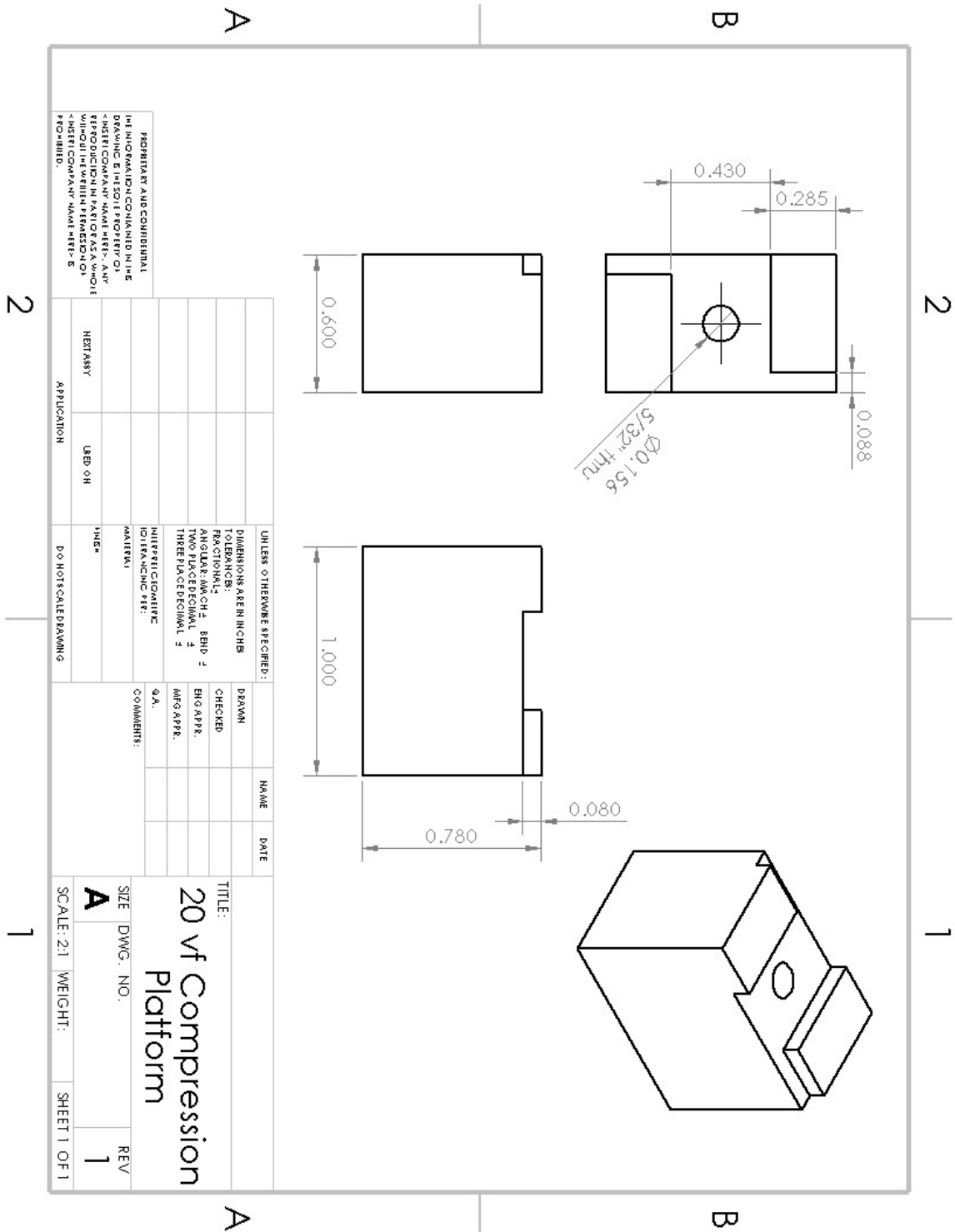
Figure A-6: Drawing of Teflon platform for compression to 20 vol% A-CNT arrays. Dimensions in inches and scale accurate for figure on a full standard letter page.

Figure A-7: Drawing of Teflon rod for compression to 20 vol% A-CNT arrays. Dimensions in inches and scale accurate for figure on a full standard letter page.

NEXT ASSY | USED ON

APPLICATION

DO NOT SCALE DRAWING

UNLESS OTHERWISE SPECIFIED:

DIMENSIONS ARE IN INCHES
TOLERANCES:
FRACTIONAL±
ANGULAR: MACH± BEND ±
TWO PLACE DECIMAL ±
THREE PLACE DECIMAL ±

INTERPRET GEOMETRIC
TOLERANCING PER:

MATERIAL

FINISH

	NAME	DATE
DRAWN		
CHECKED		
ENG APPR.		
MFG APPR.		
Q.A.		
COMMENTS:		

TITLE:

1 mm
Compression Rod

SIZE **A** | DWG. NO. | REV 1

SCALE: 2:1 | WEIGHT: | SHEET 1 OF 1

0.10 0.74 0.43

0.63

0.04

0.22

R0.02
1/32" thru

Figure A-8: Drawing of Teflon rod for compression of 1 mm-tall (30 vol%) A-CNT arrays. Dimensions in inches and scale accurate for figure on a full standard letter page.
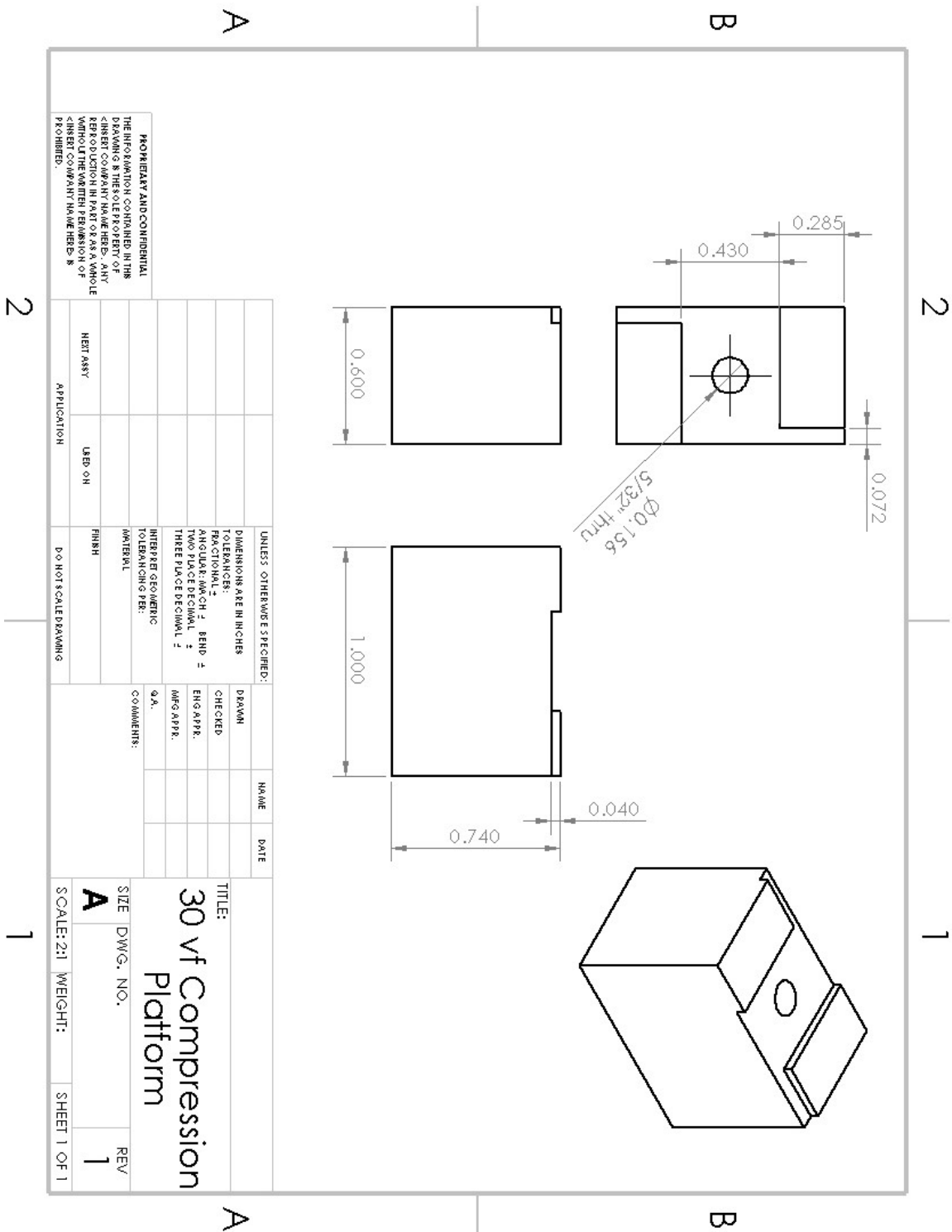
Figure A-9: Drawing of Teflon platform for compression to 30 vol% A-CNT arrays. Dimensions in inches and scale accurate for figure on a full standard letter page.
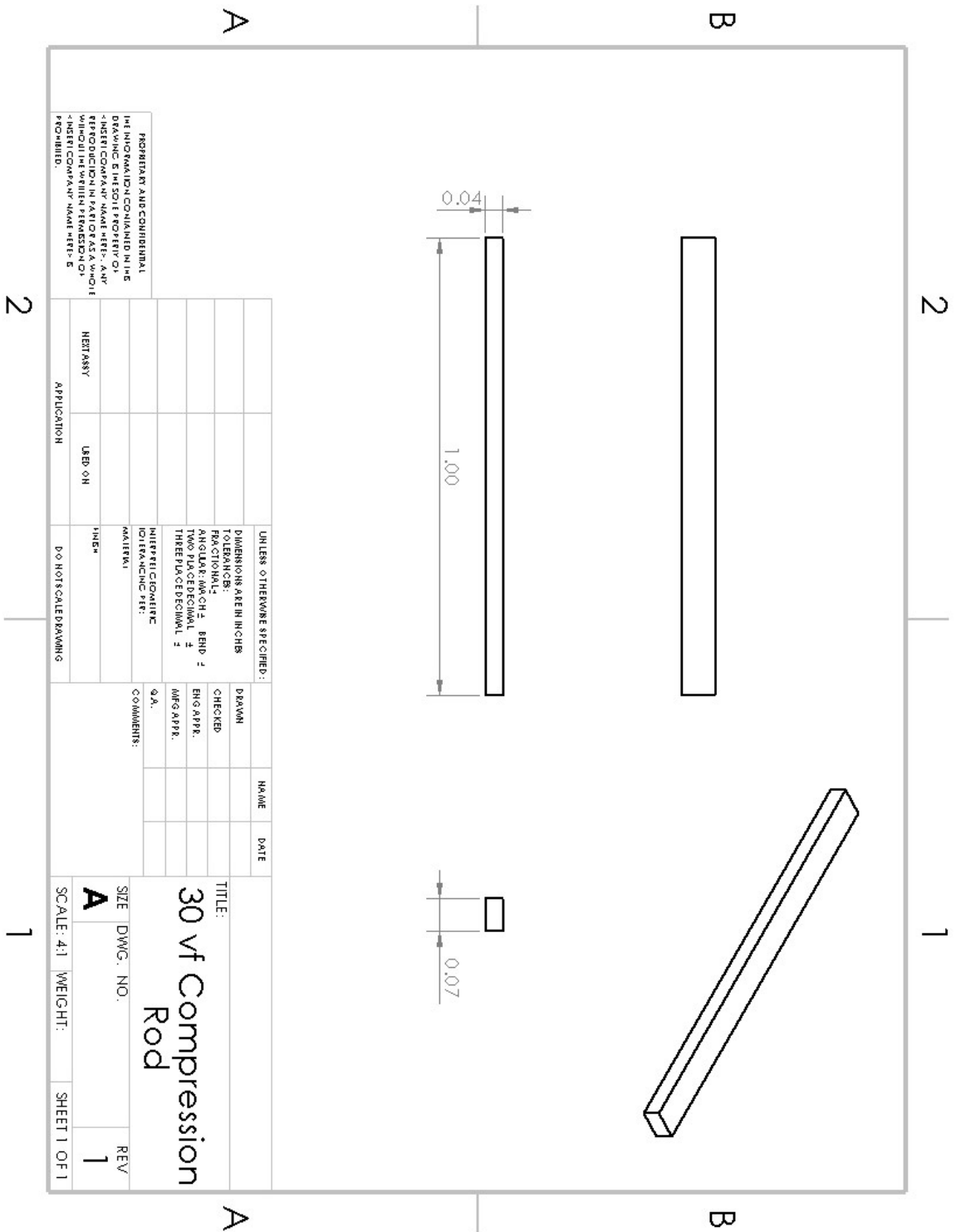
Figure A-10: Drawing of Teflon rod for compression to 30 vol% A-CNT arrays. Dimensions in inches and scale accurate for figure on a full standard letter page.
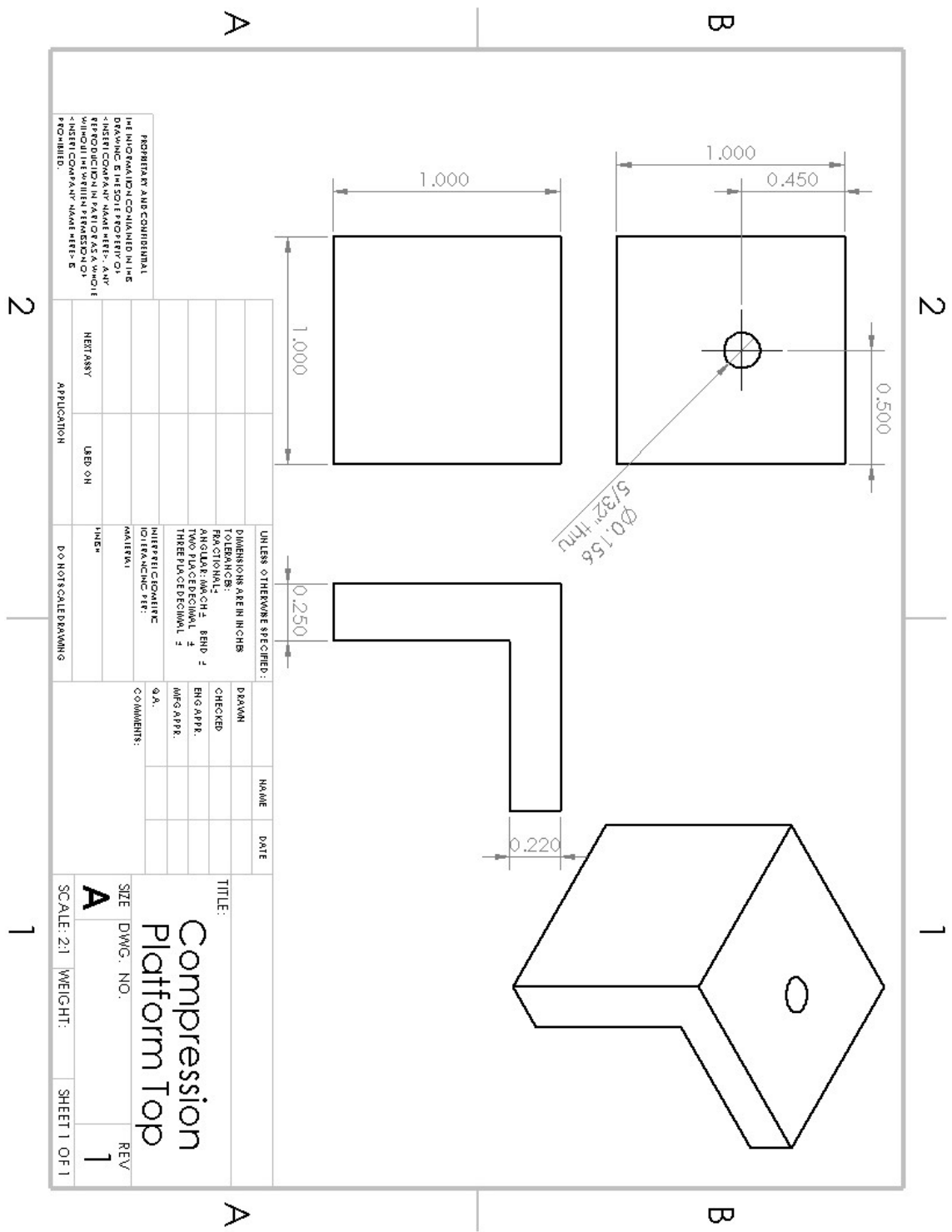
Figure A-11: Drawing of Teflon top piece used for all v_f for holding A-CNTs in compression tooling. Dimensions in inches and scale accurate for figure on a full standard letter page.

A.2 Silicone Mold

The silicone molds used for the baseline infusion process with P-F resin were fabricated by pouring silicone into an acrylic mold negative. The drawing for the mold negative, machined using the waterjet and mill, is included in Figure A-12.

Figure A-12: Drawing for the silicone mold negative, in mm. The negative is made of acrylic. 1:1 scale accurate for figure on a full standard letter page.

A.3 Steel Mold

The steel mold was designed to replace the silicone mold as part of the improved process for making A-PNCs.

The steel mold was designed in two pieces: a 321 stainless steel sheet was used for the mold itself, made with holes cut through the thickness of the material, and a 316 stainless steel strip was used as a plate, placed at the bottom of the mold. This could be sealed together using high temperature vacuum tape (Airtech International Inc., A-800-3G) for less viscous resin systems, and just placed with the mold on top of the plate for more viscous resin systems. The two-piece design was chosen both for machinability – all pieces were manufactured using the Omax Waterjet – and for ease of removing the samples from the mold. With the holes in the mold, samples can be removed from the top by pressing on the bottom. The size was driven by the size of the boat used in this process; care was taken to make the mold smaller than the quartz boat such that the mismatched coefficient of thermal expansion between the steel and the quartz boat could not cause the boat to crack. Drawings for both the mold and the plate are included in Figures A-13 and A-14 respectively.
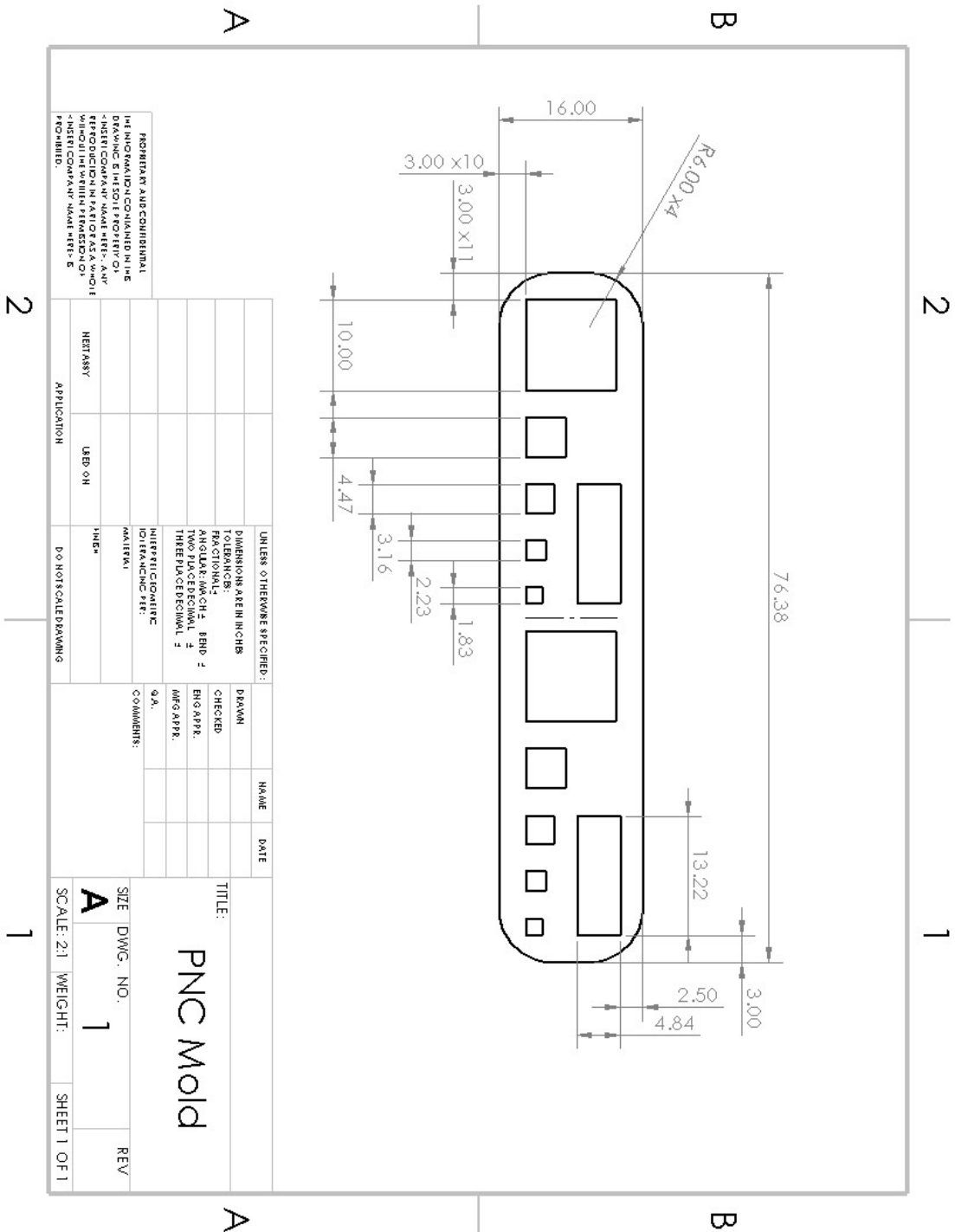
Figure A-13: Drawing for the steel mold, in mm. 2:1 scale accurate for figure on a full standard letter page.
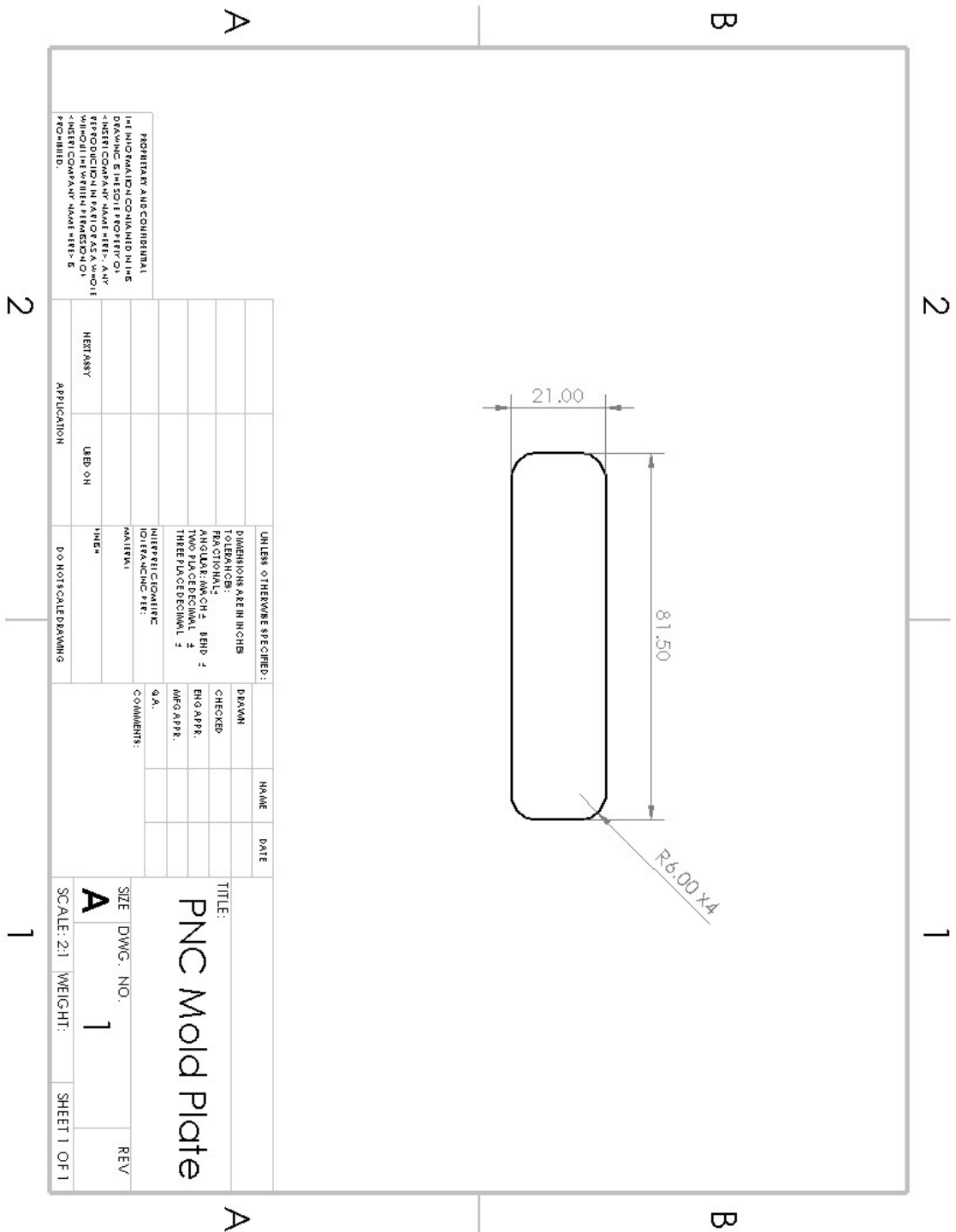
Figure A-14: Drawing for the steel mold plate, in mm. 2:1 scale accurate for figure on a full standard letter page.

Bibliography

[1] Ashley L Kaiser. Capillary Densification and Adhesion Tuning of Aligned Carbon Nanotube Arrays for Shape-Engineerable Architectures. Master's thesis, Massachusetts Institute of Technology, 2019.

[2] Qian Ming Gong, Zhi Li, Dan Li, Xiao Dong Bai, and Ji Liang. Fabrication and structure: A study of aligned carbon nanotube/carbon nanocomposites. *Solid State Communications*, 131(6):399–404, 8 2004.

[3] Konstantinos G. Dassios. A Review of the Pull-Out Mechanism in the Fracture of Brittle-Matrix Fibre-Reinforced Composites. *Advanced Composites Letters*, 16(1):096369350701600, 1 2007.

[4] Hailiang Li, Hejun Li, Jinhua Lu, Kezhi Li, Can Sun, and Dongsheng Zhang. Mechanical properties enhancement of carbon/carbon composites by in situ grown carbon nanofibers. *Materials Science and Engineering A*, 547:138–141, 2012.

[5] Z. Xia, L. Riester, W. A. Curtin, H. Li, B. W. Sheldon, J. Liang, B. Chang, and J. M. Xu. Direct observation of toughening mechanisms in carbon nanotube ceramic matrix composites. *Acta Materialia*, 52(4):931–944, 2 2004.

[6] Itai Y. Stein, Alexander J. Constable, Naomi Morales-Medina, Chlöe V. Sackier, Mackenzie E. Devoe, Hanna M. Vincent, and Brian L. Wardle. Structure-mechanical property relations of non-graphitizing pyrolytic carbon synthesized at low temperatures. *Carbon*, 117:411–420, 2017.

[7] Standard Test Method for Vickers Indentation Hardness of Advanced Ceramics. Technical report, ASTM International, West Conshohocken, 2019.

[8] Itai Y. Stein, Hanna M. Vincent, Stephen A. Steiner, Elena Colombini, and Brian L. Wardle. Processing and mechanical property characterization of aligned carbon nanotube carbon matrix nanocomposites. In *54th AIAA/ASME/ASCE/AHS/ASC Structures, Structural Dynamics, and Materials Conference*, Boston, 2013. AIAA.

[9] J. W. An, D. H. You, and D. S. Lim. Tribological properties of hot-pressed alumina-CNT composites. *Wear*, 255(1-6):677–681, 8 2003.

[10] W A Zisman. Relation of the Equilibrium Contact Angle to Liquid and Solid Constitution. In *Advances in Chemistry*. Americna Chemical Society, Washington, D. C., 1964.

[11] Joshua Pelleg. Mechanical properties of materials. *Solid Mechanics and its Applications*, 190:195–257, 2013.

[12] B. Chen, J. Shen, X. Ye, H. Imai, J. Umeda, M. Takahashi, and K. Kondoh. Solid-state interfacial reaction and load transfer efficiency in carbon nanotubes (CNTs)-reinforced aluminum matrix composites. *Carbon*, 114:198–208, 4 2017.

[13] Xin Zhang, Shufeng Li, Bo Pan, Deng Pan, Shengyin Zhou, Shenghui Yang, Lei Jia, and Katsuyoshi Kondoh. A novel strengthening effect of in-situ nano Al2O3w on CNTs reinforced aluminum matrix nanocomposites and the matched strengthening mechanisms. *Journal of Alloys and Compounds*, 764:279–288, 10 2018.

[14] Brian L. Wardle, Diego S. Saito, Enrique J. García, A. John Hart, Roberto Guzmán de Villoria, and Eric A. Verploegen. Fabrication and Characterization of Ultrahigh-Volume- Fraction Aligned Carbon Nanotube-Polymer Composites. *Advanced Materials*, 20(14):2707–2714, 7 2008.

[15] ZEISS Xradia 610 and 620 Versa.

[16] H. Wang, R. C. Reed, J. C. Gebelin, and N. Warnken. On the modelling of the point defects in the ordered B2 phase of the Ti-Al system: Combining CALPHAD with first-principles calculations. *Calphad: Computer Coupling of Phase Diagrams and Thermochemistry*, 39:21–26, 12 2012.

[17] Jean Claude Viala, Christiane Vincent, Henri Vincent, and Jean Bouix. Approche thermodynamique de l'interaction chimique entre l'aluminium et le carbure de titane. *Materials Research Bulletin*, 25(4):457–464, 4 1990.

[18] Jeffrey L. Gair. *Nanotube-Matrix Interplay and Tunability in Ultrahigh Volume-Fraction Aligned Carbon Nanotube Poly(Urethane-Urea) Nanocomposites*. PhD thesis, University of Maryland - College Park, 2017.

[19] Luv Gurnani and Amartya Mukhopadhyay. Development of Carbon Nanotube-Reinforced Ceramic Matrix Nanocomposites for Advanced Structural Applications. In *Handbook of Advanced Ceramics and Composites*, pages 1–46. Springer International Publishing, 2019.

[20] Michael F.L. De Volder, Sameh H. Tawfick, Ray H. Baughman, and A. John Hart. Carbon nanotubes: Present and future commercial applications. *Science*, 339(6119):535–539, 2 2013.

[21] Min Feng Yu, Oleg Lourie, Mark J. Dyer, Katerina Moloni, Thomas F. Kelly, and Rodney S. Ruoff. Strength and breaking mechanism of multiwalled carbon nanotubes under tensile load. *Science*, 287(5453):637–640, 1 2000.

[22] Min-Feng Yu, Bradley S Files, Sivaram Arepalli, and Rodney S Ruoff. Tensile Loading of Ropes of Single Wall Carbon Nanotubes and their Mechanical Properties. *Physical Review Letters*, 84(24):5552–5555, 2000.

[23] M. M.J. Treacy, T. W. Ebbesen, and J. M. Gibson. Exceptionally high Young's modulus observed for individual carbon nanotubes. *Nature*, 381(6584):678–680, 1996.

[24] Ling Zhang, Guang Zhang, Changhong Liu, and Shoushan Fan. High-density carbon nanotube buckypapers with superior transport and mechanical properties. *Nano Letters*, 12(9):4848–4852, 9 2012.

[25] Jeonyoon Lee, Itai Y. Stein, Mackenzie E. Devoe, Diana J. Lewis, Noa Lachman, Seth S. Kessler, Samuel T. Buschhorn, and Brian L. Wardle. Impact of carbon nanotube length on electron transport in aligned carbon nanotube networks. *Applied Physics Letters*, 106(5), 2 2015.

[26] Amy M Marconnet, Namiko Yamamoto, Matthew A Panzer, Brian L Wardle, and Kenneth E Goodson. Thermal Conduction in Aligned Carbon Nanotube Polymer Nanocomposites with High Packing Density. *ACS Nano*, 19:17, 2020.

[27] Juli Robinson and Kirt Costello, editors. *International Space Station Benefits for Humanity*. 3 edition, 6 2018.

[28] Ray H. Baughman, Anvar A. Zakhidov, and Wait A. De Heer. Carbon nanotubes - The route toward applications. *Science*, 297(5582):787–792, 8 2002.

[29] Kang Pyo So, Di Chen, Akihiro Kushima, Mingda Li, Sangtae Kim, Yang Yang, Ziqiang Wang, Jong Gil Park, Young Hee Lee, Rafael I. Gonzalez, Miguel Kiwi, Eduardo M. Bringa, Lin Shao, and Ju Li. Dispersion of carbon nanotubes in aluminum improves radiation resistance. *Nano Energy*, 22:319–327, 4 2016.

[30] E Fitzer and L M Manocha. Applications of Carbon/Carbon Composites. In *Carbon Reinforcements and Carbon/Carbon Composites*, pages 310–335. Springer-Verlag Berlin Heidelberg, Berlin, 1998.

[31] Torsten Windhorst and Gordon Blount. Carbon-carbon composites: A summary of recent developments and applications. *Materials and Design*, 18(1):11–15, 2 1997.

[32] Walter Krenkel. Carbon/Carbons and Their Industrial Applications. In *Ceramic Matrix Composites: Fiber Reinforced Ceramics and their Applications*, chapter 4. John Wiley and Sons, 2008.

[33] B. L. Wardle, J. Koo, G. M. Odegard, and G. D. Seidel. Chapter 4: Advanced Nanoengineered Materials. In B. N. Bhat, editor, *Aerospace Materials and Applications*, chapter 4. AIAA Education Series, 2018.

[34] Zhiqiang Lin, Zhiping Zeng, Xuchun Gui, Zikang Tang, Mingchu Zou, and Anyuan Cao. Carbon Nanotube Sponges, Aerogels, and Hierarchical Composites: Synthesis, Properties, and Energy Applications. *Advanced Energy Materials*, 6(17):1600554, 9 2016.

[35] Luqi Liu, Wenjun Ma, and Zhong Zhang. Macroscopic Carbon Nanotube Assemblies: Preparation, Properties, and Potential Applications. *Small*, 7(11):1504–1520, 6 2011.

[36] Yue Zhou, Xiaoxue Wang, Luiz Acauan, Estelle Kalfon-Cohen, Xinchen Ni, Yosef Stein, Karen K Gleason, Brian L Wardle, Y Zhou, L Acauan, E Kalfon-Cohen, B L Wardle, X Wang, K K Gleason, X Ni, and Y Stein. Ultrahigh-Areal-Capacitance Flexible Supercapacitor Electrodes Enabled by Conformal P3MT on Horizontally Aligned Carbon-Nanotube Arrays. *Advanced Materials*, 31(30), 2019.

[37] Jonathan N. Coleman, Umar Khan, Werner J. Blau, and Yurii K. Gun'ko. Small but strong: A review of the mechanical properties of carbon nanotube-polymer composites. *Carbon*, 44(9):1624–1652, 8 2006.

[38] Farhad Saba, Seyed Abdolkarim Sajjadi, Mohsen Haddad-Sabzevar, and Faming Zhang. Formation mechanism of nano titanium carbide on multi-walled carbon nanotube and influence of the nanocarbides on the load-bearing contribution of the nanotubes inner-walls in aluminum-matrix composites. *Carbon*, 115:720–729, 5 2017.

[39] Erik T. Thostenson, Zhifeng Ren, and Tsu Wei Chou. Advances in the science and technology of carbon nanotubes and their composites: A review. *Composites Science and Technology*, 61(13):1899–1912, 10 2001.

[40] P. Kim, L. Shi, A. Majumdar, and P. L. McEuen. Thermal Transport Measurements of Individual Multiwalled Nanotubes. *Physical Review Letters*, 87(21):215502, 10 2001.

[41] Yunxiang Bai, Rufan Zhang, Xuan Ye, Zhenxing Zhu, Huanhuan Xie, Boyuan Shen, Dali Cai, Bofei Liu, Chenxi Zhang, Zhao Jia, Shenli Zhang, Xide Li, and Fei Wei. Carbon nanotube bundles with tensile strength over 80 GPa. *Nature Nanotechnology*, 13(7):589–595, 7 2018.

[42] Robert O. Ritchie. The conflicts between strength and toughness. *Nature Materials*, 10(11):817–822, 2011.

[43] Ulrike G.K. Wegst, Hao Bai, Eduardo Saiz, Antoni P. Tomsia, and Robert O. Ritchie. Bioinspired structural materials. *Nature Materials*, 14(1):23–36, 2015.

[44] Johann Cho and Aldo R. Boccaccini. Ceramic and glass matrix composites containing carbon nanotubes. *Materials Science Forum*, 606:61–77, 2009.

[45] Hulya Cebeci, Roberto Guzman De Villoria, Brian L. Wardle, Diego S. Saito, Namiko Yamamoto, Kyoko Ishiguro, Enrique J. Garcia, A. John Hart, and Sunny Wicks. Processing of hybrid advanced composites utilizing capillarity-driven wetting of aligned carbon nanotubes. In *International SAMPE Technical Conference*, 2008.

[46] Anyuan Cao, Pamela L. Dickrell, W. Gregory Sawyer, Mehrdad N. Ghasemi-Nejhad, and Pulickel M. Ajayan. Materials science: Super-compressible foam-like carbon nanotube films. *Science*, 310(5752):1307–1310, 11 2005.

[47] Hao Liu, Yong Zhang, David Arato, Ruying Li, Philippe Mérel, and Xueliang Sun. Aligned multi-walled carbon nanotubes on different substrates by floating catalyst chemical vapor deposition: Critical effects of buffer layer. *Surface and Coatings Technology*, 202(17):4114–4120, 5 2008.

[48] Bing Yu, Chang Liu, Peng Xiang Hou, Ying Tian, Shisheng Li, Bilu Liu, Feng Li, Esko I. Kauppinen, and Hui Ming Cheng. Bulk synthesis of large diameter semiconducting single-walled carbon nanotubes by oxygen-assisted floating catalyst chemical vapor deposition. *Journal of the American Chemical Society*, 133(14):5232–5235, 3 2011.

[49] Toshiya Kinoshita, Motoyuki Karita, Takayuki Nakano, and Yoku Inoue. Two step floating catalyst chemical vapor deposition including in situ fabrication of catalyst nanoparticles and carbon nanotube forest growth with low impurity level. *Carbon*, 144:152–160, 4 2019.

[50] Rufan Zhang, Huanhuan Xie, Yingying Zhang, Qiang Zhang, Yuguang Jin, Peng Li, Weizhong Qian, and Fei Wei. The reason for the low density of horizontally aligned ultralong carbon nanotube arrays. *Carbon*, 52:232–238, 2 2013.

[51] Shaoming Huang, Mike Woodson, Richard Smalley, and Jie Liu. Growth mechanism of oriented long single walled carbon nanotubes using "fast-heating" chemical vapor deposition process. *Nano Letters*, 4(6):1025–1028, 6 2004.

[52] Xueshen Wang, Qunqing Li, Jing Xie, Zhong Jin, Jinyong Wang, Yan Li, Kaili Jiang, and Shoushan Fan. Fabrication of ultralong and electrically uniform single-walled carbon nanotubes on clean substrates. *Nano Letters*, 9(9):3137–3141, 9 2009.

[53] Shuangwen Li, Yiyu Feng, Yali Li, Wei Feng, and Katsumi Yoshino. Transparent and flexible films of horizontally aligned carbon nanotube/polyimide composites with highly anisotropic mechanical, thermal, and electrical properties. *Carbon*, 109:131–140, 11 2016.

[54] Chengzhi Luo, Qiang Fu, and Chunxu Pan. Strong magnetic field-assisted growth of carbon nanofibers and its microstructural transformation mechanism. *Scientific Reports*, 5(1):1–6, 3 2015.

[55] Ant Ural, Yiming Li, and Hongjie Dai. Electric-field-aligned growth of single-walled carbon nanotubes on surfaces. *Applied Physics Letters*, 81(18):3466, 10 2002.

[56] Yuegang Zhang, Aileen Chang, Jien Cao, Qian Wang, Woong Kim, Yiming Li, Nathan Morris, Erhan Yenilmez, Jing Kong, and Hongjie Dai. Electric-field-directed growth of aligned single-walled carbon nanotubes. *Applied Physics Letters*, 79(19):3157, 11 2001.

[57] Erin Camponeschi, Richard Vance, Marwan Al-Haik, Hamid Garmestani, and Rina Tannenbaum. Properties of carbon nanotube-polymer composites aligned in a magnetic field. *Carbon*, 45(10):2037–2046, 9 2007.

[58] E S Choi, J S Brooks, D L Eaton, M S Al-Haik, M Y Hussaini, H Garmestani, D Li, and K Dahmen. Enhancement of thermal and electrical properties of carbon nanotube polymer composites by magnetic field processing. *Journal of Applied Physics*, 94:6034, 2003.

[59] T. Kimura, H. Ago, M. Tobita, S. Ohshima, M. Kyotani, and M. Yumura. Polymer Composites of Carbon Nanotubes Aligned by a Magnetic Field. *Advanced Materials*, 14(19):1380–1383, 10 2002.

[60] Pallavi Gupta, Mohit Rajput, Nikhil Singla, Vijayesh Kumar, and Debrupa Lahiri. Electric field and current assisted alignment of CNT inside polymer matrix and its effects on electrical and mechanical properties. *Polymer*, 89:119–127, 4 2016.

[61] Prashant V. Kamat, K. George Thomas, Said Barazzouk, G. Girishkumar, K. Vinodgopal, and Dan Meisel. Self-assembled linear bundles of single wall carbon nanotubes and their alignment and deposition as a film in a dc field. *Journal of the American Chemical Society*, 126(34):10757–10762, 9 2004.

[62] X Q Chen, T Saito, H Yamada, and K Matsushige. Aligning single-wall carbon nanotubes with an alternating-current electric field. *Appl. Phys. Lett*, 78(23):3716, 6 2001.

[63] Maxim V Gorshkov, Alyona S Moskalenko, and Marina V Shcherbak. Alternating electric field effect on the alignment of carbon nanotubes during the dielectrophoresis process. In *AIP Conference Proceedings*, 2018.

[64] Hyunhyub Ko, Sergiy Peleshanko, and Vladimir V. Tsukruk. Combing and Bending of Carbon Nanotube Arrays with Confined Microfluidic Flow on Patterned Surfaces. *Journal of Physical Chemistry B*, 108(14):4385–4393, 4 2004.

[65] Pilnam Kim, Seunghyun Baik, and Kahp Y. Suh. Capillarity-Driven Fluidic Alignment of Single-Walled Carbon Nanotubes in Reversibly Bonded Nanochannels. *Small*, 4(1):92–95, 1 2008.

[66] James Hedberg, Lifeng Dong, and Jun Jiao. Air flow technique for large scale dispersion and alignment of carbon nanotubes on various substrates. *Applied Physics Letters*, 86(14):1–3, 4 2005.

[67] Yanfeng Ma, Bin Wang, Yingpeng Wu, Yi Huang, and Yongsheng Chen. The production of horizontally aligned single-walled carbon nanotubes, 11 2011.

[68] E. J. García, A. J. Hart, B. L. Wardle, and A. H. Slocum. Fabrication of composite microstructures by capillarity-driven wetting of aligned carbon nanotubes with polymers. *Nanotechnology*, 18(16), 2007.

[69] Masud Rana and M. R.Mohd Asyraf. Investigation and development of vertically aligned carbon nanotube (VACNT) forest based temperature sensor. *Microelectronic Engineering*, 162:93–95, 8 2016.

[70] Fabian Pawlitzek, Jonas Pampel, Martin Schmuck, Holger Althues, Benjamin Schumm, and Stefan Kaskel. High-power lithium ion batteries based on preorganized necklace type Li4Ti5O12/VACNT nano-composites. *Journal of Power Sources*, 325:1–6, 9 2016.

[71] Itai Y. Stein and Brian L. Wardle. Coordination number model to quantify packing morphology of aligned nanowire arrays. *Physical Chemistry Chemical Physics*, 15(11):4033–4040, 2013.

[72] Jeffrey L Gair, Robert H Lambeth, Daniel P Cole, Dale L Lidston, Itai Y Stein, Estelle Kalfon-Cohen, Alex J Hsieh, Hugh A Bruck, Mark L Bundy, and Brian L Wardle. Strong process-structure interaction in stoveable poly(urethane-urea) aligned carbon nanotube nanocomposites. *Composites Science and Technology*, 166:115–124, 3 2018.

[73] Bharath Natarajan, Itai Y Stein, Noa Lachman, Namiko Yamamoto, Douglas S Jacobs, Renu Sharma, J Alexander Liddle, and Brian L. Wardle. Aligned carbon nanotube morphogenesis predicts physical properties of their polymer nanocomposites. *Nanoscale*, 11:16327, 6 2019.

[74] Jeonyoon Lee, Xinchen Ni, Frederick Daso, Xianghui Xiao, Dale King, Jose S Anchez G Omez E, Tamara Blanco Varela, Seth S Kessler, and Brian L Wardle. Advanced carbon fiber composite out-of-autoclave laminate manufacture via nanostructured out-of-oven conductive curing. *Composites Science and Technology*, 166:150–159, 2018.

[75] Xinchen Ni, Carolina Furtado, Estelle Kalfon-Cohen, Yue Zhou, Gabriel A Valdes, Travis J Hank, Pedro P Camanho, and Brian L Wardle. Static and fatigue interlaminar shear reinforcement in aligned carbon nanotube-reinforced hierarchical advanced composites. *Composites Part A*, 120:106–115, 2019.

[76] Elsa Reichmanis, Curtis W Frank, James H O'donnell, and David J T Hill. Radiation Effects on Polymeric Materials A Brief Overview. In Elsa Reichmanis,

Curtis W Frank, James H O'donnell, and David J T Hill, editors, *Irradiation of Polymeric Materials*, chapter Radiation, pages 1–8. American Chemical Society, Washington, D.C., 1993.

[77] Itai Y. Stein, Noa Lachman, MacKenzie E. Devoe, and Brian L. Wardle. Exohedral physisorption of ambient moisture scales non-monotonically with fiber proximity in aligned carbon nanotube arrays. *ACS Nano*, 8(5):4591–4599, 2014.

[78] Itai Y Stein. *Impact of Morphology and Confinement Effects on the Properties of Aligned Nanofiber Architectures*. PhD thesis, Massachusetts Institute of Technology, Cambridge, 2016.

[79] Itai Y Stein, Ashley L Kaiser, Alexander J Constable, Luiz Acauan, and Brian L Wardle. Mesoscale evolution of non-graphitizing pyrolytic carbon in aligned carbon nanotube carbon matrix nanocomposites. *Journal of Materials Science*, 52:13799–13811, 2017.

[80] Itai Y. Stein and Brian L. Wardle. Morphology and processing of aligned carbon nanotube carbon matrix nanocomposites. *Carbon*, 68:807–813, 2014.

[81] Saswati Pujari, Thillaiyan Ramanathan, Kosmas Kasimatis, Jun'ichi Masuda, Rodney Andrews, John M. Torkelson, L. Catherine Brinson, and Wesley R. Burghardt. Preparation and characterization of multiwalled carbon nanotube dispersions in polypropylene: Melt mixing versus solid-state shear pulverization. *Journal of Polymer Science Part B: Polymer Physics*, 47(14):1426–1436, 7 2009.

[82] Jun'ichi Masuda and John M Torkelson. Dispersion and Major Property Enhancements in Polymer/Multiwall Carbon Nanotube Nanocomposites via Solid-State Shear Pulverization Followed by Melt Mixing. *Macromoleculres*, 2008.

[83] Guang Xin Chen, Yongjin Li, and Hiroshi Shimizu. Ultrahigh-shear processing for the preparation of polymer/carbon nanotube composites. *Carbon*, 45(12):2334–2340, 10 2007.

[84] S. V. Ahir, Y. Y. Huang, and E. M. Terentjev. Polymers with aligned carbon nanotubes: Active composite materials, 8 2008.

[85] Guido Pagani, Micah J. Green, Philippe Poulin, and Matteo Pasquali. Competing mechanisms and scaling laws for carbon nanotube scission by ultrasonication. *Proceedings of the National Academy of Sciences of the United States of America*, 109(29):11599–11604, 7 2012.

[86] J. Stegen. Mechanics of carbon nanotube scission under sonication. *Journal of Chemical Physics*, 140(24):244908, 6 2014.

[87] Carlo A. Amadei, Itai Y. Stein, Gregory J. Silverberg, Brian L. Wardle, and Chad D. Vecitis. Fabrication and morphology tuning of graphene oxide nanoscrolls. *Nanoscale*, 8(12):6783–6791, 3 2016.

210

[88] Yan Yan Huang and Eugene M. Terentjev. Dispersion of carbon nanotubes: Mixing, sonication, stabilization, and composite properties, 2012.

[89] Richard Li, Noa Lachman, Peter Florin, H. Daniel Wagner, and Brian L. Wardle. Hierarchical carbon nanotube carbon fiber unidirectional composites with preserved tensile and interfacial properties. *Composites Science and Technology*, 117:139–145, 9 2015.

[90] S.S. Wicks, D. Lidston, S. Kalamoun, R. Guzman deVilloria, and B.L. Wardle. Vacuum Assisted Infusion of Hybrid Aligned Carbon Nanotube-Fiber Composites for Mechanical Reinforcement. In *18th International Conference on Composite Materials*, 2010.

[91] Noa Lachman, Itai Y. Stein, Asli Ugur, Dale L. Lidston, Karen K. Gleason, and Brian L. Wardle. Synthesis of polymer bead nano-necklaces on aligned carbon nanotube scaffolds. *Nanotechnology*, 28(24):24LT01, 2017.

[92] Xiaoxue Wang, Asli Ugur, Hilal Goktas, Nan Chen, Minghui Wang, Noa Lachman, Estelle Kalfon-Cohen, Wenjing Fang, Brian L. Wardle, and Karen K. Gleason. Room Temperature Resistive Volatile Organic Compound Sensing Materials Based on a Hybrid Structure of Vertically Aligned Carbon Nanotubes and Conformal oCVD/iCVD Polymer Coatings. *ACS Sensors*, 1(4):374–383, 4 2016.

[93] Kyu Hun Kim, Youngseok Oh, and M. F. Islam. Graphene coating makes carbon nanotube aerogels superelastic and resistant to fatigue. *Nature Nanotechnology*, 7(9):562–566, 7 2012.

[94] Sang Hyuk Yum, Sung Hoon Kim, Woo Il Lee, and Hansang Kim. Improvement of ablation resistance of phenolic composites reinforced with low concentrations of carbon nanotubes. *Composites Science and Technology*, 121:16–24, 2015.

[95] Ailing Feng, Zirui Jia, Qiang Yu, Hongxia Zhang, and Guanglei Wu. Preparation and Characterization of Carbon Nanotubes/Carbon Fiber/Phenolic Composites on Mechanical and Thermal Conductivity Properties. *Nano*, 13(4), 4 2018.

[96] Howard G Maahs, Craig W Ohlhorst, David M Barrett, Philip 0 Ransone, and J Wayne Sawyer. Response of carbon-carbon composites to challenging environments. In *Symposium N – Materials Stability and Environmental Degradation*, pages 15–29, 1988.

[97] Dongmei Hu, Hongyuan Chen, Zhenzhong Yong, Minghai Chen, Xiaohua Zhang, Qingwen Li, Zhen Fan, and Zhihai Feng. Enhanced Thermal Conductivity of Carbon Nanotube Arrays by Carbonizing Impregnated Phenolic Resins. *Materials Sciences and Applications*, 04(08):453–457, 7 2013.

[98] Kimberly A. Trick and Tony E. Saliba. Mechanisms of the pyrolysis of phenolic resin in a carbon/phenolic composite. *Carbon*, 33(11):1509–1515, 1995.

[99] Yuguang Jin, Yingying Zhang, Qiang Zhang, Rufan Zhang, Peng Li, Weizhong Qian, and Fei Wei. Multi-walled carbon nanotube-based carbon/carbon composites with three-dimensional network structures. *Nanoscale*, 5(13):6181–6186, 2013.

[100] Yujun Jia, Jinshan Yang, Kewei Wang, Atiqur Rahman Chowdhury, Banghao Chen, Yifeng Su, Bill C Nickerson, and Chengying Xu. Aligned carbon nanotube/carbon (CNT/C) composites with exceptionally high electrical conductivity at elevated temperature to 400 °C. *Mater. Res. Express*, 6:116302, 2019.

[101] S D Williams, M M Gietzel, W C Rochelle, and D M Curry. TPS Design for Aerobraking at Earth and Mars. Technical report, NASA, 1991.

[102] Krishan Kumar Chawla. *Ceramic Matrix Composites*. Springier Science, 2003.

[103] Jhon Paul, G. Krishnakumar, A. Rajarajan, and S. Rakesh. Development of CNT based carbon-carbon composites for thermal management system (TMS). In *AIP Conference Proceedings*, volume 1538, pages 157–162, 2013.

[104] I. Konyashin, B. Ries, D. Hlawatschek, Y. Zhuk, A. Mazilkin, B. Straumal, F. Dorn, and D. Park. Wear-resistance and hardness: Are they directly related for nanostructured hard materials? *International Journal of Refractory Metals and Hard Materials*, 49(1):203–211, 3 2015.

[105] M. A. Moore. The relationship between the abrasive wear resistance, hardness and microstructure of ferritic materials. *Wear*, 28(1):59–68, 4 1974.

[106] P. Rama Subba Reddy, S. Geasin Savio, and Vemuri Madhu. Ceramic Composite Armour for Ballistic Protection. In *Handbook of Advanced Ceramics and Composites*, pages 1–46. Springer International Publishing, 2019.

[107] Kiran Akella. Multilayered Ceramic-Composites for Armour Applications. In *Handbook of Advanced Ceramics and Composites*, pages 1–31. Springer International Publishing, 2020.

[108] Songlin Zhang, Ayou Hao, Nam Nguyen, Abiodun Oluwalowo, Zhe Liu, Yourri Dessureault, Jin Gyu Park, and Richard Liang. Carbon nanotube/carbon composite fiber with improved strength and electrical conductivity via interface engineering. *Carbon*, 144:628–638, 4 2019.

[109] Rosalind E. Franklin and J. T. Randall. Crystallite growth in graphitizing and non-graphitizing carbons. *Proceedings of the Royal Society of London. Series A. Mathematical and Physical Sciences*, 209(1097):196–218, 1951.

[110] Swati Sharma. Glassy Carbon: A promising material for microand nanomanufacturing. *Materials*, 11(10), 2018.

[111] Maziar Ghazinejad, Sunshine Holmberg, Oscar Pilloni, Laura Oropeza-Ramos, and Marc Madou. Graphitizing Non-graphitizable Carbons by Stress-induced Routes. *Scientific Reports*, 7(1):1–10, 12 2017.

[112] Peter J. F. Harris. New Perspectives on the Structure of Graphitic Carbons. *Critical Reviews in Solid State and Materials Sciences*, 30(4):235–253, 10 2005.

[113] Leslie Joy Lanticse-Diaz, Yasuhiro Tanabe, Takashi Enami, Kazumasa Nakamura, Morinobu Endo, and Eiichi Yasuda. The effect of nanotube alignment on stress graphitization of carbon/carbon nanotube composites. *Carbon*, 47(4):974–980, 2009.

[114] Itai Y Stein. *Synthesis and Characterization of Next-Generation Multifunctional Material Architectures: Aligned Carbon Nanotube Carbon Matrix Nanocomposites*. PhD thesis, Massachussetts Institute of Technology, 2013.

[115] Xiaosong Huang. Fabrication and Properties of Carbon Fibers. *Materials*, 2(4):2369–2403, 12 2009.

[116] Zhou Zhou, Xin Wang, Shaghayegh Faraji, Philip D. Bradford, Qingwen Li, and Yuntian Zhu. Mechanical and electrical properties of aligned carbon nanotube/carbon matrix composites. *Carbon*, 75:307–313, 2014.

[117] Tse Hao Ko, Wen Shyong Kuo, and Ying Huang Chang. Raman study of the microstructure changes of phenolic resin during pyrolysis. *Polymer Composites*, 21(5):745–750, 2000.

[118] Sijia Shen, Lingwei Yang, Chuanyun Wang, and Liming Wei. Effect of CNT orientation on the mechanical property and fracture mechanism of vertically aligned carbon nanotube/carbon composites. *Ceramics International*, 46:4933–4938, 2020.

[119] Xuesong Li, Lijie Ci, Swastik Kar, Caterina Soldano, Stephen J. Kilpatrick, and Pulickel M. Ajayan. Densified aligned carbon nanotube films via vapor phase infiltration of carbon. *Carbon*, 45(4):847–851, 4 2007.

[120] Liyuan Han, Kezhi Li, Jiajia Sun, Qiang Song, and Yawen Wang. Reinforcing effects of carbon nanotube on carbon/carbon composites before and after heat treatment. *Materials Science and Engineering A*, 735:10–18, 9 2018.

[121] A. Ferrari and J. Robertson. Interpretation of Raman spectra of disordered and amorphous carbon. *Physical Review B - Condensed Matter and Materials Physics*, 61(20):14095–14107, 2000.

[122] Ardavan Zandiatashbar, Gwan Hyoung Lee, Sung Joo An, Sunwoo Lee, Nithin Mathew, Mauricio Terrones, Takuya Hayashi, Catalin R. Picu, James Hone, and Nikhil Koratkar. Effect of defects on the intrinsic strength and stiffness of graphene. *Nature Communications*, 5(1):1–9, 1 2014.

[123] Ashivni Shekhawat and Robert O. Ritchie. Toughness and strength of nanocrystalline graphene. *Nature Communications*, 7(1):1–8, 1 2016.

[124] Guillermo López-Polín, Cristina Gómez-Navarro, Vincenzo Parente, Francisco Guinea, Mikhail I. Katsnelson, Francesc Pérez-Murano, and Julio Gómez-Herrero. Increasing the elastic modulus of graphene by controlled defect creation. *Nature Physics*, 11(1):26–31, 1 2015.

[125] Erich Fitzer. The future of carbon-carbon composites. *Carbon*, 25(2):163–190, 1987.

[126] Zijiao Zhang, Hongwei Sheng, Zhangjie Wang, Bernd Gludovatz, Ze Zhang, Easo P. George, Qian Yu, Scott X. Mao, and Robert O. Ritchie. Dislocation mechanisms and 3D twin architectures generate exceptional strength-ductility-toughness combination in CrCoNi medium-entropy alloy. *Nature Communications*, 8(1):1–8, 2 2017.

[127] Sheng Yang Zhou, Ben Niu, Xu Long Xie, Xu Ji, Gan Ji Zhong, Benjamin S. Hsiao, and Zhong Ming Li. Interfacial Shish-Kebabs Lengthened by Coupling Effect of In Situ Flexible Nanofibrils and Intense Shear Flow: Achieving Hierarchy To Conquer the Conflicts between Strength and Toughness of Polylactide. *ACS Applied Materials and Interfaces*, 9(11):10148–10159, 3 2017.

[128] Chien Min Sung and Michael Sung. Carbon nitride and other speculative superhard materials. *Materials Chemistry and Physics*, 43(1):1–18, 1996.

[129] Go Yamamoto, Keiichi Shirasu, Toshiyuki Hashida, Toshiyuki Takagi, Ji Won Suk, Jinho An, Richard D. Piner, and Rodney S. Ruoff. Nanotube fracture during the failure of carbon nanotube/alumina composites. *Carbon*, 49(12):3709–3716, 10 2011.

[130] P. Zhang, S. X. Li, and Z. F. Zhang. General relationship between strength and hardness. *Materials Science and Engineering A*, 529(1):62–73, 11 2011.

[131] W C Oliver and G M Pharr. An improved technique for determining hardness and elastic modulus using load and displacement sensing indentation experiments. *Journal of Materials Research*, 1992.

[132] B. D. Fulcher, X. Y. Cui, B. Delley, and C. Stampfl. Hardness analysis of cubic metal mononitrides from first principles. *Physical Review B - Condensed Matter and Materials Physics*, 85(18):1–9, 2012.

[133] J Haines, J M Léger, and G Bocquillon. Synthesis and Design of Superhard Materials. *Annual Review of Materials Research*, 31(1):1–23, 8 2001.

[134] Ashley L. Kaiser, Itai Y. Stein, Kehang Cui, and Brian L. Wardle. Process-morphology scaling relations quantify self-organization in capillary densified nanofiber arrays. *Physical Chemistry Chemical Physics*, 20(6):3876–3881, 2 2018.

[135] Marie-Pierre G Laborie. *Investigation of the Wood/ Phenol-Formaldehyde Adhesive Interphase Morphology*. PhD thesis, Virginia Polytechnic Institute and State University, Blacksburg, 2 2002.

[136] Muhammad Mansoor and Muhammad Shahid. Carbon nanotube-reinforced aluminum composite produced by induction melting. *Journal of Applied Research and Technology*, 14(4):215–224, 8 2016.

[137] Kang Pyo So, Akihiro Kushima, Jong Gil Park, Xiaohui Liu, Dong Hoon Keum, Hye Yun Jeong, Fei Yao, Soo Hyun Joo, Hyoung Seop Kim, Hwanuk Kim, Ju Li, and Young Hee Lee. Intragranular Dispersion of Carbon Nanotubes Comprehensively Improves Aluminum Alloys. *Advanced Science*, 5(7):1800115, 7 2018.

[138] R. Pérez-Bustamante, I. Estrada-Guel, W. Antúnez-Flores, M. Miki-Yoshida, P. J. Ferreira, and R. Martínez-Sánchez. Novel Al-matrix nanocomposites reinforced with multi-walled carbon nanotubes. *Journal of Alloys and Compounds*, 2008.

[139] Yufeng Wu and Gap Yong Kim. Carbon nanotube reinforced aluminum composite fabricated by semi-solid powder processing. *Journal of Materials Processing Technology*, 211(8):1341–1347, 8 2011.

[140] Jianhua Wu, Hailong Zhang, Yang Zhang, and Xitao Wang. Mechanical and thermal properties of carbon nanotube/aluminum composites consolidated by spark plasma sintering. *Materials and Design*, 41:344–348, 10 2012.

[141] F. Rikhtegar, S. G. Shabestari, and H. Saghafian. Microstructural evaluation and mechanical properties of Al-CNT nanocomposites produced by different processing methods. *Journal of Alloys and Compounds*, 723:633–641, 11 2017.

[142] Pham Van Trinh, Nguyen Van Luan, Doan Dinh Phuong, Phan Ngoc Minh, Alicia Weibel, David Mesguich, and Christophe Laurent. Microstructure, microhardness and thermal expansion of CNT/Al composites prepared by flake powder metallurgy. *Composites Part A: Applied Science and Manufacturing*, 105:126–137, 2 2018.

[143] Khurram S. Munir, Peter Kingshott, and Cuie Wen. Carbon nanotube reinforced titanium metal matrix composites prepared by powder metallurgy - A review. *Critical Reviews in Solid State and Materials Sciences*, 40(1):38–55, 2015.

[144] I. Montealegre Melendez, E. Neubauer, P. Angerer, H. Danninger, and J. M. Torralba. Influence of nano-reinforcements on the mechanical properties and microstructure of titanium matrix composites. *Composites Science and Technology*, 71(8):1154–1162, 2011.

[145] Katsuyoshi Kondoh, Thotsaphon Threrujirapapong, Junko Umeda, and Bunshi Fugetsu. High-temperature properties of extruded titanium composites fabricated from carbon nanotubes coated titanium powder by spark plasma sintering and hot extrusion. *Composites Science and Technology*, 72(11):1291–1297, 2012.

[146] Toru Kuzumaki, Osamu Ujiie, Hideki Ichinose, and Kunio Ito. Mechanical Characteristics and Preparation of Carbon Nanotube Fiber-Reinforced Ti Composite. *Advanced Engineering Materials*, 2(7):416–418, 2000.

[147] Shufeng Li, Bin Sun, Hisashi Imai, Takanori Mimoto, and Katsuyoshi Kondoh. Powder metallurgy titanium metal matrix composites reinforced with carbon nanotubes and graphite. *Composites Part A: Applied Science and Manufacturing*, 48(1):57–66, 2013.

[148] F. X. Li, P. D. Hao, J. H. Yi, Z. Chen, K. G. Prashanth, T. Maity, and J. Eckert. Microstructure and strength of nano-/ultrafine-grained carbon nanotube-reinforced titanium composites processed by high-pressure torsion. *Materials Science and Engineering A*, 722(December 2017):122–128, 2018.

[149] K. Wilson, E. V. Barrera, and Y. Bayazitoglu. Processing of titanium single-walled carbon nanotube metal-matrix composites by the induction melting method. *Journal of Composite Materials*, 44(9):1037–1048, 2010.

[150] Fu Chi Wang, Zhao Hui Zhang, Yong Jun Sun, Ying Liu, Zheng Yang Hu, Hu Wang, Alexander V. Korznikov, Elena Korznikova, Zhen Feng Liu, and S. Osamu. Rapid and low temperature spark plasma sintering synthesis of novel carbon nanotube reinforced titanium matrix composites. *Carbon*, 95:396–407, 2015.

[151] David R. Forrest, Iwona Jasiuk, Captain Lloyd Brown, Peter Joyce, Azzam Mansour, and Lourdes Salamanca-Riba. Novel Metal-Matrix Composites with Integrally-Bound Nanoscale Carbon. In *TechConnect WORLD Summit & Innovation Showcase*, Santa Clara, 2012.

[152] Hansang Kwon, Dae Hoon Park, Jean François Silvain, and Akira Kawasaki. Investigation of carbon nanotube reinforced aluminum matrix composite materials. *Composites Science and Technology*, 70(3):546–550, 3 2010.

[153] Ziyun Yu, Zhanqiu Tan, Genlian Fan, Ding Bang Xiong, Qiang Guo, Renbang Lin, Li Hu, Zhiqiang Li, and Di Zhang. Effect of interfacial reaction on Young's modulus in CNT/Al nanocomposite: A quantitative analysis. *Materials Characterization*, 137:84–90, 3 2018.

[154] Mete Bakir and Iwona Jasiuk. Novel metal-carbon nanomaterials: A review on covetics. *Advanced Materials Letters*, pages 884–890, 2017.

[155] Dilermando N. Travessa, Geovana V.B. da Rocha, Kátia R. Cardoso, and Marcela Lieblich. Carbon Nanotube-Reinforced Aluminum Matrix Composites Produced by High-Energy Ball Milling. *Journal of Materials Engineering and Performance*, 26(6):2998–3006, 6 2017.

[156] N. Chawla and K. K. Chawla. Metal-matrix composites in ground transportation, 11 2006.

[157] Kang Pyo So, Il Ha Lee, Dinh Loc Duong, Tae Hyung Kim, Seong Chu Lim, Kay Hyeok An, and Young Hee Lee. Improving the wettability of aluminum on carbon nanotubes. *Acta Materialia*, 59(9):3313–3320, 5 2011.

[158] Afsaneh Dorri Moghadam, Benjamin F. Schultz, J. B. Ferguson, Emad Omrani, Pradeep K. Rohatgi, and Nikhil Gupta. Functional metal matrix composites: Self-lubricating, self-healing, and nanocomposites-an outlook. *The Journal of the Minerals, Metals, and Materials Society*, 66(6):872–881, 4 2014.

[159] John C. Berg. *Wettability.* Marcel Dekker, New York, 1993.

[160] Yawei Liu, Jianjun Wang, and Xianren Zhang. Accurate determination of the vapor-liquid-solid contact line tension and the viability of Young equation. *Scientific Reports*, 3(1):1–6, 6 2013.

[161] Hailong Liu and Guoxin Cao. Effectiveness of the Young-Laplace equation at nanoscale. *Scientific Reports*, 6(1):1–10, 4 2016.

[162] Frank Weaver. Epoxy Adhesive Surface Energies via the Pendant Drop Method. Technical report, Morris Brown College, Atlanta, 12 1982.

[163] K. Landry, S. Kalogeropoulou, and N. Eustathopoulos. Wettability of carbon by aluminum and aluminum alloys. *Materials Science and Engineering A*, 254(1-2):99–111, 10 1998.

[164] Brent J Carey, Jerome T Tzeng, and Shashi Karna. Carbon Nanotube Aluminum Matrix Composites. Technical report, Army Research Laboratory, 2010.

[165] Yu He, Jinyu Zhang, Yan Wang, and Zhiping Yu. Coating geometries of metals on single-walled carbon nanotubes. *Applied Physics Letters*, 96(6):063108, 2 2010.

[166] Peng Jin, Yibo Liu, Qingjie Sun, Qiaoli Lin, Junzhao Li, Kun Chen, Jianfeng Wang, Shaojun Hou, Fuxiang Li, and Jicai Feng. Wetting of liquid aluminum alloys on pure titanium at 873-973 K. *Journal of Materials Research and Technology*, 8(6):5813–5822, 11 2019.

[167] Sang Chul Roh, Eun Yub Choi, Yeon Sik Choi, and C. K. Kim. Characterization of the surface energies of functionalized multi-walled carbon nanotubes and their interfacial adhesion energies with various polymers. *Polymer*, 55(6):1527–1536, 3 2014.

[168] L. Vitos, A. V. Ruban, H. L. Skriver, and J. Kollár. The surface energy of metals, taken at melting temperature. *Surface Science*, 411(1-2):186–202, 8 1998.

[169] Fathi Aqra and Ahmed Ayyad. Surface energies of metals in both liquid and solid states. *Applied Surface Science*, 257(15):6372–6379, 5 2011.

[170] T. A. Roth. The surface and grain boundary energies of iron, cobalt and nickel. *Materials Science and Engineering*, 18(2):183–192, 4 1975.

[171] F H Howie and E D Hondros. The surface tension of tin-lead alloys in contact with fluxes. *Journal of Materials Science*, 17(0):1434–144, 1982.

[172] S. K. Rhee. Wetting of Ceramics by Liquid Aluminum. *Journal of the American Ceramic Society*, 53(7):386–389, 7 1970.

[173] Zbigniew Łodziana, Nan Yu Topsøe, and Jens K. Nørskov. A negative surface energy for alumina. *Nature Materials*, 3(5):289–293, 4 2004.

[174] Sebastian Osswald, Mickael Havel, and Yury Gogotsi. Monitoring oxidation of multiwalled carbon nanotubes by Raman spectroscopy. *Journal of Raman Spectroscopy*, 38(6):728–736, 6 2007.

[175] Baisong Guo, Xinming Zhang, Xi Cen, Biao Chen, Xinhua Wang, Min Song, Song Ni, Jianhong Yi, Tao Shen, and Yong Du. Enhanced mechanical properties of aluminum based composites reinforced by chemically oxidized carbon nanotubes. *Carbon*, 139:459–471, 11 2018.

[176] Luiz Acauan, Anna C. Dias, Marcelo B. Pereira, Flavio Horowitz, and Carlos P. Bergmann. Influence of Different Defects in Vertically Aligned Carbon Nanotubes on TiO$_2$ Nanoparticle Formation through Atomic Layer Deposition. *ACS Applied Materials & Interfaces*, 8(25):16444–16450, 6 2016.

[177] Z. Zhang and D. L. Chen. Consideration of Orowan strengthening effect in particulate-reinforced metal matrix nanocomposites: A model for predicting their yield strength. *Scripta Materialia*, 54(7):1321–1326, 4 2006.

[178] B. Chen, J. Shen, X. Ye, L. Jia, S. Li, J. Umeda, M. Takahashi, and K. Kondoh. Length effect of carbon nanotubes on the strengthening mechanisms in metal matrix composites. *Acta Materialia*, 140:317–325, 11 2017.

[179] Kang Pyo So, Xiaohui Liu, Hideki Mori, Akihiro Kushima, Jong Gil Park, Hyoung Seop Kim, Shigenobu Ogata, Young Hee Lee, and Ju Li. Ton-scale metal–carbon nanotube composite: The mechanism of strengthening while retaining tensile ductility. *Extreme Mechanics Letters*, 8:245–250, 9 2016.

[180] Riccardo Casati and Maurizio Vedani. Metal matrix composites reinforced by Nano-Particles—A review. *Metals*, 4(1):65–83, 3 2014.

[181] Z. Y. Liu, B. L. Xiao, W. G. Wang, and Z. Y. Ma. Singly dispersed carbon nanotube/aluminum composites fabricated by powder metallurgy combined with friction stir processing. *Carbon*, 50(5):1843–1852, 4 2012.

[182] Z. Zhang and D. L. Chen. Contribution of Orowan strengthening effect in particulate-reinforced metal matrix nanocomposites. *Materials Science and Engineering A*, 483-484(1-2 C):148–152, 6 2008.

[183] Fumio Ogawa, Shuji Yamamoto, and Chitoshi Masuda. Strong, ductile, and thermally conductive carbon nanotube-reinforced aluminum matrix composites fabricated by ball-milling and hot extrusion of powders encapsulated in aluminum containers. *Materials Science and Engineering A*, 711:460–469, 1 2018.

[184] M. Taya, K. E. Lulay, and D. J. Lloyd. Strengthening of a particulate metal matrix composite by quenching. *Acta Metallurgica Et Materialia*, 39(1):73–87, 1991.

[185] Amine A. Benzerga and Jean Baptiste Leblond. *Ductile Fracture by Void Growth to Coalescence*, volume 44. Elsevier, 1 2010.

[186] B. Chen, K. Kondoh, H. Imai, J. Umeda, and M. Takahashi. Simultaneously enhancing strength and ductility of carbon nanotube/aluminum composites by improving bonding conditions. *Scripta Materialia*, 113:158–162, 2016.

[187] T. Kuzumaki, K. Miyazawa, H. Ichinose, and K. Ito. Processing of carbon nanotube reinforced aluminum composite. *Journal of Materials Research*, 13(9):2445–2449, 1998.

[188] Xudong Yang, Enzuo Liu, Chunsheng Shi, Chunnian He, Jiajun Li, Naiqin Zhao, and Katsuyoshi Kondoh. Fabrication of carbon nanotube reinforced Al composites with well-balanced strength and ductility. *Journal of Alloys and Compounds*, 563:216–220, 6 2013.

[189] C. N. He, N. Q. Zhao, C. S. Shi, and S. Z. Song. Mechanical properties and microstructures of carbon nanotube-reinforced Al matrix composite fabricated by in situ chemical vapor deposition. *Journal of Alloys and Compounds*, 487(1-2):258–262, 11 2009.

[190] Julien Stein, Blanka Lenczowski, Eric Anglaret, and Nicole Fréty. Influence of the concentration and nature of carbon nanotubes on the mechanical properties of AA5083 aluminium alloy matrix composites. *Carbon*, 77:44–52, 2014.

[191] C. L. Xu, B. Q. Wei, R. Z. Ma, J. Liang, X. K. Ma, and D. H. Wu. Fabrication of aluminum-carbon nanotube composites and their electrical properties. *Carbon*, 37(5):855–858, 4 1999.

[192] B. Chen, K. Kondoh, J. Umeda, S. Li, L. Jia, and J. Li. Interfacial in-situ Al2O3 nanoparticles enhance load transfer in carbon nanotube (CNT)-reinforced aluminum matrix composites. *Journal of Alloys and Compounds*, 789:25–29, 6 2019.

[193] Xinghai Liu, Jiajun Li, Enzuo Liu, Qunying Li, Chunnian He, Chunsheng Shi, and Naiqin Zhao. Effectively reinforced load transfer and fracture elongation by forming Al4C3 for in-situ synthesizing carbon nanotube reinforced Al matrix composites. *Materials Science and Engineering A*, 718:182–189, 3 2018.

[194] Natalya Larianovsky, Vladimir Popov, Alexander Katz-Demyanetz, Alex Fleisher, Douglas E. Meyers, and Ray S. Chaudhuri. Production of Al Metal Matrix Composites Reinforced with Carbon Nanotubes by Two-Stage Melt-Based HPDC-CE Method. *Journal of Engineering Materials and Technology, Transactions of the ASME*, 141(1), 1 2019.

[195] W.C. Harrigan. Processing of Aluminum Metal-Matrix Composites. In Kevin Anderson, John Weritz, and J. Gilbert Kaufman, editors, *Aluminum Science and Technology*, volume 2A, pages 375–386. ASM International, 2018.

[196] Amit Mahajan, Angus Kingon, Ákos Kukovecz, Zoltan Konya, and Paula M. Vilarinho. Studies on the thermal decomposition of multiwall carbon nanotubes under different atmospheres. *Materials Letters*, 90:165–168, 2013.

[197] Lijie Ci, Zhenyu Ryu, Neng Yun Jin-Phillipp, and Manfred Rühle. Investigation of the interfacial reaction between multi-walled carbon nanotubes and aluminum. *Acta Materialia*, 54(20):5367–5375, 12 2006.

[198] Anastasios John Hart and Alexander H. Slocum. Rapid growth and flow-mediated nucleation of millimeter-scale aligned carbon nanotube structures from a thin-film catalyst. *Journal of Physical Chemistry B*, 110(16):8250–8257, 4 2006.

[199] Enrique J García, A John Hart, and Brian L Wardle. Long Carbon Nanotubes Grown on the Surface of Fibers for Hybrid Composites. *AIAA Journal*, 46(6):1405–1412, 2008.

[200] Sreeram Vaddiraju, Hülya Cebeci, Karen K. Gleason, and Brian L. Wardle. Hierarchical multifunctional composites by conformally coating aligned carbon nanotube arrays with conducting polymer. *ACS Applied Materials and Interfaces*, 1(11):2565–2572, 11 2009.

[201] J. D. Núñez, A. M. Benito, S. Rouzière, P. Launois, R. Arenal, P. M. Ajayan, and W. K. Maser. Graphene oxide-carbon nanotube hybrid assemblies: Cooperatively strengthened OH...O=C hydrogen bonds and the removal of chemisorbed water. *Chemical Science*, 8(7):4987–4995, 2017.

[202] Shin-Shueh Chen. Effects of annealing on the properties of hermetically carbon-coated optical fibers prepared by plasma enhanced chemical vapor deposition method. *Optical Engineering*, 46(3):035008, 2007.

[203] Wei Huang, Yao Wang, Guohua Luo, and Fei Wei. 99.9% Purity Multi-Walled Carbon Nanotubes By Vacuum High-Temperature Annealing. *Carbon*, 41(13):2585–2590, 2003.

[204] Material Safety Data Sheet: Durite SC-1008.

[205] Kaan Orhan and Arda Büyüksungur. Fundamentals of Micro-CT Imaging. In *Micro-computed Tomography (micro-CT) in Medicine and Engineering*, pages 27–33. Springer International Publishing, 2020.

[206] Chen Lin, Yuxiao Ding, Bin Xie, Zhujian Sun, Xiaogang Li, Zixian Chen, and Meng Niu. Asymptomatic novel coronavirus pneumonia patient outside Wuhan: The value of CT images in the course of the disease. *Clinical Imaging*, 63:7–9, 7 2020.

[207] C. B. Marschner, M. Kokla, J. M. Amigo, E. A. Rozanski, B. Wiinberg, and F. J. McEvoy. Texture analysis of pulmonary parenchymateous changes related to pulmonary thromboembolism in dogs - a novel approach using quantitative methods. *BMC Veterinary Research*, 13(219), 7 2017.

[208] Usman Bashir, Gurdip Azad, Muhammad Musib Siddique, Saana Dhillon, Nikheel Patel, Paul Bassett, David Landau, Vicky Goh, and Gary Cook. The effects of segmentation algorithms on the measurement of 18F-FDG PET texture parameters in non-small cell lung cancer. *EJNMMI Research*, 7(60), 7 2017.

[209] E. Maire and P. J. Withers. Quantitative X-ray tomography. *International Materials Reviews*, 59(1):1–43, 1 2014.

[210] S. R. Stock. Recent advances in X-ray microtomography applied to materials, 5 2008.

[211] Xinchen Ni, Nathan K. Fritz, and Brian L. Wardle. In Situ Testing Using Synchrotron Radiation Computed Tomography in Materials Research. *MRS Advances*, 4(51-52):2831–2841, 2019.

[212] Eric N. Landis and Denis T. Keane. X-ray microtomography, 12 2010.

[213] Matthew Andrew and Benjamin Hornberger. Iterative Reconstruction for Optimized Tomographic Imaging. Technical report, Zeiss Microscopy, 3 2018.

[214] Huixing Zhang, Eddie López-Honorato, and Ping Xiao. Fluidized bed chemical vapor deposition of pyrolytic carbon-III. Relationship between microstructure and mechanical properties. *Carbon*, 91:346–357, 2015.

[215] Steven M George. Atomic Layer Deposition: An Overview. *Chemical Reviews*, 110(1):111–131, 2010.

[216] Lanxia Cheng, Xiaoye Qin, Antonio T Lucero, Angelica Azcatl, Jie Huang, Robert M Wallace, Kyeongjae Cho, and Jiyoung Kim. Atomic Layer Deposition of a High-k Dielectric on MoS 2 Using Trimethylaluminum and Ozone. *ACS Applied Materials & Interfaces*, 6:11834–11838, 2014.

[217] J. Musschoot, Q. Xie, D. Deduytsche, S. Van den Berghe, R. L. Van Meirhaeghe, and C. Detavernier. Atomic layer deposition of titanium nitride from TDMAT precursor. *Microelectronic Engineering*, 86(1):72–77, 1 2009.

[218] Yong Wan Kim and Do Heyoung Kim. Atomic layer deposition of TiO 2 from tetrakis-dimethylamido-titanium and ozone. *Korean Journal of Chemical Engineering*, 29:969–973, 6 2012.

[219] Chunyan Jin, Ben Liu, Zhongxiang Lei, and Jiaming Sun. Structure and photoluminescence of the TiO2 films grown by atomic layer deposition using tetrakis-dimethylamino titanium and ozone. *Nanoscale Research Letters*, 10(95), 2 2015.

[220] Seenivasan Selvaraj, Hee Moon, Ju-Young Yun, and Do-Heyoung Kim. Iron oxide grown by low-temperature atomic layer deposition. *Korean J. Chem. Eng*, 33(12):3516–3522, 2016.

[221] Alex B.F. Martinson, Michael J. Devries, Joseph A. Libera, Steven T. Christensen, Joseph T. Hupp, Michael J. Pellin, and Jeffrey W. Elam. Atomic layer deposition of Fe2O3 using ferrocene and ozone. *Journal of Physical Chemistry C*, 115(10):4333–4339, 2 2011.

[222] Orvar Braaten, Arne Kjekshus, and Halvor Kvande. The possible reduction of alumina to aluminum using hydrogen. *The Journal of The Minerals, Metals & Materials Society (TMS)*, 52:47–54, 2000.

[223] Michael F. L. De Volder, Sei Jin Park, Sameh H. Tawfick, Daniel O. Vidaud, and A. John Hart. Fabrication and electrical integration of robust carbon nanotube micropillars by self-directed elastocapillary densification Precise control of elastocapillary densification of nanostructures via low-pressure condensation. *Journal of Micromechanics and Microengineering*, 21, 2011.

[224] Nuri Yazdani, Vipin Chawla, Eve Edwards, Vanessa Wood, Hyung Gyu Park, and Ivo Utke. Modeling and optimization of atomic layer deposition processes on vertically aligned carbon nanotubes. *Beilstein Journal of Nanotechnology*, 5:234–244, 3 2014.

[225] Shaoren Deng, Sammy W. Verbruggen, Zhanbing He, Daire J. Cott, Philippe M. Vereecken, Johan A. Martens, Sara Bals, Silvia Lenaerts, and Christophe Detavernier. Atomic layer deposition-based synthesis of photoactive TiO2 nanoparticle chains by using carbon nanotubes as sacrificial templates. *RSC Advances*, 4(23):11648–11653, 2 2014.

[226] W. F. Zhang, Y. L. He, M. S. Zhang, Z. Yin, and Q. Chen. Raman scattering study on anatase TiO2 nanocrystals. *Journal of Physics D: Applied Physics*, 33:916, 2000.

[227] D Bersani, P P Lottici, and Xing-Zhao Ding. Phonon confinement effects in the Raman scattering by TiO2 Nanocrystals. *Applied Physics Letters*, 72:75, 1998.

[228] Keu Hong, Eung Ju Oh, and Jae Shi Choi. Electrical Conductivity of "Hydrogen-Reduced" Titanium Dioxide (Rutile). *Journal of Physical Chemistry Solids*, 45(11/12):1265–1269, 1984.

[229] M. V. Tsarev, V. V. Mokrushin, A. V. Sten'gach, A. I. Tarasova, P. G. Berezhko, I. K. Kremzukov, and E. V. Zabavin. A Study of the Oxidation of Titanium Hydride Powder oy Measurements of Its Electrical Resistance. *Russian Journal of Physical Chemistry*, 84(4):679–683, 2010.

[230] James E Rekoske and Mark A Barteau. Isothermal Reduction Kinetics of Titanium Dioxide-Based Materials. *Journal of Physical Chemistry B*, 101:1113–1124, 1997.

[231] Jingxia Qiu, Sheng Li, Evan Gray, Hongwei Liu, Qin-Fen Gu, Chenghua Sun, Chao Lai, Huijun Zhao, and Shanqing Zhang. Hydrogenation synthesis of blue TiO2 for high-performance lithium-ion batteries. *Journal of Physical Chemistry C*, 118(17):8824–8830, 5 2014.

[232] Parthiban Pazhamalai, Karthikeyan Krishnamoorthy, Vimal Kumar Mariappan, and Sang-Jae Kim. Blue TiO2 nanosheets as a high-performance electrode material for supercapacitors. *Journal of Colloid and Interface Science*, 536:62–70, 2 2019.

[233] R. P. Muller, J. Steinle, and H. P. Boehm. Characterization of Photochemically or Electrochemically Reduced Blue Titanium Dioxide. *Zeitschrift für Naturforschung B*, 45(6), 6 2014.

[234] Vassiliki Alexandra Glezakou and Roger Rousseau. Shedding light on black titania. *Nature Materials*, 17(10):856–857, 10 2018.

[235] Ludovico Megalini. *Synthesis, modeling and testing of CNTs for nano-engineered hybrid advanced composite structures*. PhD thesis, Politecnico Di Torino, 2007.

[236] H W P Koops, R Weiel, D P Kern, and T H Baum. High-resolution electron-beam induced deposition. *Journal of Vacuum Science & Technology B: Micro-electronics Processing and Phenomena*, 6(1):477, 1 1988.

[237] C. F. Deng, X. X. Zhang, D. Z. Wang, and Y. X. Ma. Calorimetric study of carbon nanotubes and aluminum. *Materials Letters*, 61(14-15):3221–3223, 2007.

[238] Daniel Spreitzer and Johannes Schenk. Reduction of Iron Oxides with Hydrogen—A Review. *Steel Research International*, 90(10), 8 2019.

[239] Damien Wagner, Olivier Devisme, Fabrice Patisson, and Denis Ablitzer. A Laboratory Study of the Reduction of Iron Oxides by Hydrogen. In F. Kongoli and R. G. Reddy, editors, *Sohn International Symposium*, volume 2, pages 111–120, San Diego, 8 2006.

[240] Hugo Ricardo Zschommler Sandim, Bruno Vieira Morante, and Paulo Atsushi Suzuki. Kinetics of thermal decomposition of titanium hydride powder using in situ High-temperature X-ray Diffraction (HTXRD). *Materials Research*, 8(3):293–297, 2005.

[241] Yoshihiko Hirooka. Thermal decomposition of titanium hydride and its application to low pressure hydrogen control. *Journal of Vacuum Science & Technology A: Vacuum, Surfaces, and Films*, 2(1):16–21, 1 1984.

[242] Ying Zhang, Zhigang Zak Fang, Lei Xu, Pei Sun, Brian Van Devener, Shili Zheng, Yang Xia, Ping Li, and Yang Zhang. Mitigation of the Surface Oxidation of Titanium by Hydrogen. *The Journal of Physical Chemistry C*, 122:20691–20700, 2018.

[243] Yang Donghui, H E Deping, and Yang Shangrun. Thermal decomposition kinetics of titanium hydride and Al alloy melt foaming process. *Science in China Ser. B Chemistry*, 47(6):512–520, 2004.

[244] I N Frantsevich, L A Grishnova, and V L Tikush. Theory and Technology of Sintering, Thermal, and Chemicothermal Treatment Processes Reaction of Titanium with Nitrogen During Heating by Radiant Energy. Technical Report 5, Plenum Publishing Corporation, 1986.

[245] Ulrike Diebold. The surface science of titanium dioxide, 1 2003.

[246] Carl Jonas Fjellstedt and Anders E. W. Jarfors. Experimental and theoretical study of the Al-rich corner in the ternary Al-Ti-B system and reassessment of the Al-rich side of the binary Al-B phase diagram. *Zeitschrift fuer Metall-lkunde/Materials Research and Advanced Techniques*, 92, 6 2002.

[247] X M Xue, J T Wang, and M X Quan. Wettability and spreading kinetics of liquid aluminium on boron nitride. *Journal of Materials Science*, 26:6391–6395, 1991.